Combined Measurement of Single Top-Quark Production in the *s* and *t*-Channel with the ATLAS Detector and Effective Field Theory Interpretation

DISSERTATION

zur Erlangung des akademischen Grades

doctor rerum naturalium

(Dr. rer. nat.)

im Fach Physik

Spezialisierung: Experimentalphysik

eingereicht an der

Mathematisch-Naturwissenschaftlichen Fakultät

der Humboldt-Universität zu Berlin

von

M. Sc. Sören Stamm

Präsidentin der Humboldt-Universität zu Berlin
Prof. Dr.-Ing. Dr. Sabine Kunst

Dekan der Mathematisch-Naturwissenschaftlichen Fakultät
Prof. Dr. Elmar Kulke

Gutachter:	1. Prof. Dr. Thomas Lohse 2. Prof. Dr. Heiko Lacker 3. Assoc. Prof. Cen Zhang
Tag der mündlichen Prüfung:	12. März 2018

Abstract

This thesis presents a combined measurement of single top-quark production in the s and t-channel with the ATLAS detector at the Large Hadron Collider. The 2012 data set of proton–proton collisions at a centre-of-mass energy of 8 TeV corresponding to an integrated luminosity of $20.3\,\mathrm{fb}^{-1}$ is used. The event selection for both channels requires one isolated electron or muon and two jets in the final state. In order to separate signal from background events, a discriminant variable is built from likelihoods obtained with the matrix element method. The cross section for both channels are determined by a combined maximum likelihood fit, which yields $\sigma_s = 4.9 \pm 1.7\,\mathrm{pb}$ and $\sigma_t = 82.32^{+7.0}_{-5.5}\,\mathrm{pb}$ for the s-channel and t-channel, respectively. The correlation of the two cross section measurements is 8 %. These results together with an independent measurement of the associated Wt production are used to set limits on two parameters, $\bar{c}_{\phi\mathrm{q}}$ and $\bar{c}_{\mathrm{qq}}$, within the framework of an effective field theory. Acceptance corrections are derived as a function of the model parameters by using fast and simplified detector simulations. These corrections are included in the statistical model and the smallest intervals that correspond to 95.5 % probability are $-0.132 < \bar{c}_{\phi\mathrm{q}} < 0.048$ and $-0.0283 < \bar{c}_{\mathrm{qq}} < 0.0062$ for the two parameters.

Zusammenfassung

In dieser Arbeit wird eine kombinierte Messung der elektro-schwachen Produktion einzelner Top-Quarks im s- und t-Kanal vorgestellt. Der analysierte Datensatz von Proton-Proton-Kollisionsereignissen wurde im Jahr 2012 mit dem ATLAS Detektor am Large Hadron Collider bei einer Schwerpunktsenergie von 8 TeV aufgezeichnet und entspricht einer integrierten Luminosität von $20{,}3\,\mathrm{fb}^{-1}$. Die Ereignisauswahl beschränkt sich auf Ereignisse mit einem isolierten Elektron oder Myon und zwei Jets. Mit Hilfe der Matrix Element Methode werden Prozess-Likelihoods berechnet. Aus diesen wird eine Diskriminante gebildet um Signal- und Untergrundereignisse voneinander zu trennen. Die Wirkungsquerschnitte für die Produktion einzelner Top-Quarks wurden mittels eines kombinierten Maximum Likelihoods Fits zu $\sigma_s = 4{,}9 \pm 1{,}7\,\mathrm{pb}$ und $\sigma_t = 82{,}32^{+7{,}0}_{-5{,}5}\,\mathrm{pb}$ bestimmt. Die Korrelation zwischen beiden Messungen beträgt 8 %. Diese beiden Ergebnisse werden zusammen mit einer unabhängigen Messung der assoziierten Wt Produktion verwendet um zwei Parameter, $\bar{c}_{\phi\mathrm{q}}$ und $\bar{c}_{\mathrm{qq}}$, im Rahmen einer effektiven Feldtheorie zu bestimmen. Notwendige Akzeptanzkorrekturen wurden mit Hilfe schneller und vereinfachter Detektorsimulationen ermittelt. Diese Korrekturen werden in dem statistischen Modell zur Bestimmung der effektiven Feldtheorie-Parametern berücksichtigt. Die kleinsten Intervalle, welche 95,5 % des gesamten Wahrscheinlichkeitsbereichs entsprechen, sind $-0{,}132 < \bar{c}_{\phi\mathrm{q}} < 0{,}048$ und $-0{,}0283 < \bar{c}_{\mathrm{qq}} < 0{,}0062$ für die beiden Kopplungsparameter.

Contents

1. Introduction

The standard model (SM) of elementary particle physics describes the fundamental building blocks of matter and their interactions. Among all known quarks, the top-quark is by far the heaviest one. Due to its high mass, it was the last quark to be discovered in 1995 at the Tevatron [CDF95, D0 95]. In order to study the top-quark, it can be produced in proton–proton collisions in pairs via the strong interaction or singly via electro-weak interactions. Regarding the production of single top-quarks, three different production channels are distinguished. Two channels involving space-like and time-like W boson propagators exist. They are referred to as t-channel and s-channel single top-quark production. In addition, the associated production of a top-quark and a W boson is possible. All three production modes can be used to probe the electro-weak coupling of the top-quark and study the tWb vertex.

The Large Hadron Collider (LHC) started its operation in 2009 and has been providing large data sets for top-quark physics at centre-of-mass energies of 7, 8 and 13 TeV. In 2012, the discovery of a new boson was announced by the ATLAS [ATL15e] and CMS collaborations [CMS15]. This new particle behaves very much like the last missing piece of the SM, the Higgs boson. Although all particles predicted by the SM have been found, the SM is not a complete model. Some open questions remain, for example the Higgs mechanism, which explains how the charged fermions and electro-weak gauge bosons in the SM acquire their masses, can not be extended to the neutrino sector. Moreover, the masses of the fermions and gauge bosons in the SM are not predicted by the theory itself, but must be measured experimentally. Furthermore, there is no candidate in the SM that could explain the dark matter or dark energy observed in astrophysical experiments.

Besides the precise measurement of SM parameters, the major goal of the physics programme at the LHC is to search for physics beyond the SM. These searches are divided in two groups. On the one hand, many analyses search for new particles, that can be produced in proton–proton collision events. However, so far no direct search has revealed a new particle and the limits on potential new particles reach up to the TeV scale [ATL17d]. On the other hand, one can also search for new interactions of SM particles. These new interactions might be due to a much heavier particle, which is very unlikely to be produced directly at the LHC. However, it can have an impact on the interactions between SM particles. A possible extension of the SM is an effective field theory (EFT), in which new interactions are parametrized by the

coefficients of higher-dimension operators. Single top-quark production is sensitive to some of these new operators and it is possible to constrain the strength of their respective coupling by a precise cross section measurement of the single top-quark production in all three channels.

The goal of this thesis is the cross section measurement of single top-quark production in the s and t-channel using proton–proton collisions at a centre-of-mass energy of 8 TeV recorded with the ATLAS detector. The challenge of measurements in the single-top sector is that the signal contribution only accounts for a small fraction of the full data set. Therefore, the employed analysis strategy makes use of the matrix element method to discriminate signal events against the otherwise overwhelming background. A specialized toolkit to apply the matrix element method to a large data set was developed in cooperation with the experimental particle physics group at Berlin in the context of this thesis. Moreover, the s-channel cross section measurement reported in this thesis was performed using the afore mentioned toolkit and is published in [ATL16a]. The same analysis strategy was extended to the t-channel as well and the correlation between the two analyses is determined. In addition to the two cross section measurements, a combination of single-top cross section measurements in all three production channels is presented in order to constrain the coefficients of the new physics operators contained in the EFT model. An important aspect of this statistical analysis is to incorporate acceptance corrections in the statistical model. The corrections account for changes in the selection acceptance and shape of the discriminant distributions involved in the cross section measurements. These corrections will be derived by using fast detector simulations and two examples for such simulations will be given.

The content of the thesis is organized as follows. In Sec. 2, a short overview about the theoretical framework of the SM with an emphasis on top-quark physics is given. The experimental setup, the LHC and the ATLAS detector, as well as the signature of proton–proton collision events in the detector is described in Secs. 3–5. The matrix element method and its application to the single-top analysis is the topic of Sec. 6 and 7, respectively. The systematic uncertainties of the cross section measurement are discussed in Sec. 8, while the cross section measurement itself is contained in Sec. 9. Section 10 starts with a short introduction to effective field theories and its implications on the single-top sector. Emphasize is put on the acceptance corrections and how these corrections can be determined by using fast and simplified detector simulations. Finally, all three cross section measurements in the single-top sector are combined to set limits on possible new interactions, predicted by the EFT.

2. The Top-Quark and the Standard Model

The standard model of elementary particle physics comprises of fundamental particles, their properties and interactions between them. It unifies the descriptions of the strong, weak and electromagnetic forces in the framework of renormalizable quantum field theories. Table 2.1 lists the main properties of the elementary fields in the SM. Quarks and leptons are fermions, i. e. particles with spin $S = \frac{1}{2}$, and they are arranged in three generations. Each generation consists of pairs of quarks and leptons and their anti-particles. The first generation contains the up-quark (u) and down-quark (d), which are the constituents of the proton and neutron. Furthermore, it contains the lightest charged lepton, the electron and its neutrino. The strange- (s) and charm-quark (c) along with the bottom- (b) and top-quark (t) complete the second and third generation of quarks, respectively. The muon (μ), τ-lepton and their neutrinos make up the lepton sector. Interactions between particles of the standard model are mediated by gauge bosons. The gauge bosons associated with electro-weak interactions are the photon and the $W^{\pm}$ and Z boson. The photon and Z boson propagate the electromagnetic and weak neutral currents, while the $W^{\pm}$ bosons couple

Quarks: $S = \frac{1}{2}$				Leptons: $S = \frac{1}{2}$		
$Q = \frac{2}{3}$	m [GeV]	$Q = -\frac{1}{3}$	m [GeV]	$Q = -1$	m [GeV]	$Q = 0$
u	$2.20 \cdot 10^{-3}$	d	$4.70 \cdot 10^{-3}$	e	$0.51 \cdot 10^{-3}$	ν_e
c	1.27	s	0.96	μ	$105.65 \cdot 10^{-3}$	ν_μ
b	4.18	t	173.21	τ	1.78	ν_τ

Gauge Bosons: $S = 1$					Higgs Boson: $S = 0$
quanta	g_1, ..., g_8	γ	$W^{\pm}$	Z^0	h
m [GeV]	0	$<10^{-27}$ eV	80.39	91.19	125.09

Table 2.1.: Elementary particles of the standard model. Fermions are split into quarks and leptons and are grouped in three generations. Interactions are mediated by gauge bosons and particles acquire mass through interactions with the Higgs field. Natural units are used, i. e. $\hbar = 1$ and $c = 1$. Adapted table from [GGS99], information on mass measurements and their uncertainties can be found in [Pat+16].

only to left-handed fermions, i. e. particles with spin oriented opposite to the direction of motion. Quantum chromodynamics (QCD) describes strong interactions between quarks and gluons via the exchange of colour charge. Since gluons themselves carry colour charge, they can interact with one another. As a consequence, the strength of the strong force increases with the distance between two coloured objects. Therefore, quarks and gluons can not be observed as free particles, but form colour neutral bound states, called hadrons. The properties of hadrons are described by the quark model, which predicts the properties of hadrons based on the quantum numbers of their constituent quarks. All hadrons can be classified into one of two groups, mesons or baryons. Mesons are bound states of quark-antiquark pairs, whereas baryons are made from a combination of three quarks. [GGS99, Pat+16]

Fermions and bosons acquire their mass through interactions with the Higgs field. The boson associated with this field is the Higgs boson, which is so far the only spin $S = 0$ gauge boson in the standard model. The mass of quarks and charged leptons increase with every generation, while the photon and gluons are massless. The presence of neutrino oscillations requires non-vanishing neutrino masses. However, the mechanism for neutrinos to acquire mass might be different from that of other particles in the standard model. [GGS99, Pat+16]

As listed in Tab. 2.1, the top-quark is the heaviest elementary particle with a mass of $173.21 \pm 0.51 \pm 0.71\,\mathrm{GeV}$ [Pat+16]. Its Yukawa coupling to the Higgs boson is of the order of unity. The measurement of the top-quark properties, e. g. mass, couplings or cross sections, is an important test of the standard model and might reveal information on new physics. [Pat+16, Sch12, KNK08]

2.1. Top-Quark Production at Hadron Colliders

The discovery of the b-quark in 1977 [Her+77] and the measurement of its properties strongly indicated that a partner quark is required, the top-quark. Although, the search for the top-quark started around late 1970's, due to its high mass, it was discovered only in 1995 by the CDF [CDF95] and DØ [D0 95] experiments at the Tevatron, a hadron collider.

Hadron colliders, in particular proton–proton colliders, are currently the only facilities at which top-quarks can be produced efficiently and studied in detail. In contrast to electrons, protons loose less energy due to synchrotron radiations and therefore higher centre-of-mass energies can be reached. However, the proton is a composite object of quarks and gluons. Its properties are determined by the three valence quarks, two up-quarks and one down-quark. The protons total momentum is distributed to its constituent quarks and gluons, called partons. Heavy quarks are produced in deeply inelastic proton–proton collisions in a hard interaction between a constituent of each proton. The energy of this interaction is given by the individual momenta of the

colliding partons. The probability for a parton to carry a certain momentum fraction of the total proton momentum is described by parton density functions (PDF). These PDF were measured in deep inelastic scattering experiments, like HERA, and different collaborations exists to extract these functions by a fit to data.

In such collisions, top-quarks are mainly produced in pairs via the strong interaction. The corresponding Feynman diagrams of the hard process are shown in Fig. 2.1 and the largest contribution to the top-quark pair production cross section comes from the gluon-fusion process. The hard interaction can be factorized from the soft interactions and cross section predictions can be calculated using the factorization theorem [Ell+79]. In order to make use of it, two scales need to be specified, μ_F and μ_R. The factorization scale μ_F defines the hard-interaction process such that soft collinear emissions of initial state particles are absorbed in the definition of the PDFs. The renormalization scale μ_R is associated with the renormalization of the strong coupling constant α_s and indicates the effective strength of the strong interactions for such processes. The choice of the scales μ_R and μ_F depends on each process. A possible choice is to use a unified scale μ for μ_F and μ_R and set $\mu = Q^2$, where Q^2 is the negative four-momentum transfer of the hard scattering process. A schematic of the factorization theorem is depicted in Fig. 2.2. Additional soft interactions can occur between the proton remnants and low energetic particles are produced.

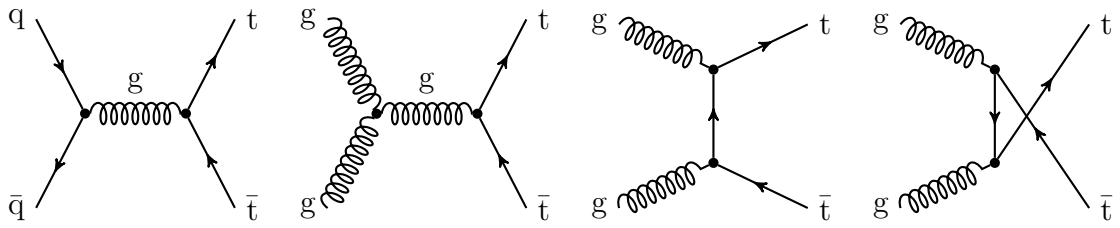

(a) $q\bar{q}$ annihilation (b) s-channel (c) t-channel (d) u-channel

Figure 2.1.: Feynman diagrams for top-quark pair production in leading order QCD. Top-quark pairs are produced in (a) quark-antiquark annihilation or by gluon fusion via (b) s-channel, (c) t-channel and (d) u-channel processes

Finally, the hadronic cross section σ for top-quark pair production in leading order QCD (LO) is given by the following equation

$$\sigma\left(\mathrm{pp} \to \mathrm{t\bar{t}}\right) = \sum_{a,b} \int \mathrm{d}x_1\, \mathrm{d}x_2 f_a(x_1, \mu_F^2) f_b(x_2, \mu_F^2)\, \mathrm{d}\hat{\sigma}_{a,b\to \mathrm{t\bar{t}}}\left(x_1 x_2 s, \mu_R^2, \mu_F^2\right). \quad (2.1)$$

Here, x_1 and x_2 denote the momentum fraction of the colliding partons and s is the squared centre-of-mass energy of the proton beams. Furthermore, $f_{a/b}$ stands for the PDFs of parton a and b, respectively, and $\hat{\sigma}$ is the partonic cross section for the hard scattering process in question. The sum in Eq. 2.1 runs over all possible initial parton combinations that contribute to top-quark pair production. The scale dependence of

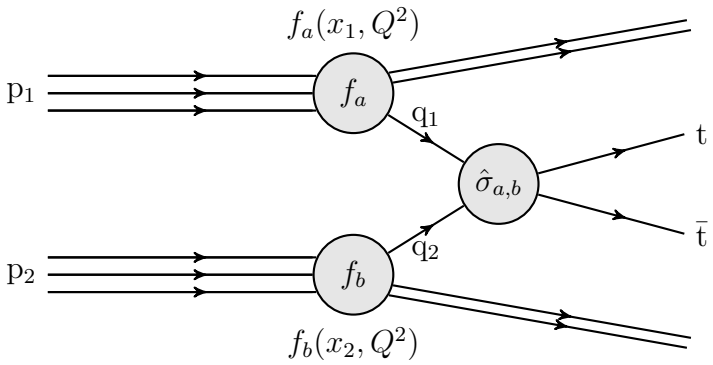

Figure 2.2.: Schematic of top-quark pair production in proton–proton collisions. The hadronic cross section σ is given by the sum of all partonic cross section $\hat{\sigma}_{a,b}$ weighted by the PDFs of the initial partons.

the total cross section is unphysical and it vanishes if the full calculation in all orders would be carried out. [Sch12, CHS07, KNK08, Pat+16]

2.2. The Top-Quark Decay

The SM prediction of the top-quark width Γ_t at next-to-leading order QCD (NLO) is

$$\Gamma_\mathrm{t} = \frac{G_\mathrm{F} m_\mathrm{t}^3}{8\pi\sqrt{2}} |V_\mathrm{tb}|^2 \left(1 - \frac{m_\mathrm{W}^2}{m_\mathrm{t}^2}\right)^2 \left(1 + 2\frac{m_\mathrm{W}^2}{m_\mathrm{t}^2}\right) \left[1 - \frac{2\alpha_s}{3\pi}\left(\frac{2\pi^2}{3} - \frac{5}{2}\right)\right]. \tag{2.2}$$

G_F is the Fermi constant, m_t and m_W denote the mass of the top-quark and the W boson, respectively. It is further assumed that $|V_\mathrm{tb}| \gg |V_\mathrm{ts}|, |V_\mathrm{td}|$, which implies that decays such as $\mathrm{t} \to \mathrm{W(d, s)}$ are strongly suppressed in the SM. The quantities $|V_\mathrm{tq}|$ refer to the magnitudes of the CKM matrix elements, which yield the probability that a top quark decays into a down-type quark of a different flavour. The branching ratios for the decays $\mathrm{t} \to \mathrm{Ws}$ and $\mathrm{t} \to \mathrm{Wd}$ are about 0.2 % and 0.005 %, respectively. Therefore, the top quark decays almost exclusively into b-quarks. Evaluating Eq. 2.2 for a top-quark mass of 173.21 GeV yields $\Gamma_\mathrm{t} = 1.33\,\mathrm{GeV}$, which corresponds to a lifetime of $\tau_\mathrm{t} \approx 5 \cdot 10^{-25}$. This is much smaller than the typical time scale $\tau \sim 1\,\mathrm{fm/c} \sim 3 \cdot 10^{-24}\,\mathrm{s}$ on which hadrons are formed. As a consequence, the top-quark decays before it hadronizes. It is the only quark that can be studied as bare quark free from hadronisation effects. Furthermore, the spin information of the top-quark is passed to its decay products. The Feynman diagram of the top-quark decay is shown in Fig. 2.3 and includes the decay of the W boson into a lepton pair. This decay mode makes up about one third of all top decays. In all other cases, the W boson decays hadronically. However, this is experimentally more difficult to measure due to large QCD background. Furthermore, electrons and muons are easier to identify. Although τ-leptons are contributing to a leptonic final state in top-quark decays too, they decay more often rapidly into

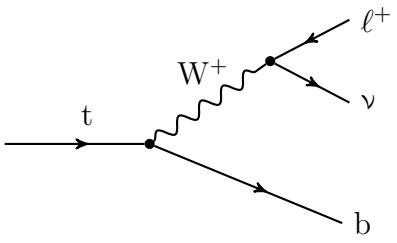

Figure 2.3: Feynman diagram of the top-quark decay into a lepton pair and a b-quark. Decay modes with quarks in the final state, i. e. when the W boson decays hadronically, account for about 2/3 of all decays, but are more difficult to measure experimentally.

hadrons than electrons or muons. Usually, they are not considered in analyses of leptonic top-quark decays. [Sch12, Pat+16]

2.3. Electro-weak Production of Top-Quarks

Top-quarks can not only be produced in pairs via strong interactions, but also singly via electro-weak processes. The latter are also referred to as single top-quark production. There exist three different LO processes in the SM and their Feynman diagrams are shown in Fig. 2.4.

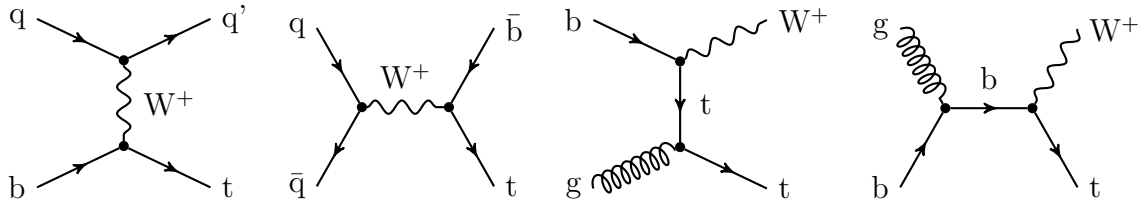

(a) t-channel (b) s-channel (c) Wt, t-channel (d) Wt, s-channel

Figure 2.4.: Feynman diagrams for electro-weak top-quark production in the (a) t-channel, (b) the s-channel and (c), (d) via the associated production of top-quarks and a W boson.

***t*-channel** A space-like W boson is exchanged between a light quark and a b-quark. The b-quark is either included in the PDF in a massless scheme or produced via an initial state gluon splitting.

***s*-channel** A time-like W boson is produced via quark-antiquark annihilation. It then decays into a $t\bar{b}$ pair.

Wt prod. The associated production of top-quarks with a W boson is possible via an s-channel or a t-channel diagram. In both cases, a W boson is radiated off a b from the initial state.

The measurement of single top-quark production is a good test of the SM predictions. Top-quarks produced via electro-weak processes are highly polarized and the top-quark spin can be analysed by measuring the angular distributions of its decay

products [ATL17c]. Furthermore, all three modes are sensitive to the Wtb vertex. They allow a direct measurement of the V_{tb} element of the CKM matrix without assuming three generations of quarks. Moreover, the unitarity of the CKM matrix can be tested. Non-standard couplings at the Wtb vertex could indicate new physics beyond the SM as for example interactions involving new heavy bosons, such as W' or H^+ [ATL15f, ATL15d]. The presence of flavour changing neutral currents at tree-level, i. e. interactions that change the flavour of a quark or a lepton by the emission of a neutral boson, can also lead to deviations in the predicted SM cross section, especially in the single-top t-channel [ATL16e]. Some of these indirect searches can be investigated in the framework of an effective field theory. The predictions for single-top cross sections extracted from these models may vary depending on the production mode. An interpretation of single top-quark measurements for such an EFT approach will be discussed in Sec. 10. In all these searches for new physics, a precise knowledge of the single top-quark production cross section is invaluable.

Single top-quark production for the s- and t-channel was first observed at the Tevatron by the DØ and CDF experiments [CDF09a, D0 09a, CDF14]. The cross section for Wt production is too small to be measured at the Tevatron. At the LHC, the t-channel and the Wt production was measured by the ATLAS [ATL12c, ATL12a] and CMS collaborations [CMS12, CMS13]. Furthermore, the ATLAS experiment published results for an s-channel search at $\sqrt{s} = 8\,\text{TeV}$, which is the first evidence for single top-quark production via the s-channel at the LHC [ATL16a]. A summary of single-top measurements from the ATLAS and CMS collaborations at $\sqrt{s} = 7$, 8 and 13 TeV along with the SM predictions is given in Fig. 2.5. The t-channel has the largest cross section of all the modes. Second largest contribution comes from the associated Wt production. Due to the quark-antiquark initial state, single top-quark production via the s-channel amounts to the lowest cross section of all three modes. Standard model cross section predictions are available at NLO QCD [BE95, SSW98, SSW97]. Moreover, calculations in NLO including resummed logarithmic corrections caused by soft gluon emissions (NLO+NNLL) [Kid11, Kid10a, Kid10b] for all three channels and an almost complete NNLO calculation for the t-channel at $\sqrt{s} = 8\,\text{TeV}$ exist [BCM14]. However, both calculations for NLO+NNLL and NNLO use a top-quark mass, which is different from the ATLAS convention of $m_t = 172.5\,\text{GeV}$. Furthermore, the NLO+NNLL calculations are based on older NLO calculations, which differs from the most recent ones. Therefore, the predictions for t-channel and s-channel single top-quark productions made by the HATHOR program [Kan$^+$15] are used as reference. For the associated Wt production the NLO+NNLL calculations are still recommended, because of the better treatment of the $t\bar{t}$ interference with Wt production at NLO. A summary of the single-top cross section predictions $\sqrt{s} = 8\,\text{TeV}$ used in this thesis is given in Tab. 2.2. [Sch12, Pat$^+$16]

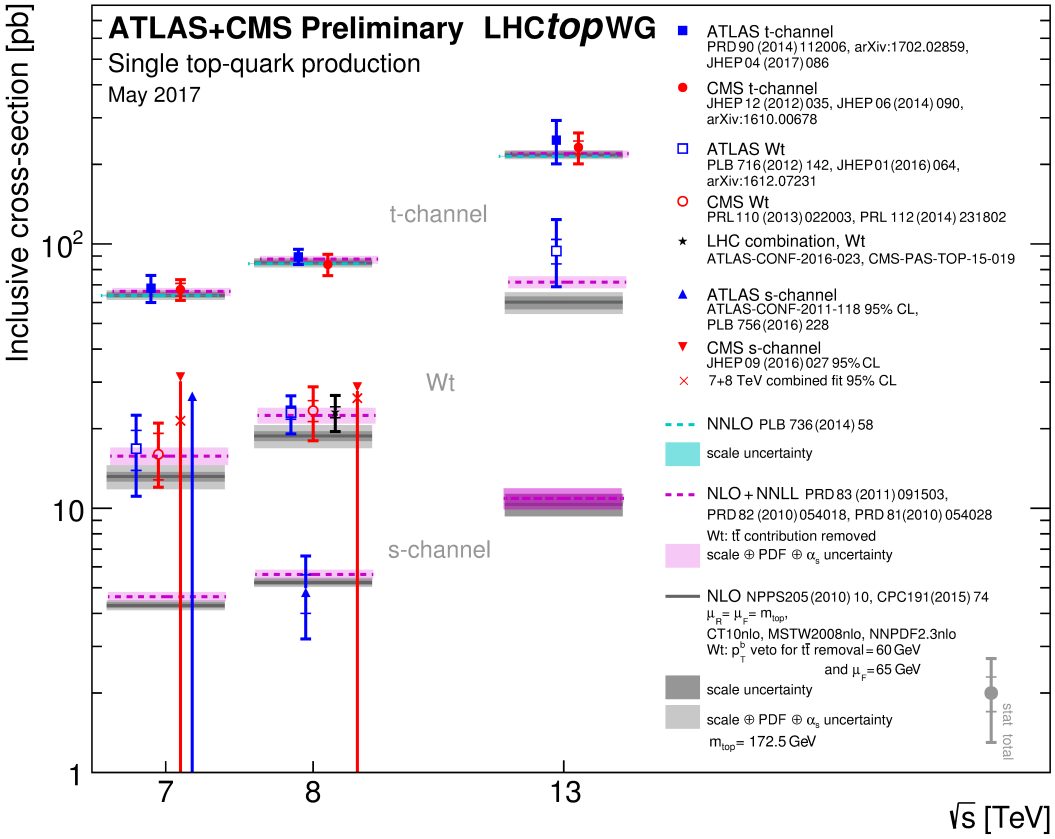

Figure 2.5.: Summary of single top-quark cross section measurements from the ATLAS and CMS collaborations at $\sqrt{s} = 7$, 8 and 13 TeV. Furthermore, standard model predictions at NLO QCD, NLO+NNLL QCD and NNLO QCD (t-channel only) accuracy are displayed.[1]

Process	$\sqrt{s} = 8$ TeV
t-channel	$84.69^{+3.76}_{-3.23}$ pb
s-channel	$5.24^{+0.22}_{-0.20}$ pb
Wt production	22.37 ± 1.52 pb

Table 2.2: Standard model predictions for single top-quark production for the LHC at $\sqrt{s} = 8$ TeV. Cross section predictions at NLO QCD are used for s-channel and t-channel [Kan+15], whereas NLO+NNLL calculations are used for predictions of the associated Wt production [Kid10b].

2.4. Event Topologies

In the following two sections, the event topologies for single top-quark production and background processes with similar final states are discussed. The measurement of single top-quark cross sections presented in this thesis is based on events with exactly

[1] ATLAS Collaboration, *Summary plots from the ATLAS Top physics group*, May 2017, URL: `https://atlas.web.cern.ch/Atlas/GROUPS/PHYSICS/CombinedSummaryPlots/TOP/`

one electron or muon in the final state. Additional quarks and gluons produced in proton–proton collisions hadronize due to the strong force and colour neutral objects are formed along the momentum direction of the initial quark or gluon. The collimated beam of particles is referred to as jet. The reconstruction of electrons, muons and jets within the ATLAS experiment is discussed in more detail in Sec. 4.

2.4.1. Single Top-Quark Processes

The single top-quark production via the t-channel diagram leads to a top-quark and a light quark in the final state. From the top-quark decay $t \rightarrow bW$ with a subsequent W boson decay into a lepton pair, events are expected to contain a charged lepton, a neutrino as well as two jets. Neutrinos can not be measured directly, but the momentum imbalance in the transverse plane can be used to constrain the transverse neutrino momentum. Jets originating from b-quarks can be to some extend distinguished experimentally from jets induced by other lighter quarks. The light quark jet is typically scattered into the forward region of the detector. In the case of the initial b-quark in Fig. 2.4(a) originating from a gluon splitting in the initial state, the second b-jet is in most cases not detected due to the limited angular coverage of the detector and the small transverse momentum of this jet.

The expected event topology for single top-quarks produced via the s-channel process are expected to contain two b quarks and one lepton pair in the final state. Furthermore, a large missing transverse momentum can be associated with such events.

The associated Wt production leads to final states with two W bosons and one b-quark. Single lepton topologies are achieved if one of the two bosons decays leptonically and the other one hadronically. In this case, up to three jets are expected. Moreover, it is possible that both W bosons decay leptonically, but only one charged lepton is identified. Here, only one b-quark induced jet would be present.

2.4.2. Top-Quark Pair and Non-top Background Processes

The event topology of single top-quark production can be mimicked by other processes with similar final states. In addition, the cross section for these processes is in general much larger or at least of equal size than that of electro-weak top-quark production. Figure 2.6 shows several cross section measurements for different SM processes.

The Feynman diagrams of the major background processes for single-top quark analyses are displayed in Fig. 2.7 and their event topologies are discussed below.

W boson production and jets The production of W bosons in association with several quarks has a much larger cross section than single top-quark production. Two possible Feynman diagrams are shown in Fig. 2.7(a) and 2.7(b). If the W boson decays into a lepton pair, a similar final state is achieved. Fake top-quark

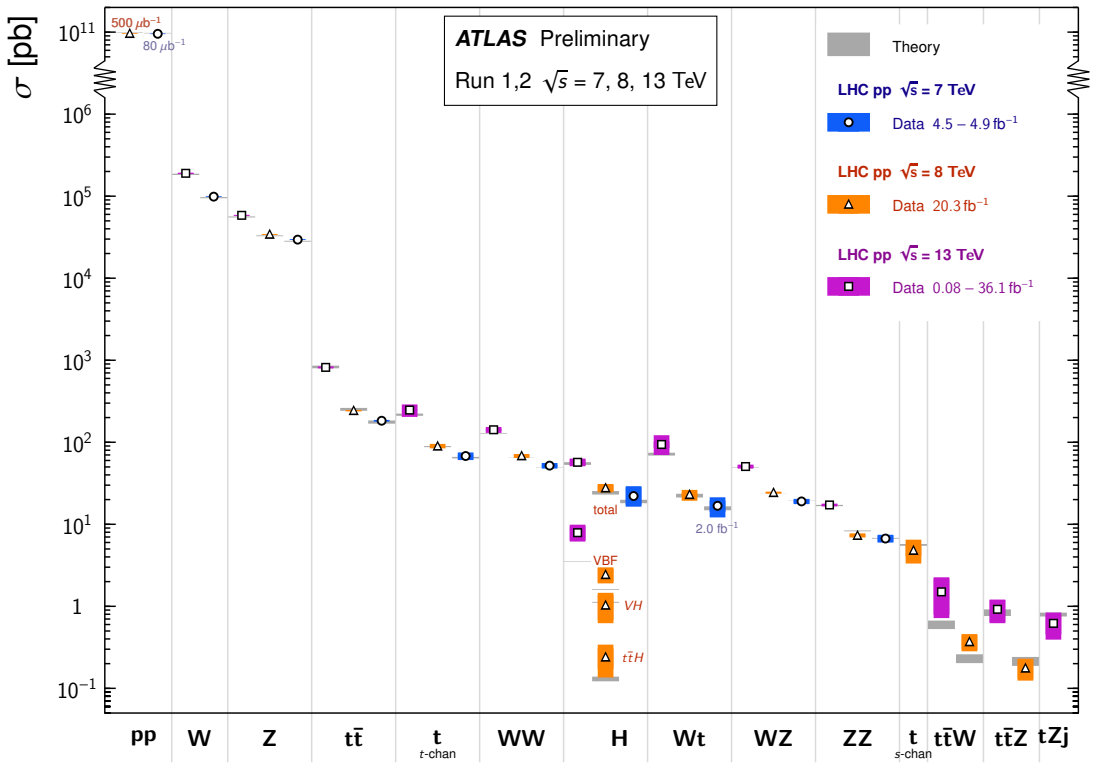

Figure 2.6.: Summary of several SM total production cross section measurements published by the ATLAS experiment. Theoretical predictions are at NLO QCD precision or higher and their uncertainties are marked as grey rectangles.[2]

candidates can be found by random combinations of W boson candidates with jets in the event.

Top-quark pair production In top-quark pair production events, c. f. Fig. 2.7(c), a large variety of final states can be achieved. On the one hand, both top quarks can decay leptonically. This leads to final state with two b-quarks and two leptons. If one of the leptons is not reconstructed, especially in case of τ-leptons, event topologies are comparable to that of electro-weak top-quark production via the *s*-channel or *t*-channel. On the other hand, only one top-quark can decay leptonically, while the other one decays hadronically. Related final states arise from partially reconstructed top-quark decays. In both cases, a large transverse momentum imbalance is expected. Full hadronic $t\bar{t}$ final states do not contribute to the background observed in single-top quark analyses.

Z boson production Events including Z boson decays into two leptons can contribute to the background if one of the leptons is not reconstructed, see

[2] ATLAS Collaboration, *Summary plots from the ATLAS Standard Model physics group*, July 2017, URL: `https://atlas.web.cern.ch/Atlas/GROUPS/PHYSICS/CombinedSummaryPlots/SM/`

Fig. 2.7(d). This results in a large missing transverse momentum. Additional jets can be produced by initial or final state radiation.

Diboson production The total cross section for the production of WW, ZZ and WZ pairs is of the same order as the associated Wt production due to the mass of the two bosons. Possible Feynman diagrams are shown in Fig. 2.7(e). Events with similar topologies occur if one boson decays leptonically, while the other one decays hadronically.

Non-prompt and fake lepton background These type of background events originate from QCD processes, such as the one depicted in Fig. 2.7(f). They typically contain a large number of jets. Misidentification of jets as electrons or semi-leptonic decays of hadrons produced in such events can contribute to fake lepton signatures. Although this misidentification rate is very low, the huge cross section of QCD multi-jet production leads to a small but sizeable contribution to the overall number of single top-quark candidate events.

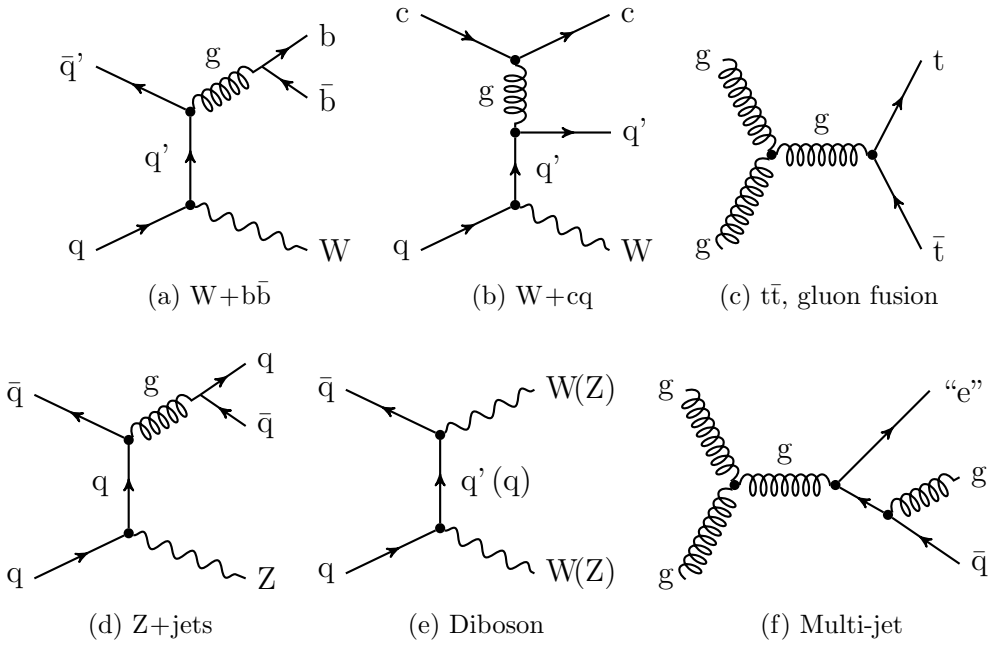

(a) W+b$\bar{\text{b}}$ (b) W+cq (c) t$\bar{\text{t}}$, gluon fusion

(d) Z+jets (e) Diboson (f) Multi-jet

Figure 2.7.: Feynman diagrams of background processes in analyses of electro-weak top-quark production. The diagrams show the production of a W boson in association of (a) two b-quarks or (b) two light quarks, (c) top-quark pair production, (d) Z boson production, (e) production of W boson or Z boson pairs and (f) QCD multi-jet production. In the case of QCD multi-jet production, a light quark jet might be misidentified as charged lepton.

3. The ATLAS Detector at the Large Hadron Collider

The European Organization for Nuclear Research (CERN) near Geneva, Switzerland, operates the Large Hadron Collider. It is the worlds most powerful proton–proton accelerator with a circumference of 26.7 km situated 100 m below ground crossing the boarder between Switzerland and France two times. The LHC machine currently runs at a centre-of-mass energy of $\sqrt{s} = 13\,\text{TeV}$. Proton–proton collisions take place at four points along the beamline. At each of them, one of the four big LHC experiments, ATLAS, CMS, LHCb and ALICE is hosted inside an underground cavern. ATLAS [ATL08b] and CMS [CMS08] are multi-purpose detectors covering a variety of SM physics processes and beyond. The asymmetric design of the LHCb detector is well-suited for research concentrating on CP violation processes in decays of B-mesons [LHC08]. The ALICE collaboration focuses on heavy-ion physics, as the LHC is able to provide collision data using lead-ions [ALI04]. The work presented in this thesis is based on proton–proton collision events recorded in the year 2012 at a centre-of-mass energy of $\sqrt{s} = 8\,\text{TeV}$ corresponding to an integrated luminosity of $20.3\,\text{fb}^{-1}$.

The LHC operated in 2012 with 1374 bunches per beam with an average bunch intensity of $1.6\text{–}1.7 \cdot 10^{11}$ protons per bunch. The bunch spacing was 50 ns and a peak luminosity of $7.7 \cdot 10^{33}\,\text{cm}^{-2}\,\text{s}^{-1}$ was achieved. The maximum mean number of events per bunch crossing was up to 40 events per crossing and the total delivered integrated luminosity in 2012 by the LHC accumulated to $23.1\,\text{fb}^{-1}$. [Lam13]

The ATLAS detector, short for **A** **T**oridal **L**HC **A**pparatu**S**, is a multi-purpose detector. For that reason, it is build symmetrically with respect to the interaction point and provides almost full angular coverage. It measures 25 m in height, 44 m in length and weights around 7 000 t. The overall detector layout is shown in Fig. 3.1. The different components of the detector will be described in Secs. 3.1–3.4. Particles produced in a collision event traverse at first the inner detector, followed by the calorimeter system and eventually the muon system. The magnet system consists of a solenoid and three toroid magnets, generating a magnetic field for the inner detector and the muon system. The initial event selection relies on the trigger system, which is described in Sec. 3.5, followed by a short summary of the simulation infrastructure in Sec. 3.6.

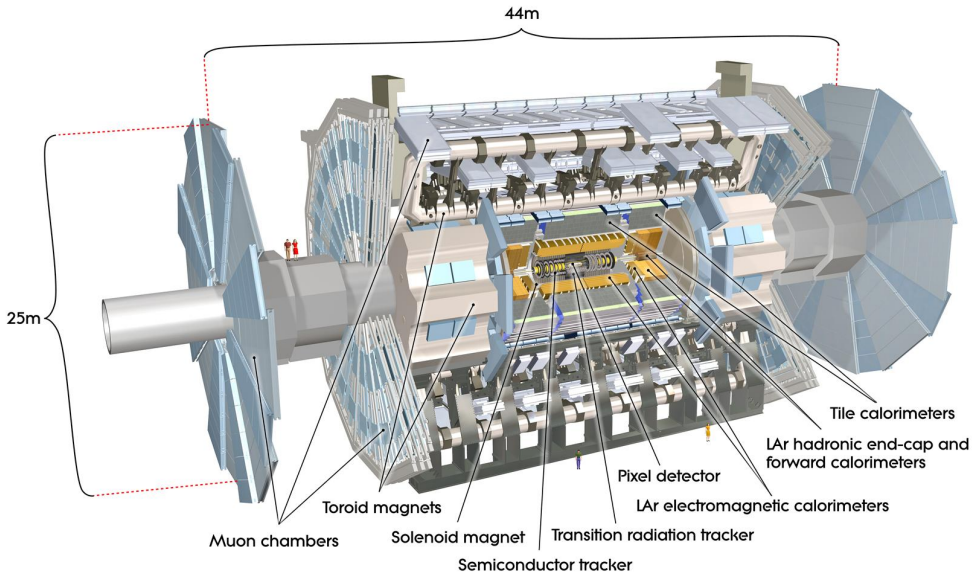

Figure 3.1.: The ATLAS detector. The Inner Detector consists of the pixel detector, the semiconductor tracker and the transition radiation tracker. It is surrounded by the solenoid magnet and the electromagnetic and hadronic calorimeters. The toroid magnets and the muon spectrometer are the outermost parts of the detector. [Peq08d, ATL08b]

The ATLAS collaboration uses a right-handed coordinate system to describe collision events. The centre of the coordinate system coincide with the nominal centre of the detector. The z-axis points along the beam axis. Perpendicular to the beam axis, the x-y plane is spanned by the x-axis pointing inwards to the centre of the LHC and the y-axis pointing upwards to the ground. Usually, vectors are described by a set of spherical coordinates. These are made up by the magnitude of the vector, the azimuth φ and the polar angle ϑ. The azimuth is measured around the beam axis and the polar angle is measured between the z-axis and the vector. When describing physic objects, a useful quantity is the so called pseudorapidity η which is defined as

$$\eta = -\ln \tan\left(\frac{\vartheta}{2}\right). \tag{3.1}$$

The advantage of this quantity is that differences in η are invariant under Lorentz transformations along the z-axis. This is useful for hadron colliders, where the partonic centre-of-mass system is not equal to the laboratory frame. However, the pseudorapidity is only defined for massless particles. For massive particles, the rapidity

$$y = \frac{1}{2}\ln\frac{E + p_z}{E - p_z} \tag{3.2}$$

is approximately equal to the pseudorapidity, if the mass of the particle can be neglected. This is the case, if the energy of the particle is much greater than the mass of the particle. This is well fulfilled for leptons and light hadrons. [ATL08b]

3.1. Magnet System

Tracks of charged particles are measured using the inner detector. A magnetic field is required to quantify the charge and momentum of a particle from its track. The ATLAS magnet system comprises several superconducting magnets, the solenoid and a system of three toroid magnets. All magnets are operated at a temperature of 4.5 K.

The central solenoid surrounds the inner detector and generates a magnetic field of 2 T along the beam axis. The employed design results in the liquid argon calorimeter and the solenoid magnet sharing a common vacuum vessel used by the cryostat system. Thus, the material in front of the calorimeters is reduced, which improves their overall performance.

The magnetic field for the muon system is produced by three separate systems. Eight racetrack-shaped coils with a length of 26 m are located symmetrically around the central calorimeter system and build the central toroid. The toroids at both ends of the detector consists of eight 5 m long coils. The peak magnetic field is 3.9 T for the central toroid and 4.1 T for the other two toroids, respectively.

3.2. The Inner Detector

The Inner Detector consists of three different tracking detectors. The system closest to the beam pipe is the pixel tracker, followed by the silicon microstrip tracker (SCT) and the Transition Radiation Tracker (TRT). The layout of the Inner Detector is depicted in Fig. 3.2. The tracking devices are arranged parallel to the beam pipe in the central region ("barrel"), whereas in the forward regions ("end-cap"), they are mounted on disks perpendicular to the beam axis.

All tracking systems are designed to provide precise track reconstruction, charge identification and a good momentum resolution of charged particles within the pseudorapidity range $|\eta| < 2.5$. In addition, the identification of the primary vertex, i. e. the position of the hard interaction, as well as the reconstruction of secondary vertices from decays of long-lived hadrons is one of the primary tasks of the inner detector. For high momentum particles, the transverse momentum resolution is about $\sigma(p_\mathrm{T})/p_\mathrm{T} = 0.05\,\% \times p_\mathrm{T}[\mathrm{GeV}] \oplus 1\,\%$ and the transverse impact parameter resolution is 10 µm. Along with the calorimeters, the tracker is vital for the identification of electrons, muons, photons and jets. [ATL08b]

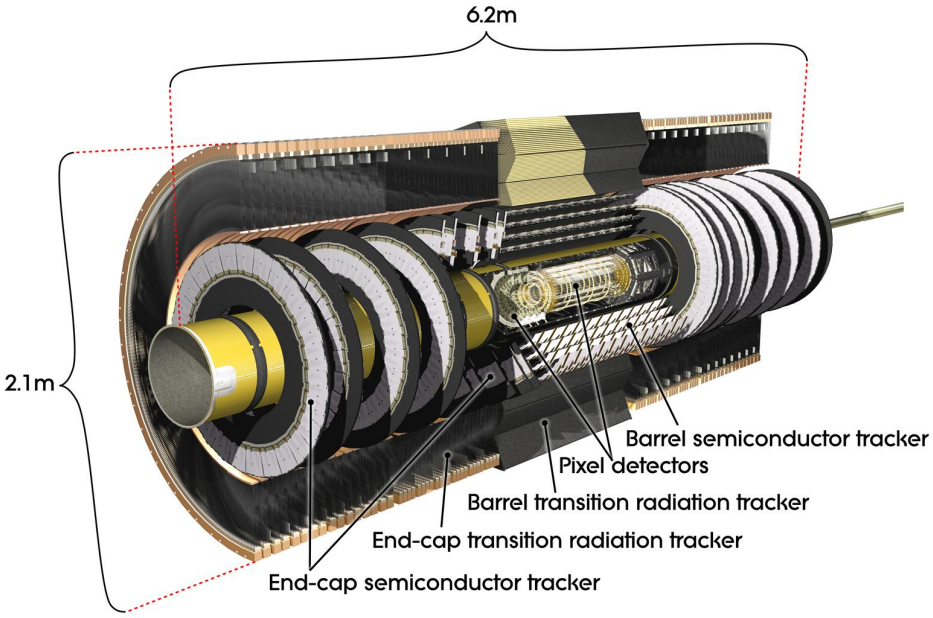

Figure 3.2.: The ATLAS Inner Detector. The three detectors, pixel detector, silicon microstrip detector and transition radiation tracker are used for track reconstruction and identification of primary and secondary vertices. Components in the barrel region are arranged parallel to the the beam pipe, while components in the end-cap regions are mounted perpendicular to the beam axis. [Peq08b, ATL08b]

3.2.1. The Pixel Detector

In the barrel region, the pixel detector consists of three concentric layers of sensors at a distance of 5 cm, 9 cm and 12 cm from the beam pipe. Furthermore, three disks are placed at each side of the detector between 50 cm and 65 cm from the nominal interaction point and extend the angular coverage up to $|\eta| < 2.5$. The intrinsic resolution for sensors in the barrel, $|\eta| < 1.7$, is $\Delta(R-\phi) \times \Delta z = 10 \times 115\,\mu\text{m}$ and $\Delta(R-\phi) \times \Delta R = 10 \times 115\,\mu\text{m}$ for the end-cap region. Due to its close proximity to the interaction point, the pixel detector is most important for the identification and reconstruction of vertices as well as the determination of impact parameters. [ATL08a, ATL08b]

3.2.2. The Silicon Microstrip Tracker

The second tracking system, the silicon microstrip tracker (SCT), is made from semiconductor sensors. A SCT tracking module covers an area of $(6.36 \times 12.8)\,\text{cm}^2$. Two of such modules are glued back-to-back at a stereo angle of 40 mrad to provide three-dimensional space point information. The barrel modules are located on four layers at radii between 299 to 520 mm, whereas for the end-cap regions, 9 disk structures

are used for each side. The layout is optimized such that the SCT can provide up to four space points for any track within $|\eta| < 2.5$. The resolution perpendicular to the strip direction for a single module is 17 µm and 580 µm along the strip direction. Two tracks can still be separated if the distance of the two track is greater than 120 µm. [ATL08b, ATL14f, Abd+06]

3.2.3. The Transition Radiation Tracker

The Transition Radiation Tracker (TRT) is built up of approximately 351 000 drift tubes and enables track measurements up to $|\eta| < 2.0$. Each straw has a diameter of 4 mm and a length of 144 cm in the barrel region and 39 – 53 cm for the end-cap disks, respectively. The straws are filled with a Xenon-based gas mixture and surrounded by radiator material. Ionization charges are collected at a gold-plated tungsten anode wire, which runs inside each drift tube. The gas can be ionized either by charged particles passing through the detector or by transition radiation photons emitted by high energetic electrons inside the radiators. The read-out electronics are able to distinguish between signals from the two sources and allow for a good electron/hadron separation. The pion misidentification probability is about 5 % at 90 % electron identification efficiency. The TRT contributes on average 34 additional hits per track with a resolution of 130 µm. [ATL08b, ATL08c, ATL11c]

3.3. Calorimeters

The calorimeter system is displayed in Fig. 3.3. It surrounds the inner detector as well as the central solenoid and extends to pseudorapidities of $|\eta| < 4.9$. ATLAS uses sampling calorimeters to provide energy measurements of electrons, photons and hadrons. Moreover, an important task of the calorimeter is to contain electromagnetic and hadronic showers and limit punch-through events in the muon system. The overall thickness of the electromagnetic calorimeter is about 22 radiation lengths, while the hadronic calorimeter is more than 10 interaction lengths thick. [ATL08b]

3.3.1. The Electromagnetic Calorimeter

ATLAS uses a liquid argon sampling calorimeter to measure the energy of electrons and photons for pseudorapidities up to $|\eta| < 3.2$. Each cell has a sequence of lead absorber plates and two layers of liquid argon. The high density of lead supports the development of electromagnetic showers, whereas liquid argon is used as active medium to generate signals in form of ionization charges. These charges are collected by applying a high voltage on the electrodes between the liquid argon layers. In the central region ($|\eta| < 2.5$), the modules of the EM calorimeter are divided into three

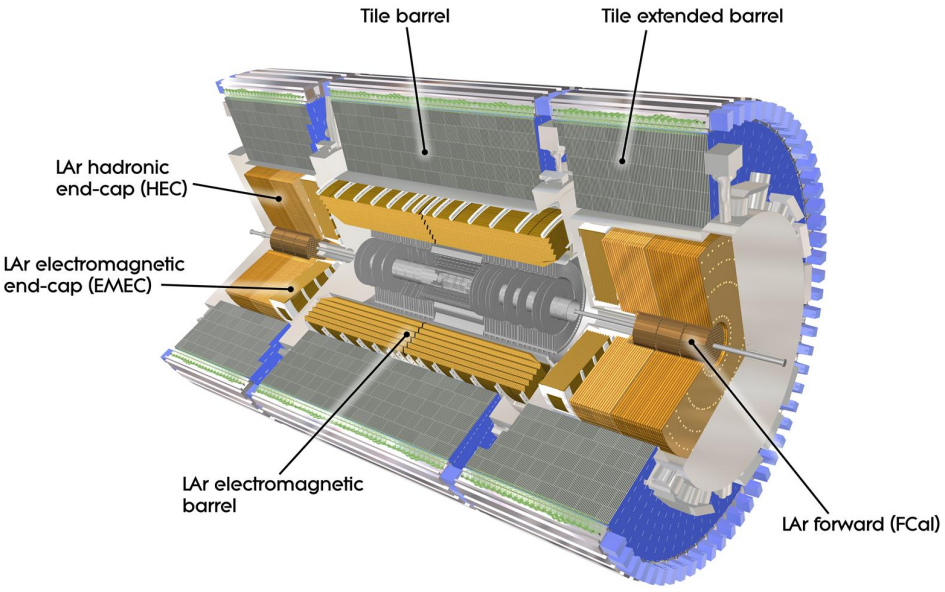

Figure 3.3.: The ATLAS Calorimeters. Liquid argon calorimeters are deployed to measure electromagnetic showers of electrons and photons over the full angular coverage, as well as hadronic showers in the end-cap regions. For the energy measurement of hadrons, ATLAS uses several tile calorimeters. [Peq08a, ATL08b]

sections, whereas for the outer regions only two sections are used. The size of the segments within each section varies from $\Delta\eta \times \Delta\phi = 0.0003 \times 0.01$ for the first section and $\Delta\eta \times \Delta\phi = 0.025 \times 0.025$ for the second section. The third section is twice as thick in η as the second one. The segmentation and the high granularity in the first section is needed for particle identification. For the forward region, only two sections are used and a lower granularity is sufficient to reach the desired performance.

The energy resolution for the electromagnetic calorimeter is

$$\frac{\sigma(E)}{E} = \frac{10\,\%}{\sqrt{E\,[\mathrm{GeV}]}} \oplus 0.7\,\%. \tag{3.3}$$

The first part is due to the sampling nature of the calorimeter, whereas the second part is caused by electronic noise or liquid argon inhomogeneities. Evaluating Eq. 3.3 for an electron with an energy of 50 GeV, yields an energy measurement uncertainty of about 1.6 %. In the area between $1.37 < |\eta| < 1.52$, the energy measurement is degraded, caused by additional material from support lines in front of the calorimeter. Thus, this region is not used for the reconstruction of electrons or photons (c. f. Sec. 4.2). [ATL96b, ATL96a, ATL08b, ATL99]

3.3.2. The Hadronic Calorimeters

The hadronic calorimeter uses two different types of calorimeters. For the central region, three tile calorimeters cover the pseudorapidity range $|\eta| < 1.7$. They consist of alternating tiles made of steel plates and scintillator material. The scintillator tiles are connected via wavelength shifting fibres with two separate photomultiplier tubes for the read-out. The range of the tile calorimeters is extended up to $|\eta| < 4.9$ by two liquid argon calorimeters: the hadronic end-cap calorimeter and the forward calorimeter. The first one covers the range $1.5 < |\eta| < 3.2$. It consists of two wheels per end-cap with a total of four layers. While the active medium in these layers is liquid argon, copper plates are used as absorber material. The forward calorimeter completes the hadronic calorimeter between $3.1 < |\eta| < 4.9$. Besides using a different design, the operation mode is the same as for the other liquid argon calorimeters. Three modules are used per end-cap for the forward calorimeter, one optimized for electromagnetic interactions and two for hadronic interactions.

The energy of hadrons can not be measured as precise as the energy of electrons or photons. A large fraction of the energy is deposited in the absorber material and inaccessible for the energy measurement. Moreover, hadronic cascades are much more variable than electromagnetic showers in terms of lost energy and the production of secondary neutral particles. Therefore, the energy of hadronic showers measured by the hadron calorimeter needs to be scaled to account for the non-detected fraction. The designed energy resolution of the hadronic calorimeter for $|\eta| \leq 3$ is

$$\frac{\sigma(E)}{E} = \frac{50\,\%}{\sqrt{E\,[\mathrm{GeV}]}} \oplus 3\,\%. \tag{3.4}$$

For the forward calorimeters, the resolution is less precise. The coefficient of the sampling term as well as the constant term is a factor of two larger than the one for the tile calorimeters. [Pat+16, ATL08b, ATL96c, ATL10b, ATL99]

3.4. The Muon Spectrometer

The detectors of the muon spectrometer enclose the calorimeter system and cover the pseudorapidity range $|\eta| < 2.7$. Muons loose far less energy when passing through matter than electrons or hadrons. Thus, muons are usually the only particles that reach the muon detectors. The various parts, which build the muon detector system, are depicted in Fig. 3.4. Overall, four different detector systems are installed. Two detectors are dedicated to high precision track measurement, while the other two systems are optimized for triggering events. Detectors in the barrel region are mounted parallel to the beam pipe, whereas the ones in the end-cap regions are mounted on disk structures perpendicular to the beam axis.

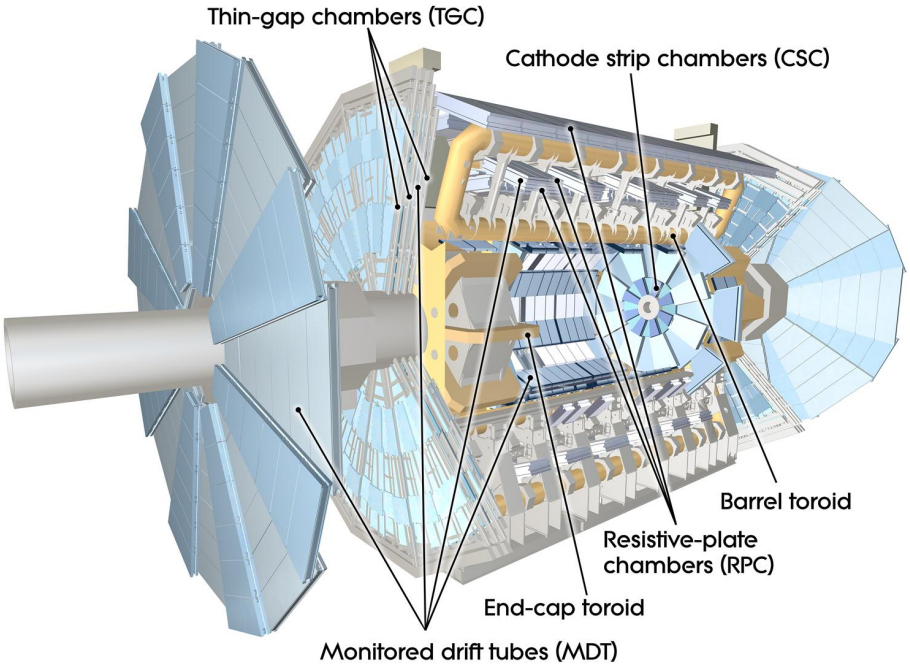

Figure 3.4.: The ATLAS Muon Spectrometer. This detector system consists of four different module types. The monitored drift tubes and cathode strip chambers are high precision tracking devices, while thin-gap chambers and resistive-plate chambers are used for fast trigger decisions. [Peq08c, ATL08b]

Monitored Drift Tubes (MDT) and Cathode Strip Chambers (CSC) are used for high precision track measurement. A MDT module consists of 2×3 or 2×4 aluminium straws arranged in a honeycomb structure. The straw diameter is 30 mm and has a wire of 50 µm diameter. Their length varies between 0.5 to 2 m depending on their position within the detector. The straws are filled with an Ar-CO_2 mixture. The space resolution of a single tube is 80 µm. MDTs are deployed over most of the acceptance, while CSCs are used in the end-cap inner region due to their better performance at high background rates. The CSCs are multiwire proportional chambers. The anode-cathode spacing is equal to the anode wire pitch of 2.54 mm. The resolution of 50 µm is achieved by measuring the charge induced on the cathode strips positioned on the cathode plates. The muon momentum measurement with an uncertainty in the transverse momentum varies from 3 % at 100 GeV to 10 % at 1 TeV.

Two different type of modules are deployed over the muon system for triggering events. On the one hand, Resistive Plate Chambers (RPC) are used in the central region for pseudorapidities $|\eta| < 1.1$. A module is made of two resistive plates at a distant of 2 mm with respect to each other. On the other hand, Thin Gap Chambers are installed in the end-cap regions. TGCs are multiwire proportional chambers with a wire layout optimized for good time resolution. The fast response time and excellent time resolution of the trigger modules allow to identify more than 99 % of

the bunch-crossings. Moreover, they contribute track coordinates in the direction orthogonal to the one provided by the MDTs and CSCs. [ATL08b, ATL10a, ATL97]

3.5. The Trigger System

In order for an event to be recorded by ATLAS, it has to pass three different trigger levels. The trigger system consists of a hardware-based trigger (level-1 trigger, L1), and two software based triggers, the level-2 trigger (L2) and the event filter. The last two triggers are also referred to as High Level Trigger (HLT). The system is designed to cope with input rates of up to 40 MHz at L1. Due to the number of read-out channels, the available disk space and the processing time per event, the number of events that can be written to disk is limited to a few hundred events per second.

The time for the first trigger decision is less than 2.5 µs and the level-1 trigger has only limited information. For the first decision, the transverse muon momentum is reconstructed using the RPCs and TGCs. The calorimeter system provides information on electrons, photons and jets, as well as large missing transverse momentum. The segmentation of the calorimeters allows to apply simple isolation criteria based on reduced-granularity information. The central trigger processor can combine results from the L1 muon or calorimeter triggers depending on the physics requirements. The L1 triggers reduce the input rate to a maximum of 75 kHz. The level-2 trigger evaluates detailed information, such as tracking information from the inner detector and the precision chambers of the muon system in the regions of interests defined by the L1 trigger. Furthermore, the energy and momentum measurement is more precise and improved isolation criteria can be applied. The level-2 trigger processing time per event is about 40 ms. The trigger rate is reduced to approximately 3.5 kHz. The last trigger decision is made by the event filter within a few seconds. At this stage, the full event information is available and more advanced algorithms can be evaluated. [ATL08b, ATL99, ATL12e]

3.6. Detector Simulation

The analysis presented in this thesis relies on accurate and precise simulation of proton–proton collision events. Simulations were performed of single-top events as well as the main backgrounds.

The simulation of an ATLAS event can be separated in three main steps. The first step is the event generation. This covers the generation of the four-vectors of incoming and outgoing particles of the hard scattering process as well as the hadronisation of quarks and gluons and initial and final state radiation. In addition, the underlying event which summarizes all soft hadronic activity that is not part of

the hard interaction, is taken into account. Furthermore, the simulation accounts for additional proton–proton interactions, so called pile-up, in the same bunch-crossings or in bunch-crossings shortly before or after the collision of interest. The second step, the passage of particles through the detector is simulated by Geant4 [Ago+03]. Besides the detectors modules and the supporting structure, the magnetic field configuration is included in the design of the virtual ATLAS detector. The last step of the simulation is called digitization. This covers the response of the electronic read-out system and the simulation of the trigger system. [ATL99]

4. Reconstruction of Single-Top Events

In the following parts, the reconstruction, calibration and selection of physical objects relevant for the study of single top-quark events are discussed. The analysis presented in this theses focuses on semi-leptonic single top-quark events with one electron or one muon in the final state. The used object definitions follow the recommendations described in [Ach+13].

4.1. Trigger

Candidate events with an electron are triggered by the L1 if the transverse energy deposit in the electromagnetic calorimeter is above $E_{\mathrm{T}} > 18\,\mathrm{GeV}$. The maximum energy deposit that is allowed in hadronic calorimeter cells behind the electromagnetic cluster associated with the electron is 1 GeV [Pas+15]. At the HLT, tracking information and the full granularity of the calorimeter are available. A track is matched to the calorimeter cluster and the trigger threshold is raised to $E_{\mathrm{T}} > 24\,\mathrm{GeV}$. In addition, the triggered electron object is required to be isolated. In order to increase the efficiency for electrons with $E_{\mathrm{T}} > 80\,\mathrm{GeV}$ a second set of trigger configurations is employed. At L1, a threshold of 30 GeV is required, whereas the HLT is set to $E_{\mathrm{T}} > 60\,\mathrm{GeV}$ without isolation criteria. [ATL14c, Sol12, ATL12e]

Events containing a muon are triggered by requiring an isolated muon track with a transverse momentum of $p_{\mathrm{T}} > 24\,\mathrm{GeV}$ at L1. The track is defined as isolated, if the sum of the transverse momenta of all tracks within a cone of size $\Delta R < 0.2$[1] around the muon, does not exceed 12 % of the total muon transverse momentum. In addition, a second trigger with a threshold of $p_{\mathrm{T}} > 36\,\mathrm{GeV}$ is used without any isolation requirement. The latter increases the efficiency for muons with large transverse momenta. [ATL15c, ATL12e]

[1] The angular distance between two objects is defined as $\Delta R = \sqrt{(\Delta\eta)^2 + (\Delta\varphi)^2}$.

4.2. Electrons

Electrons are reconstructed from energy deposits in the electromagnetic calorimeter and associated tracks in the inner detector. Electromagnetic clusters are seeded by initial clusters with a transverse energy of $E_{\mathrm{T}} > 2.5\,\mathrm{GeV}$. The cluster reconstruction efficiency for true electrons from Monte Carlo (MC) simulations with $E_{\mathrm{T}} > 7\,\mathrm{GeV}$ is about 95 % and 99 % at $E_{\mathrm{T}} > 15\,\mathrm{GeV}$. In the end-cap region, the efficiency decreases with increasing pseudorapidity. The transverse energy $E_{\mathrm{T}} = E/\cosh\eta$ is calculated from the cluster energy and the direction of the associated track.

Only electron candidates in the central region with associated clusters at $|\eta_{\mathrm{cl}}| < 2.47$ and with a transverse energy of $E_{\mathrm{T}} > 30\,\mathrm{GeV}$ are selected. Candidates which fall in the transition region between the central and end-cap calorimeters at $1.37 < |\eta_{\mathrm{cl}}| < 1.52$ are excluded from the analysis. Furthermore, the quality of electron objects is classified based on a set of cuts which include requirements on the cluster energy distribution, matching of the track to the calorimeter cluster as well as information on the track quality.

Signal electrons from prompt W boson decays have to fulfil the most stringent set of cuts, also referred to as `tight++` quality. In order to reduce the amount of background objects, such as hadronic jets and electrons from photon conversions, additional isolation requirements are imposed. These isolation requirements are based on the transverse energy deposited in the calorimeter cells within a cone of $\Delta R = 0.2$ and the sum of the transverse momenta of all tracks in a cone of size 0.3. The threshold of the isolation variables results in a simulated isolation efficiency of 90 % for each isolation requirement. Moreover, the longitudinal impact parameter z_0, i. e. the distance of the track to the primary vertex in z-direction, should be less than 2 mm.

For the data-driven estimate of multi-jet events, c. f. Sec. 5, electron candidates with relaxed identification criteria are selected. For these electrons of `medium++` quality, electrons from photon conversions are rejected and no isolation cuts are applied.

Identification and reconstruction efficiencies for electrons are measured in data and simulated $\mathrm{Z} \to \mathrm{ee}$ events using a tag-and-probe method. To account for the different efficiencies determined in data and simulations, simulation-to-data correction factors are derived as a function of the electron transverse energy and pseudorapidity. [ATL14c]

4.3. Muons

Muon candidates are built from high quality track segments reconstructed in the inner detector and the muon spectrometer. The combined track has to consist of a certain number of track hits based on the various tracking detectors used in its reconstruction. Furthermore, the longitudinal impact parameter of a muon candidate needs to fulfil

$z_0 < 2\,\text{mm}$. Finally, all candidates have to pass tight identification criteria and have a transverse momentum of $p_\text{T} > 30\,\text{GeV}$ and a pseudorapidity of $|\eta| < 2.5$.

Isolation requirements are imposed on muon candidates in order to reduce the number of events containing muons from B-meson decays. Due to hadronisation effects, these kind of muons are usually contained within a jet. A muon is isolated if the transverse momentum sum of all tracks within a cone around the candidate does not exceed 5 % of the muon transverse momentum. The cone size $\Delta R = 10/(p_\text{T}^\mu\,[\text{GeV}])$ scales with the muon transverse momentum [RT11]. Furthermore, any muon is removed if the distance to a reconstructed jet with a transverse momentum of $p_\text{T} > 25\,\text{GeV}$ is below $\Delta R < 0.4$.

Muon candidates without isolation requirements are selected to determine the fake and real selection efficiencies needed for the data-driven background estimate of multi-jet background (c. f. Sec. 5).

The reconstruction efficiencies for muons have been measured using $\text{Z} \to \mu\mu$ events using a tag-and-probe method. The different efficiencies found in data and MC samples are corrected by efficiency scale factors. These factors are derived as a function of pseudorapidity and azimuth of the muon and are independent of the transverse momentum of the muon. [ATL14e]

4.4. τ-Leptons

In contrast to electrons and muons, τ-leptons can only measured by reconstructing and identifying their decay products. The hadronic decay channel for τ-leptons, i. e. τ decays into one or three pions[2] and a τ-neutrino, is favoured over the leptonic decay into an electron or a muons and the respective neutrinos with a ratio of approximately 2 : 1 [Pat+16].

The reconstruction algorithm for hadronic τ decays is seeded by jet candidates with a $p_\text{T} > 10\,\text{GeV}$ and $|\eta| < 2.5$. A detailed description of jet candidates is given in the next section. In order to suppress the background originating from jets and electrons, two separate boosted decision trees (BDT) are utilized using track based and calorimeter based quantities. Based on the BDT response, the τ candidate can be classified as being of loose, medium or tight quality. [ATL15b]

The reconstruction efficiency for τ-leptons with a transverse momentum $p_\text{T} > 15\,\text{GeV}$ and a pseudorapidity $|\eta| < 2.5$ of loose quality is much lower compared to the reconstruction efficiencies of electrons or muons of tight quality [ATL15b]. Therefore, a dedicated selection of single-top events with a τ final state is not considered. However, electron and muon candidates with relaxed identification requirements and a transverse momentum of $p_\text{T} > 5\,\text{GeV}$ are selected in order to identify leptonically

[2] The decay into pions accounts for about 94 % of all hadronic decay modes.

decaying τ-leptons. The selected electrons and muons are removed if they overlap within $\Delta R < 0.4$ of any tight electron, tight muon or any jet reconstructed following the description in the next section.

4.5. Jets

The reconstruction of jets used in this analysis starts by clustering topologically connected calorimeter cells. The local cluster weighting calibration method is applied to each clusters and corrects for signal losses due to noise threshold effects and energy lost in non-instrumented regions. It further accounts for the calorimeter non-compensation, which refers to the partial measurement of energy deposited by hadrons. Jets are formed from these calibrated cluster information using the anti-k_t algorithm [CSS08a] with a radius parameter of 0.4. The direction of the jet is corrected such that its origin coincides with the primary vertex instead of the centre of the ATLAS detector.

The jet energy is corrected for pile-up effects using an algorithm based on the jet area and the energy density per event [Arg$^+$13, CSS08b, CS08]. This allows to derive an event-by-event and jet-by-jet pile-up subtraction. Finally, a residual correction is derived as a function of the number of primary vertices in the event and the mean number of inelastic proton–proton interactions per bunch-crossing. These scale factors depend on the jet transverse momentum and pseudorapidity and relate the jet energy to the hadronic scale [ATL13d]. In addition to the jet area based pile-up suppression, the jet vertex fraction is used to identify the origin vertex of a jet. It is given by the ratio of the transverse momentum sum of all tracks of the jet associated with the primary vertex to the transverse momentum sum of all tracks of the jet. The best suppression of jets from additional proton–proton collisions in the same bunch-crossing, "in-time pile-up", is achieved by requiring a jet vertex fraction larger than 0.5 for jets with $p_{\mathrm{T}} < 50\,\mathrm{GeV}$ and $|\eta| < 2.4$. [MSS09, Arg$^+$13]

Jet candidates are removed from the event if they are reconstructed from noisy calorimeter cells and their transverse momentum is greater than $p_{\mathrm{T}} > 10\,\mathrm{GeV}$. Electrons are likely to be reconstructed as jets. Therefore the jet closest to an electron candidate is removed, if they overlap within a cone of $\Delta R < 0.2$. The electron is discarded if any remaining jet with $p_{\mathrm{T}} > 25\,\mathrm{GeV}$ is found within a cone of $\Delta R < 0.4$ around the electron.

All jets with a transverse momentum of $p_{\mathrm{T}} > 25\,\mathrm{GeV}$ and a pseudorapidity of $|\eta| < 4.5$ are considered for this analysis.

4.6. b-Jets

While all quarks and gluons produced in proton–proton collisions initiate jets, it is to some extend possible to identify jets originating from b-quarks. The algorithms presented in this section exploit that b-quarks preferably form B-mesons. These mesons have a relatively long life time and in combination with their large lorentz-boost, the vertex reconstructed from tracks of charged B-meson decay products is displaced with respect to the primary vertex. The distance between the secondary vertex and the primary vertex can be up to a few millimetres. The ATLAS inner detector is able to identify such displaced vertices.

For this analysis, two different neural-network based algorithms, named MV1 and MV1c, are used to assign weights to each jet. A jet with a weight above a certain threshold, so-called working point, is referred to as b-tagged jet, or short b-jet. The efficiency for correctly identifying jets initiated by b-quarks depends on the employed algorithm and the working point. It further defines the efficiencies for tagging jets initiated by c-quarks, light-flavoured quarks (u, d, s) or gluons. Non-b-tagged jets are named light-flavoured jets.

The input to the neural-network based MV1 algorithm [ATL12b] are the weights of three b-tagging algorithms, IP3D, SV1 and JetFitterCombNN. The first two algorithms employ a likelihood ratio method, which compares the measured value of a discriminating variable to pre-defined normalized distribution of b-jets and light-flavoured jets obtained from simulation. The b-tag weight is calculated as the sum of the ratios for the signal and background hypotheses [ATL09]. The IP3D algorithm [ATL11a] utilizes the two-dimensional distribution of the signed transverse impact parameter significance, d_0/σ_{d_0}, and longitudinal impact parameter significance, z_0/σ_{z_0}. The variables d_0 and z_0 are the transverse and longitudinal impact parameters, whereas σ_{d_0} and σ_{z_0} denote the corresponding uncertainties. The SV1 algorithm [ATL11a] exploits the two-dimensional distributions of the invariant mass of all tracks associated with the vertex and the ratio of their energy sum to the total energy of all tracks associated with the jet. Furthermore, the number of two track vertices is utilized. The third algorithm, JetFitterCombNN [ATL11a, ATL12d], combines the JetFitter and IP3D algorithms along with additional variables describing the topology of decay chain of weak b- and c-hadron decays using neural network techniques. The JetFitter [ATL11a, PW08] algorithm is based on a Kalman Filter for the reconstruction of an approximate flight path for the b-hadron. The MV1c algorithm uses the same input variables as the MV1 algorithm. While MV1 was optimized to reject light-flavoured jets, MV1c was trained against a mixture of c and light-flavoured jets to improve the c-jet rejection.

For both algorithms, MV1 and MV1c, the b-tagging efficiency is measured in data by using methods based on dijet samples with muons in the final state [ATL12b]. Simulated top pair events with a di-leptonic final state are used to extract the expected b-tagging efficiency [ATL12d]. The analyses presented in [ATL12b] and [ATL12d]

have been updated using the 2012 data set [ATL14a]. Furthermore, the efficiency for the misidentification of c-quark or light-flavoured quark induced jets as b-jets is measured separately in a D-meson enriched region and in inclusive jet samples, respectively [ATL14b]. Scale factors are derived as a function of the jet transverse momentum and pseudorapidity to correct for differences in efficiencies found in data and simulation. For this analysis, the employed working points correspond to a b-tagging efficiency of 70 % and 50 % for MV1 and MV1c, respectively. The rejection factor for c-jets, i. e. the inverse of the c-tagging efficiency, is about five for MV1, while it is five times larger for MV1c.

4.7. Missing Transverse Momentum

The missing transverse momentum is defined as the momentum imbalance in the plane perpendicular to the beam axis. Neutrinos or other weakly-interacting particles can escape the ATLAS detector undetected and contribute to the momentum imbalance.

The missing transverse momentum is calculated from calibrated energy clusters in the calorimeters and muons reconstructed in the muon spectrometer. The contribution from calorimeter clusters is split into different components and further enhanced by matching calibrated reconstructed objects to the individual cluster information. Moreover, the detector coverage, including the transition regions between calorimeters, the presence of dead region and electronic noise is taken into account. [ATL13e]

5. Estimation of Non-prompt and Fake Lepton Background

The expected signature of single top-quark events as well as background processes with similar final states was discussed in Sec. 2.4. Simulated samples are used to describe a large variety of the background processes. However, the background from non-prompt and fake leptons is induced by QCD multi-jet events, which can not be simulated precisely. This section describes the data-driven method [ATL14d], so called matrix method, which is used to estimate the number background events from multi-jet production.

In the context of single top-quark analyses, charged isolated leptons coming from W boson or Z boson decays are referred to as prompt or real leptons. The signature of such leptons can be mimicked by leptons originating from other sources. The background contributions for electrons arise from semi-leptonic B- or D-meson decays or photon conversions. Furthermore, jets with a large energy deposit in the electromagnetic calorimeter can fake an electron's signature. Particles that punch-through the calorimeters into the muon spectrometer can contribute to fake muon background as well as muons originating from semi-leptonic meson decays. Despite the tight object requirements imposed on selected leptons, the background from multi-jet production is significant due to its large cross section compared to single top-quark production.

In the following, leptons will be classified as being of loose or tight quality, according to the definitions in Secs. 4.2 and 4.3. The number of events containing a single lepton can be split into contributions from events with a loose and tight leptons

$$\begin{aligned} N^{\text{loose}} &= N^{\text{loose}}_{\text{real}} + N^{\text{loose}}_{\text{fake}} \\ N^{\text{tight}} &= \epsilon_{\text{real}} N^{\text{loose}}_{\text{real}} + \epsilon_{\text{fake}} N^{\text{loose}}_{\text{fake}} . \end{aligned} \tag{5.1}$$

Here, the superscript denotes the object definition of the lepton, 'loose' or 'tight', while the subscript defines its origin, prompt (real) or non-prompt (fake) lepton. The efficiencies ϵ_{real} and ϵ_{fake} stand for the fraction of real and fake leptons passing the the tight selection requirements, respectively. If the real efficiency ϵ_{real} and fake efficiency ϵ_{fake} are known, the number of events with fake leptons passing the tight selection $N^{\text{tight}}_{\text{fake}} = \epsilon_{\text{fake}} N^{\text{loose}}_{\text{fake}}$ can be calculated from Eqs. 5.1 by

$$N^{\text{tight}}_{\text{fake}} = \frac{\epsilon_{\text{fake}}}{\epsilon_{\text{real}} - \epsilon_{\text{fake}}} (\epsilon_{\text{real}} N^{\text{loose}} - N^{\text{tight}}). \tag{5.2}$$

The final background estimate coming from non-prompt or fake lepton background is determined by selecting data events with a single lepton of loose quality. The number of background events is given by the sum of all events weighted by

$$w_i = \frac{\epsilon_{\text{fake}}}{\epsilon_{\text{real}} - \epsilon_{\text{fake}}}(\epsilon_{\text{real}} - \delta_i) \tag{5.3}$$

where δ_i equals unity if the lepton passes the loose requirements and zero otherwise.

The real efficiency ϵ_{real} is measured using a tag-and-probe method for $\mathrm{Z} \to \mathrm{ee}$ and $\mathrm{Z} \to \mu\mu$ events. Subsequently, the efficiency for electrons is corrected to match the expected efficiency in $\mathrm{t\bar{t}}$ events. This accounts for the higher jet multiplicity found in $\mathrm{t\bar{t}}$ events with respect to Z+jets events. The fake efficiency is determined from events selected in control regions populated by non-prompt or fake lepton background. It is calculated as the ratio of single lepton events containing a tight lepton to events containing a loose lepton. Both efficiencies are parametrized using variables describing the lepton and jet kinematics, such as p_{T} and η, and the event topology, like the jet and b-jet multiplicity of the event.

6. The Matrix Element Method

Analysis techniques in high energy particle physics can be divided into three groups. The common goal of all these methods is to identify interesting events from collision data, called signal, and separate them from events originating from uninteresting or already known background processes. The first and simplest approach to enrich signal events is to use a cut-based method. This technique defines a set of selection cuts based on kinematic variables describing the event topology. The threshold of each cut is often motivated by studying the response of Monte Carlo simulations for signal and background processes or is derived from theory predictions of the event signature. The second set of methods are machine learning techniques such as neural networks or boosted decision trees. Usually, special algorithms are trained on Monte Carlo simulations or on events from side band regions to distinguish between signal and background events. The third and last group of techniques incorporates hypothesis tests. For example, the top-quark decay chain $t \to \mathrm{Wb} \to \ell\nu\mathrm{b}$ can be reconstructed by including the measured objects and their uncertainties in a χ^2-fit. In particular, the (unmeasured) neutrino momentum can be deduced from the fit by including additional constrains on the W boson and top-quark mass [Beu+12, Her14, Rie10]. Moreover, such techniques can be extended by including the detector response in the hypothesis test [Erd+14]. In most cases, an analysis does not rely on a single method, but uses a combination of two or more techniques.

In this context, the matrix element method [Kon88] is part of the last group of techniques. It further extends the idea of hypothesis testing by using information contained in the matrix element, hence the name of the method. For each event, a likelihood value is computed by relating the expected event topology as described by the matrix element to the measured objects in the detector. Thus, many different hypotheses can be tested. Furthermore, information from the event is used most efficiently, as the event kinematics and the detector response is taken into account. In addition, the initial state is also part of the hypothesis test in contrast to kinematic fits that only model certain parts, often decay chains of heavy particles in the event. Machine learning techniques can suffer from insufficient training statistics or overtraining, which is not the case for the Matrix element method. However, it is a very CPU intensive method and requires large computation times.

One of the first measurements including the matrix element method was conducted at the Tevatron for the determination of the top-quark mass [D0 04] and for single-top cross section measurements [CDF09b, D0 09b]. Furthermore, the method is becoming

more popular at the LHC and was used in recent publications of the ATLAS and CMS collaborations [ATL15e, CMS15, ATL16a, CMS16]. Up to now, all applications used LO approximations for the matrix element. Recently, an extension of the method to NLO accuracy has been published [MU15]. A description of the method using the LO approximations is given in the next section.

6.1. Process Likelihood

The key elements of the matrix element method are the so-called process likelihoods. For each observed event with reconstructed momenta $X = \{p_i^{\text{rec}}\}$, the likelihood describes the probability to observe the event configuration X given the hypothesis H for a certain scattering process. In this regard, it is necessary to relate the phase space of the final state momenta Φ for the process under study, also referred to as parton level, to the measured objects at the detector level.

The description of the likelihoods starts with the factorization theorem discussed in Sec. 2.1. The hard scattering process is described by the partonic cross section $\hat{\sigma}$ and soft QCD effects of the initial state are absorbed in the PDFs. In the subsequent hadronisation of quarks and gluons, many particles are produced and particle jets are formed. For the matrix element method in leading order, one particle jet is associated with one final state quark or gluon. These jets induced by final state partons are reconstructed in the detector. The transition from parton level to detector level objects is modelled by a transfer function $T(X|\Phi)$. This function includes reconstruction efficiencies for each final state particle and represents the finite energy and angular resolutions of the detector. Additional reconstructed jets can arise from from pile-up interactions or higher order effects. As those effects are not modelled by the leading order matrix elements, the phase space of reconstructed events has to be restricted to events with a jet multiplicity that is equal to the number of final state particles. Otherwise, additional jets have to be excluded from the computation of the process likelihoods. Finally, the likelihood for a specific process hypothesis H is given by a convolution of the hadronic cross section with the transfer function $T(X|\Phi)$:

$$\mathscr{L}_H(X) = \frac{1}{c_H} \sum_{a,b} \int \mathrm{d}x_1 \, \mathrm{d}x_2 f_a(x_1) f_b(x_2) \, \mathrm{d}\hat{\sigma}^H_{a,b} \, T_H(X|\Phi). \tag{6.1}$$

The subscript and superscript letter H marks all terms that are process specific, i. e. the likelihood normalization constant c_H, the differential partonic cross section, $\mathrm{d}\hat{\sigma}^H_{a,b}$, and the transfer function. The indices a and b denote the possible flavours of the initial state partons. The likelihoods $\mathscr{L}_H(X)$ are proportional to the differential partonic cross section

$$\mathrm{d}\hat{\sigma} = \frac{|\mathcal{M}^H_{a,b}|^2}{2\hat{s}} \, \mathrm{d}\Phi \,, \tag{6.2}$$

which contains the matrix elements $\mathcal{M}_{a,b}^{H}$ that contribute to the process H. Equation 6.2 includes the flux factor for massless initial state partons with a partonic centre-of-mass energy $\sqrt{\hat{s}} = \sqrt{x_1 x_2 s}$. The N-body phase space $\mathrm{d}\Phi$ with final state momenta p_i is given by

$$\mathrm{d}\Phi = (2\pi)^4 \delta^{(4)}(P_1 + P_2 - \sum_i p_i) \prod_{i=1}^{N} \frac{\mathrm{d}^3 p_i}{(2\pi)^3 2E_i}. \tag{6.3}$$

and contains the energy-momentum conservation requirement between the initial and final state momenta. The momenta of the initial state partons are denoted by P_1 and P_2, respectively. Moreover, Eq. 6.1 contains an additional factor c_H to ensure a proper normalization of the likelihood. The determination of this constant is related to the transfer function normalization and further explained in the following paragraphs.

The transfer function $T(X|\Phi)$ consists of the response functions of the detector to individual final state particles, i. e. leptons, quarks and gluons. The association of final state momenta p with reconstructed momenta p^{rec} is arbitrary and therefore all possible combinations need to be considered. Furthermore, depending on the process, some final state particles might be left unmatched to a measured object due to inefficiencies in the reconstruction. The most general form for $T(X|\Phi)$ is given by

$$T_H(X|\Phi) = \frac{1}{N_{\mathrm{perm}}} \sum_{i \,\in\, \mathrm{perm}} w_i \prod_{j \,\in\, \mathrm{matched}} \varepsilon(p_{ij}) W_{\mathrm{res}}(p_{ij}^{\mathrm{rec}}, p_{ij}) \prod_{k \,\in\, \mathrm{unmatched}} (1 - \varepsilon(p_{ik})). \tag{6.4}$$

The index i marks a specific combination of a reconstructed object with its matched counterpart at the parton level. A weight w_i is assigned to each of these permutations and the sum of weights is equal to the number of all possible permutations N_{perm}.[1] Furthermore, Eq. 6.4 contains efficiency terms $\varepsilon(p)$ and $(1 - \varepsilon(p))$ for matched and unmatched final state particles, as well as terms denoted by W_{res} describing the finite detector resolution. The latter are defined as the conditional probability to measure a reconstructed momentum p^{rec} given a final state momentum p and are normalized to unity:

$$\int \mathrm{d}^3 p^{\mathrm{rec}} W_{\mathrm{res}}(p^{\mathrm{rec}} | \, p) = 1. \tag{6.5}$$

The normalization condition of Eq. 6.5 reflects that for each final state momentum at the parton level, a reconstructed momentum can be found. The resolution transfer functions W_{res} need to be determined over the full detector acceptance. A specific parametrization of the resolution functions is discussed in the next section as well as the reconstruction efficiencies $\varepsilon(p)$.

The normalization constant c_H can be computed by integrating the likelihood $\mathscr{L}_H(X)$ (c. f. Eq. 6.1) over the full phase space X of all reconstructed momenta and by using

[1] A priori, the weight of each permutation is equal to one. However, the list of permutations might contain identical assignments of reconstructed objects to particle level objects. In that case, the permutation in question is evaluated only once and weighted accordingly. This increases the performance of the likelihood computation.

the normalization condition of the transfer function given in Eq. 6.5:

$$c_H = \int \mathrm{d}x_1\, \mathrm{d}x_2 f_a(x_1) f_b(x_2)\, \mathrm{d}\hat{\sigma}^H_{a,b}\, \varepsilon_H(\Phi) \tag{6.6}$$

The constant c_H does not only depend on the process H, but is furthermore unique for each reconstructed event topology. The latter is a consequence of the efficiency term

$$\varepsilon_H(\Phi) = \frac{1}{N_{\text{perm}}} \sum_{i \in \text{perm}} w_i \prod_{j \in \text{matched}} \varepsilon(p_{ij}) \prod_{k \in \text{unmatched}} (1 - \varepsilon(p_{ik})) \tag{6.7}$$

which depends on the number and type of reconstructed objects in the measured event. It contains the product of all efficiencies as well as the sum over all permutations of Eq. 6.4.

6.2. Transfer Functions

The transfer function $T(X|\Phi)$ models the detector response and is composed of functions describing the finite detector resolution and reconstruction efficiencies.

6.2.1. Resolutions

The transfer functions described in this section are provided by the KLFitter group [Erd+14] within the ATLAS collaboration. Simulated top-quark pair events are used to determine the resolution functions for the energy of electrons and jets as well as for the transverse momentum of muons.

The detector level objects are selected by using cuts similar to those defined in Sec. 4. Subsequently, the reconstructed objects are matched to a final state particle if their distance in ΔR is smaller than 0.3 and the matching is unique. Finally, the relative energy difference between the parton level and detector level objects is calculated for various regions in pseudorapidity and energy of the final state particle. The resulting distribution is parametrized by a double Gaussian function

$$W_{\text{res}}(E^{\text{rec}}|E) = \frac{1}{E} \frac{1}{\sqrt{2\pi}\,(p_2 + p_3 p_5)} \left[\exp\left(-\frac{(\Delta E - p_1)^2}{2p_2^2} \right) + p_3 \exp\left(-\frac{(\Delta E - p_4)^2}{2p_5^2} \right) \right] \tag{6.8}$$

with the relative energy difference defined as

$$\Delta E = \frac{E - E^{\text{rec}}}{E}. \tag{6.9}$$

The energy of the final state particle at the parton level is denoted as E, while the reconstructed energy is E^{rec}. The final parameter values in Eq. 6.8 for each type of

particle are obtained in a two-step procedure. First, the individual distributions in bins of the final state particle energy are fitted with the double Gaussian function. This initial parameter estimate is then extended to the full energy range by a multi-dimensional global fit of all distributions optimized by a Markov Chain Monte Carlo using the BAT program [CKK09]. Although, the energy resolutions might be better described by the local fits, the final global fit is an analytic function and valid over the full energy range.

The resolution functions are obtained for different pseudorapidity regions. Examples of their probability density distributions for the reconstructed energies are shown in Fig. 6.1. The definition of the pseudorapidity intervals is motivated by the detector geometry and takes into account the transition region between the central and forward detectors. The energy resolution for leptons is much better than those of jets. Although, transfer functions of pseudorapidity and polar angle exist, they are not used in the context of this thesis.

6.2.2. Efficiencies

The reconstruction efficiencies for a final state particle to be reconstructed as electrons, muons, or jet in the detector are determined using simulated single-top t-channel events. In addition, the b-tagging efficiency was estimated using the MV1 algorithm. A dedicated measurement for the MV1c algorithm was not conducted, because the dependence of the efficiency on the transverse momentum and pseudorapidity is very similar between the two tagging algorithms. Any constant factor in the transfer function is cancelled by the likelihood normalization. Moreover, the misidentification rate of b-jets for both algorithms is assumed to be constant and was not determined more precisely. The single-top t-channel sample was chosen, as it contains exactly one light-flavoured quark, b-quark and one electron or one muon in the final state. Jets induced by quarks and gluons can not be distinguished experimentally and the efficiencies obtained with light-flavoured quarks are also used for gluons.

The definitions in Sec. 4 were used to select the detector level objects. Leptons are required to be matched to a trigger object. No further selection cuts were imposed on the events to avoid a possible bias by the chosen Monte Carlo sample. The reconstructed objects are matched to final state particles by requiring a maximum distance of $\Delta R < 0.4$ between them. The reconstruction efficiencies are given by the ratio of all matched final state particles to all particles of that type. The fraction of b-jets in a sample of b-quarks matched to jets provides a measure for the b-tagging efficiency.

All efficiencies are parametrized as a function of the transverse momentum and pseudorapidity of the final state particle. The parametrization takes the different detector geometry in the central and forward regions into account. The efficiencies are displayed in Fig. 6.2. They increase rapidly at the threshold value of $p_{\mathrm{T}} = 25\,\mathrm{GeV}$

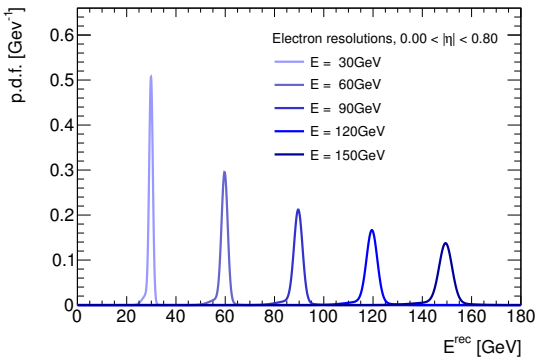

(a) Electron resolutions

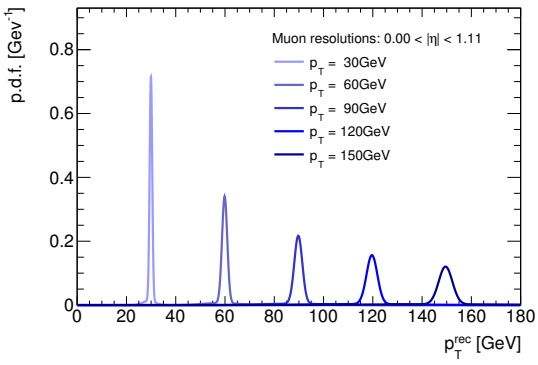

(b) Muon resolutions

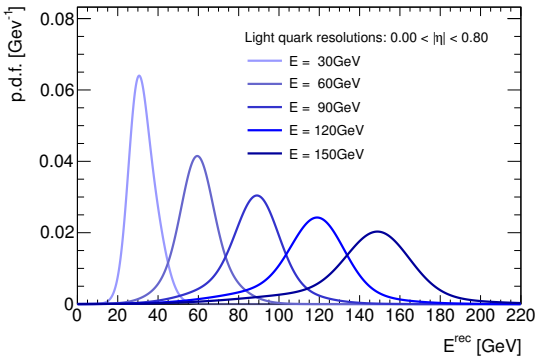

(c) Light-flavoured quark resolutions

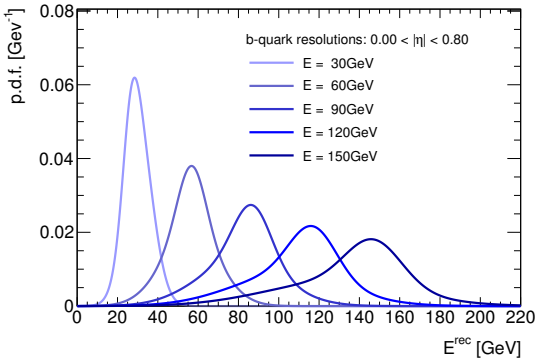

(d) b-quark resolutions

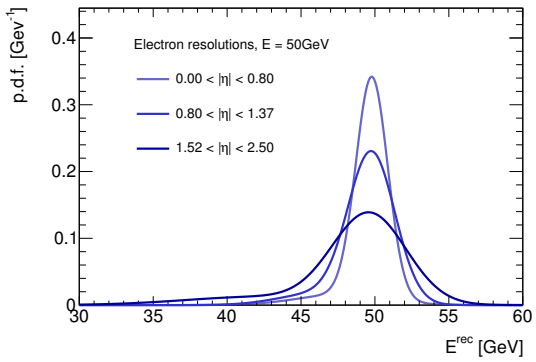

(e) Electron resolutions

Figure 6.1.: The resolution functions show the conditional probability to obtain a certain reconstructed energy or transverse momentum given the final state parton momentum: (a) electrons, (b) muons, (c) light-flavoured quarks (u, d, s, c) and gluons and (d) b-quarks. The panel (e) displays the probability for three different pseudorapidity intervals and given a fixed electron energy.

resulting from the object definition and reach a plateau of constant efficiency around 60 GeV. Furthermore, the transition region between barrel and end-cap parts is clearly visible. [Kin+14, Kin+15, Rie16]

6.3. The Matrix Element Toolkit

Any program that provides matrix element likelihoods has to compute the integral in Eq. 6.1 and as a consequence, these programs have to handle the following aspects:

- Evaluation of matrix elements and PDFs;
- Parametrization of the initial and final state phase space;
- Transfer function evaluation, including detector resolutions and all possible permutations between the parton level and detector level;
- Numerical computation of the integral (Eq. 6.1).

In addition, the normalization constant c_H has to be computed by an evaluation of Eq. 6.6.

The first highly automated tool for computing likelihoods was the MadWeight package [Art+10], which is related to the MadGraph5_aMC@NLO [Alw+14] software. The advantage of this program is that any LO matrix elements are provided directly by MadGraph. Furthermore, the phase space parametrization was automated by using a number of building blocks for almost any phase space topology in an efficient manner. However, this automation of the phase space parametrization works best for topologies, where all final state particles are matched to a reconstructed object. In general, this is not the case for events with single-top topologies. Another disadvantage of this package is the text-based input/output that makes it not applicable to large data sets common in ATLAS analyses. In addition, the high grade of automation prevents the user from altering the code, for example to implement efficiencies terms in the transfer functions. Recently, the MoMEMta project[2] officially released their code [Wer16]. It uses the automated phase space generator, but the main interface is written in C++ and based on common libraries such as ROOT [BR97] and CUBA [Hah06] for input/output and numerical integration.

The Matrix Element Method Toolkit [Kin+], short MEM$\mathbb{T}_k$, is another approach for computing matrix element likelihoods. It was developed in the context of this thesis, especially for the analysis of single top-quark production via the s-channel [ATL16a]. At the beginning of the MEM$\mathbb{T}_k$ development, Matrix Element Method implementations were highly specialized and often incorporated only one or two processes. Moreover, the goal of the project was to provide a modular and simple framework for discrimination and parameter fits. Its layout is depicted in Fig. 6.3. The toolkit uses the PDF

[2] `https://momemta.github.io/`, April 2017

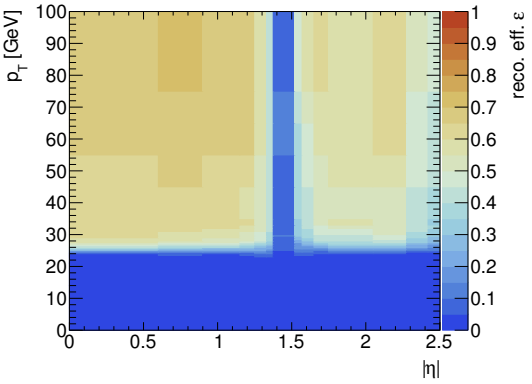

(a) Electron reconstruction efficiency

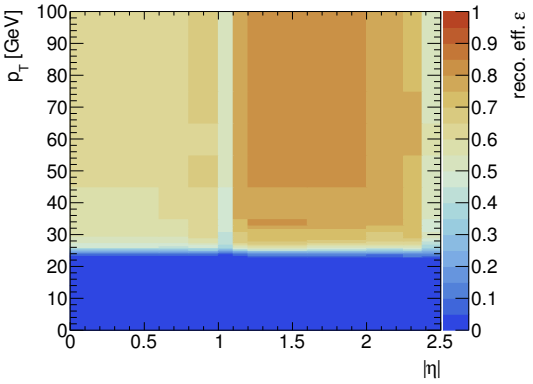

(b) Muon reconstruction efficiency

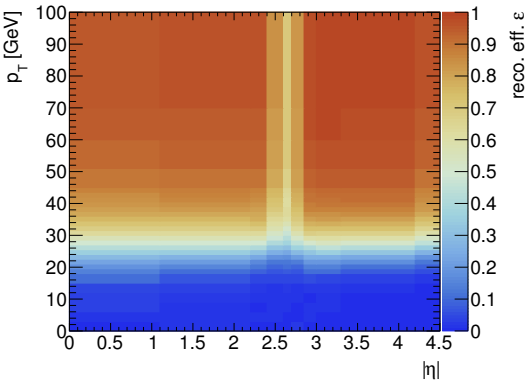

(c) Light-flavoured quark reconstruction efficiency

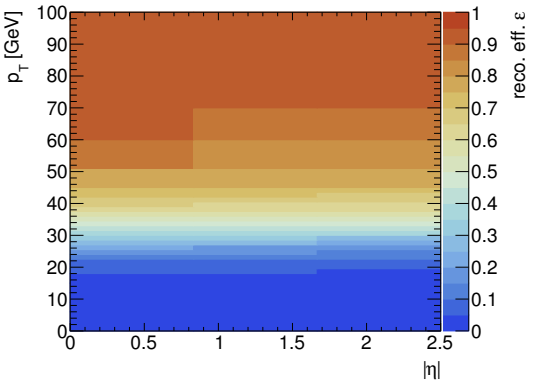

(d) b-quark reconstruction efficiency

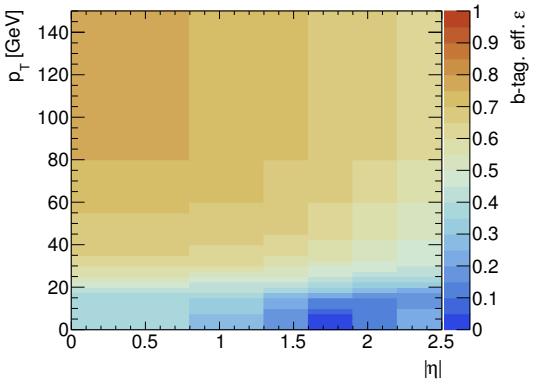

(e) b-tagging efficiency

Figure 6.2.: Reconstruction and tagging efficiencies of final state particles at the parton level as a function of their transverse momentum p_{T} and pseudorapidity η. Reconstruction efficiencies are shown for (a) electrons, (b) muons, (c) light-flavoured quarks (u, d, s, c) and gluons and (d) b-quarks. The trigger match requirement is included in the lepton efficiencies. Figure (e) depicts the b-tagging efficiency, which corresponds to the working point of the MV1 algorithm with an overall efficiency of 70 %.

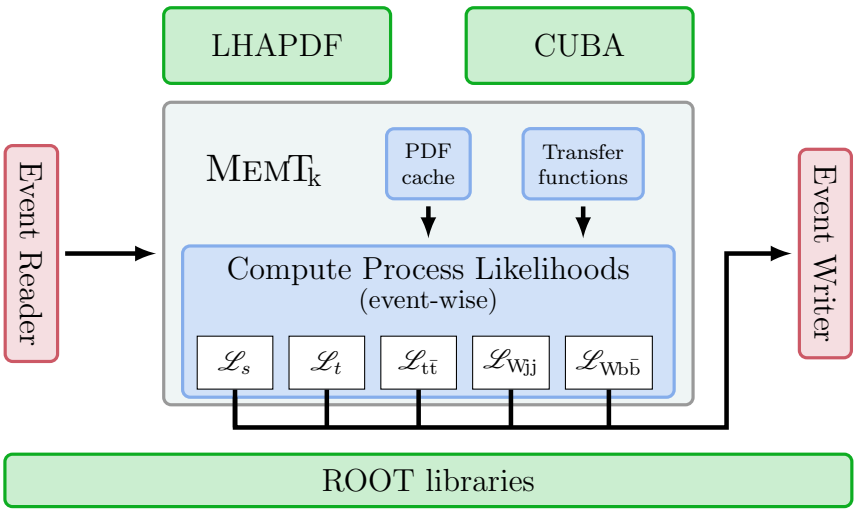

Figure 6.3.: General structure of the Matrix Element Toolkit. ROOT libraries are used for fast input/output. External libraries, such as LHAPDF and CUBA, are used for evaluating the PDFs and numerical integration, respectively. The processes for which likelihoods $\mathscr{L}_H$ currently can be computed are listed in Sec. 6.3.2.

library LHAPDF [WBG05] for the evaluation of the parton density functions and the matrix elements are imported from MCFM [CE10] in the current version. Due to the modular structure, it can be easily extended to incorporate other code for matrix element evaluation. Common classes for transfer functions and phase space parametrization exists and are fully customizable. The numerical integration is done by using the VEGAS [Lep78] algorithm which is provided by the CUBA library. The toolkit is able to read ROOT ntuples of a pre-defined generic format, or the user can provide his or her own reader to convert experimental data into MEMTk's event format.

6.3.1. Implementation

In this section, each aspect of the implementation is reviewed in more detail.

Parton density functions The parton density functions are provided by the LHAPDF library. The factorization scale Q at which the PDFs are evaluated can be set individually for each process. Moreover, a PDF caching system is installed to speed up the computation.

Matrix elements A common base class for matrix elements is provided and any matrix element code can be incorporated. Currently, all scattering amplitudes are taken from MCFM. The interface to the FORTRAN routines need to be changed to transfer the four-momenta and configuration variables, such as the strong coupling constant α_s to the MCFM matrix element evaluation. Checks

were performed by computing the total inclusive cross section using the MEMTk and the MCFM code. The available processes are listed in Sec. 6.3.2.

Numerical integration The numerical integration of the likelihood integral is performed by using Monte Carlo techniques, in particular the VEGAS algorithm provided by the CUBA library. In an iterative procedure, the likelihood function is evaluated multiple times. The algorithm uses importance sampling to focus on regions where the integrand is large in magnitude. The advantage of the VEGAS algorithm is that it adapts the distribution of random numbers at each iteration step. Therefore, the algorithm performs best if the parametrization is chosen such that peaks in the integrand are aligned with the coordinate axes. The parameters that define the Monte Carlo integration, such as number of calls or required precision of the result, can be set individually for each process.

The CUBA library provides further algorithms for numerical integration, which can be used for the likelihood calculations [Kap15].

Phase space parametrization The VEGAS algorithm converges faster, if the parametrization takes into account the characteristics of the integrand. In particular, the transfer functions have a Gaussian shape and it is in most cases optimal to choose the parametrization along the variables used for transfer function evaluation. Furthermore, analytic expressions have to be derived to account for the integration of the δ-function in the phase space definition, e. g. to fulfil the energy-momentum conservation. Additional, δ-functions can arise from ideal transfer functions or by including additional constrains when using the top-quark mass as integration variable. An automated procedure to derive phase space parametrizations exists and is described in [Art+10]. However, these phase space parametrizations work best, if all final state particles can be matched to reconstructed objects. In single-top event topologies, this is not always the case, especially for $t\bar{t}$ processes with unmatched final state particles. For each process that is discussed in Sec. 6.3.2, an optimized phase space transformation was developed and can be found in [Kin+14, Kin+15, Rie16].

Transfer function The interface for transfer functions needs to cover resolution functions, efficiencies and all possible permutations of parton level to detector level assignments.

The energy resolution functions provided by the KLFitter group (c. f. Sec. 6.2.1) are implemented in the toolkit. In order to speed up the likelihood computations, perfect resolution for the measured angles ϑ and φ of reconstructed objects is assumed. Therefore, the resolution function of a single particle matched to a detector level object is described by

$$W_{\mathrm{res}}(p^{\mathrm{rec}}|p) = \frac{1}{|\det J|} W_{\mathrm{res}}(E^{\mathrm{rec}}|E) \cdot \delta(\cos\vartheta^{\mathrm{rec}} - \cos\vartheta) \cdot \delta(\varphi^{\mathrm{rec}} - \varphi). \quad (6.10)$$

Consequently, the phase space parametrization has to be performed in terms of $\mathrm{d}^3p = E^2\,\mathrm{d}E\,\mathrm{d}\cos\vartheta\,\mathrm{d}\phi$. The Jacobian determinant contained in Eq. 6.10 accounts for the transformation of variables. This is in particular true for muons as their resolution function is defined using the transverse momentum p_T and not the energy E of the final state particle.

The reconstruction and b-tagging efficiencies are provided in the form of two dimensional histograms. For each matched and unmatched particle the appropriate reconstruction efficiency terms are taken into account, depending on the final state particle. In case of b-quarks, an extra factor of $\varepsilon_{\text{b-tag}}$ is taken into account for tagged reconstruction objects. Otherwise the inefficiency $(1 - \varepsilon_{\text{b-tag}})$ for tagging a b-jet is used. For light-flavoured quarks or gluons, a constant mis-tag efficiency is used.

Finally, all permutations of final state particle to detector level object associations need to be considered, when evaluating the transfer function for a process in a specific event. The number of all possible permutations is reduced by considering only those permutations that contribute significantly to the process likelihood. Therefore, electrons and muons on particle level are matched to their corresponding counterpart on detector level, because the identification requirements on reconstructed leptons are very strict. A possible lepton charge misidentification is neglected as well. The matching of quarks to jets in the event can be done in two ways. On the one hand, the b-tag information can be used and thus only b-quarks are allowed to be matched to b-jets. On the other hand, for some processes without any b-quarks in the final state, it is necessary to relax the matching requirements and allow for light-flavoured quarks to be matched to b-jets as well. The default setting is to match only b-quarks to b-jets to speed up the computation, and only if no possible permutations are found, light-flavoured quarks are matched to b-jets. In any case, b-quarks can always be matched to untagged jets if possible. For identical permutations, the likelihood calculation is performed only once and the weight w_i in Eq. 6.4 is adapted accordingly.

Normalization constant The normalization constant can be computed by removing the resolution functions from the likelihood integral. Special phase space parametrizations are used to efficiently calculate these factors.

Validation The validation of the matrix element method has to cover the three main building blocks of the likelihood integral in Eq. 6.1, namely the matrix element, the transfer functions and the phase space parametrization. First, the matrix element can be tested at specific phase space points and its value can be compared directly to the one obtained with MCFM. Moreover, the likelihood integral can be used to calculate the cross section of a specific process by removing the transfer function $T_H(X|\Phi)$ and the normalization constant c_H from Eq. 6.1. Second, the normalization of the transfer function can be checked by evaluating Eq. 6.5. At last, the phase space volumes for n final state particles

produced in hadron–hadron collisions at $\sqrt{s} = 1\,\text{TeV}$ are listed in [Art+10] and can be used to validate the phase space parametrization.

6.3.2. Available Processes

In the current version, matrix elements for eight different processes are made available using MCFM routines. In case of ambiguities in the parton level to detector level assignments, the matching of the final state to events with single-top topologies is discussed. Such events contain a single reconstructed electron or muon, and two jets. One or two of these jets might be b-tagged.

Single top-quark production, *s*-channel with two final state partons The electroweak production of top-quarks via the s-channel is shown in Fig. 2.4(b), Sec. 2.3. The matrix element includes the top-quark decay into a lepton pair and a b-quark.

Single top-quark production, *s*-channel with three final state partons This matrix element includes the real radiation corrections to the LO process above. The integration diverges if the radiation is too soft or collinear. Therefore, the phase space region is limited to cases for which the radiated light-flavoured quark or gluon has a transverse momentum larger than 10 GeV and the invariant mass of the radiated quark or gluon with any other initial or final state particle is larger than 10 GeV. The modelling of the s-channel process is improved by including the real radiation into the likelihood computation, because transverse momenta of the top-quark are now possible. Light-flavoured quarks or gluons in the final state are matched to light-flavoured jets, only.

Single top-quark production, *t*-channel The t-channel process for single top-quark production is included in the four-flavour scheme, i. e. the initial state is a light-flavoured quark or gluon. The Feynman diagram is similar to the one in Fig. 2.4(a), the only difference is that the initial state b-quark originates from a gluon splitting into a $\mathrm{b\bar{b}}$ pair. In the likelihood calculation, the narrow-width approximation[3] for the top-quark is used, which speeds up the calculation.

$\mathrm{t\bar{t}}$ production, single-lepton final state This process models top-quark pair production with one lepton pair and four quarks in the final state. Two of the four quarks are b-quarks originating from the top-quark decays. In single-top event topologies with one or two b-jets, two quarks are not matched to a reconstructed object. Only permutations of b-quarks matched to b-jets are considered.

$\mathrm{t\bar{t}}$ production, di-lepton final state In contrast to the previous process, both top-quarks decay leptonically. This leads to a final state with two charged leptons, two neutrinos and two b-quarks.

[3] In the limit of a vanishing top-quark width, the Breit-Wigner function of the top-quark propagator can be replaced by a Dirac delta-function.

$\mathbf{W}$ + two light partons In order to match the event topology of single top-quark events, the two light partons in this process can be matched to b-jets. The W boson decays leptonically.

$\mathbf{W + b\bar{b}}$ production This process describes the W boson production with a $b\bar{b}$ pair. The corresponding Feynman diagram is depicted in Fig. 2.7(a).

$\mathbf{W}$ + c + light parton production This matrix element models the process of W boson production in association with a c-quark and another light parton, and includes the leptonic decay of the W boson. The Feynman diagram is shown in Fig. 2.7(b).

7. Single Top-Quark Analysis

In this section, the necessary steps for measuring the single top-quark cross section for the s-channel and t-channel processes are described. The overall analysis outline is depicted in Fig. 7.1. Events from data or Monte Carlo simulations are subject to a common event reconstruction. This first analysis step is done using a common analysis framework [Sta13], which is responsible for applying event quality cuts as well as defining and selecting objects based on the definitions discussed in Sec. 4. In addition, systematic variations are provided for dedicated studies (c. f. Sec. 8). At this point, the analysis presented in this thesis is split into two parts. On the one hand, an event selection dedicated to measure the s-channel single-top cross section is conducted. After this event selection, the matrix element method is used to compute process likelihoods for all events and a discriminant, which is based on these likelihoods, is built. This part is entirely based on the ATLAS s-channel analysis [ATL16a], which was the first application of the MEM$_{\text{T}\bar{\text{t}}}$ software and was performed in collaboration with my colleagues from the experimental particle group at the Humboldt University Berlin. Furthermore, the subsequent steps of this analysis including the statistical evaluation and cross section measurement are applied as well. On the other hand, a dedicated analysis for the single-top t-channel cross section is performed. The event selection is based on the current ATLAS t-channel measurement at $\sqrt{s} = 8\,\text{TeV}$ [ATL17a]. However, since the aim of this analysis is a combined measurement of the s-channel and t-channel single top-quark cross sections, the two signal regions are not allowed to overlap in order to have two independent data sets. Furthermore, the treatment of systematic uncertainties need to be unified between these two analysis parts. Otherwise, a straightforward combination of the two cross section measurements is not possible. For all those reasons, the event selection for the t-channel part was altered with respect to the current one, in particular with regard to the application of the matrix element method. Finally, the predicted and observed distributions for the matrix element discriminant are analysed using a combined maximum likelihood fit, discussed in Sec. 9.1, and the combined cross section measurement is performed.

The data set and Monte Carlo samples used in this analysis are presented in Sec. 7.1. The event selections for the two different analysis parts are discussed in Secs. 7.2 and 7.3 for the s-channel and t-channel, respectively. A fit of the SM prediction to the data is performed in different kinematic regions defined by the event selection in order to check the modelling of basic kinematic distributions. This likelihood fit is outlined in Sec. 7.4 and the modelling of some distributions is improved by

applying a reweighting procedure described in Sec. 7.5. Secs. 7.6 and 7.7 comprise the predicted and observed event yields as well as the kinematic distributions. The process likelihoods and the event classification is described in Sec. 7.8.

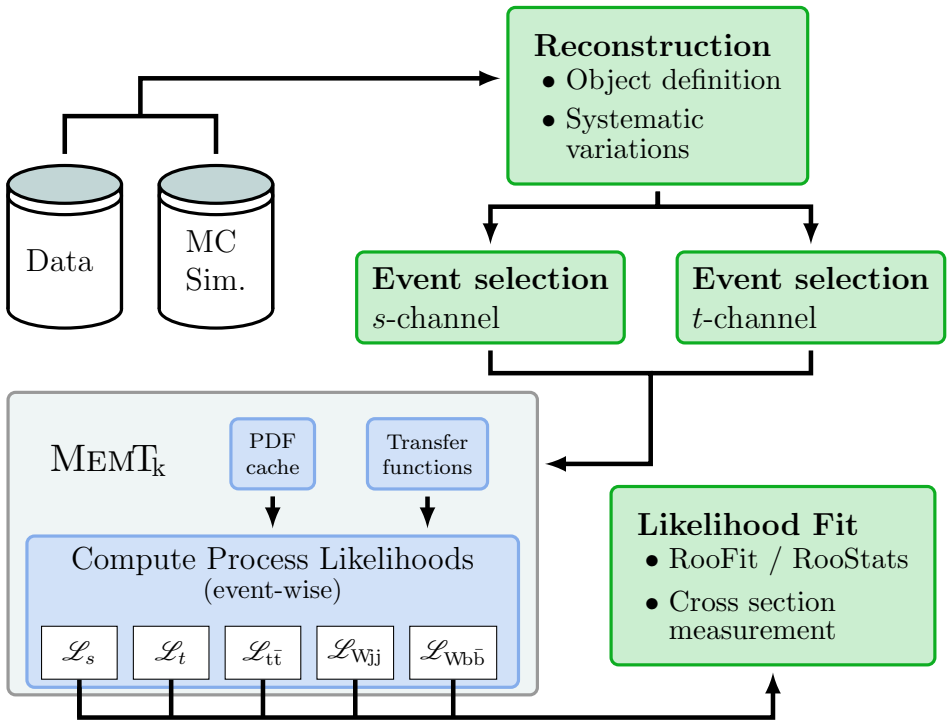

Figure 7.1.: Analysis Outline. First, events from data and MC simulations are reconstructed using the common object definitions in Sec. 4. Subsequently, a dedicated event selection is performed to enrich events with an s-channel or t-channel event topology. Then, events are classified based on the likelihoods computed with the MEMTk. Finally, the cross section of s-channel and t-channel single top-quark production is extracted using a maximum likelihood fit.

7.1. Data and Simulation Samples

The analysis uses proton–proton-collision data at a centre-of-mass energy of 8 TeV recorded with the ATLAS detector at the LHC in the year 2012. Unprescaled single electron and single muon triggers, as described in Sec. 4, were used. For the analysis of events with top-quark topologies, a good performance of all detector components is required. After applying data quality criteria offline, the data set corresponds to an integrated luminosity of $(20.3 \pm 0.6)\,\text{fb}^{-1}$.[1] The luminosity measurement was

[1] After the analysis was finished, the luminosity measurement was improved [ATL16b]. The relative uncertainty was reduced to 1.9 % and the central value changed by −0.19 % to $(20.2 \pm 0.4)\,\text{fb}^{-1}$. The updated luminosity measurement could not be incorporated in this thesis, however the effects on the results are tiny.

performed using beam-separation scans at the end of the data-taking period. A description of the method can be found in [ATL13a].

Monte Carlo simulations are used to study single top-quark processes as well as the main background processes (c. f. Sec. 2.4) with the exception of the QCD multi-jet background. The latter is estimated using a data driven method (c. f. Sec. 5). For some Monte Carlo simulations, a fast simulation package AtlFast2 [ATL98] is used instead of the full detector simulation, in particular for samples involved in studies on systematic uncertainties discussed in Sec. 8.

The hard scattering process for single top-quark production and top-quark pair production is simulated by the POWHEG-Box generator [FNO07] in NLO accuracy. The parton shower and hadronisation as well as the underlying event is modelled by PYTHIA6 [SMS06]. POWHEG uses the NLO CT10 parton distribution function [Lai$^+$10], while PYTHIA uses the Perugia 2011C [Ska10] tune and the LO CTEQ6L1 PDF. The modelling of all processes involving top-quarks is studied by using alternative simulation samples. Additional samples for s-channel and t-channel single top-quark production are generated using the MadGraph5_aMC@NLO generator [Alw$^+$14] interfaced with HERWIG [Cor$^+$01] and JIMMY [BFS96] for parton shower and underlying event simulation, respectively. The ATLAS tune AUET2 [ATL11b] and CT10 PDFs are used. Furthermore, single top-quark events at LO are produced by the AcerMC generator [KR13], while the parton distribution functions are evaluated using the CTEQ6L1 PDFs. The parton shower is provided by PYTHIA with the same configurations as for the other samples. In order to study differences in the parton shower model, the POWHEG generator linked with HERWIG is used to generate events using CT10 PDFs. Variations of the renormalization and factorization scales are studied by interfacing the POWHEG generator to PYTHIA with different parton shower tunes. Top-quark pair events and single-top Wt events are produced using MC@NLO [Fri$^+$06] coupled to HERWIG for parton shower and hadronisation and JIMMY for the underlying event. The effects of initial and final state radiation are studied by using the POWHEG and PYTHIA6 setup, but with varied parameters for the QCD radiation.

All top-quark samples are generated assuming a top-quark mass of 172.5 GeV. They are normalized to cross section predictions, which use the same value for the top-quark mass. The predictions for single top-quark production are given in Sec. 2.3. The top-quark pair production cross section is calculated at NNLO in QCD including the resummation of next-to-next-to-leading logarithmic soft gluon terms [Cac$^+$12, BCM12, CM12, CM13, CFM13, CM11] and is $\sigma_{t\bar{t}} = 253^{+13}_{-15}$ pb. The uncertainties correspond to the quadratic sum of the uncertainties on the renormalization and factorization scale and on the PDFs.

The production of W bosons with additional jets is modelled by the SHERPA generator [Gle$^+$09]. SHERPA covers the event generation, parton shower and the underlying event and uses CT10 PDFs. In addition to these samples, the modelling of W boson production is studied using ALPGEN [Man$^+$03] samples combined with

PYTHIA6 and CTEQ6L1 PDFs. Furthermore, the same setup is used to generate events for Z boson production. The production of diboson events (WW, WZ and ZZ) with at least one lepton is done with HERWIG. The simulation samples for single boson and diboson productions are normalized to cross section predictions at NNLO [Ana+04] and NLO [CEW11] accuracy.

The effect of pile-up is included into the simulation by adding additional minimum bias events to each hard interaction. All events are reweighted by using the average number of inelastic interactions per bunch crossing to match the conditions found in data. Furthermore, a scale factor is applied to adjust the correlation between the mean number of interactions and the number of reconstructed primary vertices.

The complete list of all Monte Carlo samples used in this thesis are given in Tabs. A.1–A.3 in App. A. These tables also contains the cross section values used for the normalization of each sample.

7.2. Event Selection, s-Channel

The event selection for the s-channel part comprises of four different kinematic regions. The signal selection is used to enrich events with s-channel topology. Additional regions are defined for the main background processes, W+jets production and $\mathrm{t\bar{t}}$ production. As described in Sec. 2.4, events with reconstructed τ-leptons are not part the event selections. Therefore, from now on the term lepton will refer to electrons and muons, only.

For the event selection, only objects, which comply with the definitions in Sec. 4, are considered. Therefore, any event selected for one of the four regions, need to have exactly one single electron or one single muon present. The lepton must have a transverse momentum larger than $p_{\mathrm{T}} > 25\,\mathrm{GeV}$ and a pseudorapidity of $|\eta| < 2.5$. Additional leptons selected with less strict identification and isolation criteria may be included in the event. Furthermore, selected events must contain at least one jet with a transverse momentum of $p_{\mathrm{T}} > 25\,\mathrm{GeV}$ and $|\eta| < 4.5$. Jets with a transverse momentum lower than 25 GeV do not meet the object requirements of Sec. 4 and are not considered in this analysis. All events need to fulfil general quality requirements in order to remove mis-reconstructed events. Non-collision background is rejected by requiring at least one good primary vertex candidate, which is reconstructed from at least five tracks.

7.2.1. Signal Selection

Signal events are selected by requiring an isolated charged lepton with a transverse momentum of $p_{\mathrm{T}} > 30\,\mathrm{GeV}$. Furthermore, selected events must have exactly two b-tagged jets within $|\eta| < 2.5$. The MV1 algorithm is used to identify b-jets and is

operated at a working point that corresponds to an efficiency of 70 %. The transverse momentum of the leading jet needs to be larger than 40 GeV, while for the other jet, a transverse momentum of $p_{\mathrm{T}} > 30\,\mathrm{GeV}$ is required. Additional jets with a transverse momentum between 25 GeV and 30 GeV are not allowed. In order to reject events from multi-jet background, a missing transverse momentum of $E_{\mathrm{T}}^{\mathrm{miss}} > 35\,\mathrm{GeV}$ and a transverse mass of the W boson[2] of $m_{\mathrm{T}}^{\mathrm{W}} > 30\,\mathrm{GeV}$ is required.

The main source of background for events with two b-tagged jets is coming from top-quark pair production. In particular, di-leptonic events contribute to about 75 % of all $\mathrm{t\bar{t}}$ events in the signal region. A large fraction of these events contain at least one τ-lepton, which is not part of the object definitions and it may not be reconstructed as jet. In order to reduce the amount of di-leptonic $\mathrm{t\bar{t}}$ events in the signal region, the event selection makes use of the additional leptons selected with a lower momentum threshold of $p_{\mathrm{T}} > 5\,\mathrm{GeV}$ and less stringent quality requirements, as defined in Sec. 4.4. The lower momentum lepton can be associated with one of the top-quarks, either to a leptonic top-quark decay into an electron or muon or indirectly from a leptonic decaying τ-lepton. Any event with such additional leptons is rejected. This reduces the amount of background events from top-quark pair production by about 30 %, while the signal contribution is almost unchanged (-0.4 %).

7.2.2. Background Selection for W + jets Production

The normalization and modelling of the W + jets background is investigated in a region with a selection similar to the signal selection. The same requirements for the transverse momenta of electrons, muons and jets are imposed. Furthermore, the same selection cuts for $E_{\mathrm{T}}^{\mathrm{miss}}$ and $m_{\mathrm{T}}^{\mathrm{W}}$ of 35 GeV and 30 GeV are used. In contrast to the signal region, jets are tagged using the MV1 algorithm with a different working point. This leads to a higher b-tagging efficiency of 80 %, but also results in a less pure selection of b-jets. Events with two b-tags corresponding to the MV1 working point of the signal region are removed as depicted in Fig. 7.2. The veto on additional jets as well as the veto on additional leptons is not applied in this region.

7.2.3. Background Selection for $\mathrm{t\bar{t}}$ Production

Events with a single isolated lepton and three or four jets are selected to enrich $\mathrm{t\bar{t}}$ events. Independent from the jet multiplicity, each jet needs to have a transverse momentum of $p_{\mathrm{T}} > 25\,\mathrm{GeV}$ and need to be located in the central region with $|\eta| < 2.5$. Furthermore, two b-jets identified by the MV1 70 % working point are required. The lepton transverse momentum need to be higher than $p_{\mathrm{T}} > 30\,\mathrm{GeV}$. The same

[2] The transverse mass of the W boson, $m_{\mathrm{T}}^{\mathrm{W}}$, is calculated from the lepton transverse momentum p_{T}^{ℓ} and the difference of the azimuth, $\Delta\varphi$, between the lepton and the missing transverse momentum as $m_{\mathrm{T}}^{\mathrm{W}} = \sqrt{2 E_{\mathrm{T}}^{\mathrm{miss}} p_{\mathrm{T}}^{\ell} \left(1 - \cos(\Delta\varphi(E_{\mathrm{T}}^{\mathrm{miss}}, p_{\mathrm{T}}^{\ell}))\right)}$.

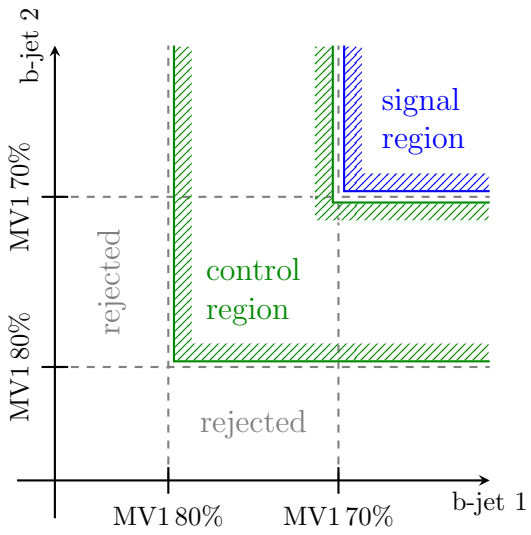

Figure 7.2: The signal selection requires two jets to be b-tagged by the MV1 algorithm with a 70 % working point (blue area). The W+jets control region (green area) contains also two b-tagged jets, but the tagging is performed with the MV1 80 % working point. An overlap with the signal region is avoided by requiring that at least one of the jet has to have a weight below the 70 % threshold.

threshold values for $E_{\mathrm{T}}^{\mathrm{miss}}$ and $m_{\mathrm{T}}^{\mathrm{W}}$ of 35 GeV and 30 GeV are used in this region, too. Although, the contribution from signal events is higher for a three-jet selection, the main motivation is that the region defined by this selection is kinematically closer to the signal region than the four-jet selection. As for the W+jets selection, no veto on additional jets nor leptons is performed.

7.3. Event Selection, *t*-Channel

The event selection presented in this section is used to study events with single top-quark t-channel topology as well as two important background processes with similar final state, W+jets and $\mathrm{t\bar{t}}$ production. All reconstructed objects satisfy the conditions defined in Sec. 4 and the event selection includes the general event quality requirements given at the beginning of Sec. 7.2.

7.3.1. Signal Preselection

The preselection of signal events requires a charged lepton with transverse momentum $p_{\mathrm{T}} > 30\,\mathrm{GeV}$ and two jets within a pseudorapidity interval of $|\eta| < 4.5$. As for the s-channel signal region, the transverse momentum threshold for the leading jet is 40 GeV, while the second jet must have a transverse momentum larger than 35 GeV. No other jets with momentum between 25 to 35 GeV are allowed. One of these two jets must be identified as b-jet by the MV1c algorithm using a working point that corresponds to a 50 % b-tag efficiency.

The background events contain a contribution of equal size from semi-leptonic and di-leptonic $\mathrm{t\bar{t}}$ events. Nevertheless, events that contain additional leptons with loose

selection requirements and $p_{\mathrm{T}} > 5\,\mathrm{GeV}$ are rejected to further reduce the background from top-quark pair events by 23 %. Furthermore, non-top background events are removed from the selected events by requiring a missing momentum of $E_{\mathrm{T}}^{\mathrm{miss}} > 30\,\mathrm{GeV}$ and $m_{\mathrm{T}}^{\mathrm{W}} > 50\,\mathrm{GeV}$.

7.3.2. Signal Selection

A similar event selection to the one defined in the previous section was used for the latest single top-quark t-channel measurement at $\sqrt{s} = 8\,\mathrm{TeV}$ [ATL17a]. In contrast to the neural network that was used for this measurement, the matrix element method is rather CPU expensive. In order to analyse all signal events on a feasible time-scale, the number of processed events need to be reduced compared to the signal preselection.

As a consequence, an optimized selection with respect to an increased signal-to-background ratio was studied in a dedicated analysis [Bey17]. Additional variables for the cut-based selection are identified by using the ranking of input parameters from the neural network analysis. In addition to the preselection cuts, the transverse momentum sum of all objects, $H_{\mathrm{T}}(\ell, E_{\mathrm{T}}^{\mathrm{miss}}, jets)$, must be larger than 180 GeV. The transverse W boson mass must not exceed 125 GeV. The invariant mass of the isolated lepton, ℓ, and the b-tagged jet, j_{b}, must be in the range of $40\,\mathrm{GeV} < m(\ell, j_{\mathrm{b}}) < 160\,\mathrm{GeV}$, and the invariant mass of both jets, $m(j_{\mathrm{lf}}, j_{\mathrm{b}})$, must be greater than 80 GeV. The light-flavoured jet is denoted as j_{lf}. Finally, the following condition for H_{T} and $m(j_{\mathrm{lf}}, j_{\mathrm{b}})$ must be fulfilled: $\frac{20}{19} H_{\mathrm{T}} - \frac{4800}{19} < m(j_{\mathrm{lf}}, j_{\mathrm{b}})$. The distribution of the four quantities used in the refined event selection are shown in Fig. 7.3[3]. The cut thresholds are visualized by the grey exclusion lines. The signal-to-background ratio is improved from 23 % to 39 % by imposing these additional cuts, while the number of expected signal events is reduced by 15 %.

The two signal regions are separated by removing all events from the t-channel signal region that contain two jets, which are tagged by the MV1 algorithm used in the s-channel signal region. This reduces the amount of t-channel events by 3.4 % and the background contribution by 9.4 %.

7.3.3. Background Selection for W + jets

The modelling of the W+jets background processes is studied in a dedicated region. Events are selected using the preselection cuts, but with a different b-tag requirement. The MV1c algorithm with a working point with 80 % efficiency is used to identify b-jets. Furthermore, events that contained exactly one b-tagged jet using the MV1c 50 % working point are removed in order to avoid an overlap with the signal region.

[3] The first and last bin in each distribution contains overflow events.

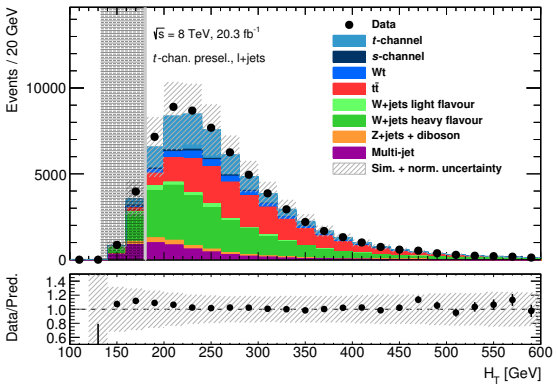

(a) Sum of the transverse momentum of all objects

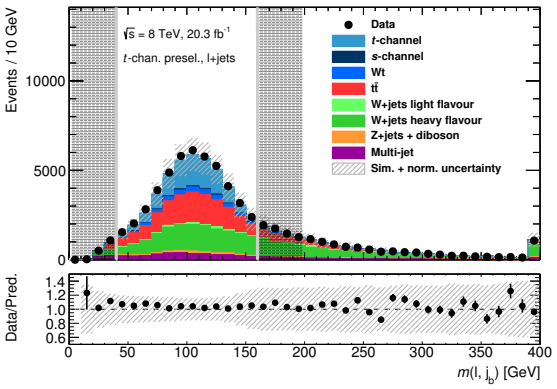

(b) Invariant mass of the lepton and b-tagged jet

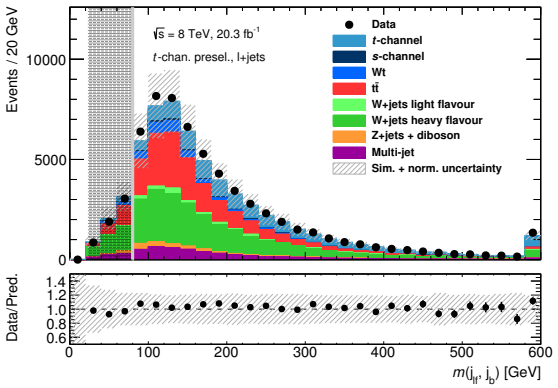

(c) Invariant mass of the two jets

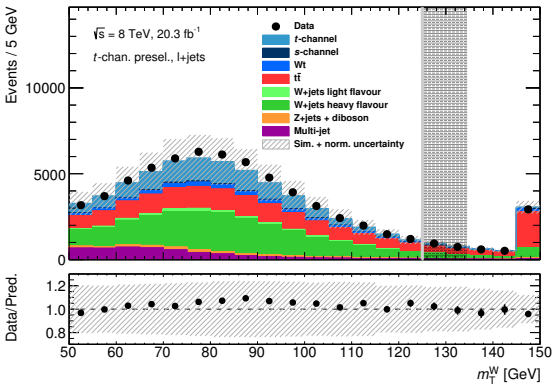

(d) Transverse W boson mass

Figure 7.3.: Distribution of selection variables in the region defined by the t-channel signal preselection. (a) Sum of the transverse momentum of all objects H_T, (b) invariant mass of the lepton and b-tagged jet, $m(\ell, j_\mathrm{b})$, (c) invariant mass of the two jets, $m(j_\mathrm{lf}, j_\mathrm{b})$, and (d) transverse W boson mass. All simulated distributions are normalized to the data luminosity. The uncertainty bands correspond to the uncertainties due to the finite sample statistics and the normalization uncertainties by theory.

7.3.4. Background Selection for $\mathrm{t\bar{t}}$ Production

The $\mathrm{t\bar{t}}$ control regions consists of events with a single isolated lepton with a transverse momentum of $p_\mathrm{T} > 30\,\mathrm{GeV}$ and three or four jets with $p_\mathrm{T} > 30\,\mathrm{GeV}$ and $|\eta| < 4.5$. All events are required to have two b-tagged jets irrespective of the number of selected jets. The MV1c algorithm with the 50 % working point is used. The requirements for $E_\mathrm{T}^\mathrm{miss}$ and m_T^W are 30 GeV and 50 GeV, respectively. Events that contain additional jets below 30 GeV as well as additional loose leptons are rejected.

7.4. Standard Model Fit

In the following sections, distributions of kinematic variables are shown. In order to compare the predicted distributions to the observed one, a maximum likelihood fit is performed. The model used for the likelihood fit describes the data distribution as sum of all individual distributions from Monte Carlo simulations and the data driven multi-jet background estimate. The normalization of each sample is a fit parameter, which is constrained by the theoretical uncertainty on the corresponding cross section. A detailed discussion of the likelihood fit model is given in Sec. 9.1. In contrast to this model, the signal parameters for the s and t-channel normalization are constrained as well and no systematic variations are taken into account. The transverse W boson mass is chosen as discriminant variable for the fit, as this variable is robust for all regions. The results are given in Tab. 7.1 for each region. The deviations for each normalization parameter are compatible within their uncertainties. In the following, the samples in all control distributions are scaled with these fit results and the uncertainty bands are computed as the quadratic sum of the statistical and normalization uncertainty of each sample. The normalization uncertainty corresponds to the uncertainty on the respective normalization parameter associated with each sample.

	s-channel selection				t-channel selection			
Process	signal	W+jets	$t\bar{t}$ 3j	$t\bar{t}$ 4j	signal	W+jets	$t\bar{t}$ 3j	$t\bar{t}$ 4j
s-channel	1.00	1.00	1.00	1.00	1.00	1.00	1.00	1.00
t-channel	1.00	1.00	1.00	1.00	1.00	1.00	1.00	1.00
Wt	0.99	1.00	0.99	0.99	0.99	0.99	0.99	0.99
$t\bar{t}$	0.93	0.99	1.03	1.00	0.98	0.99	1.05	1.03
W+light jets	0.82	0.85	0.92	0.92	0.87	1.34	0.93	0.93
W+heavy flavour	1.63	1.35	1.10	1.48	1.19	0.97	0.87	0.91
Z+jets & diboson	1.03	0.81	0.82	0.73	0.76	0.75	0.79	0.80
Multi-jet	0.74	0.73	0.70	0.71	0.85	0.88	0.90	0.86

Table 7.1.: Results for the likelihood fit to the $m_{\mathrm{T}}^{\mathrm{W}}$ distribution, separately for each selection. Relative normalization uncertainties of 4 to 7 % (top quark processes), 30 % (W + heavy flavour, Z + jets, diboson production) and 60 % (multi-jet and W + light-flavour jet production) are used as input for the fit (c. f. Tab. 8.1 in Sec. 8.2).

7.5. Reweighting of W + jets Events

In the context of modelling studies performed in the dedicated W+jets background region for the single-top t-channel selection, a mis-modelling in two distributions was

observed. The distribution for $E_{\mathrm{T}}^{\mathrm{miss}}$ shows discrepancies at low and high values. The same trend is observed for the transverse momentum of the W boson, $p_{\mathrm{T}}(\mathrm{W})$, as well. Both distributions are shown in Fig. 7.4.

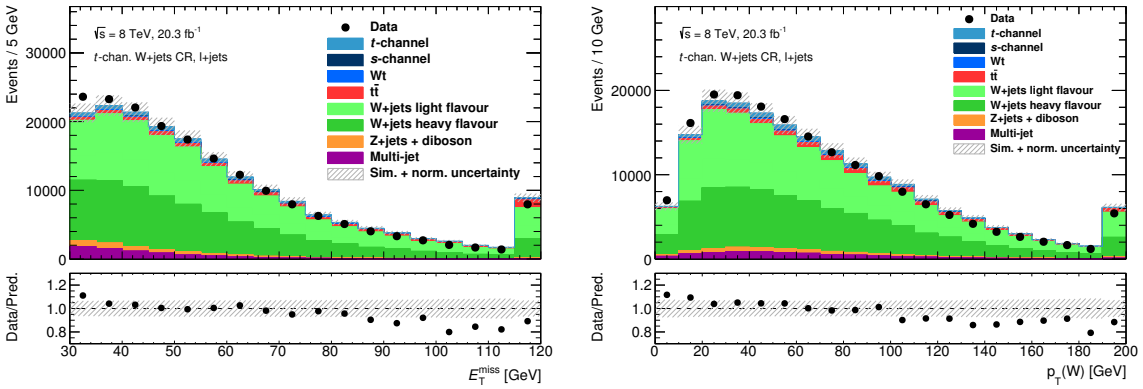

(a) Missing transverse momentum

(b) W boson transverse momentum

Figure 7.4.: Distributions of (a) missing transverse momentum and (b) transverse momentum of the W boson in the t-channel W+jets control region. All simulated distributions are fitted to data within their SM constraints. The uncertainty bands correspond to the uncertainties due to the finite sample statistics and the normalization uncertainties by theory.

In order to improve the modelling of these distributions, scale factors are derived using the $p_{\mathrm{T}}(\mathrm{W})$ distribution. First, the SM background, i. e. single-top, $\mathrm{t\bar{t}}$, Z+jets/diboson and multi-jet production, is subtracted from data. In a second step, the SM subtracted data distribution and the W+jets distribution, combining heavy and light-flavour jet production, are normalized to unity. Scale factors are given by the ratio of these two normalized distributions and are determined separately for events containing electrons or muons. The result is shown in Fig. 7.5. For this procedure, an appropriate binning is chosen to limit the influence of statistical fluctuations in each bin. Normalized distributions are used in order to preserve the overall number of events in the W+jets region after reweighting. The relatively low statistics for W+jets production in the s-channel W+jets region, does not allow to derive separate scale factors for this region. However, the scale factors derived in the t-channel region were validated for both regions and a consistent treatment of both s-channel and t-channel regions is achieved. Similar reweighting procedures were also carried out by other ATLAS analyses [And$^+$14, Ars$^+$14, Coc$^+$13].

The scale factors are applied as an additional event weight for each W+jets event in the signal and W+jets and regions of both channels. The W+jets contribution in both $\mathrm{t\bar{t}}$ control regions is less than 8 % and therefore it is not applied in those region. The differences on the predicted number of events in the signal regions is less than 2 %. More information on the reweighting procedure can be found in [Kin$^+$15]. The

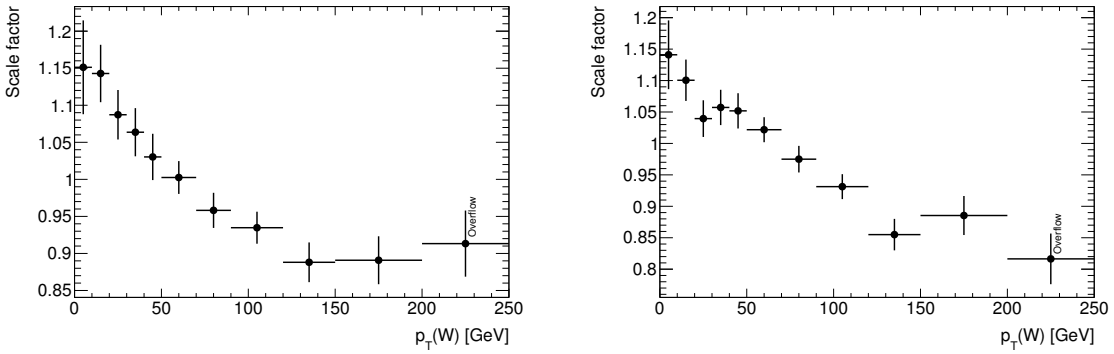

(a) e + jets selection (b) μ + jets selection

Figure 7.5.: Scale factors for the (a) e + jets selection and the (b) μ + jets selection in the t-channel. The correction is derived from the normalized $p_{\mathrm{T}}(\mathrm{W})$ distributions of data with the SM background subtracted and W+jets production. The scale factor for events with $p_{\mathrm{T}}(\mathrm{W}) > 200\,\mathrm{GeV}$ is given in the last bin of each figure (overflow).

reweighted distributions for $E_{\mathrm{T}}^{\mathrm{miss}}$ and $p_{\mathrm{T}}(\mathrm{W})$ are shown in Fig. 7.6. The modelling of all other distributions shown in the next sections also receive minor improvements due to the application of the reweighting scale factors.

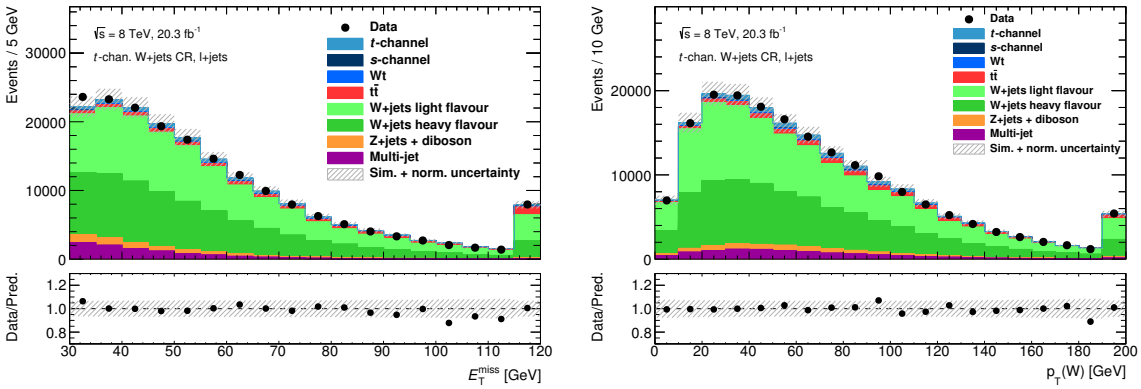

(a) Missing transverse momentum (b) W boson transverse momentum

Figure 7.6.: Distributions of (a) missing transverse momentum and (b) W boson transverse momentum in the t-channel W + jets control region after applying the reweighting scale factors. All simulated distributions are fitted to data within their SM constraints. The uncertainty bands correspond to the uncertainties due to the finite sample statistics and the normalization uncertainties by theory. A perfect agreement between predicted and observed distributions for $p_{\mathrm{T}}(\mathrm{W})$ after reweighting is not expected, because a different binning was used for the scale factors determination. However, the modelling of both distributions improves and the trend, that was visible in the ratio diagrams, vanished.

7.6. Event Yields and Control Distributions, s-Channel

In this section, the event yields for the four different selections defined in Sec. 7.2 are collected. Furthermore, distributions for kinematic variables in those regions are shown as well in order to demonstrate the good modelling of all processes.

The predicted and observed event yields for the signal region are shown in Tab. 7.2, separately for the electron + jet selection and muon + jet selection, as well as for the sum of both selections. The numbers include the additional event weight from the W+jets reweighting scale factors, discussed in the previous section, and are normalized to the theoretical cross section predictions. In addition, the signal-over-background ratios, S/B, are provided. The main background contribution in the signal region originates from $\mathrm{t\bar{t}}$ production, which represents about 57 % of all events in this region. The second and third largest contributions come from W+jets production and other single top-quark processes. The overall signal-over-background ratio is 4 %, while an overall difference between predicted and observed event yields of 5 % is found.

The event yields for the W+jets selection and the two $\mathrm{t\bar{t}}$ selections with either three or four jets can be found in Tab. 7.3. The W+jets production contributes to about 46 % of all events in the dedicated W+jets region. The signal-to-background is only about 1 %. Both $\mathrm{t\bar{t}}$ control regions are highly enriched with $\mathrm{t\bar{t}}$ events, which represent

Process	e + jets	μ + jets	ℓ + jets
s-channel	250.2 ± 1.5	317.0 ± 1.7	567.2 ± 2.2
t-channel	538.4 ± 6.5	658.0 ± 7.5	1 196.4 ± 9.9
Wt	186 ± 12	229 ± 13	414 ± 17
$\mathrm{t\bar{t}}$	3 864 ± 15	4 632 ± 17	8 495 ± 23
W+light-flav. jets	42 ± 19	261 ± 94	303 ± 96
W+heavy flavour	1 246 ± 28	1 581 ± 31	2 827 ± 42
Z+jets & diboson	135.0 ± 6.5	208.9 ± 9.7	344 ± 12
Multi-jet	449 ± 16	264 ± 13	713 ± 20
Total expectation	6 710 ± 43	8 151 ± 100	14 860 ± 110
Data	6 914	8 642	15 556
S/B [%]	3.9	4.1	4.0

Table 7.2.: Predicted and observed event yields in the signal region for the s-channel selection. The number are given separately for the electron and muon selection, as well as for the combination of both selection. Only statistical uncertainties are provided. The last row shows the signal-to-background ratios, S/B.

Process	W+jets	$t\bar{t}$ 3-jet	$t\bar{t}$ 4-jet
s-channel	175.5 ± 1.3	285.2 ± 1.6	88.74 ± 0.89
t-channel	841.5 ± 8.4	2 195 ± 14	702.4 ± 7.7
Wt	390 ± 17	1 391 ± 31	1 256 ± 30
$t\bar{t}$	4 704 ± 17	36 548 ± 48	39 107 ± 50
W+light-flav. jets	1 940 ± 140	266 ± 62	79 ± 27
W+heavy flavour	4 990 ± 79	3 581 ± 44	1 859 ± 31
Z+jets & diboson	549 ± 20	515 ± 13	240.8 ± 9.0
Multi-jet	1 010 ± 24	727 ± 25	202 ± 23
Total expectation	14 610 ± 170	45 510 ± 100	43 534 ± 76
Data	15 458	46 674	45 104

Table 7.3.: Predicted and observed event yields for the three background selections for the s-channel. Electron and muon selections are combined, the uncertainties correspond to statistical uncertainties, only.

80 % and 90 %, respectively, of all events. The contribution from s-channel single top-quark events is negligible.

Distributions of some kinematic variables in the signal region are shown in Fig. 7.7. In Figs. 7.8 and 7.9 additional distributions for the W+jets selection and both $t\bar{t}$ selections are presented. All distributions in this section and the following ones are scaled within their SM constrains according to the results, given in Tab. 7.1, from a fit of the corresponding $m_{\mathrm{T}}^{\mathrm{W}}$ distribution to data. The uncertainty band corresponds to the combination of the statistical uncertainty in each bin and the normalization uncertainty from the likelihood fit added in quadrature. All distributions shown here and in the following show a perfect modelling. This is also true for many other variables, which can be found in [Kin+15].

7.7. Event Yields and Control Distributions, t-channel

The predicted and observed event yields for the signal selection as well as for the background selections, defined in Sec. 7.2, can be found in Tabs. 7.4 and 7.5, respectively.

In the signal region, the two main backgrounds with similar contributions to the overall event yield are W+jets with 32 % and $t\bar{t}$ with 24 %. The signal contribution is about 30 % as well. An overall difference between data and prediction of around 3 % is observed.

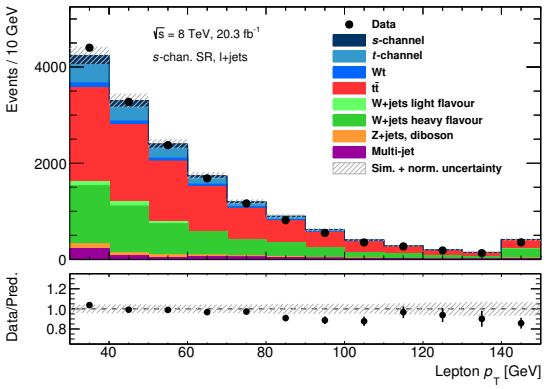

(a) Lepton transverse momentum

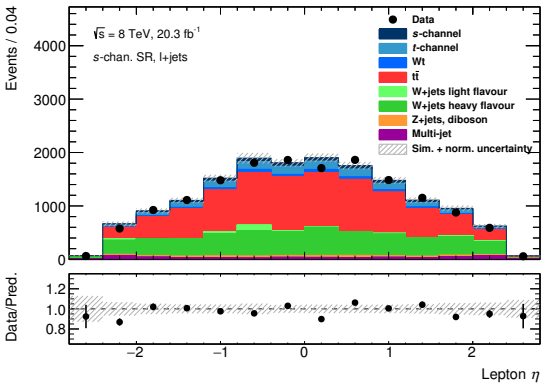

(b) Lepton pseudorapidity

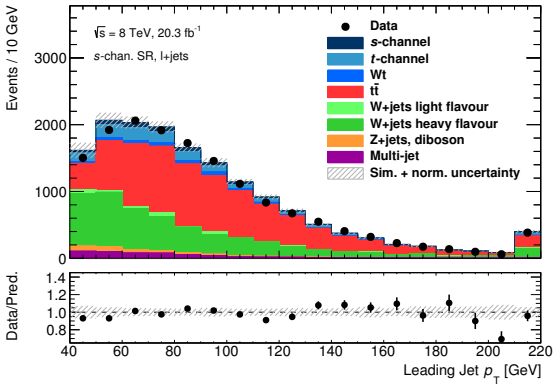

(c) Leading jet transverse momentum

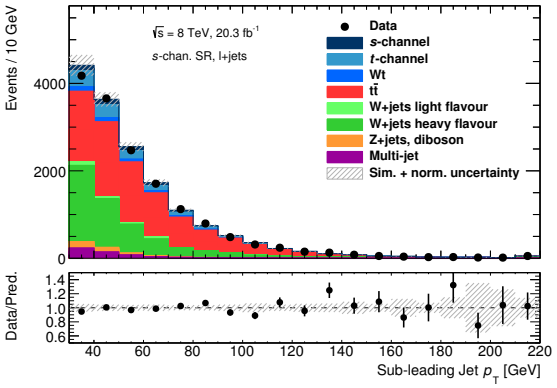

(d) Sub-leading jet transverse momentum

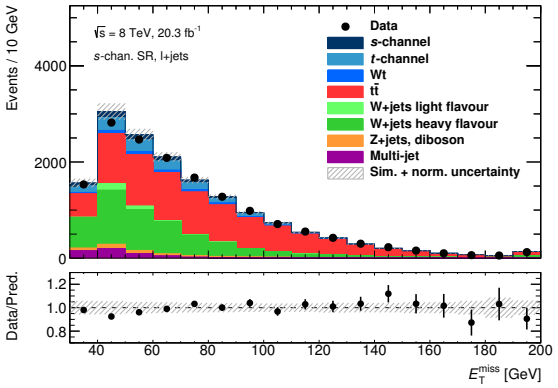

(e) Missing transverse momentum

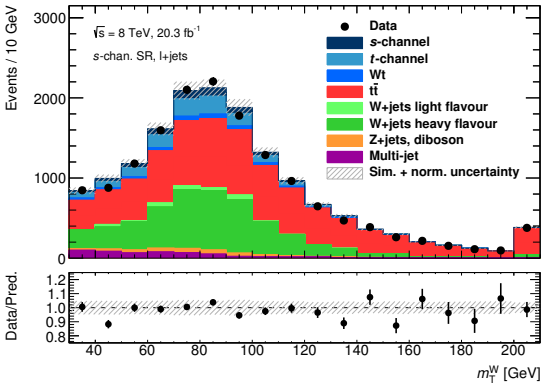

(f) Transverse W boson mass

Figure 7.7.: Kinematic distributions in the *s*-channel signal region. (a) lepton transverse momentum, (b) lepton pseudorapidity, (c) leading jet transverse momentum, (d) sub-leading jet transverse momentum, (e) missing transverse momentum and (f) transverse W boson mass.

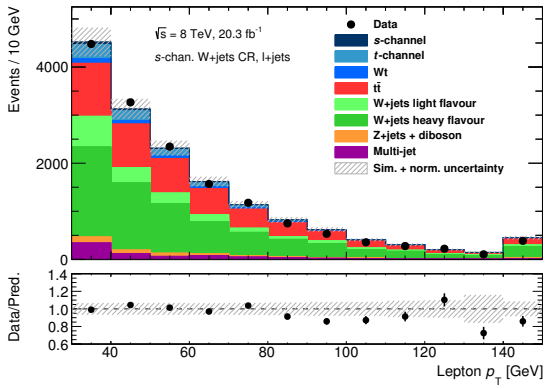

(a) Lepton transverse momentum

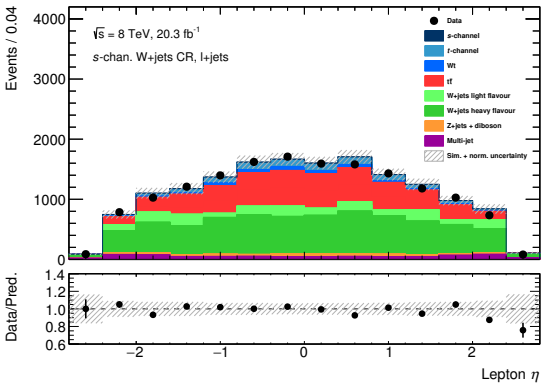

(b) Lepton pseudorapidity

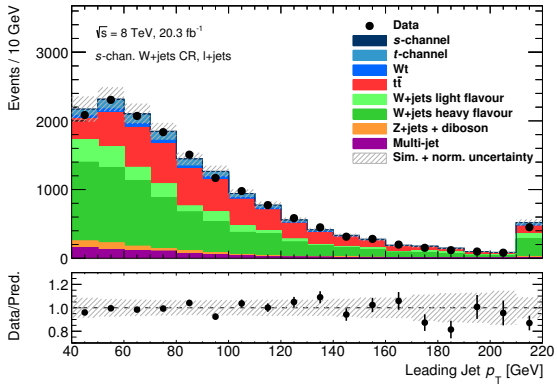

(c) Leading jet transverse momentum

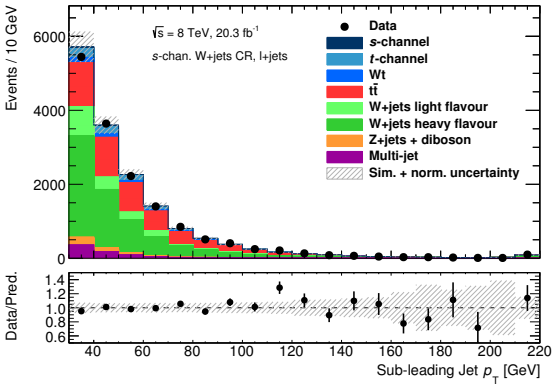

(d) Sub-leading jet transverse momentum

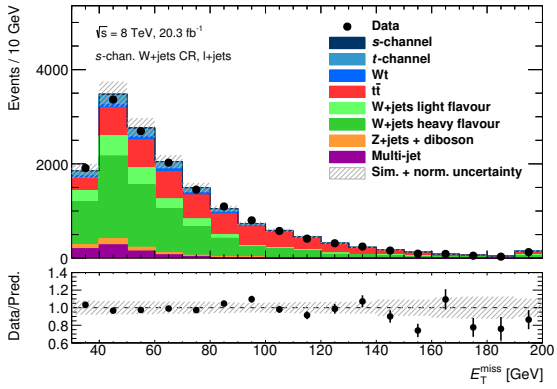

(e) Missing transverse momentum

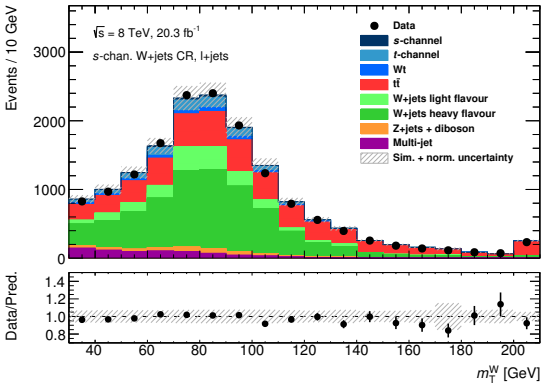

(f) Transverse W boson mass

Figure 7.8.: Kinematic distributions in the W+jets control region for the *s*-channel analysis. (a) lepton transverse momentum, (b) lepton pseudorapidity, (c) leading jet transverse momentum, (d) sub-leading jet transverse momentum, (e) missing transverse momentum and (f) transverse W boson mass.

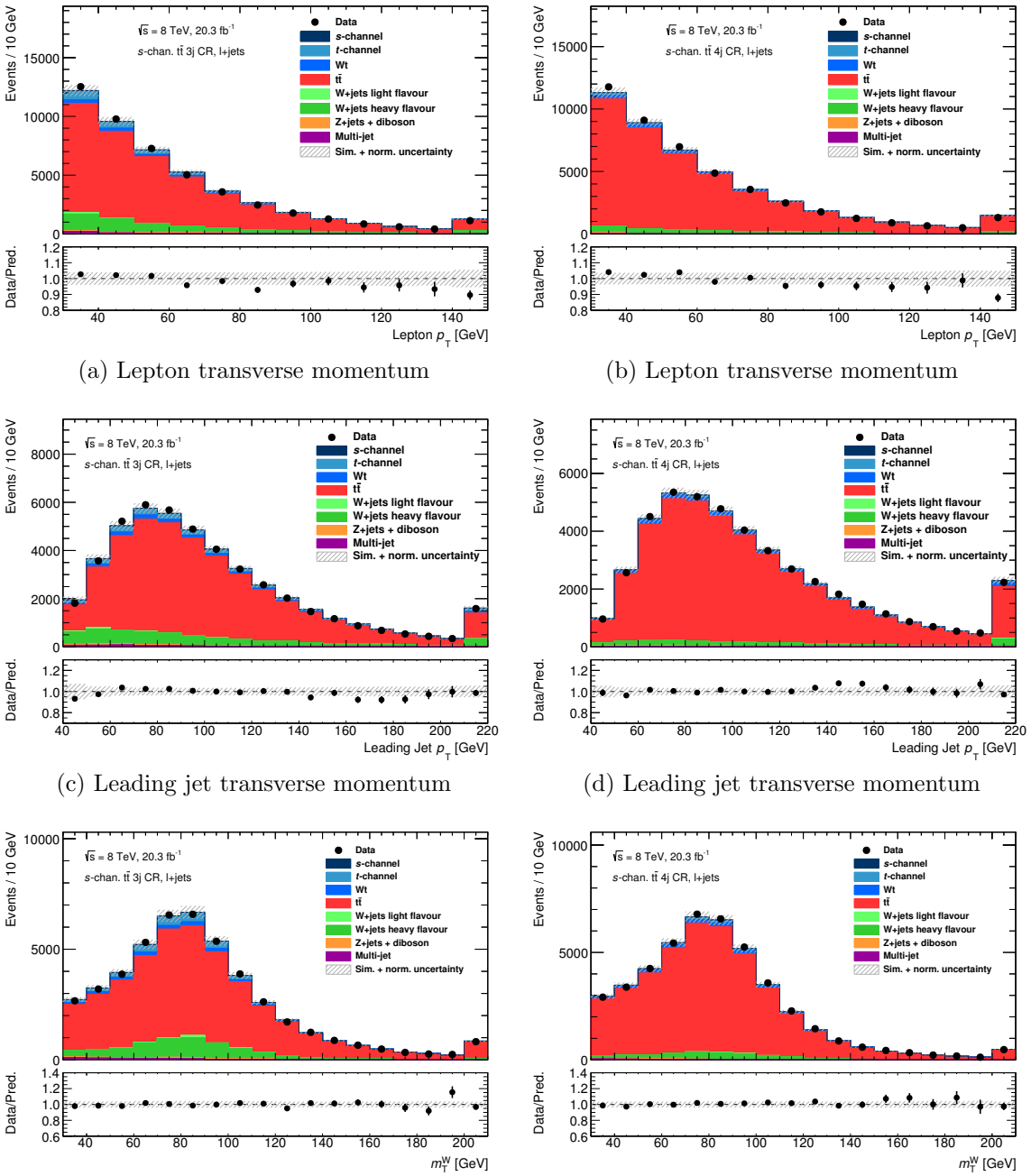

(a) Lepton transverse momentum

(b) Lepton transverse momentum

(c) Leading jet transverse momentum

(d) Leading jet transverse momentum

(e) Transverse W boson mass

(f) Transverse W boson mass

Figure 7.9.: Kinematic distributions in the two $t\bar{t}$ control region for the *s*-channel analysis. (a) lepton transverse momentum, (c) leading jet transverse momentum, (e) transverse W boson mass for the $t\bar{t}$ three-jet selection. The panels (b), (d) and (f) show the same kinematic variables, but for the $t\bar{t}$ four-jet selection.

The W+jets processes represent about 79 % of all events in the region defined by the W+jets selection, while the signal-to-background ratio is only 3.7 %. Differences of about 8 % between predicted and observed event yields are found.

The top-quark pair production makes up 84 % and 92 % events of all events in the $t\bar{t}$ region for the three-jet and four-jet selection, respectively. About 8 % of t-channel signal events are found in the three-jet selection, while in the four-jet region the contribution is about 0.2 %.

Process	e + jets	μ + jets	ℓ + jets
t-channel	4 217 ± 17	5 321 ± 20	9 538 ± 27
s-channel	144.7 ± 1.1	195.7 ± 1.4	340.4 ± 1.8
Wt	711 ± 22	856 ± 25	1 567 ± 33
$t\bar{t}$	3 405 ± 14	4 228 ± 17	7 633 ± 22
W+light-flav. jets	270 ± 65	409 ± 88	679 ± 110
W+heavy flavour	4 177 ± 66	5 620 ± 76	9 800 ± 100
Z+jets & diboson	382 ± 12	326 ± 15	708 ± 19
Multi-jet	834 ± 19	1 119 ± 24	1 953 ± 31
Total expectation	14 140 ± 100	18 070 ± 120	32 220 ± 160
Data	14 646	18 532	33 178
S/B [%]	42	42	42

Table 7.4.: Predicted and observed event yields in the signal region for the t-channel selection. Only statistical uncertainties are given. The last row shows the signal-to-background ratios, S/B.

Kinematic distributions for the signal region are shown in Fig. 7.10, while for the background selections, some examples are shown in Figs. 7.11 and 7.12. A minor mis-modelling is observed for the lepton transverse momentum in the region defined by the $t\bar{t}$ four-jet selection, which is, however, far away from the signal region. No other distributions show a similar trend. In addition, there is a good agreement between predicted and observed distributions for the lepton transverse momentum in the $t\bar{t}$ three-jet region, which is kinematically closer to the t-channel signal region. Additional figures can be found in [Kin+15]. Here also, no major discrepancies between data and predictions are found.

Process	W+jets	$t\bar{t}$ 3-jet	$t\bar{t}$ 4-jet
t-channel	5 986 ± 21	1 103.4 ± 9.7	276.8 ± 4.9
s-channel	225.7 ± 1.5	80.77 ± 0.84	19.34 ± 0.41
Wt	1 612 ± 34	275 ± 14	257 ± 14
$t\bar{t}$	7 690 ± 22	11 065 ± 26	9 329 ± 24
W+light-flav. jets	60 060 ± 650	537 ± 11	248.1 ± 8.0
W+heavy flavour	74 560 ± 320		
Z+jets & diboson	8 082 ± 76	73.2 ± 3.5	32.5 ± 2.4
Multi-jet	11 259 ± 96	112 ± 12	6 ± 10
Total expectation	169 470 ± 740	13 247 ± 35	10 169 ± 31
Data	184 944	13 598	10 678

Table 7.5.: Predicted and observed event yields in all background regions for the combination of both, electron and muon selections in the t-channel. The uncertainties correspond to the uncertainty due to limited sample statistics.

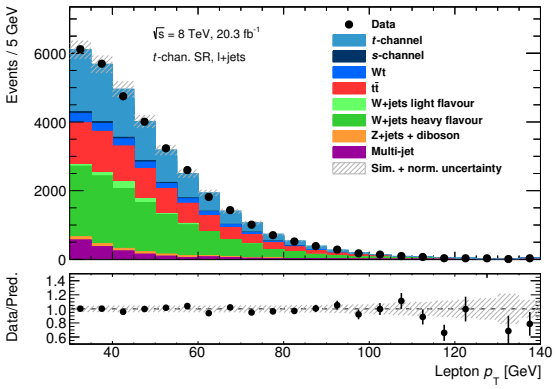

(a) Lepton transverse momentum

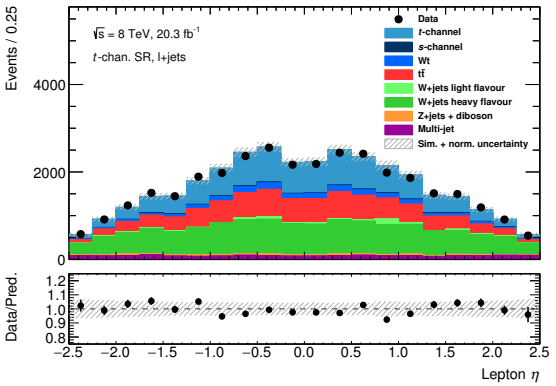

(b) Lepton pseudorapidity

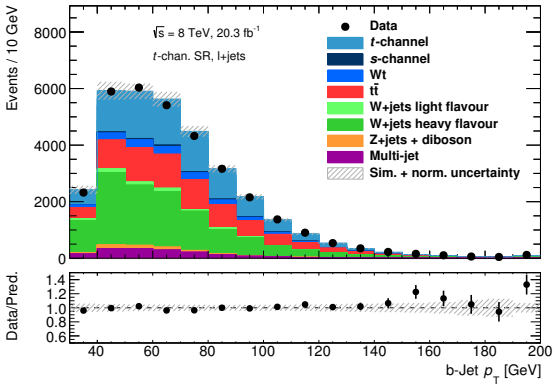

(c) b-jet transverse momentum

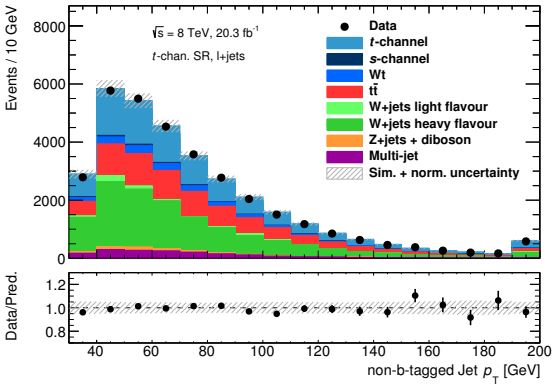

(d) Non-b-tagged jet transverse momentum

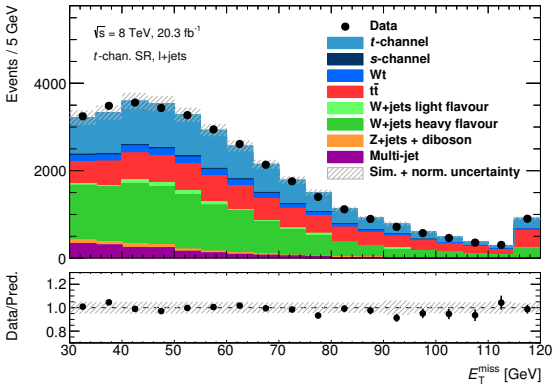

(e) Missing transverse momentum

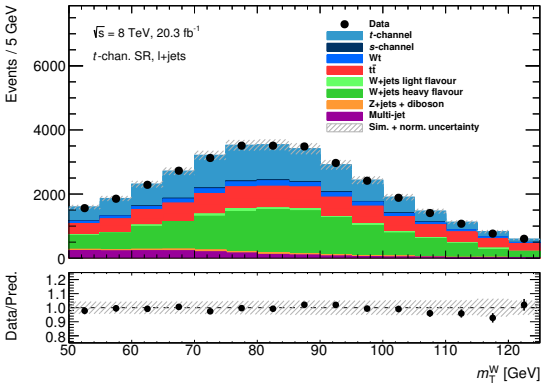

(f) Transverse W boson mass

Figure 7.10.: Kinematic distributions in the t-channel signal region. (a) lepton transverse momentum, (b) lepton pseudorapidity, (c) b-jet transverse momentum, (d) non-b-tagged jet transverse momentum, (e) missing transverse momentum and (f) transverse W boson mass.

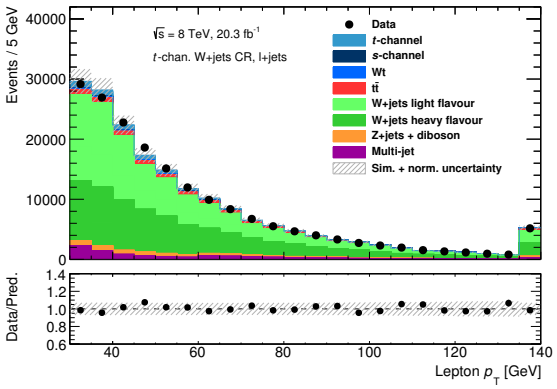

(a) Lepton transverse momentum

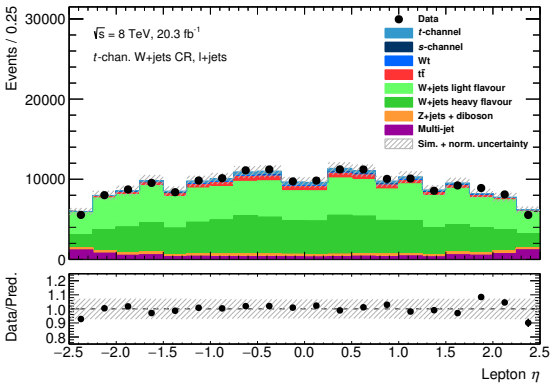

(b) Lepton pseudorapidity

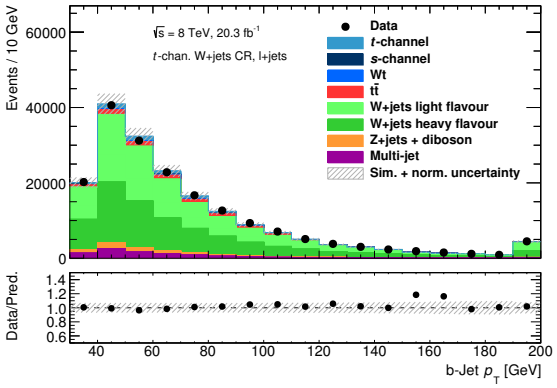

(c) b-jet transverse momentum

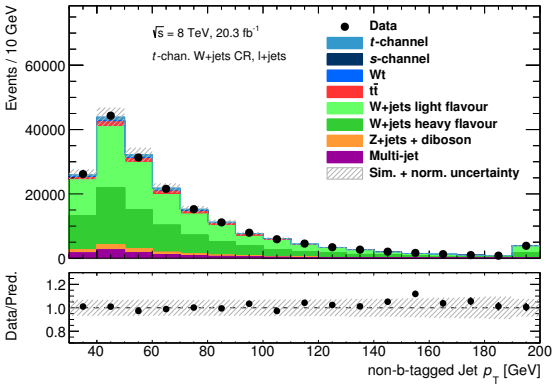

(d) Non-b-tagged jet transverse momentum

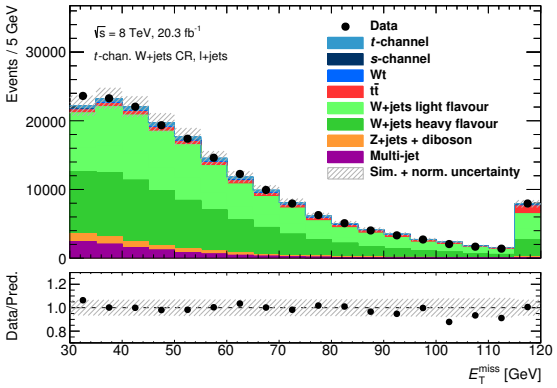

(e) Missing transverse momentum

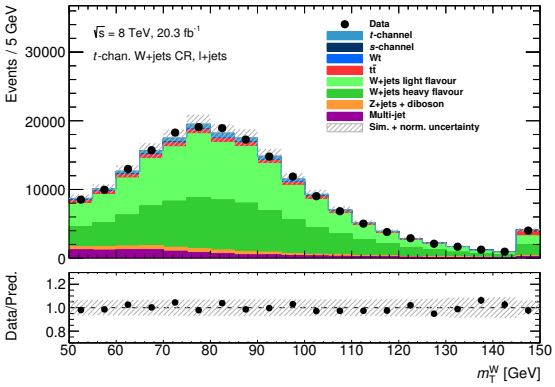

(f) Transverse W boson mass

Figure 7.11.: Kinematic distributions for the W + jets selection of the t-channel analysis. (a) lepton transverse momentum, (b) lepton pseudorapidity, (c) b-jet transverse momentum, (d) non-b-tagged jet transverse momentum, (e) missing transverse momentum and (f) transverse W boson mass.

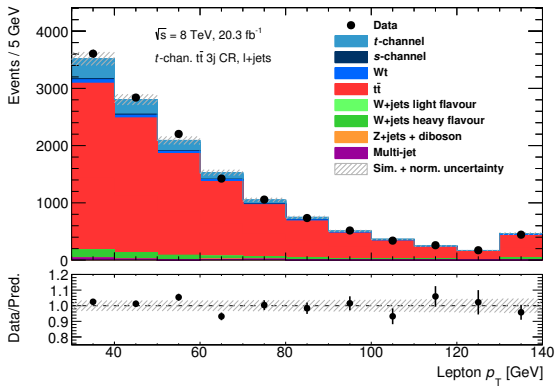

(a) Lepton transverse momentum

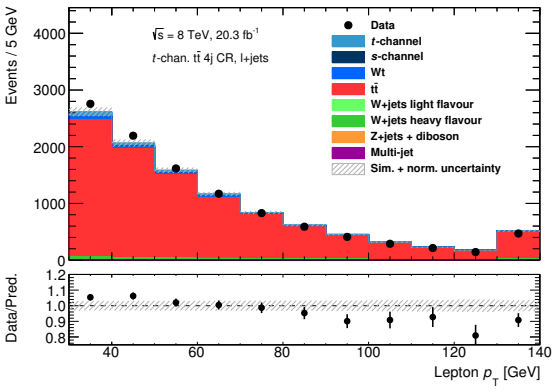

(b) Lepton transverse momentum

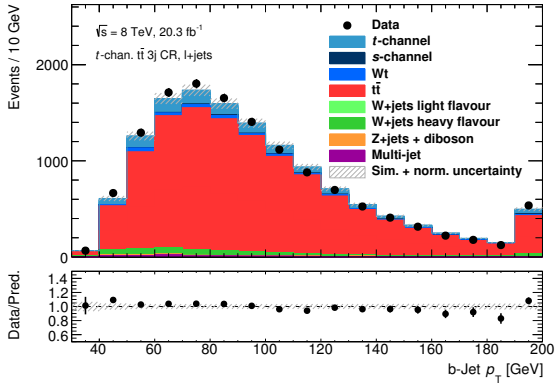

(c) b-jet transverse momentum

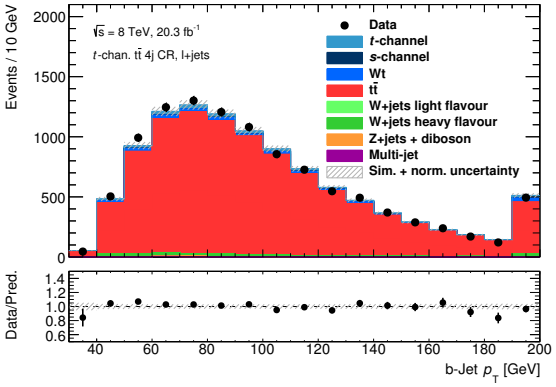

(d) b-jet transverse momentum

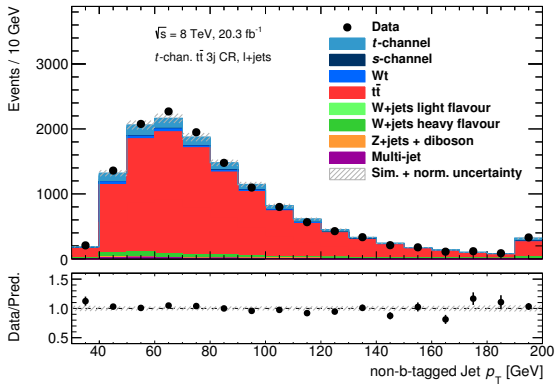

(e) Non-b-tagged jet transverse momentum

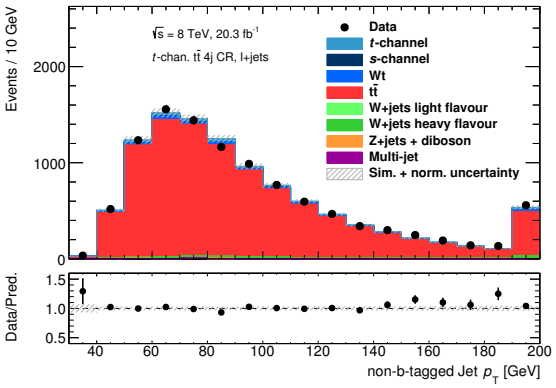

(f) Non-b-tagged jet transverse momentum

Figure 7.12.: Kinematic distributions in the two $t\bar{t}$ control region for the *s*-channel analysis. The panels for the $t\bar{t}$ three-jet selection show (a) lepton transverse momentum, (c) b-jet transverse momentum and (e) non-b-tagged jet transverse momentum. The same kinematic variables are displayed in panels (b), (d), (f) for the $t\bar{t}$ four-jet selection.

7.8. Event Classification

An analysis using a cut-based event selection is not sensitive enough to obtain a precise measurement of the single-top cross sections, especially for the single-top s-channel. Therefore, the process likelihoods computed by the matrix element method are used to build a discriminant. This allows to separate signal events from background contributions and improve the performance of the likelihood fit (c. f. Sec. 9.1).

The kinematic variables that were presented in the previous section, such as the transverse momenta of leptons and jets, are the input quantities for the calculation of the process likelihoods and are described well by the simulations. Nevertheless, it is important to check the modelling of the individual process likelihoods to validate the matrix element method. The likelihoods used to separate the two signal processes from background will be discussed in Secs. 7.8.1 and 7.8.2. Subsequently, the method for building the discriminant is discussed in Sec. 7.8.3.

7.8.1. Likelihood Distributions, s-channel

Likelihoods are computed for eight processes (c. f. Sec. 6.3.2) in all four region defined by the s-channel selection in Sec. 7.2. The likelihoods in the signal region for the signal and main background hypotheses are presented in Fig. 7.13. The predicted distribution agree within their uncertainties with data and no mis-modelling is observed.

Figure 7.14 shows likelihood distributions for the s-channel process and W+jets processes in the W+jets region. The double-peak structure is likely to arise from the fact that a different b-tagging working point was used for selecting the events. The less stringent tagging requirement together with the removal of all events with two b-tags leads to a slightly different event topology. The assignment of b-tags to jets within the MEM$_{\text{T}_\text{k}}$ software uses the tight b-tagging requirement. Therefore, instead of two b-jets, events contain only one or even no b-jet. Thus, the two different event topologies can be associated with each peak in the likelihood distribution. Nevertheless, the data is described well by the SM predictions.

Events, selected by the s-channel $\mathrm{t\bar{t}}$ selection, contain either three or four reconstructed jets. Except for the $\mathrm{t\bar{t}}$ semi-leptonic process, the number of reconstructed jets that can be assigned to final state partons, is limited to two for any process. Therefore, the jets that are used in the likelihood calculations need to be defined. In the four jet region, a subset of events are selected by requiring that the two leading jets have to be b-tagged. The remaining two jets must have a momentum lower than $p_{\mathrm{T}} < 60\,\mathrm{GeV}$. Only the two b-jets are considered for the likelihood computation. In the three-jet $\mathrm{t\bar{t}}$ region, likelihoods are computed for all events. The untagged jet is discarded irrespective of its transverse momentum and only the two b-jets are used for the evaluation of the matrix element method. Figure 7.15 shows the $\mathrm{t\bar{t}}$ likelihoods for the three-jet $\mathrm{t\bar{t}}$ region and the subset of events in the four-jet $\mathrm{t\bar{t}}$ region.

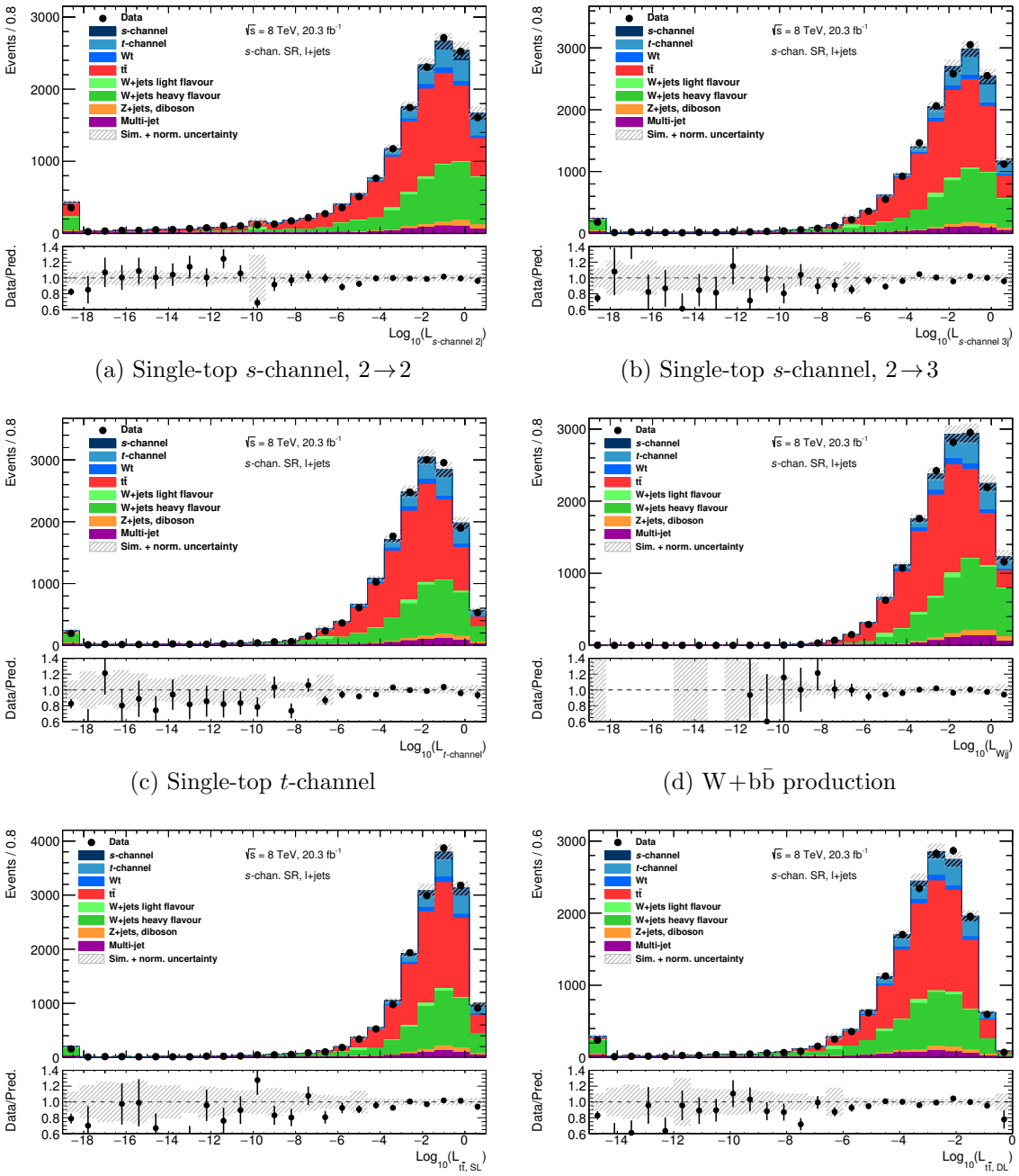

(a) Single-top s-channel, $2\to2$

(b) Single-top s-channel, $2\to3$

(c) Single-top t-channel

(d) $\mathrm{W}+\mathrm{b\bar{b}}$ production

(e) $\mathrm{t\bar{t}}$ production (single-lepton)

(f) $\mathrm{t\bar{t}}$ production (di-lepton)

Figure 7.13.: Event likelihood distributions for different processes in the s-channel signal region. (a) s-channel $2\to2$ process, (b) s-channel $2\to3$ process, (c) t-channel process, (d) $\mathrm{W}+\mathrm{b\bar{b}}$ production, (e) $\mathrm{t\bar{t}}$ production (single-lepton), (f) $\mathrm{t\bar{t}}$ production (di-lepton).

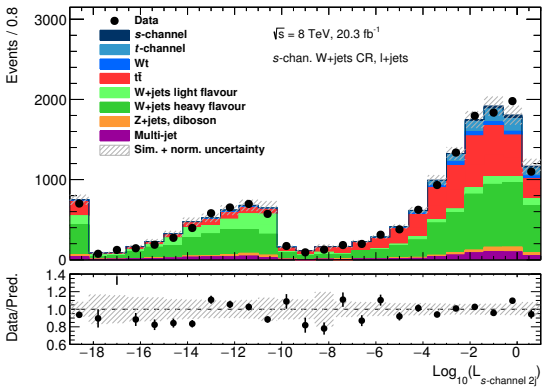

(a) Single-top s-channel, $2 \to 2$

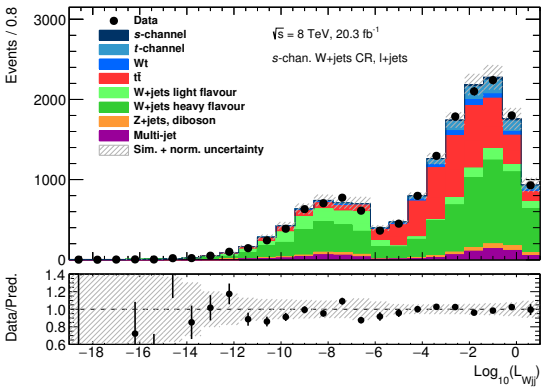

(b) W+jj production

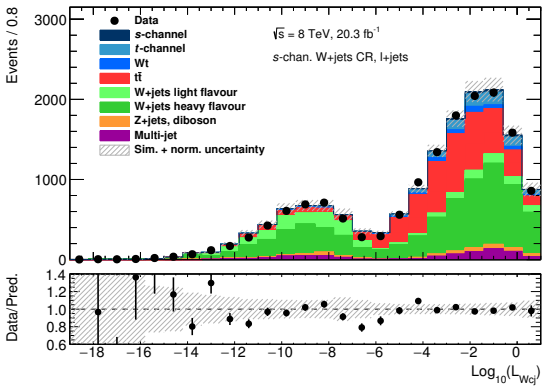

(c) W+c+jet production

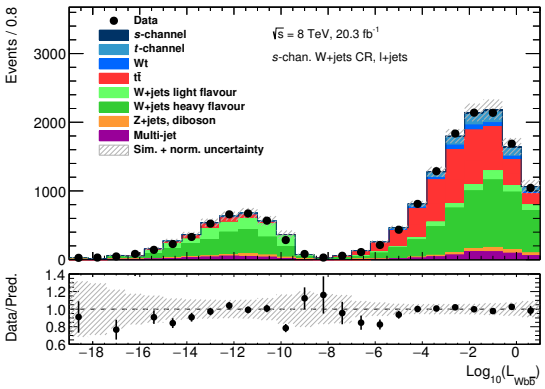

(d) W+b$\bar{\text{b}}$ production

Figure 7.14.: Event likelihood distributions of the signal process and W+jets processes using the s-channel W+jets selection. (a) s-channel $2 \to 2$ process, (b) W+jj production, (c) W+c+jet production, (d) W+b$\bar{\text{b}}$ production.

All likelihood distributions show good agreement between data and predicted likelihood values. More distributions can be found in [Kin+15].

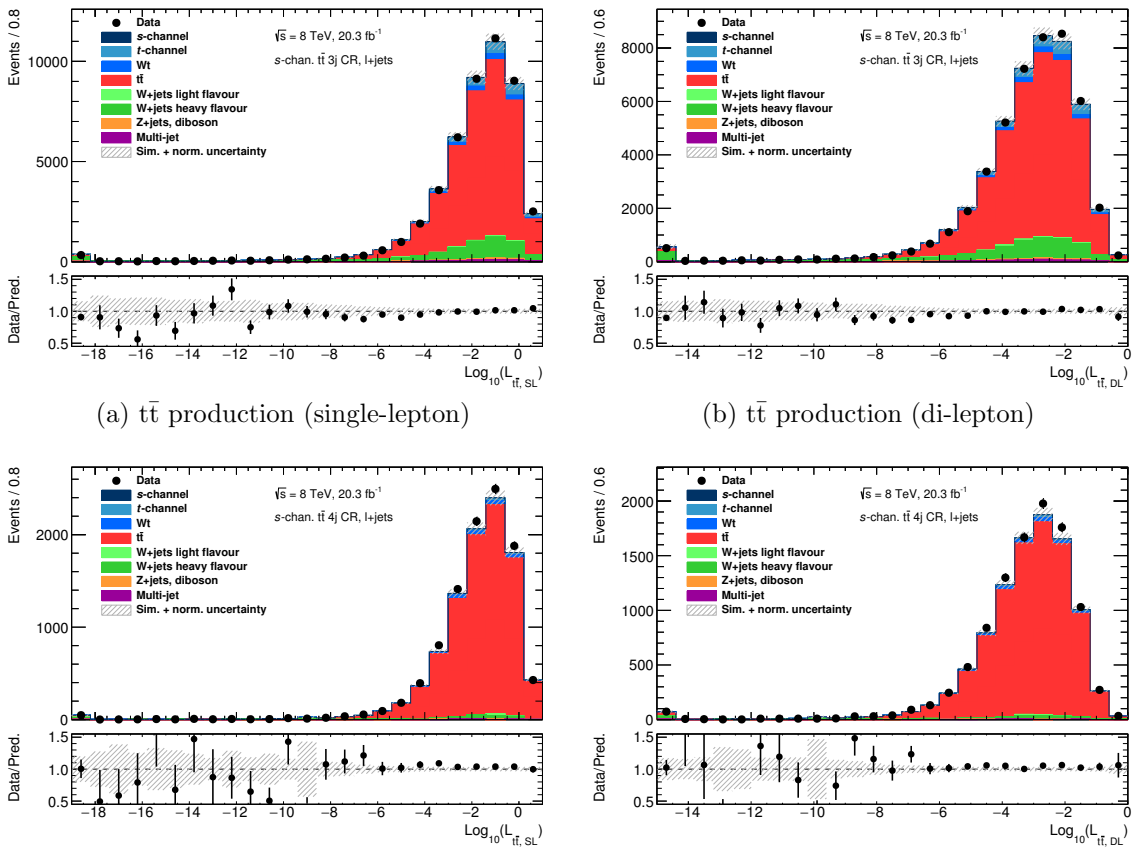

(a) $t\bar{t}$ production (single-lepton)

(b) $t\bar{t}$ production (di-lepton)

(c) $t\bar{t}$ production (single-lepton)

(d) $t\bar{t}$ production (di-lepton)

Figure 7.15.: Event likelihood distributions of the $t\bar{t}$ processes in the s-channel $t\bar{t}$ control region with three or four selected jets. (a) $t\bar{t}$ production (single-lepton) (b) $t\bar{t}$ production (di-lepton) for the $t\bar{t}$ three-jet selection. Panels (c) and (d) show the same likelihoods, but for a subset of events in the $t\bar{t}$ four-jet region.

7.8.2. Likelihood Distributions, t-channel

For the t-channel signal region, only seven different likelihoods were computed. In contrast to the s-channel selection, the s-channel $2 \to 3$ process is omitted, because the s-channel contribution is negligible and therefore an improved modelling of this process as in the s-channel signal region is not necessary. The likelihood distributions for the t-channel signal region are shown in Fig. 7.16.

In order to calculate the likelihoods for the $t\bar{t}$ control region, only the two b-tagged jets have been considered. No further requirements for the transverse momentum of the untagged jets are made. The likelihoods for the W+jets and $t\bar{t}$ background selections are shown in Figs. 7.17–7.19. All likelihoods show good agreement with data. The complete set of likelihoods can be found in [Kin+15].

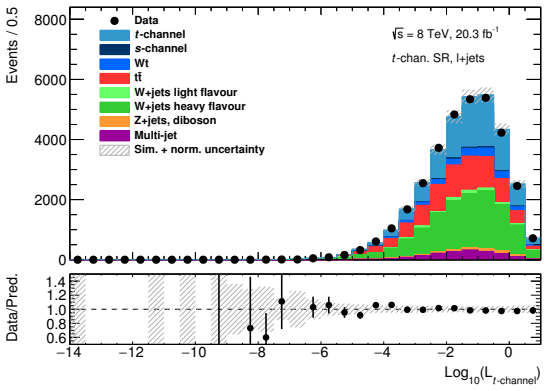

(a) Single-top t-channel

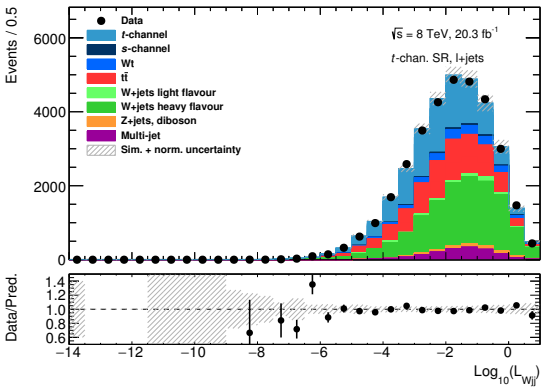

(b) W+jj production

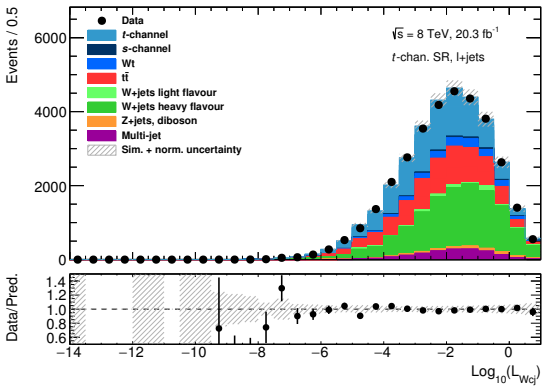

(c) W+c+jet production

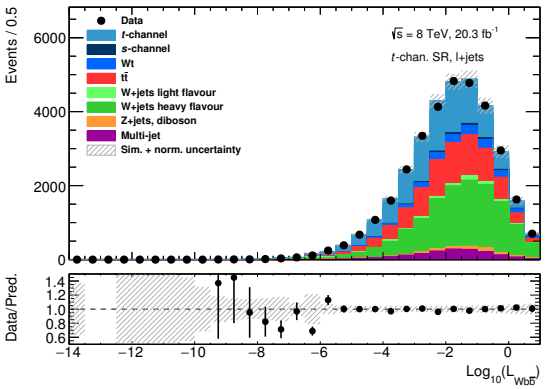

(d) W+b$\bar{\text{b}}$ production

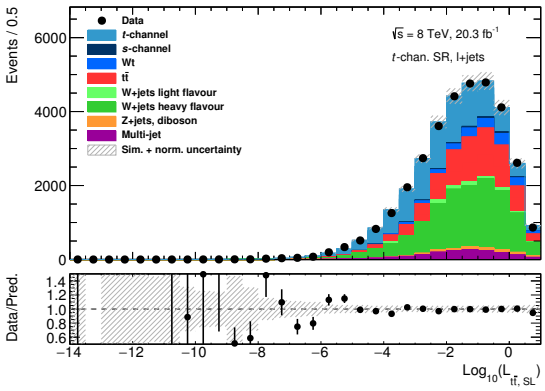

(e) t$\bar{\text{t}}$ production (single-lepton)

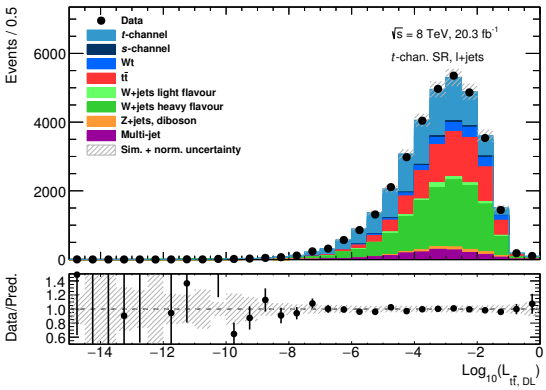

(f) t$\bar{\text{t}}$ production (di-lepton)

Figure 7.16.: Event likelihood distributions for different processes in the t-channel signal region. (a) t-channel process, (b) W+jj production, (c) W+c+jet production, (d) W+b$\bar{\text{b}}$ production, (e) t$\bar{\text{t}}$ production (single-lepton), (f) t$\bar{\text{t}}$ production (di-lepton).

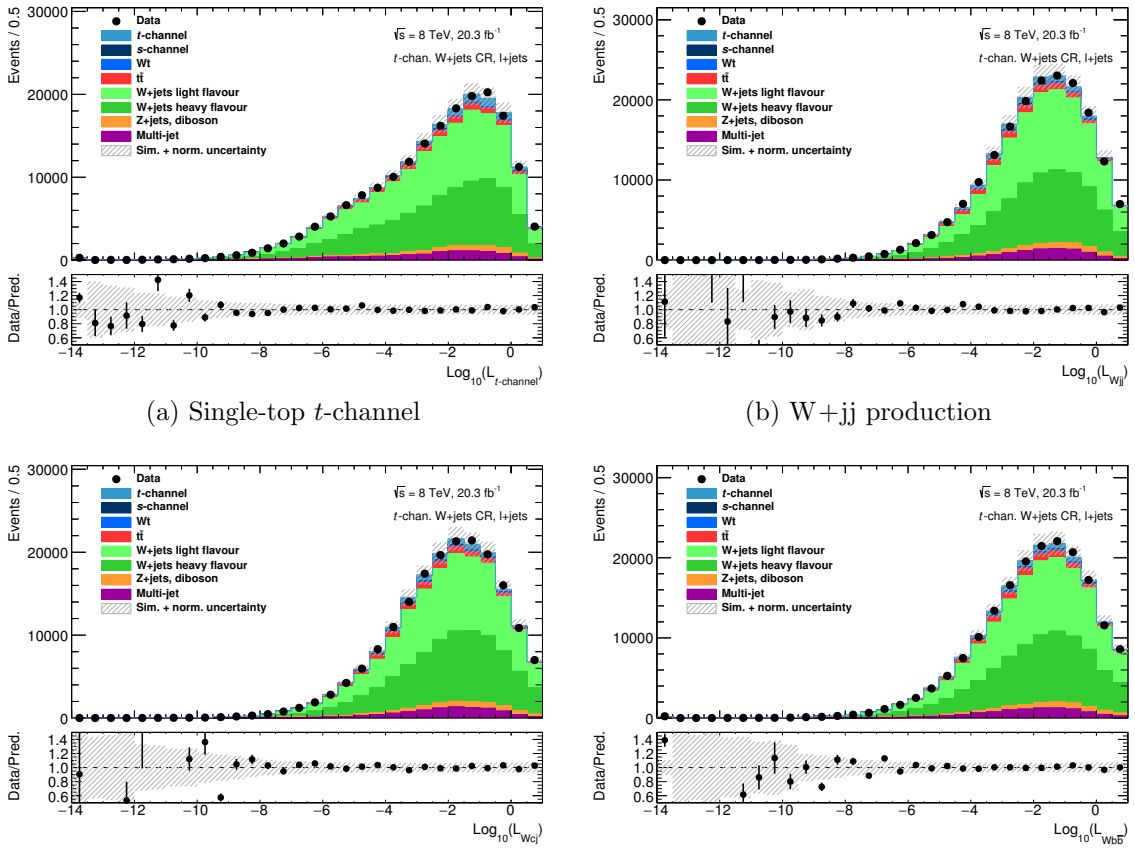

(a) Single-top t-channel (b) W+jj production

(c) W+c+jet production (d) W+b$\bar{\text{b}}$ production

Figure 7.17.: Event likelihood distributions of the signal process and W+jets processes using the s-channel W+jets selection. (a) s-channel $2\to2$ process, (b) W+jj production, (c) W+c+jet production, (d) W+b$\bar{\text{b}}$ production.

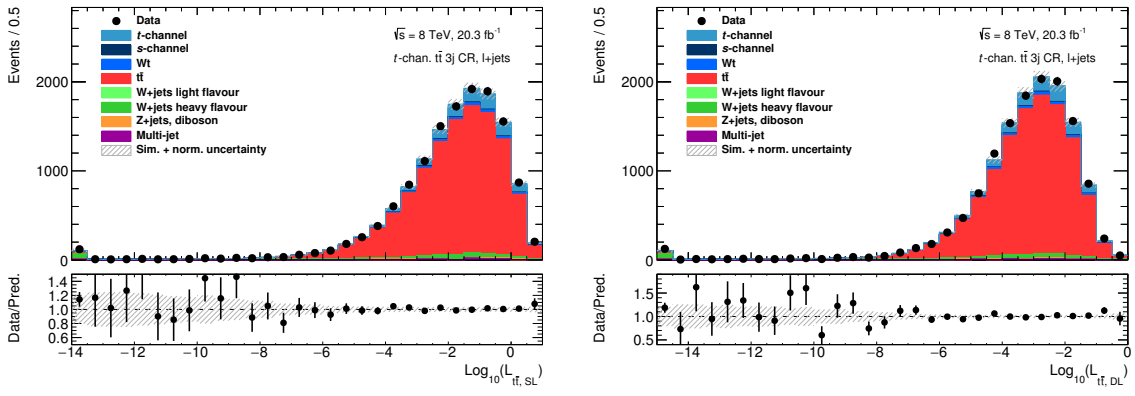

(a) t$\bar{\text{t}}$ production (single-lepton) (b) t$\bar{\text{t}}$ production (di-lepton)

Figure 7.18.: Event likelihood distributions of the t$\bar{\text{t}}$ processes in the t-channel t$\bar{\text{t}}$ control region with three selected jets. (a) t$\bar{\text{t}}$ production (single-lepton) and (b) t$\bar{\text{t}}$ production (di-lepton)

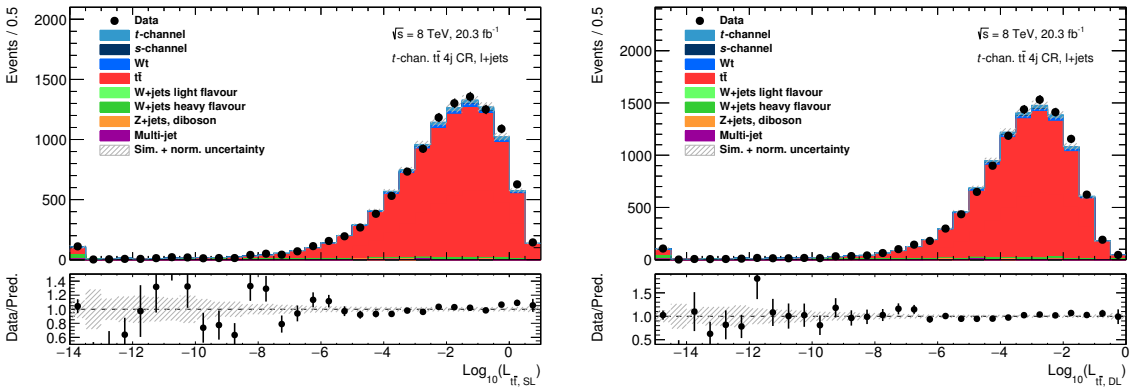

(a) $t\bar{t}$ production (single-lepton) (b) $t\bar{t}$ production (di-lepton)

Figure 7.19.: Event likelihood distributions of the $t\bar{t}$ processes in the t-channel $t\bar{t}$ control region with four selected jets. (a) $t\bar{t}$ production (single-lepton) and (b) $t\bar{t}$ production (di-lepton).

7.8.3. Discriminant Distributions

The individual separation power of each process likelihood can be increased by combining them into a discriminant. In this context, the process likelihoods $\mathscr{L}_H(X)$ are interpreted as the conditional probability, $\mathcal{P}(X|H)$, for observing an event configuration X given the hypothesis for process H. The signal probability [Rie16, Kin+14] that can be defined using these conditional probabilities is motivated by the Neyman-Pearson lemma [NP33] and is given by the following equation

$$\mathcal{P}(S|X) = \frac{\sum_i P(S_i)\mathcal{P}(X|S_i)}{\sum_i P(S_i)\mathcal{P}(X|S_i) + \sum_j P(B_j)\mathcal{P}(X|B_j)}. \tag{7.1}$$

Here, S_i and B_i denote all signal and background processes that are considered. Each process is split further into individual contributions distinguished by the charge and the flavour of the charged lepton (e^+, e^-, μ^+, μ^-). The top-quark pair production processes are charge symmetric and therefore their contributions for positive and negative charged leptons is equal. The a-priori probabilities in Eq. 7.1 are given by the relative event yields of each process obtained by Monte Carlo simulations in each signal region.

The s-channel discriminant is built from all eight processes defined in Sec. 6.3.2. The signal likelihood is given by the sum of the likelihoods for the s-channel $2 \to 2$ process and the s-channel $2 \to 3$ process. The different contributions are weighted according to the ratio of their likelihood normalization factors c_H (c. f. Eq. 6.6), because an a-priori probability can only be assigned to the sum, but not the individual likelihoods. The ratio of the normalization factors is approximately 0.65/0.35 in favour of the $2 \to 2$ process. All other process likelihoods are used for computing the corresponding background likelihoods. The distribution for the s-channel discriminant is shown

Fig. 7.20 in the signal region. The binning of the discriminant is non-linear as indicated by the discriminant x-axis. The bin width is optimized as a function of the number of signal events and the estimated background uncertainty for certain bin intervals. The score function with two free parameters, which is used to define these intervals in terms of discriminant values, is documented in [Kin+14, Rie16]. The optimal choice of the parameters of the score function was studied extensively in the context of the previous analysis [ATL16a] and the same binning is used in this thesis as well. Signal events are accumulated at high probability values with a signal-to-background ratio of almost 25 % in the right-most bin of the discriminant. Background events are gathered at low probabilities.

The t-channel discriminant is built using the same processes as for the s-channel discriminant, except for the s-channel $2 \to 3$ process. The same procedure for optimizing the binning of the t-channel discriminant was applied, too. However, due to the large statistics in the t-channel signal region, the choice of the binning is less important than in the s-channel. In addition, the chosen binning for the t-channel discriminant is similar to a binning using a constant bin width.

In order to check the modelling of both discriminants before unblinding the analysis, the discriminants were calculated using events collected by the different background selections. The distributions for the s-channel and t-channel discriminants in the corresponding background regions are shown in Fig. 7.22.

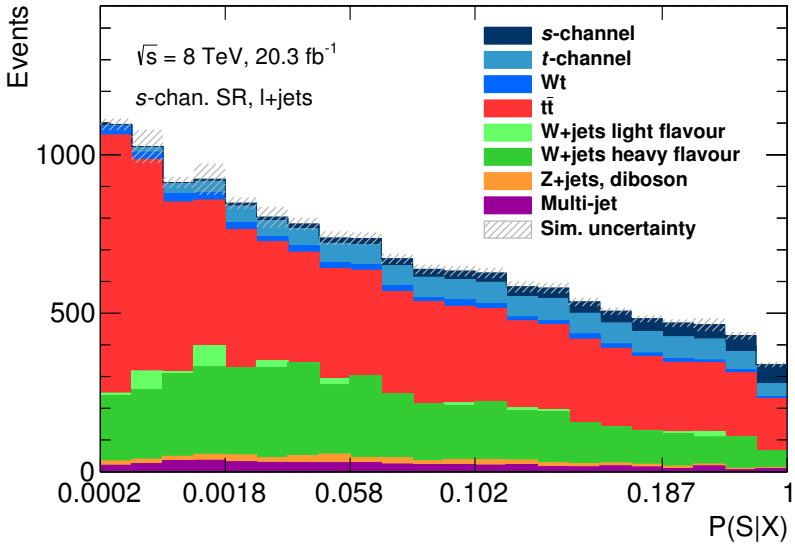

Figure 7.20.: The s-channel signal probability in the s-channel signal region. The signal is accumulated at high values of the discriminant and the background is cumulated at low probabilities. The binning is optimized in order to achieve a good signal-to-background ratio, while the statistical uncertainty on the background in each bin needs to be lower than 10 %.

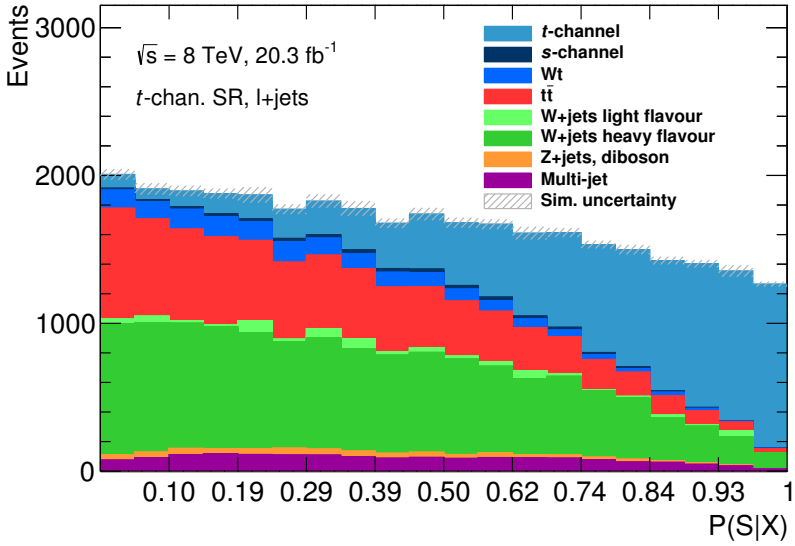

Figure 7.21.: The t-channel signal probability in the t-channel signal region. The discriminant shows an excellent separation between signal and background events. As for the s-channel discriminant, signal events are cumulated at high probabilities.

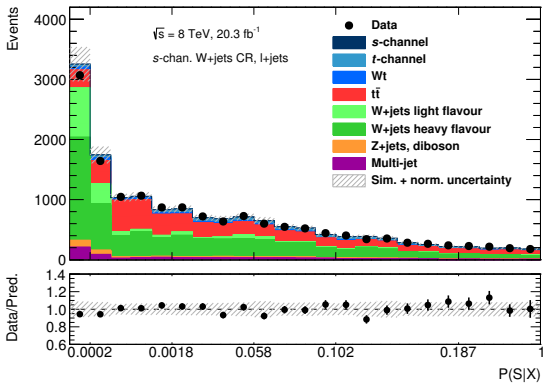

(a) W+jets region, s-channel selection

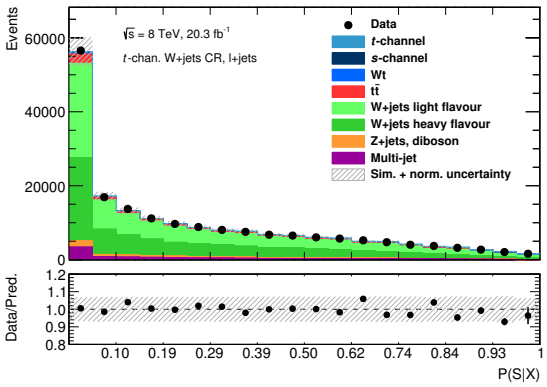

(b) W+jets region, t-channel selection

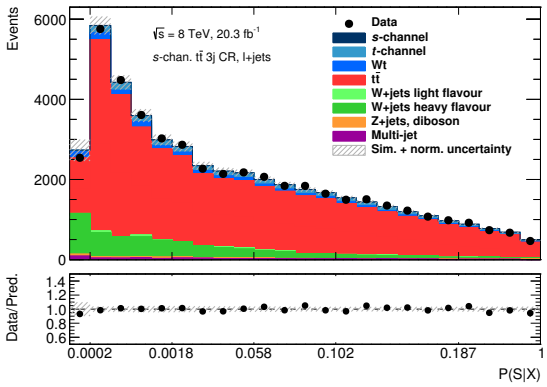

(c) Three-jet $t\bar{t}$ region, s-channel selection

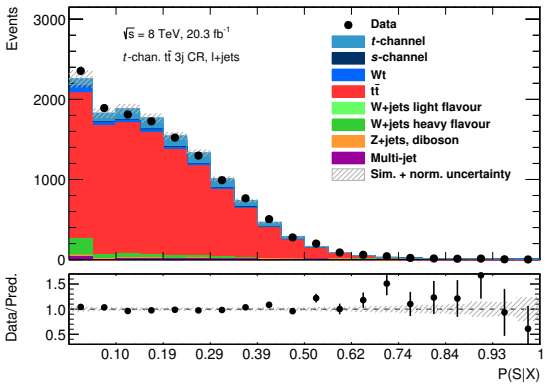

(d) Three-jet $t\bar{t}$ region, t-channel selection

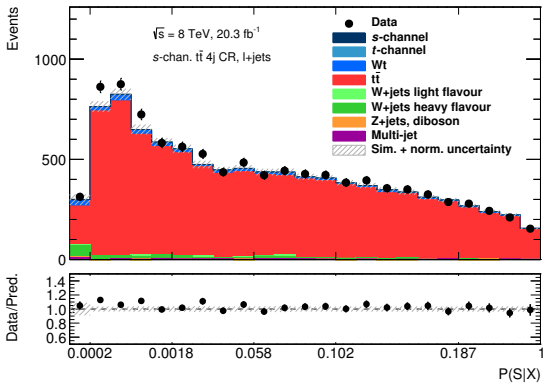

(e) Four-jet $t\bar{t}$ region, s-channel selection

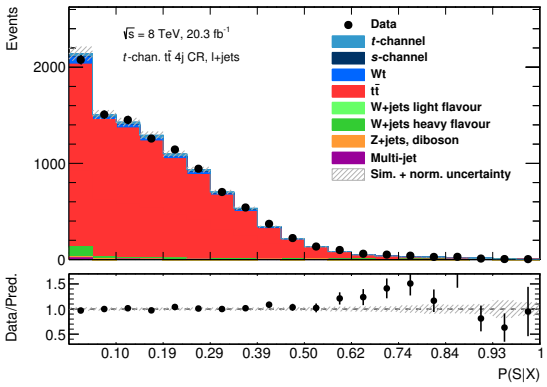

(f) Four-jet $t\bar{t}$ region, t-channel selection

Figure 7.22.: The signal probability for different background regions. The s-channel discriminant is shown in the (a) s-channel W+jets region, (c) s-channel three-jet $t\bar{t}$ region and (e) s-channel four-jet $t\bar{t}$ region. For the four-jet $t\bar{t}$ region only a subset of events as defined in Sec. 7.8.1 is used. The t-channel discriminant is presented in the (b) t-channel W+jets region, (d) t-channel three-jet $t\bar{t}$ region and (f) t-channel four-jet $t\bar{t}$ region.

8. Systematic Uncertainties

The cross section measurement of single-top s-channel and t-channel production, discussed in Sec. 9, is subject to various sources of uncertainties. Besides statistical uncertainties due to finite sample sizes and a limited data set, the remaining systematic sources of uncertainties can be grouped into three categories: normalization, instrumental and model uncertainties. All of these uncertainties have an impact on the predicted event yields for the signal and background processes as well as on the shape of the discriminant distribution.

In the following Secs. 8.1–8.4, the different sources of uncertainties relevant for this analysis and the evaluation of their impact on the cross section measurement is described. Subsequently, the effect on the predicted event yields is provided in Sec. 8.5. In Sec. 8.6, the evaluation of shape uncertainties is discussed.

8.1. Statistical uncertainties

Statistical uncertainties of the Monte Carlo simulations and of the multi-jet estimate, as well as from the finite data statistics are taken into account. The first two uncertainties are included in the likelihood model via a light-weight version of the Barlow–Beeston approach [BB93], which is discussed in Sec. 9.1.

8.2. Normalization uncertainties

The normalization uncertainties for the simulated samples and the multi-jet estimate and are described in the following. A summary of these uncertainties is given in Tab. 8.1.

Cross section normalization The normalization uncertainties for single-top and $t\bar{t}$ production are based on the theoretical calculations for the cross sections given in Secs. 2.3 and 7.1. Thus, uncertainties of $\pm 4\,\%$, $\pm 4\,\%$ and $\pm 7\,\%$ are assigned to the single-top s-channel, t-channel and Wt processes, respectively. An uncertainty of $\pm 6\,\%$ is used for $t\bar{t}$ production. The uncertainty on the s-channel and t-channel normalization only enters in fits of control distributions discussed in Sec. 7.4.

For the Z+jets process, a total cross section uncertainty of 60 % is used. A theory uncertainty of 5 % for the Z boson inclusive process, an uncertainty of 24 % per additional jet, the so-called Berends' scaling [EKS85, Ber+91] and an additional heavy-flavour uncertainty of 50 % are added in quadrature. The uncertainty for the diboson contribution is 10 %.

In the model for the likelihood fit (c. f. Sec. 9.1), the normalization of the W+jets background contribution in the s and t-channel signal region is allowed to vary independently from each other. Furthermore, different uncertainties are used for the W+jets normalization in each region. In the t-channel signal region, the W + jets contribution is split into contributions from W + b-jets and W + c|lf-jets. For the s-channel event selection of the W + jets sample, the normalization uncertainty is estimated in the same way as for the Z+jets contribution. A relative normalization uncertainty of 60 % is assigned based on the combination of the inclusive theory uncertainty (4 %), the Berends' scaling (24 % per additional jet) and the heavy-flavour uncertainties (50 %). This uncertainty estimate was already used for the s-channel measurement [ATL16a]. For the recent t-channel cross section measurement presented in [ATL17a], a dedicated study on the W+jets normalization uncertainty was conducted by varying parameters of the generator used for producing W+jets events. As a result of this study, an uncertainty of only 20 % is assigned to W+jets production, independently of W+jets production in association with either light-flavoured or heavy-flavoured jets [Tep+15].

The contributions from Z + jets and diboson production are are merged in the statistical analysis. The cross section uncertainty of the sum is given by the combination of the individual uncertainties weighted by their relative contribution.

Multi-jet normalization The normalization of the multi-jet background is obtained by the data-driven method described in Sec. 5. The uncertainty for the normalization is estimated by the variation of the fake and real efficiencies in the computation of the weights. Moreover, effects from changing the parametrization of the efficiencies as well as a the impact on the predicted background event yields from simulations are taken into account. The quadratic sum of all these variations leads to a systematic uncertainty of 40 % and 30 % for the multi-jet background in the s-channel and t-channel analysis, respectively.

8.3. Instrumental uncertainties

The following list of instrumental uncertainties is considered for this analysis. For their estimate the common recommendations for top-quark analyses within the ATLAS collaboration [Ach+13] are followed.

Process	Rel. unc. [%]
s-channel	± 4
t-channel	± 4
Assoc. Wt production	± 7
$t\bar{t}$ production	± 6
W+jets, s-channel selection	± 60
W+jets, t-channel selection	± 20
Z+jets	± 60
Diboson	± 10
Multi-jet, s-channel selection	± 40
Multi-jet, t-channel selection	± 30

Table 8.1: Summary of the relative uncertainties for the different processes. The uncertainties are based on theoretical calculations, except for the multi-jet normalization, which is estimated by variations of the data-driven technique.

Lepton energy scale and resolution The impact on the cross section measurement is evaluated by varying the energy scale and resolution parameters [ATL14c, ATL14e] used for calibrating leptons in the simulation by $\pm 1\sigma$ of their corresponding uncertainty in the simulation. Afterwards, the same object and event selections are applied to those leptons. Both uncertainties have an effect of less than 2 % on the signal and background rates.

Lepton trigger and identification efficiency Scale factors are applied to the MC simulation in order to reproduce the trigger and identification efficiencies measured in data. The uncertainty associated with lepton reconstruction and identification [ATL14c, ATL14e] is derived from a variation of the scale factors by $\pm 1\sigma$ leading to a variation of the predicted event yields by less than 2 %.

Jet energy scale The jet energy scale (JES) uncertainty [ATL13b, ATL13d] consists of different components, which are grouped according to different aspects of this systematic. These groups are based on the detector description, physics modelling, the employed methods or the mixing between detector and modelling. A set of uncorrelated components is derived and in total 26 different variations are considered. All systematic components are evaluated by rescaling the jet energy of each simulated jet corresponding to a $\pm 1\sigma$ variation. Their effects on the single-top processes and main backgrounds, like $t\bar{t}$ and W+jets, is about 1 to 5 %.

Jet energy resolution The uncertainty on the jet energy resolution [ATL13c] is dominated by the precision of the MC simulation comparison to data. For every event, the energy of the simulated jets are smeared by the 1σ interval of the resolution. The uncertainty is estimated by symmetrizing the difference between the nominal scale and the systematic variation[1]. The size of this systematic is about 3 % for single-top processes and less than 2 % for background processes.

[1] In general, for systematics that only consist of one-sided variation, their uncertainty is converted into a two-sided variation by symmetrization. The upward and downward variation is computed as $N_{\text{nominal}} \pm (N_{\text{systematic}} - N_{\text{nominal}})$ for each bin of the distribution.

Jet reconstruction efficiency Differences in the jet reconstruction efficiency between data and simulations [ATL13c] is taken into account by randomly discarding jets below the efficiency plateau at $p_{\mathrm{T}} = 30\,\mathrm{GeV}$ from simulated events. This procedure has an negligible effect on the predicted event yields.

Jet vertex fraction efficiency The threshold used for rejecting jets from pile-up based on the jet vertex fraction [Arg+13] is varied up and down to cover the discrepancy between data and MC simulations found in samples of $\mathrm{Z} \to \mathrm{ee}$ events. A maximal variation of 1.5 % in the predicted event yields is observed for $\mathrm{t\bar{t}}$ and Wt events. For all other processes, a lower value is found.

Tagging of b-jets Scale factors are defined for b-quark, c-quark and light-flavoured jets to correct differences in the tagging efficiencies between data and MC simulation. The uncertainty for each type of scale factor [ATL12b, ATL14b] is included in the analysis by re-applying the scale factors to each simulated jet after shifting its central value up or down by 1σ. The effect on the predicted event yields depends on the processes and the source of the uncertainty. The b-tagging uncertainty is typically around 5 % for events containing top-quarks, while lower values are observed for other background processes. The uncertainties on c-tagging and mis-tagging efficiencies are below 2 % for single-top s-channel and t-channel processes as well as top-quark pair production. Larger values between 3–8 % are observed in case of Wt production and W+jets processes.

Missing transverse momentum The missing transverse momentum is calculated as the sum of several terms. Contributions from calorimeter entries which are either associated with jets with energies below 20 GeV or detached from any reconstructed object, are varied within their uncertainties. The energy scale and resolution uncertainties are of the order of 8 % and 2.5 %, respectively. No specific uncertainty is taken into account for terms associated with reconstructed leptons or jets. Instead, their energy shift is propagated to the missing transverse momentum calculations, when evaluating the dedicated systematic uncertainties for those objects. [ATL13e] The impact on the analysis is almost imperceptible.

Luminosity The uncertainty on the integrated luminosity is 2.8 %. The normalization of all simulation samples is varied accordingly.

8.4. Model uncertainties

The modelling of the signal and background processes is taken into account by evaluating different samples for the same process. They are treated as uncorrelated uncertainties in the context of the likelihood model, discussed in Sec. 9.1.

MC generator and parton shower modelling Systematic uncertainties that arise from using different MC generators or different parton shower models from

the default choice are evaluated in the following way. For the s-channel single top-quark production, the effects of both, MC generator and parton shower, are evaluated by comparing the default POWHEG+PYTHIA sample with an alternative sample produced with aMC@NLO+HERWIG. In case of single-top t-channel production, the impact on the measurement from an alternative event generator is estimated by the comparison between samples produced with POWHEG+HERWIG and aMC@NLO+HERWIG. In addition, the parton shower modelling is evaluated by analysing events produced with POWHEG+PYTHIA and POWHEG+HERWIG. The uncertainties associated with event generator and parton shower for top-quark pair and single-top Wt production is estimated by the comparison of MC simulations using POWHEG+PYTHIA and MC@NLO+HERWIG settings. Moreover, for the associated Wt production, two POWHEG+PYTHIA samples are produced using different NLO calculations schemes, namely the so-called diagram removal (DR) and diagram subtraction (DS). The default scheme is DR.

For each comparison, the relative differences in the acceptance between the two MC samples is calculated and symmetrized. For the combined uncertainty of event generator and parton shower, uncertainties of about 3–4 %, 5–10 %, 1–4 % are found for single-top s-channel, Wt production and $t\bar{t}$ production, respectively. The Wt calculation scheme has an effect of 2–10 % on the predicted event yields. For all these uncertainties, the effects are larger in the t-channel signal region than in the s-channel signal region. For the t-channel a sizeable effect of 5 % and 15 % is found for the comparisons of parton shower and event generator for the s-channel signal region. The same impact from the parton shower is found in the t-channel signal region, while the differences between the two event generators is negligible in this region.

For the s-channel measurement presented in [ATL16a], a combined uncertainty was used for the t-channel event generator and parton shower modelling. Although the method used here is different, the resulting effect on the event yields is compatible with the former analysis.

W + jets modelling The modelling of W+jets events is studied with a comparison of the default SHERPA sample and the alternative ALPGEN+PYTHIA sample. The difference between these to samples is symmetrized and used as uncertainty estimate. For the s-channel signal region, a difference of 14 % is found, whereas in the t-channel signal region, this difference is only about 1 %.

$t\bar{t}$ initial and final state radiation The amount of QCD radiation is studied by using dedicated samples produced with POWHEG+PYTHIA. In addition to the variation of the so-called h_{damp} parameter, that controls the hardness of the hardest emission, the renormalization and factorization scales are varied. A study [ATL15a] showed that an envelope, build from the minimum and maximum variation in each bin of a distribution, covers all individual variations of these three parameters. Therefore, such an envelope is calculated using the

discriminant distributions and the uncertainty estimate for initial and final state radiation (ISR/FSR) is about 4–6 %.

Parton distribution functions The systematic uncertainty related to the PDFs is evaluated by reweighting all events from the signal and background samples. The reweighting procedure is described in [Ale+11, Bot+11] and three different PDF sets, CT10nlo [Lai+10], MSTW2008nlo68cl [Mar+09] and NNPDF2.3 [Bal+13], are used. For each PDF set, an estimate for the predicted event yield as well as an uncertainty is obtained. The envelope that covers all three uncertainty bands is used to estimate the systematic uncertainty. Variations of less than 3.5 % are found.

The information that is needed for estimating the PDF uncertainty is not available in the default top-quark simulation samples. Therefore, the relative systematic uncertainty, which is calculated using alternative samples listed in Tab. A.3, is used in the statistical evaluation.

Scale uncertainties The scale dependence of the s-channel and t-channel event generation is estimated by comparing POWHEG+PYTHIA samples with varied renormalization and factorization scales with respect to the nominal settings. The scales are varied by a factor of $\frac{1}{2}$ and 2. In case of the s-channel generator, these variations are performed independently of each other, while for the t-channel generator, both scales are varied in the same direction. The uncertainty is evaluated by using the maximum and minimum variations in each bin. The estimated uncertainty is about 7 % for the s-channel process and about 5 % for the t-channel process.

W boson p_{T} reweighting The uncertainty for reweighting of the W + jets events (c. f. Sec. 7.5) is estimated by calculating the difference between the original and reweighted distributions. The effect is symmetrized around the reweighted distribution.

8.5. Rate Uncertainties

The relative systematic uncertainties on the predicted event yields for the different signal and background processes are listed in Tab. 8.2 for the s-channel signal region and in Tab. 8.3 for the t-channel signal region. Only the instrumental uncertainties as well as the modelling uncertainties are provided. The multi-jet contribution is estimated using a data-driven method. Therefore, no instrumental uncertainties are considered, but all uncertainties related to the application of the matrix method are contained in the normalization systematic uncertainty.

	Rate uncertainty [%]											
Process	s-channel		t-channel		Wt prod.		$t\bar{t}$ prod.		W+jets		Z+jets & diboson	
Systematic	up	down	up	down	up	down	up	down	up	down	up	down
Jet energy res.	−3.2	3.2	−2.8	2.8	−3.0	3.0	−2.1	2.1	1.2	−1.2	−0.6	0.6
Jet reco. eff.	0.0	0.0	0.0	0.0	0.5	−0.5	0.1	−0.1	0.1	−0.1	0.1	−0.1
Jet vertex fraction	0.1	−0.2	0.1	−0.2	1.4	−0.6	1.1	−0.9	0.2	0.0	0.2	−0.4
$E_{\mathrm{T}}^{\mathrm{miss}}$ resolution	0.1	−0.1	−0.2	−0.2	−0.2	−0.2	0.0	0.0	0.0	0.1	0.4	0.6
$E_{\mathrm{T}}^{\mathrm{miss}}$ scale	0.1	−0.2	0.1	−0.2	−0.4	0.0	0.0	−0.1	0.6	−0.1	0.9	−0.9
El. energy res.	0.1	0.0	−0.3	−0.1	1.0	0.0	0.0	0.0	−0.5	−0.2	−0.5	−0.2
El. energy scale.	0.8	−0.8	0.6	−0.8	0.9	0.4	0.4	−0.4	0.6	−0.7	0.3	−0.3
Muon ID	0.0	0.0	0.1	−0.1	0.0	0.0	0.0	0.0	0.1	−0.1	0.0	0.0
Muon mom. res.	0.0	0.0	0.0	0.0	−0.5	0.5	0.0	0.0	0.0	0.0	0.3	−0.3
Muon mom. scale	0.0	−0.1	0.1	0.0	0.3	0.1	0.0	0.0	0.0	0.0	0.0	0.0
Lepton reco.	0.2	−0.2	0.2	−0.2	0.2	−0.2	0.2	−0.2	0.2	−0.2	0.2	−0.2
Lepton ID	1.3	−1.3	1.3	−1.3	1.3	−1.3	1.3	−1.3	1.2	−1.2	1.2	−1.2
Lepton trigger	−0.8	0.8	−0.8	0.8	−0.8	0.8	−0.8	0.8	−0.9	0.9	−0.9	0.9
b-tagging	4.6	−4.5	3.9	−3.9	3.1	−3.1	4.3	−4.2	2.4	−2.3	3.5	−3.4
c-tagging	0.0	0.0	1.2	−1.2	3.3	−3.3	0.6	−0.6	4.4	−4.2	1.5	−1.4
mis-tagging	0.1	−0.1	1.5	−1.5	1.5	−1.5	0.2	−0.2	7.8	−6.9	3.3	−3.0
PDF	1.3	−1.3	2.0	−2.0	2.3	−2.3	3.1	−3.1	3.0	−3.0	3.3	−3.3
b-JES	1.1	−1.1	1.3	−1.6	0.4	−0.7	0.7	−0.6	0.5	−2.0	1.4	−1.5
η-intercalib. model	−0.3	0.2	−2.0	1.5	−1.0	1.4	−1.3	1.5	−0.8	−0.3	−0.8	0.3
η-intercalib. stat.	−0.1	0.1	−0.8	0.3	−1.4	1.3	−0.9	1.0	−0.7	−0.3	−0.4	−0.5
JES eff. det. 1	0.1	−0.1	0.0	−0.2	−1.0	0.8	−0.2	0.3	−0.3	−0.1	−0.1	0.0
JES eff. det. 2	0.0	0.0	−0.1	−0.1	−0.5	0.9	−0.2	0.3	−0.5	−0.1	−0.4	−0.1
JES eff. det. 3	0.0	0.0	−0.1	−0.1	−0.4	−0.2	0.0	0.1	−0.5	−0.1	−0.3	−0.2
JES eff. mix. 1	0.1	−0.1	−0.1	−0.1	−1.2	0.6	−0.4	0.4	−0.3	−0.1	0.1	−0.1
JES eff. mix. 2	0.0	0.0	0.0	−0.3	1.8	−1.1	0.6	−0.5	0.1	−0.4	−0.4	0.0
JES eff. mix. 3	0.0	0.1	−0.2	0.0	−0.2	0.9	−0.1	0.2	−0.7	0.1	−0.3	−0.4
JES eff. mix. 4	0.0	0.0	−0.1	−0.1	0.0	0.0	0.1	0.1	−0.6	−0.7	−0.7	−0.1
JES eff. model 1	−0.1	−0.2	−1.4	0.2	−3.2	3.6	−3.2	3.4	1.0	−1.2	0.6	−2.1
JES eff. model 2	0.0	0.0	−0.1	−0.1	0.8	−0.4	0.1	0.0	0.0	−0.5	−0.4	−0.7
JES eff. model 3	−0.1	0.1	−0.3	0.1	−1.0	1.1	−0.2	0.3	−1.0	0.1	−0.7	−0.1
JES eff. model 4	0.0	0.0	−0.1	−0.2	0.0	−0.2	0.0	0.1	−0.5	−0.7	−0.4	−0.5
JES eff. stat. 1	−0.1	0.1	−0.7	0.2	−2.2	1.6	−1.3	1.4	0.0	−0.5	−0.2	−0.3
JES eff. stat. 2	0.0	0.0	−0.1	−0.2	0.6	0.0	0.1	−0.1	−0.1	−0.7	−0.2	−0.6
JES eff. stat. 3	−0.2	0.2	−0.3	0.1	0.3	0.0	0.0	0.1	−1.0	−0.4	−0.4	0.2
JES eff. stat. 4	0.0	0.0	−0.1	−0.2	−0.3	1.0	−0.1	0.2	−0.5	−0.2	−0.3	−0.3
JES pile-up μ	0.0	−0.1	0.4	−1.0	1.8	0.2	0.6	−0.5	−0.4	−0.1	−0.3	−0.1
JES pile-up # PV	−0.1	0.0	−0.2	−0.5	1.0	−0.6	0.8	−0.7	−0.6	0.3	−0.3	1.0
JES pile-up p_{T}	0.0	0.0	−0.1	−0.2	−0.3	−0.2	0.0	0.0	−0.5	−0.6	−0.1	−0.2
JES pile-up ρ	−0.2	0.0	−1.2	0.3	−2.8	3.1	−2.5	2.6	0.6	−0.9	0.1	−0.9
JES flavor comp.	−1.8	1.7	−3.9	2.9	−4.7	3.8	−5.0	5.3	−1.6	1.2	−2.2	0.5
JES flavour resp.	1.1	−1.2	2.1	−2.8	2.5	−3.8	3.6	−3.3	0.5	−0.6	0.0	−2.1
JES punch through	0.0	0.0	−0.2	−0.2	−0.3	−0.3	0.1	0.1	−0.6	−0.6	−0.5	−0.6
JES single part.	0.0	0.0	−0.2	−0.2	−0.3	−0.3	0.1	0.1	−0.6	−0.6	−0.6	−0.6
s-channel gen.	3.4	−3.4	–	–	–	–	–	–	–	–	–	–
t-channel gen.	–	–	15.6	−15.6	–	–	–	–	–	–	–	–
Scalevar. s-channel	6.6	−7.3	–	–	–	–	–	–	–	–	–	–
Scalevar. t-channel	–	–	3.0	−3.8	–	–	–	–	–	–	–	–
Shower t-channel	–	–	−5.3	5.3	–	–	–	–	–	–	–	–
Wt DS	–	–	–	–	−1.6	1.6	–	–	–	–	–	–
Wt generator	–	–	–	–	−4.6	4.6	–	–	–	–	–	–
$t\bar{t}$ generator	–	–	–	–	–	–	0.6	−0.6	–	–	–	–
ISR/FSR	–	–	–	–	–	–	2.7	−6.7	–	–	–	–
W+jets generator	–	–	–	–	–	–	–	–	−13.7	13.7	–	–
p_{T}(W) reweighting	–	–	–	–	–	–	–	–	0.8	−0.8	–	–

Table 8.2.: Overview of all rate uncertainties for the studied systematic effects in the s-channel signal region (upward and downward variations). All numbers are given in %.

	Rate uncertainty [%]											
Process	t-channel		s-channel		Wt prod.		$t\bar{t}$ prod.		W+jets		Z+jets & diboson	
Systematic	up	down	up	down	up	down	up	down	up	down	up	down
Jet energy res.	−3.2	3.2	−2.4	2.4	−3.0	3.0	−1.1	1.1	−0.4	0.4	1.2	−1.2
Jet reco. eff.	0.0	0.0	0.0	0.0	0.0	0.0	0.1	−0.1	0.1	−0.1	0.0	0.0
Jet vertex fraction	0.2	−0.2	0.3	−0.3	1.1	−0.7	1.5	−1.3	0.4	−0.3	0.5	−0.5
$E_{\mathrm{T}}^{\mathrm{miss}}$ res.	0.1	0.1	0.0	−0.1	0.3	−0.1	0.0	−0.1	0.0	−0.4	0.8	−0.3
$E_{\mathrm{T}}^{\mathrm{miss}}$ scale	0.1	0.0	0.1	−0.1	−0.5	0.1	0.0	0.0	−0.1	−0.3	1.4	−0.9
El. energy res.	0.0	0.0	−0.1	−0.1	0.7	0.3	0.0	0.0	−0.9	−0.3	0.3	0.3
El. energy scale.	0.9	−0.9	0.8	−0.9	0.6	−0.5	0.4	−0.4	0.6	−0.7	1.5	−1.7
Muon ID	0.0	0.0	0.0	0.0	−0.2	0.2	0.0	0.0	0.0	0.0	0.1	−0.1
Muon mom. res.	0.0	0.0	0.0	0.0	−0.3	0.3	0.0	0.0	0.1	−0.1	0.0	0.0
Muon mom. scale	0.1	−0.1	0.1	0.0	0.0	0.0	0.0	0.0	0.1	−0.2	0.0	−0.1
Lepton reco.	0.2	−0.2	0.2	−0.2	0.2	−0.2	0.2	−0.2	0.2	−0.2	0.2	−0.2
Lepton ID	1.3	−1.3	1.2	−1.2	1.3	−1.3	1.3	−1.3	1.2	−1.2	1.4	−1.4
Lepton trigger	−0.8	0.8	−0.8	0.8	−0.8	0.8	−0.8	0.8	−0.8	0.8	−0.6	0.6
b-tagging	2.6	−2.6	0.9	−1.0	2.6	−2.6	1.9	−1.9	1.2	−1.2	1.7	−1.7
c-tagging	0.0	0.0	0.0	0.0	0.0	0.0	0.0	0.0	7.6	−7.6	3.0	−3.0
mis-tagging	0.0	0.0	0.0	0.0	0.0	0.0	0.0	0.0	2.1	−2.1	1.9	−1.9
PDF	1.2	−1.2	1.3	−1.3	2.5	−2.5	3.3	−3.3	2.9	−2.9	3.1	−3.1
b-JES	0.3	−0.3	0.9	−1.0	0.6	−0.3	−0.4	0.3	0.3	−0.6	1.3	−0.3
η-intercalib. model	0.3	−0.4	0.0	−0.2	0.0	0.9	−1.5	1.6	−0.3	−1.0	0.2	0.4
η-intercalib. stat.	−0.2	0.1	−0.1	0.0	0.2	1.2	−1.4	1.3	−0.2	−0.4	0.2	0.4
JES eff. det. 1	0.1	−0.1	0.1	−0.1	0.5	0.4	−0.5	0.4	−0.1	−0.6	0.4	0.1
JES eff. det. 2	0.0	0.0	0.0	0.0	0.4	0.6	−0.4	0.3	−0.1	−0.4	0.1	0.0
JES eff. det. 3	0.0	0.0	0.0	−0.1	0.5	0.5	−0.1	0.0	−0.2	−0.3	0.1	0.0
JES eff. mix. 1	0.1	−0.1	0.1	−0.1	0.5	0.6	−0.6	0.5	0.0	−0.8	0.4	0.1
JES eff. mix. 2	0.0	−0.1	0.0	−0.1	0.8	0.2	0.7	−0.8	−0.3	−0.1	0.3	0.3
JES eff. mix. 3	−0.1	0.1	−0.1	0.1	0.2	0.6	−0.3	0.2	−0.3	−0.3	−0.1	0.1
JES eff. mix. 4	0.0	0.0	0.0	0.0	0.4	0.4	0.0	0.0	−0.1	−0.3	0.0	0.0
JES eff. model 1	0.1	−0.4	0.2	−0.3	−1.1	2.4	−4.2	4.2	0.6	−1.0	2.1	−1.2
JES eff. model 2	0.0	0.0	−0.1	0.0	0.5	0.4	0.1	−0.1	−0.4	−0.1	0.0	0.0
JES eff. model 3	−0.2	0.3	−0.3	0.3	0.0	0.9	−0.5	0.4	−0.8	0.1	−0.4	0.5
JES eff. model 4	0.1	0.0	0.0	−0.1	0.5	0.4	−0.1	0.0	−0.2	−0.5	0.0	0.0
JES eff. stat. 1	−0.2	0.1	−0.2	0.1	−0.2	1.8	−1.8	1.8	−0.3	−0.4	−0.1	0.4
JES eff. stat. 2	0.1	0.0	0.0	−0.1	0.6	0.3	0.1	−0.2	−0.3	−0.3	0.0	−0.1
JES eff. stat. 3	−0.2	0.3	−0.3	0.3	0.3	0.8	−0.2	0.1	−0.9	0.2	−0.2	0.5
JES eff. stat. 4	0.0	0.0	0.0	−0.1	0.4	0.5	−0.3	0.3	−0.2	−0.4	0.3	0.1
JES pile-up μ	−0.1	−0.1	−0.1	0.0	0.2	0.7	0.7	−0.7	−0.3	−0.4	0.2	0.4
JES pile-up # PV	0.0	−0.1	−0.1	0.0	0.8	0.0	1.0	−1.1	−0.5	−0.1	0.3	0.2
JES pile-up p_{T}	0.1	0.0	0.1	−0.2	0.5	0.2	0.0	−0.1	−0.4	−0.5	0.2	−0.3
JES pile-up ρ	−0.2	0.0	−0.2	0.0	−0.8	2.0	−3.4	3.4	−0.4	−0.5	0.4	0.0
JES flavour comp.	−0.4	0.1	−1.5	1.3	−2.8	3.5	−4.7	4.8	−0.4	−0.2	0.6	−0.3
JES flavour resp.	−0.1	−0.1	0.8	−1.0	2.5	−1.5	3.1	−3.1	−0.7	−0.5	−0.2	0.1
JES punch through	0.0	0.0	0.0	0.0	0.4	0.4	0.0	0.0	−0.2	−0.2	0.0	0.0
JES single part.	0.0	0.0	0.0	0.0	0.4	0.4	0.0	0.0	−0.1	−0.1	0.0	0.0
t-channel gen.	−0.6	0.6	–	–	–	–	–	–	–	–	–	–
s-channel gen.	–	–	−4.1	4.1	–	–	–	–	–	–	–	–
Shower t-channel	−2.9	2.9	–	–	–	–	–	–	–	–	–	–
Scalevar. s-channel	–	–	5.4	−6.6	–	–	–	–	–	–	–	–
Scalevar. t-channel	2.6	−5.2	–	–	–	–	–	–	–	–	–	–
Wt DS	–	–	–	–	10.1	−10.1	–	–	–	–	–	–
Wt generator	–	–	–	–	9.4	−9.4	–	–	–	–	–	–
$t\bar{t}$ generator	–	–	–	–	–	–	−3.7	3.7	–	–	–	–
ISR/FSR	–	–	–	–	–	–	0.7	−2.8	–	–	–	–
W+jets generator	–	–	–	–	–	–	–	–	1.2	−1.2	–	–
p_{T}(W) reweighting	–	–	–	–	–	–	–	–	−1.7	1.7	–	–

Table 8.3.: Overview of all rate uncertainties for the studied systematic effects in the t-channel signal region (upward and downward variations). All numbers are given in %. For the W+jets background, only the rate uncertainty for the combination of W + heavy flavour and light flavour production is listed.

8.6. Shape Uncertainties

All systematic uncertainties, except for luminosity, can have an impact on the shape of the discriminant distributions. These shape uncertainties need to be included into the likelihood model in addition to differences in the number of predicted events. However, not all shape variations are due to systematic shifts, but are statistical variations caused by the limited size of the used samples. Including all of these variations would artificially increase the uncertainty of the measurement, as the statistical uncertainties would be counted twice.

Therefore, a χ^2-test is performed between the nominal distribution and the one obtained by systematic variations for all processes and all sources of uncertainties. Most of the systematic uncertainties are evaluated by using the same simulated events and the nominal and systematically varied distributions are highly correlated. In order to avoid comparing the correlated distributions, two disjoint sets of events are formed by using even and odd event numbers. For modelling uncertainties, which are evaluated using different event samples, the events are not split into two samples, but rather the full available statistics is used. In addition, both distributions are normalized to the same number of events, because only differences in the shape of the distributions are considered. Figure 8.1 shows two examples of systematic variations of the discriminant distribution in the s-channel signal region. The differences in shapes are considered if the p-value of the χ^2-test is below 5 % and thus significant. This decision is taken separately for up- and downward variations. For systematic variations with a p-value greater than 5 %, the nominal shape is used.

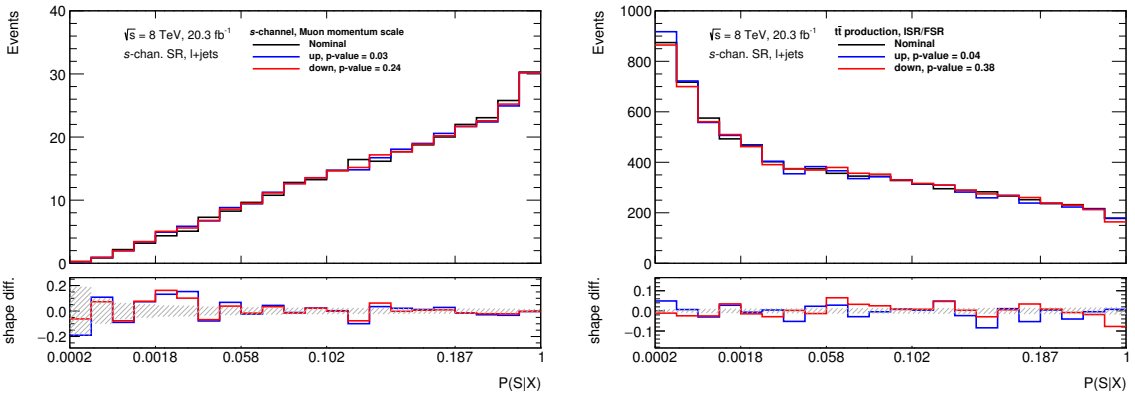

(a) s-channel, muon momentum scale (b) $t\bar{t}$ production, ISR/FSR

Figure 8.1.: Examples of systematic variations of the discriminant distribution in the s-channel signal region. (a) s-channel, muon momentum scale systematic and (b) $t\bar{t}$ production, ISR/FSR systematic. Each systematic variation is normalized to the expected number of events of the nominal scale. The uncertainty band in the lower panels corresponds to the statistical uncertainty of the nominal template.

This procedure was already used for the s-channel measurement [Kin$^+$14] to determine significant shape differences. Moreover, the impact on the s-channel significance was found to be independent over a wide range of p-values. Tables 8.4 and 8.5 provide a list of uncertainties, for which the differences in shape between the nominal scale and the systematic variation are considered for the s-channel and t-channel signal region, respectively.

Systematic	s-channel	t-channel	$t\bar{t}$	other bkg. processes
Jet energy res.	✓ / –	✓ / –	–	–
Muon mom. scale	✓ / –	–	–	–
η-intercalib. model	✓ / –	–	–	–
JES eff. det. 1	–	✓ / –	–	–
JES eff. det. 3	– / ✓	–	–	–
JES eff. model 3	–	✓ / –	–	–
JES eff. stat. 1	–	– / ✓	–	–
JES eff. stat. 2	–	✓ / –	–	–
JES eff. stat. 4	–	✓ / –	–	–
ISR/FSR ($t\bar{t}$)	–	–	✓ / –	–

Table 8.4.: Overview of systematic uncertainties in the s-channel signal region. Systematic uncertainties for which shape variations for a specific process are included in the statistical model are marked. The checkmark's position indicates whether the shape variation correspond to the upward (✓/–) or downward (–/✓) variation. All systematics with a preceding "JES" as well as the η-intercalibration uncertainty are components of the jet energy scale uncertainty.

Systematic	s-channel	t-channel	Wt	$t\bar{t}$	W + c-jets W + lf-jets	Z+jets, diboson
Jet energy res.	–	–	–	–	✓ / –	–
$E_{\mathrm{T}}^{\mathrm{miss}}$ res.	–	✓ / –	–	–	–	–
El. energy res.	–	✓ / –	–	–	–	–
Muon mom. scale	✓ / –	–	–	–	–	–
η-intercalib. stat.	–	– / ✓	–	–	–	–
JES eff. det. 2	–	–	–	–	–	– / ✓
JES eff. mix. 1	✓ / –	–	–	–	– / ✓	–
JES eff. mix. 3	–	✓ / –	–	–	–	–
JES eff. mix. 4	–	✓ / –	–	–	–	–
JES eff. model 1	–	–	–	–	✓ / –	–
JES eff. model 2	–	– / ✓	– / ✓	–	–	–
JES eff. stat. 2	– / ✓	–	–	–	–	✓ / –
JES eff. stat. 3	–	–	✓ / –	–	–	✓ / –
JES eff. stat. 4	–	–	–	–	– / ✓	–
JES pile-up μ	–	–	✓ / –	–	–	–
JES flavour comp.	–	–	–	–	✓ / –	–

Table 8.5.: Overview of shape variation systematic uncertainties for the t-channel signal region. The systematic uncertainties included as a shape variation in the signal extraction for a particular process are marked. All systematics with a preceding "JES" as well as the η-intercalibration uncertainty are components of the jet energy scale uncertainty.

9. Single-Top Cross Section Measurement

The simultaneous measurement of the single-top cross section in the s and t-channel is extracted by a fit of the predicted matrix elment (ME) discriminant distributions to data. The statistical model of this fit, encoded in the likelihood function, is described in Sec. 9.1. Furthermore, the results of the measurement are given in Sec. 9.2.

9.1. Fit Model

The statistical evaluation of the cross section measurement presented in this thesis uses three programs, RooFit [VK03], RooStats [Mon+10] and HistFactory [Cra+12]. The basic statistical entities such as probability density functions and techniques for minimization and integration are provided by RooFit, while RooStats contains a set of tools for hypothesis testing and the construction of confidence intervals. HistFactory is based on the RooStats/RooFit framework and can be used to create a statistical model.

The statistical model used in this thesis is constructed by HistFactory and contains several parameters to relate the predicted distribution to the observed one. It contains two parameters, $\mu_s = \sigma_s/\sigma_s^{\mathrm{SM}}$ and $\mu_t = \sigma_t/\sigma_t^{\mathrm{SM}}$, which are defined as the ratio of the measured cross section normalized to their standard model prediction. These signal strength parameters are unconstrained, except for the requirement $\mu_{s|t} \geq 0$. In addition, statistical and systematic uncertainties, described in the Sec. 8, are included in the model in the form of nuisance parameters, θ. These parameters are in general constrained by auxiliary knowledge. For the determination of the signal strength parameters, the likelihood function is maximized with respect to the signal strength parameters and nuisance parameters. Therefore, nuisance parameters can be in principle constrained based on the information contained in the data distribution. Such constraints of nuisance parameters need to be reviewed, as they could hint to a possible mis-modelling of the data distribution by the statistical model.

The likelihood function describes the data distribution of the ME discriminants in the s-channel signal region and t-channel signal region. For writing down this likelihood function, the following terminology is established. The two signal regions, the s-channel signal selection and t-channel signal selection, are referred to as "channels".

Each channel consists of different samples corresponding to the different groups of processes depicted in Figs. 7.20 and 7.21.[1] A template histogram is associated with each sample. The likelihood function of the two ME discriminants is given by

$$L(n_{cb}, a_p|\mu_s, \mu_t, \theta_p, \gamma_b) = \prod_{c\,\in\,\text{channels}} \prod_{b\,\in\,\text{bins}} \text{Pois}(n_{cb}|\nu_{cb}) \cdot G(\mathcal{L}_0|\lambda, \Delta_\mathcal{L}) \prod_{p\,\in\,\text{syst}} f_p(a_p|\theta_p). \tag{9.1}$$

It contains a Poisson term, $\text{Pois}(\text{n}_{\text{cb}}|\nu_{\text{cb}})$, for each bin of the discriminant distribution in each channel. In addition, a Gaussian constraint term, $G(\mathcal{L}_0|\lambda, \Delta_\mathcal{L})$, for the luminosity parameter λ is included as well as constraint terms for the systematic uncertainties, $f_p(a_p|\theta)$. The number of observed events is denoted by n_{cb}, while the expected mean number of events in a given bin is

$$\nu_{cb}(\mu_s, \mu_t, \theta_p, \gamma_b) = \gamma_{cb} \cdot \left(\sum_{i\,\in\,\{s,t\}} \mu_i \lambda_{ci} \eta_{ci}(\boldsymbol{\theta}) \sigma_{cbi}(\boldsymbol{\theta}) + \sum_{j\,\in\,\{\text{bkgs}\}} \lambda_{cj} \eta_{cj}(\boldsymbol{\theta}) \sigma_{cbj}(\boldsymbol{\theta}) \right). \tag{9.2}$$

The parameters in Eqs. 9.1 and 9.2 are defined as follows:

λ_{ci} - Luminosity parameter for a given channel c and sample i. The overall normalization is varied for samples obtained from Monte Carlo simulations simultaneously, while for the data-driven background it is fixed to the nominal luminosity $\mathcal{L}_0$ of the measurement. The width of the Gaussian constraint term is given by the luminosity uncertainty $\Delta_\mathcal{L}$.

γ_{cb} - The statistical uncertainties are incorporated into the model via a light-weight Barlow–Beeston approach [BB93]. One parameter is assigned to each bin and it can vary the expected number of events within the combined statistical uncertainty of all samples in that bin.

$\eta_{ci}(\boldsymbol{\theta})$ - The normalization uncertainties of each sample as well as all instrumental and modelling uncertainties are included by a normalization factor. A polynomial interpolation and exponential extrapolation is used for incorporating the changes in normalization between the nominal normalization and the $\pm 1\sigma$ variations $\eta_{ip}^{\pm}$ for each sample i and each systematic p. The normalization factor η for the sample i in a specific channel is given by

$$\eta_i(\boldsymbol{\theta}) = \prod_{p\,\in\,\text{syst.}} I_{\text{poly|exp.}}(\theta_p; 1, \eta_{ip}^{+}, \eta_{ip}^{-}, \theta_0) \tag{9.3}$$

with

$$I_{\text{poly|exp.}}(\theta; I^0, I^+, I^-, \theta_0) = \begin{cases} (I^+/I^0)^{\theta} & \theta \geq \theta_0 \\ 1 + \sum_{i=1}^{6} a_i \theta^i & |\theta| < \theta_0 \\ (I^+/I^0)^{-\theta} & \theta \leq \theta_0 \end{cases}. \tag{9.4}$$

[1] For the single-top s-channel, the two samples for W+jets background are merged, as the statistics for W boson production with light-flavoured jets is limited. For the t-channel, the W+jets contribution is split into one for W + b-jets production and the other one for W + c-jets and W+ light-flavoured jets.

The coefficients of the polynomial are fixed by the boundary conditions $\eta(\theta = \pm\theta_0)$, $\mathrm{d}\eta/\,\mathrm{d}\theta|_{\theta=\pm\theta_0}$ and $\mathrm{d}^2\eta/\,\mathrm{d}\theta^2|_{\theta=\pm\theta_0}$. The default boundary is $\theta_0 = 1$, as the systematic uncertainties correspond to a $\pm1\sigma$ variation and the nominal model is obtained if $\theta_p = 0$ for all systematic variations p. The exponential extrapolation in combination with Gaussian constraints on the nuisance parameters θ is equivalent to a linear extrapolation and using log-normal constraint in $\ln(\theta)$. The polynomial interpolation avoids discontinuous first and second derivatives at $\theta = 0$, which can be a problem for numerical minimization programs such as MINUIT [JR75].

$\sigma_{cbi}(\boldsymbol{\theta})$ - This factor is a function of the nuisance parameters θ and describes the predicted number of events in each bin b for the sample i of channel c. In addition, shape variations of the discriminant by systematic uncertainties are included. The same interpolation and extrapolation algorithm is used as for the normalization uncertainties. The shape of the $\pm1\sigma$ systematic variation p is obtained for $\sigma(\theta_p = \pm1)$.

$f_p(a_p|\theta_p)$ - Constraint terms for describing the auxiliary knowledge of the nuisance parameters. By default, a Gaussian constraint term,

$$G(\theta_p|a_p, \sigma_p) = \frac{1}{\sqrt{2\pi\sigma_p^2}} \exp\left[-\frac{(a_p - \theta_p)^2}{2\sigma_p^2}\right] \tag{9.5}$$

is used for each nuisance parameter θ_p and for the statistical parameters γ. As described above, the nominal model is obtained for $\theta = 0$, while the $\pm1\sigma$ systematic variations correspond to $\theta = \pm1$. Therefore, a Gaussian constraint $G(0|\theta_p, 1)$ is chosen for all nuisance parameters θ and the corresponding systematic uncertainties are scaled such that $\sigma_p = 1$ by default.

9.2. Results

In this section, the analysis results for the cross section measurement are collected. The expected results are given by the analysis of the so-called Asimov data, which is constructed from the sum of all signal and background contributions obtained from MC simulations or data-driven methods. The use of the Asimov data allows to test the likelihood fit avoiding any potential bias based on observed distributions.

9.2.1. Maximum Likelihood Fit

Asimov Data

The likelihood function defined by Eq. 9.1 is fitted to the Asimov data by using MINUIT. The result for the signal strength parameters is given in Tab. 9.1.

	μ_s	μ_t
Parabolic unc.	1.00 ± 0.30	1.000 ± 0.073
MINOS	$1.00^{+0.33}_{-0.29}$	$1.000^{+0.083}_{-0.067}$

Table 9.1.: Results for the signal strength parameters and their 1σ interval for the fit to the Asimov data. The parabolic uncertainty corresponds to the symmetric uncertainty interval assuming a parabolic shape of the log-likelihood function around the minimum, while the asymmetric interval provided by MINOS does not rely on this assumption [JR75].

Figure 9.1 shows the 1σ, 2σ and 3σ contour of the likelihood function as a function of the two signal strength parameters, μ_s and μ_t. The dot represents the maximum of the likelihood function and coincides with the SM prediction as expected.

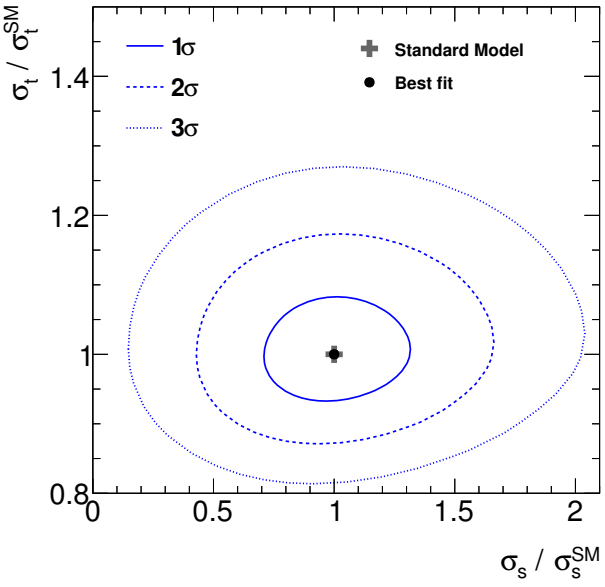

Figure 9.1: The 1σ, 2σ and 3σ contour of the likelihood function as a function of the signal strength parameters. The result for the fit to the Asimov data is marked with the black dot and is identical to the SM prediction (cross).

The likelihood function contains several nuisance parameter that describe the response of the measurement to a certain systematic uncertainty. The pull of a nuisance parameter is defined as the difference between the best estimator $\hat{\theta}$ and the expected value $\theta_0 = 0$ for this nuisance parameter divided its uncertainty $\Delta\theta$. Figure 9.2 exhibits the pulls of several nuisance parameter from the fit to Asimov data. Usually, the Asimov data does not contain any information to constrain a nuisance parameter nor cause a deviation between the expected value θ_0 and the best estimator $\hat{\theta}$. This expected behaviour is observed for most of the pulls shown in Fig. 9.2. One exception is the nuisance parameter that describes the normalization of the W+jets background in the s-channel signal region. The estimated uncertainty for this background is 60 % and such a large fluctuation in the W+jets contribution is not compatible with the

expected data statistics. Therefore, this nuisance parameter can be constrained in a fit to Asimov data and the background normalization uncertainty is reduced to about 20 % only. Some minor constraints are observed for parameters associated with the MC statistics[2] or systematics for which shape information is included in the fit. The constraints for the statistical parameters are caused by limited statistics for the W + light-flavoured jets sample used to describe this background.

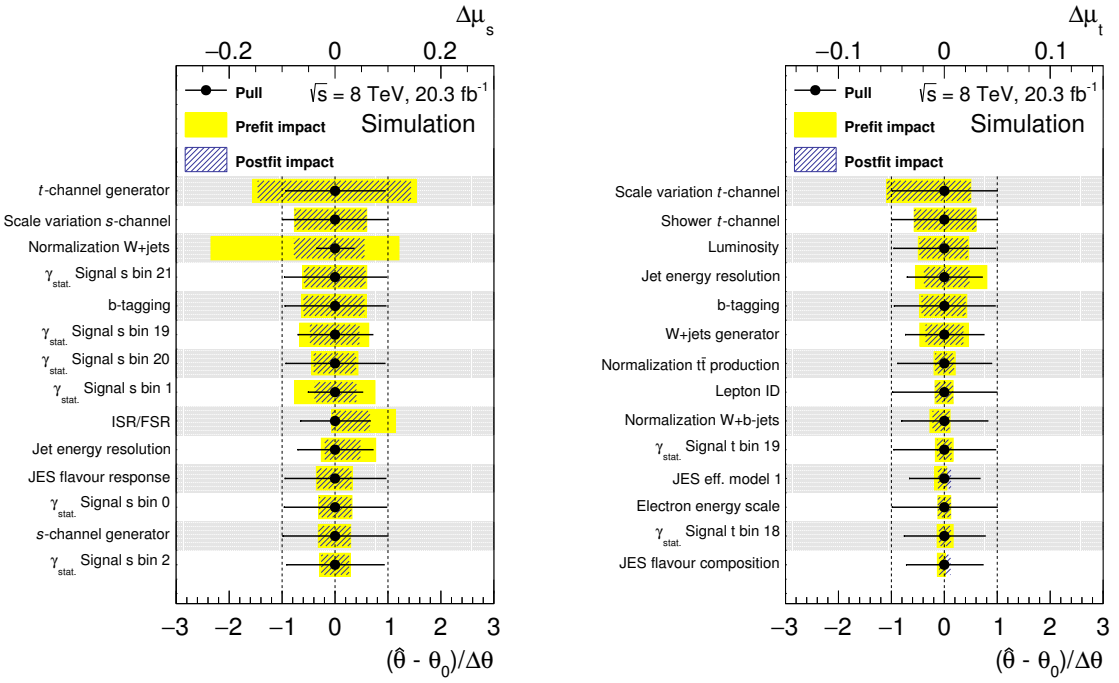

(a) Pulls and impact $\Delta\mu$, s-channel

(b) Pulls and impact $\Delta\mu$, t-channel

Figure 9.2.: Maximum likelihood fit results for selected nuisance parameters used in the fit to the Asimov data. The parameters corresponding to the statistical uncertainty of a certain bin are denoted as $\gamma_{\text{stat.}}$. Furthermore, the prefit and postfit impact of the nuisance parameters on (a) the s-channel signal strength μ_s and (a) t-channel signal strength μ_t are shown. The entries are ordered by their postfit impact.

In addition to the pulls, the prefit and postfit impact $\Delta\mu$ of a certain nuisance parameter on the signal strength parameters is displayed in Fig. 9.2. In order to determine the prefit or postfit impact, a second fit is performed for which the nuisance parameter in question is fixed to $\theta = \hat{\theta} \pm 1\sigma$. The difference between the signal strength parameters in those two fits defines the impact $\Delta\mu$. The prefit impact is obtained by a variation of ± 1, while for the postfit impact, the variation is performed using the parameter uncertainty from the global fit. The nuisance parameters listed in Fig. 9.2 are ordered by their postfit impact. For unconstrained nuisance parameters,

[2]These parameters are denotes as "$\gamma_{\text{stat.}}$ Signal s|t bin X", where 's|t' indicates the s-channel or t-channel signal region and 'X' denotes the bin of the discriminant distribution, starting with 0.

the prefit and postfit impact are equal. The postfit impact is reduced for the nuisance parameter corresponding to the W+jets normalization as expected. The impact on the s-channel signal strength parameter in Fig. 9.2 is asymmetric. The reason is that for the downward variation, the ISR/FSR parameter only changes the normalization of the $t\bar{t}$ background contribution, while for the upward variation also shape variations are taken into account. This leads to the asymmetric impact on the signal strength parameter. The pulls as well as the prefit and postfit impact for the remaining nuisance parameters can be found in [ATL16a].

The correlation matrix for the fit to the Asimov data is presented in Fig. 9.3. Only parameters which exhibit a correlation with any other parameter larger than 32 % are shown. The correlation between the two signal strength parameters μ_s and μ_t is about 6 %. The normalization of the W+jets background contribution in the s-channel signal region and the normalization of W+b-flavoured jets in the t-channel signal region are highly correlated. This correlation is expected as the W+jets contribution in the s-channel signal region is dominated by W boson production with b-flavoured jets. In addition, the signal strength parameters are highly correlated with the modelling uncertainties, which are also the systematics uncertainties with the largest impact on the signal strength parameters.

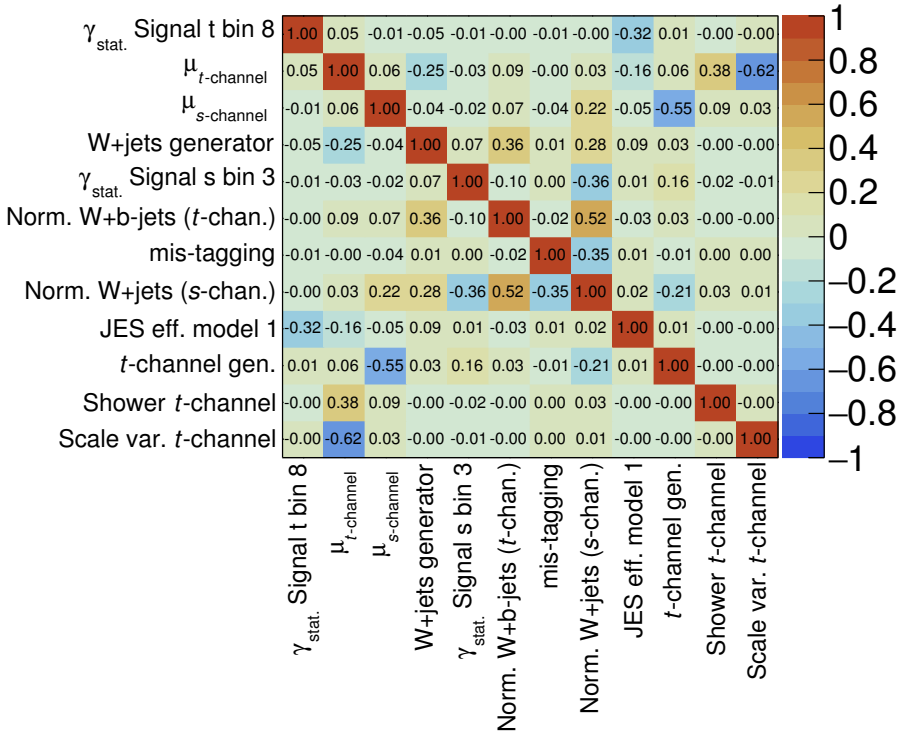

Figure 9.3.: Correlation matrix of the parameters of interest and all nuisance parameters of the maximum likelihood fit to the Asimov data. Only parameters which have at least one correlation of more than 32% are shown, as most pairs of parameters are only weakly correlated.

Real Data

After verifying the modelling in the different regions and checking the likelihood fit using the Asimov data, the analysis is unblinded and the fit to the real data distribution is performed. The best estimators for the signal strength parameters are given in Tab. 9.2.

Table 9.2: Results for the signal strength parameters and their 1σ interval for the fit to real data. The uncertainty definitions are the same as in Tab. 9.1.

	μ_s	μ_t
Parabolic unc.	0.94 ± 0.32	0.972 ± 0.075
MINOS	$0.94^{+0.33}_{-0.32}$	$0.972^{+0.083}_{-0.067}$

The 1σ, 2σ and 3σ contours of the likelihood function as well as the best fit result and the SM prediction are shown in Fig. 9.4. The observed signal strengths are compatible with the SM prediction within the 1σ contour.

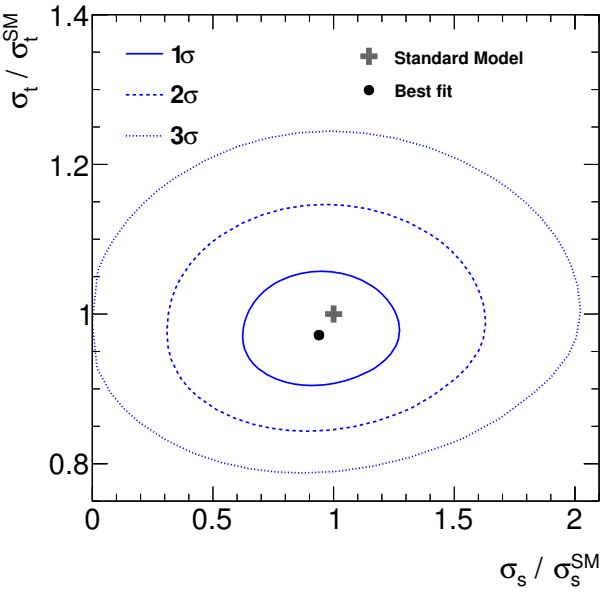

Figure 9.4: The 1σ, 2σ and 3σ contour of the likelihood function as a function of the signal strength parameters for real data. The fit result for the signal strength parameters (dot) is compatible within their uncertainty with the SM prediction (cross).

The pulls of the nuisance parameters with the largest postfit impact on the signal strength parameters are depicted in Fig. 9.5. The pulls as well as the prefit and postfit impact for the remaining nuisance parameters can be found in App. B. Most of the nuisance parameters are unconstrained and their deviations from $\theta_0 = 0$ are compatible within their uncertainties. The largest deviation are observed for the nuisance parameters associated with the single-top t-channel generator and the W+jets generator. In both cases, the variation of these parameters corresponds to a change of the normalization of the corresponding processes. Furthermore, the pulls for these two systematics are similar to the ones found in the previous s-channel

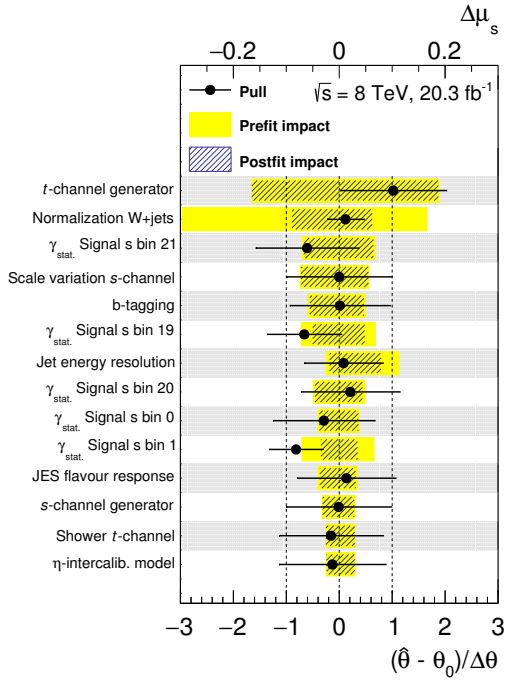

(a) Pulls 1–14 and impact $\Delta\mu$, s-channel

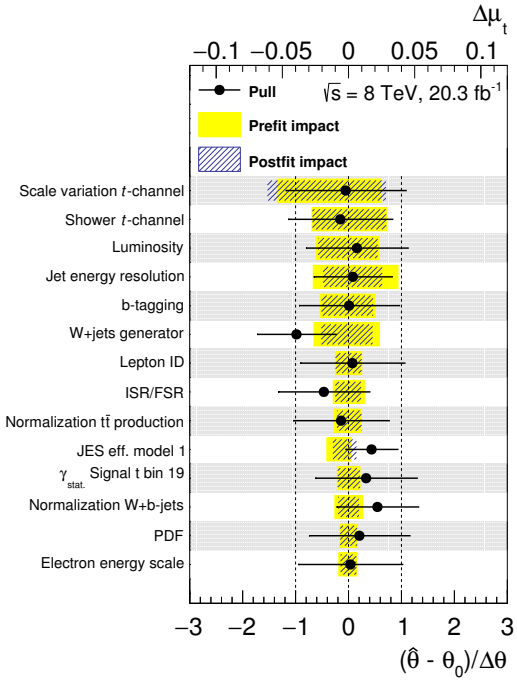

(b) Pulls 1–14 and impact $\Delta\mu$, t-channel

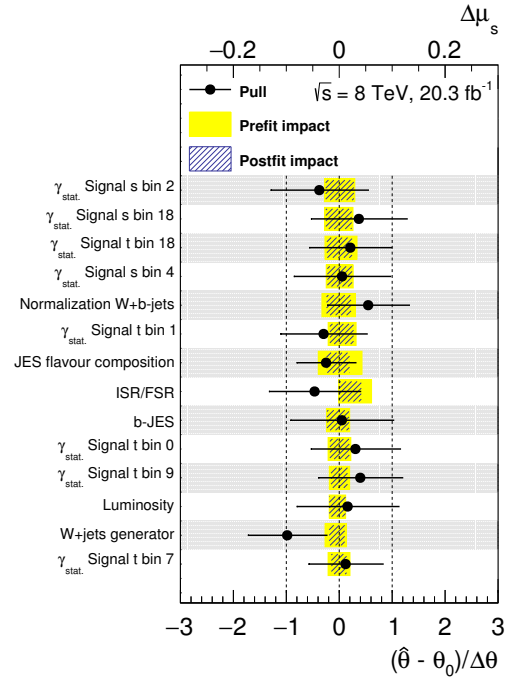

(c) Pulls 15–28 and impact $\Delta\mu$, s-channel

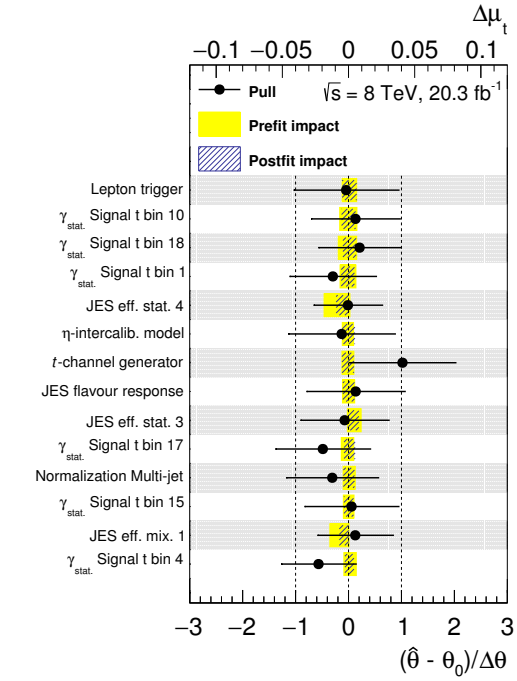

(d) Pulls 15–28 and impact $\Delta\mu$, t-channel

Figure 9.5.: Maximum likelihood fit results for selected nuisance parameters used in the fit to the data distribution. Entries denoted with $\gamma_{\text{stat.}}$ represent the statistical uncertainty of the given bin. Moreover, the panels (a) and (c) show the impact of the nuisance parameters on the s-channel signal strength, while the panels (b) and (d) include the impact on the t-channel signal strength. The entries for each signal strength parameter are ordered by their postfit impact.

analysis [ATL16a]. The observed constraint of the W+jets normalization parameter in the s-channel signal region is expected. It is caused by the large input uncertainty of 60 %, as discussed previously. The parameters describing the W+jets background in the t-channel signal region are less constrained as the uncertainty for these two parameters is 20 %. The nuisance parameters associated with the MC statistics are adjusted by the fit to match the bin-by-bin fluctuations in the data distribution. A similar behaviour was also observed in the previous s-channel analysis, especially for nuisance parameters associated with bins with limited W+light-flavoured jets contribution.

The correlation matrix for the signal strength parameters and several nuisance parameters is shown in Fig. 9.6. As for the Asimov data, only parameters for which at least one correlation coefficient is larger than 32 % are shown. Sizeable correlations are observed between the signal strength parameters and the signal modelling uncertainties. Moreover, the nuisance parameter associated with the W+jets normalizations feature high correlation coefficients. As expected, a positive correlation coefficient is observed

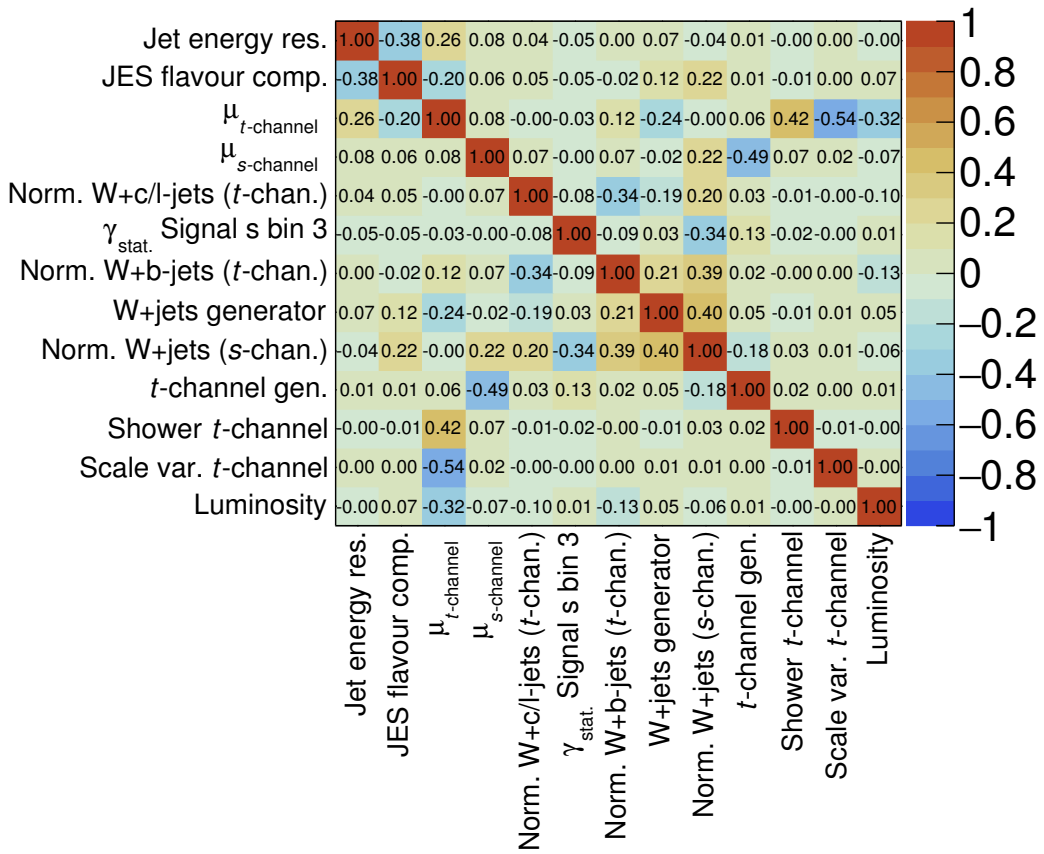

Figure 9.6.: Correlation matrix of the parameters of interest and all nuisance parameters of the maximum likelihood fit to real data. Only parameters which have at least one correlation of more than 32% are shown, as most pairs of parameters are only weakly correlated.

between the two normalizations corresponding to the W+b-flavoured jets across the two signal regions, while the two normalization parameters for W+jets in the t-channel region are anti-correlated. The nuisance parameters for the jet energy resolution and the jet flavour composition, one of the jet energy scale components, exhibit a sizeable correlation. This is likely to originate from the shape uncertainties, which are considered for these two systematics. The observed correlation between the signal strength parameters is 8 % and close to the expected correlation. A priori, one would expect a negative correlation between the signal strength parameters. The reason for a positive correlation is the large impact from the systematic uncertainties. In fact, the s-channel signal strength parameter and the nuisance parameter corresponding to the t-channel generator uncertainty are anti-correlated. The reason is that the t-channel generator uncertainty is one of the dominant systematic uncertainties to the s-channel cross section measurement.

9.2.2. Break-down of Uncertainties

The different sources of systematic uncertainties are ranked by their contribution to the overall uncertainty and listed in Tabs. 9.3 and 9.4 for the s-channel and t-channel signal strength parameter, respectively. Each entry in these tables correspond to the relative postfit impact on the signal strength. The contributions to the impact from the upward and downward variation of the nuisance parameter are averaged. The numbers given in the brackets correspond to the expected uncertainty from the fit to the Asimov data. The individual contributions from MC statistics parameters as well as the nuisance parameters associated with the jet energy scale components are added in quadrature and only the sum is provided in the tables. The contribution from finite amount of data is extracted in a separate maximum likelihood fit for which no systematic uncertainties are considered.[3]

9.2.3. Discriminant Distributions

The results of the maximum likelihood fit are presented in Fig. 9.7. The signal and background processes for each discriminant distribution are scaled according to the parameter values obtained in the fit to the observed data distribution. This includes in particular the parameter values for nuisance parameters associated with systematic uncertainties. The uncertainty band shown in Fig. 9.7 corresponds to the combined uncertainty of all signal and background processes. All correlations between the nuisance parameters are included. The observed data distribution is well modelled by the signal and background samples obtained from MC simulations and data-driven methods.

[3]Only the normalization uncertainty for the background processes are considered.

Table 9.3: Break-down of systematic uncertainties for the s-channel signal strength using the real data set. The expected results from the fit to the Asimov data are given in brackets. The relative uncertainty reflects the impact of each systematic on the signal strength parameter. The entries for the jet energy scale and for the MC statistics denotes the quadratic sum of all individual components for these systematics. The total uncertainty contains several minor contributions which are all smaller than 1.5%.

Type	Rel. uncertainty [%]	
Data statistics	21.1	(22.8)
t-channel generator	18.8	(14.5)
MC statistics	12.7	(11.1)
W+jets normalization	8.6	(7.2)
s-channel scale variation	6.8	(6.8)
Jet energy scale	6.1	(5.3)
b-tagging	5.4	(5.8)
Jet energy resolution	5.2	(3.4)
s-channel generator	3.2	(3.0)
t-channel shower modelling	2.9	(1.9)
ISR/FSR	2.2	(3.6)
Luminosity	1.6	(2.0)
W+jets generator	1.6	(0.6)
Other	$<$ 1.5	–
Total	34.0	(30.0)

Table 9.4: Break-down of systematic uncertainties for the t-channel signal strength using real data. The expected results obtained by a fit to the Asimov data are given in brackets. Each entry denotes the contribution of each systematic to the total uncertainty of the t-channel signal strength parameter. The total uncertainty contains several minor contributions which are all smaller than 0.8%. For the entries of the jet energy scale and the MC statistics, the individual contributions are added quadratically and only the sum is provided.

Type	Rel. uncertainty [%]	
Data statistics	3.5	(3.5)
t-channel scale variation	4.6	(4.0)
t-channel shower modelling	2.9	(2.9)
Luminosity	2.3	(2.3)
Jet energy resolution	2.3	(2.2)
b-tagging	2.0	(2.1)
W+jets generator	2.0	(1.8)
Jet energy scale	1.6	(1.3)
MC statistics	1.6	(1.3)
Lepton identification	1.0	(0.8)
ISR/FSR	1.0	(0.5)
$t\bar{t}$ normalization	1.0	(0.9)
W+jets normalization	0.8	(0.8)
Other	$<$ 0.8	–
Total	7.7	(7.3)

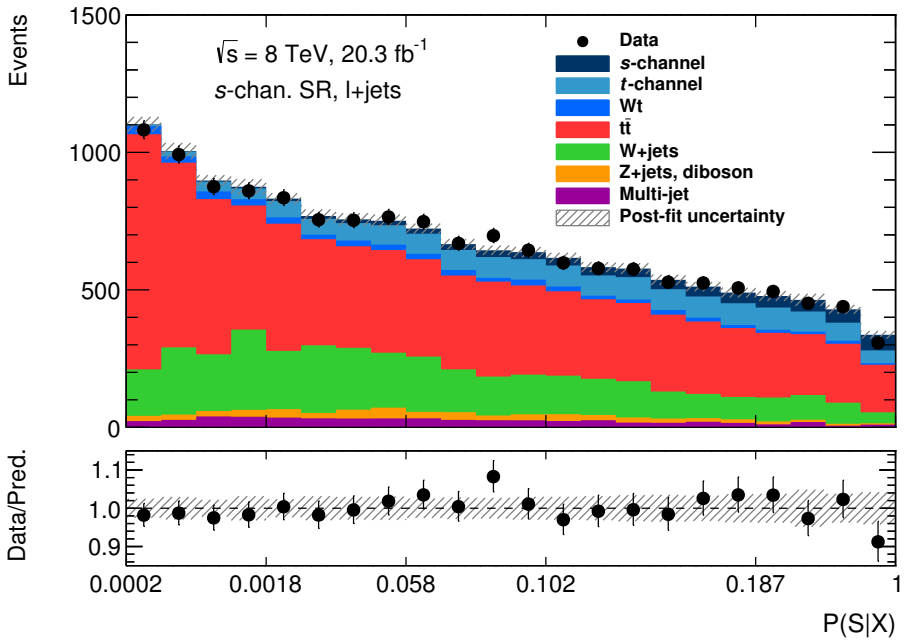

(a) ME discriminant, s-channel signal region

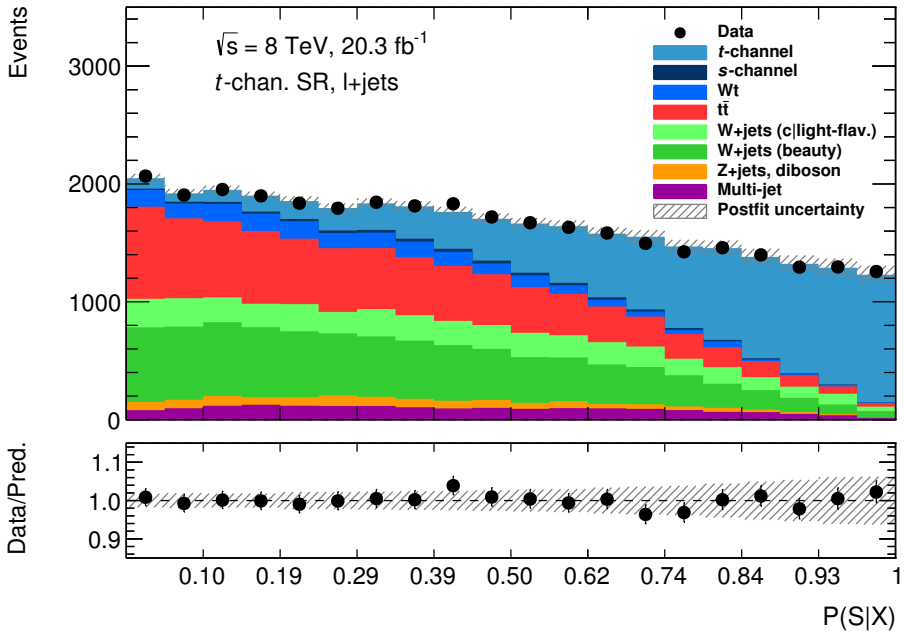

(b) ME discriminant, t-channel signal region

Figure 9.7.: Distributions for the matrix element discriminants in the two signal regions. (a) s-channel signal region, (b) t-channel signal region. All samples are scaled by the fit result utilizing all fit parameters. The hatched bands indicate the complete uncertainty of the postfit result including all correlations.

9.2.4. Comparison to Existing ATLAS Analyses

The results presented in this note are extracted from a combined fit of the single-top s-channel and t-channel cross section to data. ATLAS already published two separate analyses for each channel, one for the s-channel [ATL16a] and one for the t-channel [ATL17a]. The cross section values for these two publications, the result of this analysis as well as the theoretical predictions in NLO QCD and NNLO QCD are summarized in Tab. 9.5.

Analysis / Theory	σ_s [pb]	$\Delta\sigma_s/\sigma_s$ [%]	σ_t [pb]	$\Delta\sigma_t/\sigma_t$ [%]
s|t-combination	$4.9^{+1.7}_{-1.7}$	$^{+35}_{-34}$	$82.32^{+7.0}_{-5.5}$	$^{+8.5}_{-6.9}$
s-channel [ATL16a]	$4.8^{+1.8}_{-1.6}$	$^{+38}_{-33}$	–	–
t-channel [ATL17a]	–	–	$89.6^{+7.1}_{-6.3}$	$^{+7.9}_{-7.0}$
HATHOR (NLO) [Kan$^+$15]	$5.24^{+0.22}_{-0.20}$	$^{+4.2}_{-3.8}$	$84.69^{+3.76}_{-3.23}$	$^{+4.4}_{-3.8}$
NNLO [BCM14]	–	–	$83.9^{+0.3}_{-0.8}$	$^{+0.4}_{-1.0}$

Table 9.5.: Comparison of ATLAS measurement results for the single-top s-channel and t-channel cross section and theory predictions in NLO QCD and NNLO QCD.

For the s-channel measurement presented in [ATL16a], the expected significance is 3.9σ and the observed one is 3.2σ. In order to obtain an estimate of the significance of the s-channel signal strength for the analysis presented in this thesis, the fit model needs to be altered. Instead of using an unconstrained parameter for the t-channel normalization, a Gaussian constrained term for the t-channel normalization parameter is added to the likelihood model. The width of the Gaussian corresponds to the observed uncertainty of 7.7 %. As before, the fit to the observed data distribution is performed simultaneously in the s-channel and t-channel signal region. Subsequently, the significance for the s-channel signal strength parameter is determined by using the asymptotic formulae described in [ATL16a]. The expected and observed significance is 3.5σ and 3.0σ, respectively. Both results are slightly lower than in [ATL16a]. However, it should be noted that in contrast to the 7.7 % uncertainty for the t-channel normalization, an uncertainty of only 4 % was used in [ATL16a]. Moreover, the fit model for the combined analysis does not include a dedicated W+jets region in the fit. Such a region was used to constrain the large W+jets background contribution. The t-channel signal region can only partially compensate the missing W+jets region, because three separate nuisance parameters are used for the W+jets background normalizations. Nevertheless, the observed significance is close to the already published result. Moreover, the central values are almost identical, despite the fact that different theoretical predictions for the single-top s-channel and t-channel cross sections are used in this thesis and [ATL16a]. In this thesis, the cross section predictions provided by the HATHOR programme [Kan$^+$15] are used, while in [ATL16a], the cross section predictions are taken from [Kid10a, Kid11].

Both measurements for the single-top t-channel listed in Tab. 9.5 agree with the SM prediction within their uncertainties. Furthermore, the two measurements are included by each others 2σ interval. However, both measurements are not independent, because they use the same data set. In contrast to the analysis presented in this thesis, the analysis in [ATL17a] uses a different and much looser event selection. The cut thresholds on the lepton and jet transverse momentum are lower than the ones used in this analysis. Furthermore, the di-lepton veto only uses additional leptons with an opposite charge to the prompt isolated lepton and a transverse momentum larger than $p_{\mathrm{T}} > 10\,\mathrm{GeV}$. Especially the di-lepton veto leads to a different selection efficiency between the two analyses. In addition, in neither of the two analyses, a (possible) difference in the efficiency that may be found in data and simulation is corrected. Furthermore, an alternative data-driven method to estimate the multi-jet background is used in [ATL17a]. Instead of the matrix element method, a multivariate technique is employed in [ATL17a] to discriminate signal events from background. Finally, the statistical analysis for extracting the single-top t-channel cross section differs, too. The W+jets background contribution is separated by the charge of the lepton in the event and parametrized by two parameters in the employed statistical model. The normalization of the Z+jets, diboson and multi-jet backgrounds are fixed to their estimated value obtained from MC simulations or the data-driven method. In addition, the systematic uncertainties are evaluated by pseudo-experiments. Therefore, a thorough comparison between both analyses would be a very complex task. It is in any way beyond the scope of this thesis.

10. Interpretation

Although the SM is very successful in describing the current experimental data, it is not yet a final description of nature. There are many issues, such as the origin of dark matter or dark energy that currently lack a sufficient description within the SM. Furthermore, there are many arbitrary parameters, such as the quark masses and mixing angles, that can not be derived from the theory itself, but must be measured in experiments. All these open issues drives the search for new physics beyond the standard model.

The search for new physics can be performed in two ways. One the one hand, many analyses search for new particles. These searches are driven by specific models, for example supersymmetry (SUSY) or models that predict more than one Higgs boson [TY00]. So far, no evidence for new particles beyond the SM has been found. Instead, limits on the mass of those potential new particles are set and reach up to 2 TeV in some cases [ATL17d]. On the other hand, one can search for new interactions of SM particles. These new interactions have to be formulated in terms of a new model extending the existing one. The requirements of such an extension are manifold. First of all, such an extension should respect the symmetries of the SM, namely Lorentz invariance and gauge symmetries. Furthermore, all cross sections that can be calculated within the model should not exceed the unitarity bound. These two properties are satisfied by a quantum field theory. The SM itself has been tested with a high accuracy and involves calculations in higher orders of perturbation theory. Therefore, the new physics model should allow calculations of radiative corrections in any order in the SM model and ideally in any order of the new physics interactions. More importantly, the extension should also contain the SM in an appropriate limit. A model independent approach, that fulfils all these requirements is an effective field theory, which will be described in more detail in the next section. [WZ14, Deg$^+$13]

10.1. Effective Field Theory

An effective field theory [WZ14, Deg$^+$13] of the SM is also a quantum field theory and contains an energy scale Λ, which can be interpreted as the scale at which new physics effects might be observed directly. If this energy scale is much larger than the typical centre-of-mass energy of the relevant hard process, the effects of physics beyond the SM can be parametrized by higher-dimension operators. All operators in

the SM, that are compatible with its gauge symmetries, have mass dimension four or less. The operators associated with the new physics interactions are products of SM fields and are suppressed by inverse powers of the scale Λ. The effective Lagrangian reads

$$\mathscr{L}_{\text{eff}} = \mathscr{L}_{\text{SM}} + \frac{1}{\Lambda}\mathscr{L}_1 + \frac{1}{\Lambda^2}\mathscr{L}_2 + \dots \tag{10.1}$$

The SM Lagrangian is denoted as $\mathscr{L}_{\text{SM}}$, while the new physics interactions of mass dimension five and six are contained in the Lagrangians $\mathscr{L}_1$ and $\mathscr{L}_2$. This expansion can be continued to any order in Λ^{-1}. However, for each order in Λ^{-1} that is added to Eq. 10.1, new operators may need to be added as well. From Eq. 10.1 follows that the SM is recovered in the limit $\Lambda \to \infty$. There is only one operator of mass dimension five for one generation of fermions that can be build from SM fields. This operator leads to Majorana masses for neutrinos [Wei79, BW86]. The current limits for the neutrino masses suggests that the scale associated with such an effective theory would be around $10^{15}\,\text{GeV}$, which is not within the energy range of the LHC. It is therefore neglected in this thesis. The dimension six operators can be divided into two classes. The first class consists of operators that violate baryon number and lepton number. The operators from this class that involve light quarks and leptons are constrained by experimental data of the proton decay, and these operators will not be discussed in this thesis. The second type of operators conserve baryon and lepton number and are less constrained. The effective field theory of the SM that conserves baryon number and lepton number can be written as

$$\mathscr{L}_{\text{eff}} = \mathscr{L}_{\text{SM}} + \sum_i \frac{c_i}{\Lambda^2} O_i + \mathcal{O}\left(\frac{1}{\Lambda^4}\right). \tag{10.2}$$

The operators of the new interactions are denoted as O_i and a dimensionless Wilson coefficient c_i is associated with each of them. The next higher order term in Eq. 10.2 is of the order of Λ^{-4}, because all operators that are proportional to an odd power of $1/\Lambda$ do not conserve baryon or lepton number [Deg+13].

An example for an effective field theory is given by adding an operator for a new heavy Z' boson to the SM Lagrangian. The Feynman diagrams that are associated with such a new interaction are depicted in Fig. 10.1. In this example, the Z' boson interacts with the SM fermion fields. For energies above the new physics scale Λ, the new particle can be observed directly. If the energies at the LHC are not sufficient enough, the effects of this new particle can still be observed indirectly. The exchange of a Z' boson would appear as a four-fermion interaction. The dimension-six operator associated with this interaction can be written as a product of four fermion fields, each of them having a mass dimension of 3/2. The propagator of the Z' boson in Fig. 10.1 is proportional to $1/m^2_{\text{Z}'}$ if the momentum of the Z' is neglected. Thus the scale Λ can be associated with the mass of the Z' boson, while the coefficient c_i defines the coupling strength at the four-fermion vertex.

The effective field theory description of the four-fermion interaction is the equivalent of Fermis theory of the weak interaction. This is also an effective theory, which is a

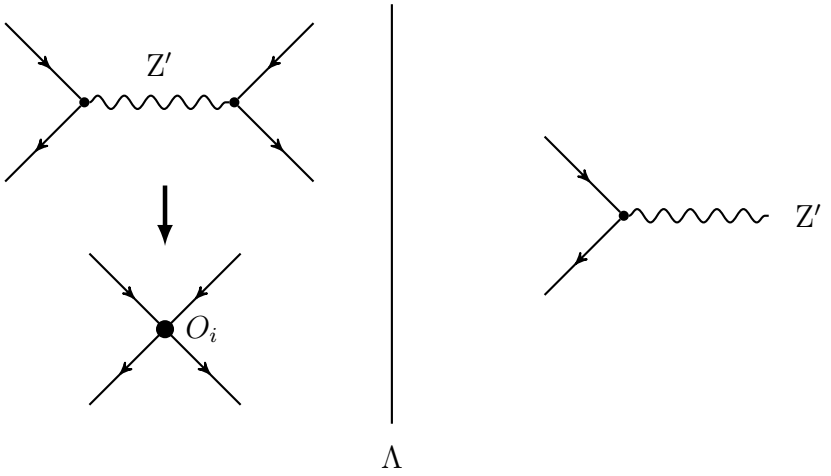

Figure 10.1.: Possible Feynman diagrams for an interaction of a Z′ boson with SM fermions. The Z′ boson can be observed directly for energies above the new physics scale Λ. For energies below that scale, the exchange of a Z′ boson can be described by an effective four-fermion vertex interaction. The coupling strength at this vertex is proportional to the coefficient c_i associated with the operator O_i. Figure adapted from [ZW10].

good approximation for weak interactions at energies below the mass of the W boson. Therefore, also the effective field theory discussed above is only valid up to the scale of the new physics, Λ. Unfortunately, this scale Λ can not be measured, only the ratio c_i/Λ. Similar, the effective theory of weak interactions is sufficient to describe the decay of the muon, $\mu \to e\nu\bar{\nu}$, for energies below m_W. The effective coupling at this four-fermion vertex is given by

$$\frac{G_F}{\sqrt{2}} = \frac{g^2}{8m_W^2}. \tag{10.3}$$

However, only the ratio of the coupling g to the scale, m_W, is revealed. Once the underlying theory of electro-weak interactions was established and with it information on the coupling g, predictions for the mass of the W and Z boson were possible. This analogy can also be used to motivate the measurements of these effective couplings, or to be more precise, of the ratio of c_i/Λ. The parameters of the effective field theory can be interpreted as masses or couplings in other new physics models. [Deg+13, WZ14, ZW11, Con+16]

10.1.1. Operators and Top-Quark Physics

Many dimension-six operators can be build from SM fields. However, not all of these operators are independent. The first attempt to provide a complete set of operators was made by Buchmüller and Wyler [BW86], who used the equation of motions

to limit the number of gauge-invariant dimension-six operators to 80. This list of operators was further reduced by different groups [Grz+04, Agu09] and a complete basis contains not more than 59 operators for one generation [Grz+10]. In this thesis, I will use the notation by Zhang and Willenbrock [ZW11, WZ14], which they refer to as the Buchmüller and Wyler basis.

The top-quark is an ideal candidate to study new physics interactions. It is much heavier than all other quarks and leptons in the SM and new physics at higher scales might be detectable in low-energy interactions involving top-quarks. Given the complete basis of 59 operators for one generation, 15 dimension-six operators can be identified to be relevant to top-quark physics. These operators have effects on the top-quark decay, top-quark pair production and single top-quark production. An analysis of all operators at once is not within the scope of the analysis presented in this thesis.[1] The focus of the remaining parts of this thesis will be on single top-quark production and only a subset of the 15 dimension-six operators will be discussed. A detailed discussion of all 15 operators is given in [ZW11].

The following operators contribute to single top-quark production via the s and t-channel:

$$O_{\phi \mathrm{q}}^{(3)} = i(\phi^+ \tau^I D_\mu \phi)(\bar{q}\gamma^\mu \tau^I q), \tag{10.4}$$

$$O_{\mathrm{tW}} = (\bar{q}\sigma^{\mu\nu}\tau^I t)\tilde{\phi} W^I_{\mu\nu}, \tag{10.5}$$

$$O_{\mathrm{qq}}^{(1,3)} = (\bar{q}^i \gamma_\mu \tau^I q^j)(\bar{q}\gamma^\mu \tau^I q). \tag{10.6}$$

The notation is taken from [ZW11]. The first two operators modify the SM Wtb vertex and the coefficients of these operators are complex. The imaginary part of the coefficient $O_{\phi \mathrm{q}}^{(3)}$ can be removed using the equations of motion. The interference between the SM Lagrangian and the operator $O_{\phi \mathrm{q}}^{(3)}$ simply rescales the Wtb vertex by a factor of $(1 + \frac{c_{\phi \mathrm{q}}^{(3)} v^2}{\Lambda^2 V_{\mathrm{tb}}})$. Here, v denotes the vacuum expectation value for the Higgs field of $v = 246\,\mathrm{GeV}$. Contributions from this operator to single top-quark production do not affect any kinematic distribution. This is different for the operators O_{tW} and $O_{\mathrm{qq}}^{(1,3)}$. In this analysis the operator O_{tW} is neglected in order to simplify the evaluation presented in Secs. 10.2–10.6. The third operator, $O_{\mathrm{qq}}^{(1,3)}$, adds a four-quark interaction to the s-channel and t-channel. There exists also another possible four-quark operator that can contribute, but it can be expressed as a linear combination of $O_{\mathrm{qq}}^{(1,3)}$ and other four-quark operators using the Fierz identity. These additional four-quark operators have different isospin and colour structures and do not contribute neither to s-channel nor t-channel single top-quark production [ZW11]. The possible Feynman diagrams for the s-channel and t-channel are depicted in Fig 10.2.

The associated Wt production gets contributions from the $O_{\phi \mathrm{q}}^{(3)}$ and O_{tW} operators,

[1] However, this analysis is intended to be the basis for more complex EFT interpretations in the future.

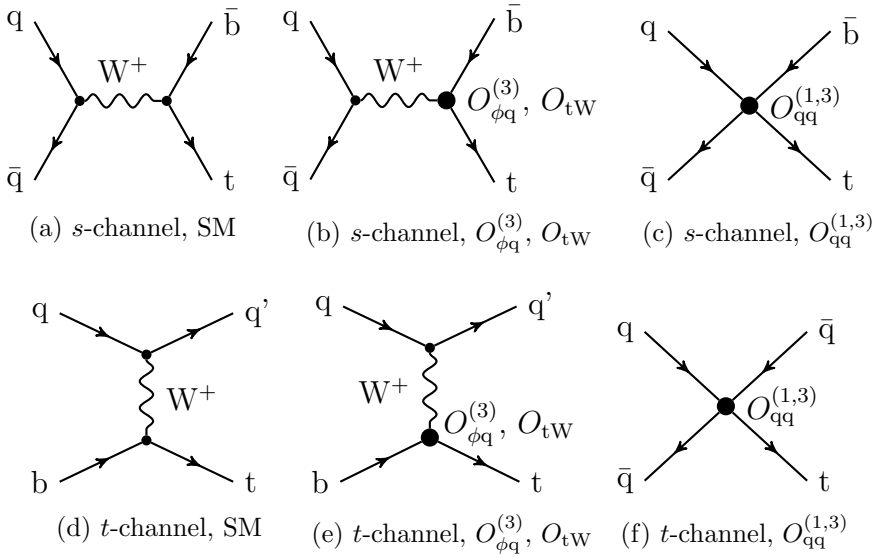

(a) s-channel, SM (b) s-channel, $O_{\phi q}^{(3)}$, O_{tW} (c) s-channel, $O_{qq}^{(1,3)}$

(d) t-channel, SM (e) t-channel, $O_{\phi q}^{(3)}$, O_{tW} (f) t-channel, $O_{qq}^{(1,3)}$

Figure 10.2.: Feynman diagrams for single top-quark production via (a)–(c) s-channel and (d)–(f) t-channel. The diagrams (a), (d) correspond to the SM amplitude, while (b), (e) and (c), (f) show the correction from the $O_{\phi q}^{(3)}$, O_{tW} and $O_{qq}^{(1,3)}$ operators, respectively. [ZW11]

as well as from the "chromomagnetic moment" operator O_{tG}

$$O_{tG} = (\bar{q}\sigma^{\mu\nu}\tau^I t)\tilde{\phi}G^A_{\mu\nu}. \tag{10.7}$$

This operator modifies the gtt coupling and its contribution is neglected in the vertex-function approach [ZW10] as well as in this thesis. The Feynman diagrams for Wt production are shown in Fig. 10.3. [ZW11]

All operators related to top-quark pair production are neglected, since the measurement of the s-channel and t-channel single top-quark production might not be very sensitive to these operators. Ideally, all 15 operators are determined in a global fit, for example

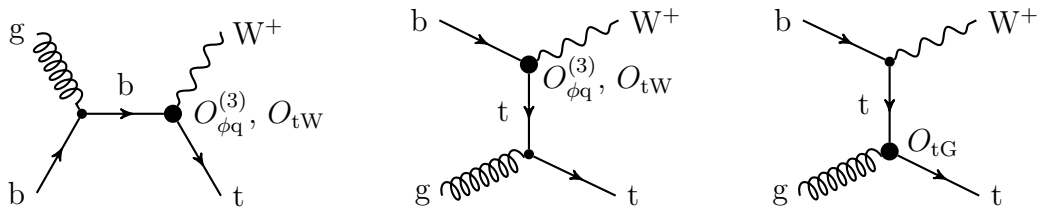

(a) Wt, s-channel, $O_{\phi q}^{(3)}$, O_{tW} (b) Wt, t-channel, $O_{\phi q}^{(3)}$, O_{tW} (c) Wt, t-channel, O_{tG}

Figure 10.3.: Feynman diagrams for the associated Wt production. Only the diagrams for the correction due to the (a), (b) $O_{\phi q}^{(3)}$, O_{tW} operators and (c) O_{tG} operator are shown. The SM diagrams are depicted in Fig. 2.4. [ZW11]

as in [Buc+15][2]. The limits that are obtained by neglecting operators are usually more restrictive than the limits extracted from a global fit using all operators. It will be pointed out in the next sections, that such fits need to include acceptance corrections that allow for a consistent interpretation of SM measurements in the context of effective field theories. In most cases, these corrections can only be estimated by the experimental group that performed the measurement. The focus of the next sections will be on these acceptance corrections and how they can be estimated. A tool for the combination of several measurements, which is also used to extract limits for the two couplings $c_{\phi q}^{(3)}$ and $c_{qq}^{(1,3)}$ is introduced in Sec. 10.6.1.

10.1.2. Event Generation

The effective field theory described in [ZW11] is implemented in LO QCD in the MadGraph event generator package. An UFO [Deg+12] model was generated by using FeynRules [Chr+11] and contains all 15 operators relevant to top-quark physics. Subsequent tests [Deg15] were performed to validate the model, such as comparing the cross section predictions made with the model with the calculations in [ZW11].

In order to generate events, the squared amplitude including the contribution from the new operators has to be evaluated:

$$|\mathcal{M}_{\mathrm{SM}} + \mathcal{M}_{\Lambda^{-2}}|^2 = |\mathcal{M}_{\mathrm{SM}}|^2 + 2\Re(\mathcal{M}_{\mathrm{SM}} M^*_{\Lambda^{-2}}) + |\mathcal{M}_{\Lambda^{-2}}|^2, \tag{10.8}$$

where $\mathcal{M}_{\mathrm{SM}}$ denotes the SM amplitude and $\mathcal{M}_{\Lambda^{-2}}$ is the $O(1/\Lambda^2)$ amplitude of all the diagrams containing a new physics interactions described by the dimension-six operators. The last term in Eq. 10.8 is proportional to $\mathcal{O}(1/\Lambda^4)$ as it contains the squared amplitudes of two dimension-six operators. This term can be much larger than the interference term due to less constrained operator coefficients, i. e. $c_i^2 \frac{E^4}{\Lambda^4} > c_i \frac{E^2}{\Lambda^2} > 1$. This does not violate the validity of the EFT expansion as long as the expansion in E^2/Λ^2 still converges and $\frac{E^2}{\Lambda^2} < 1$ is satisfied. The contributions from the interference term might be suppressed due to symmetries or kinematics [Bes+16]. Additional contributions of $\mathcal{O}(1/\Lambda^4)$ arise from the interference of dimension-eight operators with the SM. For the validity of the EFT expansion, these contributions must be less than the contributions from dimension-six operators. However, these operators are not part of the model and therefore can not contribute here by definition. Extending the model to dimension-eight operators would require the complete knowledge of all these operators and increase the complexity of the already challenging problem to extract limits for the dimension-six operators. In general, it is expected that dimension-eight operators only add a minor contribution to the result of Eq. 10.8 and that these operators can be neglected. A discussion of situations for which that is not the case can be found in [Con+16]. [MVZ16]

[2]The global fit presented in [Buc+15] neglected all contributions from CP-odd operators, which includes neglecting the imaginary parts of O_{tG} and O_{tW}, because currently there is no evidence for CP-violation in the top-sector beyond the minimal flavour violation assumption.

For the studies presented in the following sections, events have been generated for single-top s and t-channel production using the MadGraph LO QCD model [Deg15]. The configuration of the model in MadGraph allows to set the real and imaginary parts of the coefficients c_i of all 15 operators discussed in [ZW11] independently as well as the new physics scale Λ. The event generation for s-channel events uses MadGraph 2.4.2 with the LO NNPDF 2.3 PDF set, while the top-quark decay is simulated by MadSpin [Art+13, Fri+07]. Single-top t-channel events can be generated using either the five-flavour or four-flavour scheme[3]. The name refers to whether the initial state contains a b-quark or not. A better modelling of the kinematic distributions is achieved by using the four-flavour scheme, in which the b-quark in the initial state originates from a gluon splitting inside the matrix element computation rather than using the b-PDF. Therefore, events are generated using the four-flavour scheme to study kinematic distributions in Secs. 10.3–10.5. When using the four-flavour scheme, it is important to separate s-channel and t-channel contributions. The Feynman diagrams for the t-channel processes of pp $\rightarrow$ tbj [4] are shown in Fig. 10.4. In the SM case, the diagrams in Figs. 10.4(a) and 10.4(c) are associated with the s-channel, while the diagrams in Figs. 10.4(e) and 10.4(g) are counted as t-channel contribution. The same approach is taken for the new physics diagrams. Figures 10.4(f) and 10.4(h) are therefore added to the t-channel contribution in the four-flavour scheme, while the other diagrams (Figs. 10.4(b) and 10.4(d)) have to be excluded from the event generation for single-top t-channel production. The ability to remove Feynman diagrams based on selection rules was only added recently to MadGraph 2.5.2 and this version is used for generating single-top t-channel events with the same PDF set as for the s-channel event generation. Due to technical limitations concerning the diagram removal process, MadSpin can not be used for the top-quark decay. Instead the top-quark decay is simulated by MadGraph directly. Spin correlations of the top-quark decay products are still included. For both s-channel and t-channel events, only leptonic final states (including τ-leptons) are considered for the top-quark decay. For all studies presented in this thesis, the new physics scale was set to $\Lambda = 2\,\text{TeV}$.

10.2. Cross-Section-to-Couplings Relations

The first step towards an interpretation of the measurement performed in Sec. 9 within the context of an effective field theory is to determine the dependence between the cross section and the couplings c_i. As described in the previous section, any measurement is only sensitive to the ratio of c_i/Λ and it is common to use the $\bar{c}$-notation, which is defined as

$$\bar{c} = \frac{c_i v^2}{\Lambda^2}. \tag{10.9}$$

[3]The Feynman diagrams in Fig. 10.2(d)–10.2(f) correspond to the five-flavour scheme.
[4]The character j indicates a quark or gluon

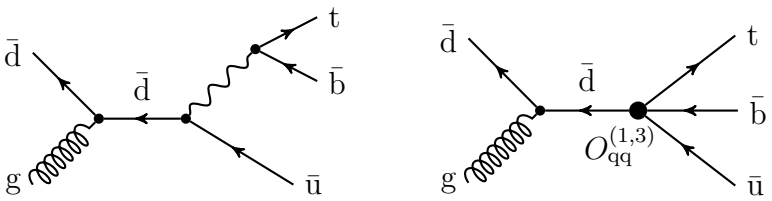

(a) s-channel, SM

(b) s-channel, EFT

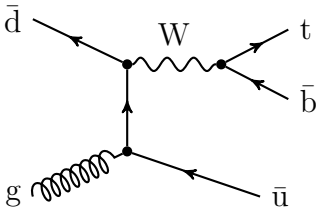

(c) s-channel, SM

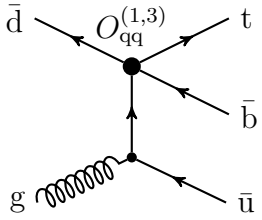

(d) s-channel, EFT

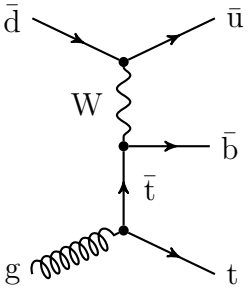

(e) t-channel, SM

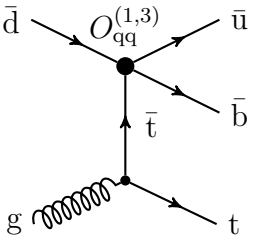

(f) t-channel, EFT

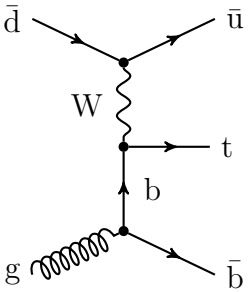

(g) t-channel, SM

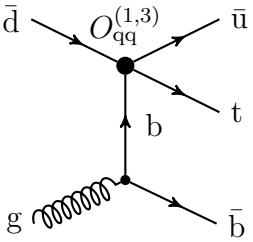

(h) t-channel, EFT

Figure 10.4.: Feynman diagrams for s and t-channel single top-quark production in the four-flavour scheme. The diagrams on the left show the SM case: (a) and (c) correspond to the s-channel production, while the diagrams (e) and (g) are associated with the t-channel production. The diagrams on the right side are obtained by replacing the W boson line by the effective four-fermion vertex interaction of the operator $O_{qq}^{(1,3)}$. Therefore, the diagrams (b) and (d) are defined as s-channel contribution and (f) and (h) as t-channel contribution.

The advantage of this notation is that it is independent from the choice of the value for the new physics scale Λ. In some sense, it is the equivalent to G_F, which defines the coupling strength at the four-fermion vertex in the effective theory of weak interactions.

The MadGraph model described in Sec. 10.1.2 is used to obtain cross section predictions at $\sqrt{s} = 8\,\mathrm{TeV}$ as a function of the two effective couplings $\bar{c}_{\phi\mathrm{q}}$ and $\bar{c}_{\mathrm{qq}}$. The parameter space for the effective couplings is defined by a rectangular grid in the $\bar{c}_{\phi\mathrm{q}}$–$\bar{c}_{\mathrm{qq}}$ plane. The grid consists of 72 points and its specifications are given in Tab. 10.1. For each grid point, the cross section is determined by a sample of 50 000 events generated with MadGraph, which corresponds to a statistical precision of about 0.5 %.

Table 10.1: Settings for the rectangular grid in the $\bar{c}_{\phi\mathrm{q}}$–$\bar{c}_{\mathrm{qq}}$ plane used for the cross section calculation. The grid consists of 72 sampling points.

	minimum	step size	maximum
$\bar{c}_{\phi\mathrm{q}}$	−0.303	0.061	+0.182
$\bar{c}_{\mathrm{qq}}$	−0.076	0.015	+0.030

The relation between the inclusive cross section and the effective couplings is extracted by a fit to the predicted cross section. The most general function to describe the cross section as a function of $\bar{c}_{\phi\mathrm{q}}$ and $\bar{c}_{\mathrm{qq}}$ is given by

$$\sigma_\mathrm{ch}^\mathrm{EFT} = \sigma_\mathrm{ch}^\mathrm{SM}\left(1 + \alpha_{\phi\mathrm{q}}^\mathrm{ch}\,\bar{c}_{\phi\mathrm{q}} + \beta_{\phi\mathrm{q}}^\mathrm{ch}\,\bar{c}_{\phi\mathrm{q}}^2 + \alpha_{\mathrm{qq}}^\mathrm{ch}\,\bar{c}_{\mathrm{qq}} + \beta_{\mathrm{qq}}^\mathrm{ch}\,\bar{c}_{\mathrm{qq}}^2 + \gamma^\mathrm{ch}\,\bar{c}_{\phi\mathrm{q}}\bar{c}_{\mathrm{qq}}\right). \quad (10.10)$$

Here, σ^SM denotes the standard model cross section, while "ch" denotes either s-channel, t-channel or associated Wt production. However, not all of the parameters in Eq. 10.10 are independent and it can be simplified to

$$\sigma_\mathrm{ch}^\mathrm{EFT} = \sigma_\mathrm{ch}^\mathrm{SM}\left(\left(1 + \frac{\bar{c}_{\phi\mathrm{q}}}{V_\mathrm{tb}}\right)^2 + \alpha_{\mathrm{qq}}^\mathrm{ch}\left(1 + \frac{\bar{c}_{\phi\mathrm{q}}}{V_\mathrm{tb}}\right)\bar{c}_{\mathrm{qq}} + \beta_{\mathrm{qq}}^\mathrm{ch}\,\bar{c}_{\mathrm{qq}}^2\right) \quad (10.11)$$

by using that the operator $O_{\phi\mathrm{q}}^{(3)}$ simply rescales the Wtb vertex. Therefore, SM processes with a V_tb vertex and processes involving the $O_{\phi\mathrm{q}}^{(3)}$ operator can be combined into one process with a V_tb vertex coupling scaled by $(1+\frac{\bar{c}_{\phi\mathrm{q}}}{V_\mathrm{tb}})$. Thus, the coefficients for the coupling $\bar{c}_{\phi\mathrm{q}}$ in Eq. 10.10 can be determined to be $\alpha_{\phi\mathrm{q}} = 2$, $\beta_{\phi\mathrm{q}} = 1$ and $\gamma^\mathrm{ch} = \alpha_{\mathrm{qq}}^\mathrm{ch}$ for all three channels. The CKM element V_tb is set to $V_\mathrm{tb} = 1$ in the employed model. The result of the fit for the coefficients $\alpha_{\mathrm{qq}}^\mathrm{ch}$ and $\beta_{\mathrm{qq}}^\mathrm{ch}$ for single-top s-channel and t-channel production is given in Tab. 10.2. The associated Wt production does not depend on the $O_{\mathrm{qq}}^{(1,3)}$ operator. Therefore, only the SM cross section needs to be calculated and the remaining parameters can be determined analytically.

The cross sections for single top-quark production via the s-channel and t-channel as a function of the two couplings $\bar{c}_{\phi\mathrm{q}}$ and $\bar{c}_{\mathrm{qq}}$ is visualized in Fig. 10.5. The one-dimensional projections on each axis are displayed in Fig. 10.6. Of all three single top-quark production channels, the s-channel is most sensitive to corrections by the $O_{\mathrm{qq}}^{(1,3)}$ operator, while the dependence on $\bar{c}_{\phi\mathrm{q}}$ is the same for all channels.

	s-channel	t-channel	Wt prod.
σ^{SM}	3.319 ± 0.001	45.231 ± 0.012	22.37 ± 1.52
$\alpha_{\phi\mathrm{q}}$	2 (fixed)	2 (fixed)	2 (fixed)
$\beta_{\phi\mathrm{q}}$	1 (fixed)	1 (fixed)	1 (fixed)
α_{qq}	33.283 ± 0.010	-6.422 ± 0.007	0
β_{qq}	761.99 ± 0.26	34.39 ± 0.15	0

Table 10.2.: Results for the LO SM cross section σ^{SM} and the coefficients α_{qq} and β_{qq}. The values are obtained from a fit using Eq. 10.11 to the predicted cross sections calculated with MadGraph for 72 points in the $\bar{c}_{\phi\mathrm{q}}$-$\bar{c}_{\mathrm{qq}}$ plane. The result is given in the notation of Eq. 10.10. The parameter γ is equal to α_{qq}. For the associated Wt production, no fit is needed and the analytic result for the coefficients is used. The cross section for this channel corresponds to the NLO+NNLL prediction [Kid10b].

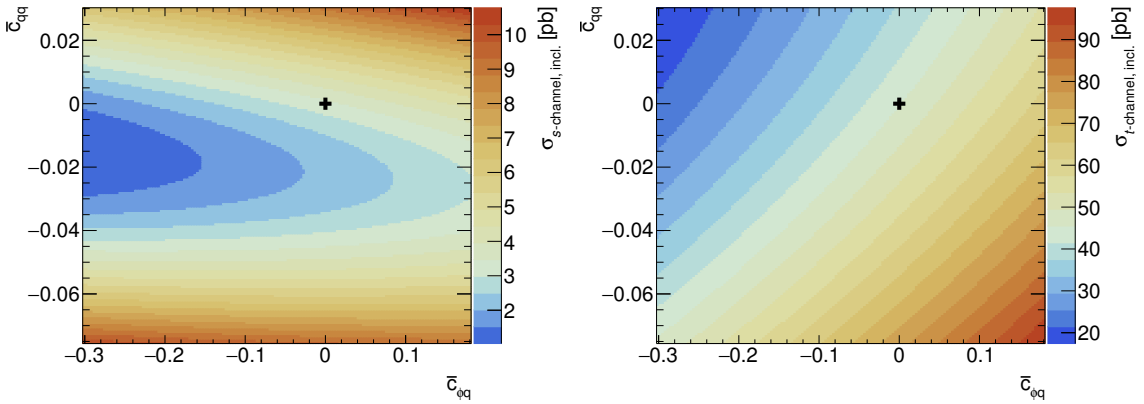

(a) $\sigma_{s,\mathrm{incl.}}(\bar{c}_{\phi\mathrm{q}}, \bar{c}_{\mathrm{qq}})$ (b) $\sigma_{t,\mathrm{incl.}}(\bar{c}_{\phi\mathrm{q}}, \bar{c}_{\mathrm{qq}})$

Figure 10.5.: Cross section predictions for single top-quark production in the (a) s-channel and (b) t-channel as a function of the coefficients $\bar{c}_{\phi\mathrm{q}}$ and $\bar{c}_{\mathrm{qq}}$. The predictions are obtained from a fit to 72 cross section values in the $\bar{c}_{\phi\mathrm{q}}$–$\bar{c}_{\mathrm{qq}}$ plane. The cross indicates the SM cross section.

10.3. Simple Detector Simulations

Detector simulations play a vital role for almost all ATLAS analyses. For example, the modelling of signal and background processes in this thesis, except for the multi-jet background, relies on an accurate description of the ATLAS detector response used in MC simulations. A large fraction of the time for these simulations is needed to compute the interaction of particles with the detector material, especially the propagation of particle showers in the calorimeters. Moreover, the large amount of data collected with the ATLAS detector requires an increasing demand for high-statistics MC simulations for all signal and background processes. Therefore, most of the modelling systematics

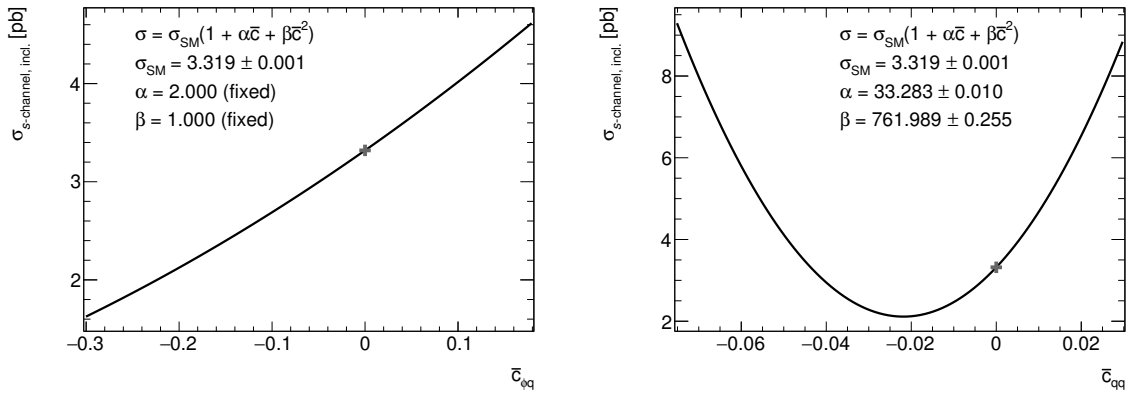

(a) $\sigma_{s,\mathrm{incl.}}(\bar{c}_{\phi\mathrm{q}}, 0)$ (b) $\sigma_{s,\mathrm{incl.}}(0, \bar{c}_{\mathrm{qq}})$

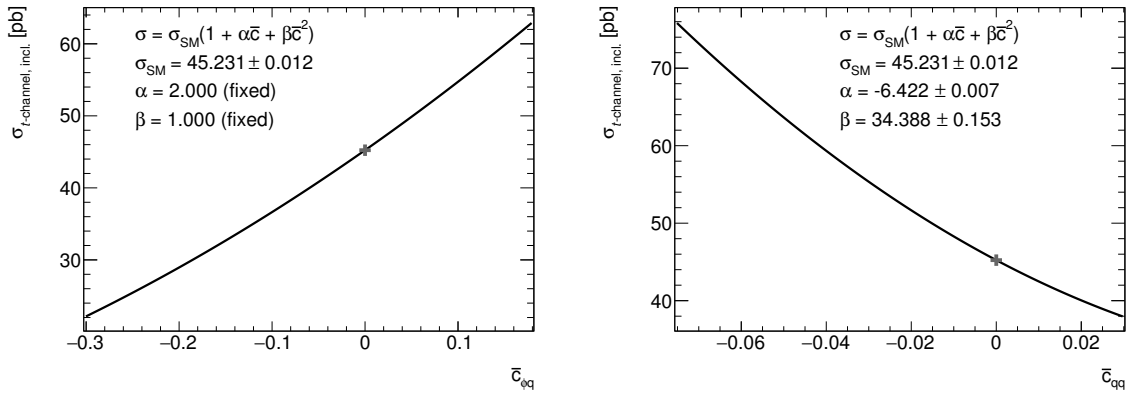

(c) $\sigma_{t,\mathrm{incl.}}(\bar{c}_{\phi\mathrm{q}}, 0)$ (d) $\sigma_{t,\mathrm{incl.}}(0, \bar{c}_{\mathrm{qq}})$

Figure 10.6.: Cross section predictions for single top-quark production. The predictions are obtained from a fit to 72 cross section values in the $\bar{c}_{\phi\mathrm{q}}$–$\bar{c}_{\mathrm{qq}}$ plane. The cross indicates the SM cross section. The four panels show the dependence of the cross section on a single parameter. Panels (a) and (b) show the single-top s-channel cross section as a function of $\bar{c}_{\phi\mathrm{q}}$ and $\bar{c}_{\mathrm{qq}}$, respectively, while (c) and (d) present the single-top t-channel cross section predictions.

are evaluated by using the fast detector simulation, AtlFast-II. Here, the computation time is reduced with respect to the full simulation by using pre-simulated "frozen" showers for low energetic particles in the calorimeter. In addition, a fast calorimeter simulation parametrizes the calorimeter response based on the longitudinal and lateral energy profile of the shower. A more detailed overview of the ATLAS simulation infrastructure can be found in [Luk12, ATL10c]. Fast simulations require much less computing time and therefore allow higher statistics for MC simulations. On the contrary, the simulations are less precise, because approximations for complex physics processes are used. Nevertheless, fast simulations are often the only solution in order to provide the necessary MC simulations for physics analyses.

As discussed in the previous section, new physics interactions can change the normalization of single-top processes and can cause changes to the differential distributions. The latter can lead to a different acceptance in the observed distributions and such effects have to be incorporated in the interpretation of cross section measurements in the context of an effective field theory interpretation and will be discussed in Sec. 10.6. In order to obtain these corrections, it is necessary to simulate the detector response for events that are generated with the new physics model described in Sec. 10.1.2. Moreover, any correction that is derived from the simulation is likely to be a function of the coupling strength parameters of the effective field theory model. The number of single-top s-channel events needed for such a study can be estimated by the following considerations: The samples that are used to evaluate the PDF systematic for the single-top s-channel production contain 600 000 events. If the corrections are evaluated based on 20 samples with similar statistics and each sample corresponds to a different choice for the two coupling coefficients $\bar{c}_{\phi \mathrm{q}}$ and $\bar{c}_{\mathrm{qq}}$, the amount of events that is required for such a study easily exceeds 6 million events. Although, this number is not large compared to the size of other samples, the production of such samples, even with simulations using AtlFast-II, might take some months[5]. Since such a study has not been conducted within the ATLAS collaboration before, there exists no estimate on how large these corrections might be. Furthermore, these samples may only be used in the context of this analysis. These arguments make it difficult to justify the production of millions of events without knowing the potential impact on the analysis. For future analyses, the number of events might even increase, if more and more operators are considered in the analysis.

In order to be able to conduct a study on the corrections mentioned above, there is obviously the need for much faster detector simulations. In the following sections, two alternative detector simulations, DetSimFast and Delphes, are presented.

10.3.1. Detector Simulation Fast

The first package to be introduced in this thesis for emulating the response of the ATLAS detector, is the so-called DetSimFast package (DSF). The idea of this package is to make use of the existing transfer functions and reconstruction efficiencies that have been discussed in Sec. 6.2 and are used within the MEM$_{\mathrm{t\bar{t}}}$ software to relate final state particles to detector level objects. In the following, the event generation of single-top events and the subsequent application of a fast detector simulation is explained.

The LO MadGraph model of Sec. 10.1.2 is used to generate the four-momenta of the single-top s-channel and single-top t-channel final states. The resolution

[5] This does not correspond to the actual CPU time, but rather to the estimated time, when the sample might be available to the analysis, as those samples would be produced with a low priority with regard to other samples.

functions define the probability to reconstruct a detector level object with a certain momentum given the initial momentum at the parton level. By generating random numbers according to the transfer functions, the reconstructed energy of quarks, gluons, electrons and muons is obtained. In addition, the reconstruction efficiencies for electrons and muons are taken into account[6]. Objects similar to those in Sec. 4, are defined in the following way:

Charged leptons: The four-momenta of electrons and muons in the final state is taken from the LHE event info [Alw+07] obtained from the event generation with MadGraph. Charged leptons are discarded randomly according to their reconstruction efficiency depicted in Figs. 6.2(a) and 6.2(b) for electrons and muons, respectively. The reconstructed energy of electrons is generated according to the probability densities defined by the energy resolution function. In the case of muons, the transverse momentum is used instead. Although, transfer functions exist for the pseudorapidity η and the azimuth φ, these values are left unchanged to speed up the computation. Furthermore, these quantities are measured more precisely than the energy and the reconstructed values for η and φ should be close to those on parton level. Electrons or muons are required to be isolated and leptons that are within $\Delta R < 0.4$ of a jet, are removed.

Jets: The event generation does not include any parton shower generator such as PYTHIA, because the transfer functions for strongly interacting particles are only valid for quarks and gluons and not for hadrons. Therefore, each final state quark or gluon is supposed to form one jet. The jet energy is determined by smearing the energy of the initial particle based on the transfer functions. The reconstruction efficiencies for jets are not taken into account and the jets direction is identical to the final state particle without applying any resolution functions. No checks are performed whether two jets overlap within a certain distance ΔR of each other. For single top-quark production, the two or three quarks or gluons in the final state should be separated in most cases. The impact from neglecting possible overlaps should be minor.

b-Jets: Jets originating from b-quarks are tagged as b-jets according to the b-tagging efficiencies of the MV1 and MV1c algorithm. The b-tagging efficiency as a function of the jet transverse momentum is extracted from the ATLAS publications [ATL12b] and [ATL14a] and is shown in Fig. 10.7.

Both efficiencies are parametrized by the following function

$$\varepsilon_{\mathrm{b-tageff.}} = \varepsilon_0 \frac{\sqrt{a \cdot p_{\mathrm{T}}}}{1 + b \cdot p_{\mathrm{T}}} \,. \tag{10.12}$$

The parameter values for the MV1 and MV1c algorithm are determined by a fit to the respective data distribution. The results of the two fits are provided

[6] In general, it is possible to include reconstruction efficiencies for quarks and gluons as well. However, a better agreement with the full ATLAS simulation is found if these efficiencies are not used.

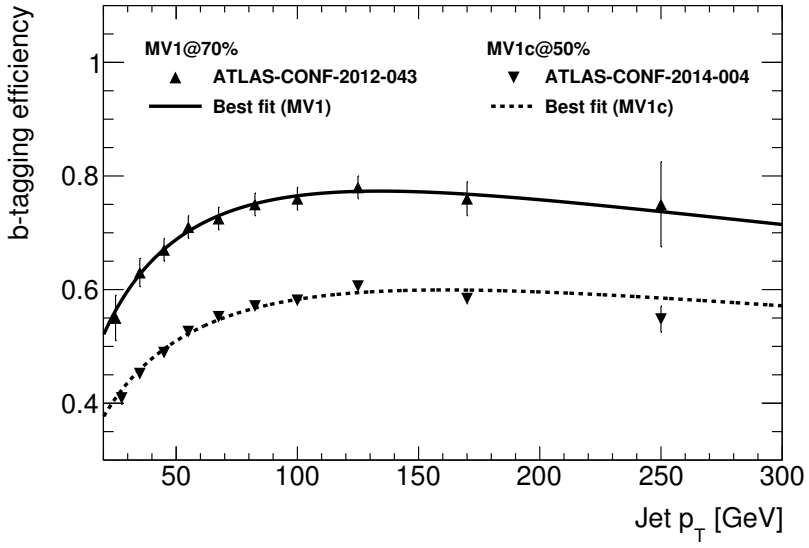

Figure 10.7.: The b-tagging efficiency as a function of the transverse momentum of the jet. The data is taken from the published b-tagging efficiencies for MV1 [ATL12b] and MV1c [ATL14a]. The b-tagging efficiency is parametrized and estimates for the parameters are obtained by a fit to data.

in Tab. 10.3. One could use the b-tagging efficiency that is included in the MEM$_{\text{TTk}}$ (c. f. Fig. 6.2(e)). However, this efficiency is only valid for the MV1 algorithm. Furthermore, it only shows a small dependence on the pseudorapidity and the parametrization given by Eq. 10.12 is sufficient to describe the b-tagging efficiency.

	ε_0	a	b
MV1	0.65 ± 0.08	0.042 ± 0.001	0.0075 ± 0.0007
MV1c	0.54 ± 0.03	0.031 ± 0.003	0.0062 ± 0.0002

Table 10.3.: Results for the b-tagging efficiency parameters obtained from a fit to the data distributions shown in Fig. 10.7.

Missing transverse momentum: The missing momentum imbalance, $E_{\text{T}}^{\text{miss}}$, is estimated based on the transverse momentum of the neutrino. The transfer functions that are used to relate the neutrino transverse momentum to the reconstructed $E_{\text{T}}^{\text{miss}}$ on detector level are not part of the KLFitter transfer functions, but have been derived separately in the context of the previous s-channel analysis [Rie16]. This was necessary, as the calculation of the missing transverse momentum depends on the object definition and providing a transfer function that can be used by all ATLAS analyses is difficult.

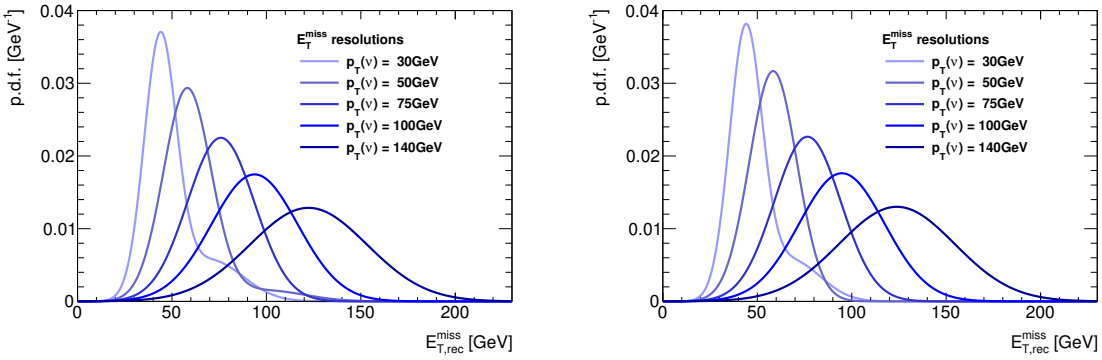

(a) $E_{\mathrm{T}}^{\mathrm{miss}}$ transfer function (s-channel)

(b) $E_{\mathrm{T}}^{\mathrm{miss}}$ transfer function (t-channel)

Figure 10.8.: Transfer functions for $E_{\mathrm{T}}^{\mathrm{miss}}$ for different neutrino transverse momenta. The probability density function is parametrized by a double Gaussian function.

The technique that is used to obtain the parameter estimates for the $E_{\mathrm{T}}^{\mathrm{miss}}$ transfer function is similar to the one used by KLFitter group. First, a basic event selection is defined that requires one isolated lepton with a transverse momentum of $p_{\mathrm{T}} > 30\,\mathrm{GeV}$ and exactly two b-tagged jets with a transverse momentum of $p_{\mathrm{T}} > 25\,\mathrm{GeV}$. The MV1 algorithm with an efficiency of 70 % is used to identify b-jets. The threshold for the missing transverse momentum is $E_{\mathrm{T}}^{\mathrm{miss}} > 35\,\mathrm{GeV}$. The relative difference between the neutrino transverse momentum and $E_{\mathrm{T}}^{\mathrm{miss}}$ is calculated in eight regions defined by the neutrino p_{T}. For each region, the best values for the double Gaussian parameter set have been determined by a χ^2-fit. The parameter range is extended to the full energy range by a global analysis of the results obtained in the various regions. [Kin+15]

The transfer functions for the missing transverse momentum are shown in Fig. 10.8 and have been derived separately using simulated single-top s-channel and t-channel events. The transfer functions in both regions are very similar. In Sec. 10.4, a detailed study is presented that compares the distributions that are obtained using the ATLAS simulation and the fast simulations of this section. During this study, it was noticed that the $E_{\mathrm{T}}^{\mathrm{miss}}$ distribution is not well modelled by the neutrino transfer functions described above. A possible cause could be the rather high threshold $E_{\mathrm{T}}^{\mathrm{miss}} > 35\,\mathrm{GeV}$ used in the event selection for the transfer functions or that possible contributions from pile-up are disregarded. An example of the mis-modelling in the s-channel signal region is shown in Fig. 10.9. The event selection for ATLAS and DetSimFast is identical. However, the ATLAS simulation uses a NLO QCD event generator, while events for the fast simulation are only calculated in LO QCD. More details will be provided in Sec. 10.4. In order to mitigate the problem and improve the modelling of this particular distribution, the following ad hoc pile-up correction for the $E_{\mathrm{T}}^{\mathrm{miss}}$ transfer function is derived. In addition to the smearing of the neutrino transverse momentum according to the transfer functions, two pile-up

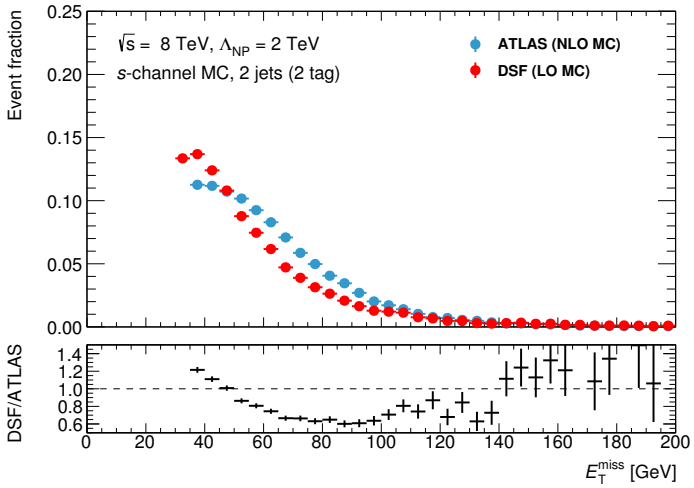

Figure 10.9: The $E_{\mathrm{T}}^{\mathrm{miss}}$ distribution obtained from event samples using the ATLAS simulation (blue) and DetSimFast package (red). Both distributions are normalized and the same event selection is used for both samples. The lower figure shows the ratio between the two simulations. The disagreement between ATLAS and DetSimFast is clearly visible.

corrections p_1 and p_2 are derived in the following way. First, two numbers g_1 and g_2 are calculated according to:

$$g_1 = \begin{cases} \mathrm{Gaus}(E_{\mathrm{T}}(\nu), \mu_1, \sigma_1^+); & E_{\mathrm{T}}(\nu) > \mu_1 \\ \mathrm{Gaus}(E_{\mathrm{T}}(\nu), \mu_1, \sigma_1^-); & E_{\mathrm{T}}(\nu) < \mu_1 \end{cases} \tag{10.13}$$

$$g_2 = \begin{cases} \mathrm{Gaus}(E_{\mathrm{T}}(\nu), \mu_2, \sigma_2^+); & E_{\mathrm{T}}(\nu) > \mu_2 \\ \mathrm{Gaus}(E_{\mathrm{T}}(\nu), \mu_2, \sigma_2^-); & E_{\mathrm{T}}(\nu) < \mu_2 \end{cases} \tag{10.14}$$

The term "Gaus" denotes a Gaussian distribution with mean μ and a standard deviation σ. Second, the corrections p_1 and p_2 are computed by the following equations

$$p_1 = s_1 + r_1 b_1; \quad g_1 < U(0,1) \tag{10.15}$$

$$p_2 = s_2 + r_2 b_2; \quad g_2 < U(0,1) \tag{10.16}$$

and are added to the missing transverse momentum if random numbers drawn from a uniform distribution $U(0,1)$ are greater than g_1 and g_2, respectively. The random numbers r_1 and r_2 that are used in Eqs. 10.15–10.16 follow a Gaussian distribution with a mean value of zero and a standard deviation of one. All parameters that appear in Eqs. 10.13–10.16 have been optimized in a dedicated study [Sch17] to improve the modelling of the $E_{\mathrm{T}}^{\mathrm{miss}}$ distribution. The values for which the best agreement with the ATLAS simulation is found are listed in Tab. 10.4. On the one hand, the corrections are needed to improve the modelling of the $E_{\mathrm{T}}^{\mathrm{miss}}$ distribution. The impact of these corrections on other distributions than the one for $E_{\mathrm{T}}^{\mathrm{miss}}$ is minor. On the other hand, a better understanding why the initial transfer functions are not sufficient to describe the missing transverse momentum resolution is desired, but could not be studied in more detailed within the time scale of this thesis. The $E_{\mathrm{T}}^{\mathrm{miss}}$ response function, which is the combination of the transfer function and pile-up corrections described above, is shown in Fig. 10.10. The resulting $E_{\mathrm{T}}^{\mathrm{miss}}$ distribution can be found in Sec. 10.4.

$\mu_1 = 61.2$	$\sigma_1^+ = 50$	$\sigma_1^- = 9.5$	$s_1 = -12.3$	$b_1 = 8$
$\mu_2 = 87$	$\sigma_2^+ = 3.1$	$\sigma_2^- = 2.9$	$s_2 = 4$	$b_2 = 2$

Table 10.4.: Parameters used for the missing momentum pile-up correction. The parameters have been optimized with respect to the best agreement between the fast simulation and the ATLAS full simulation.

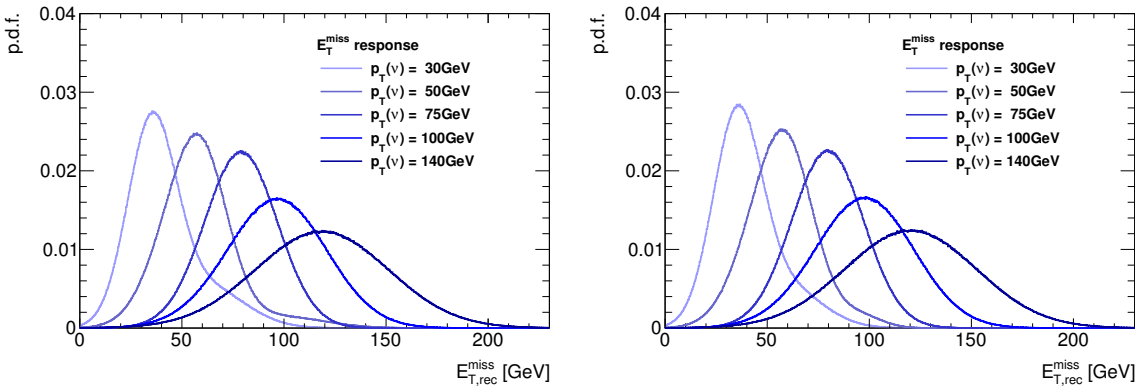

(a) $E_{\mathrm{T}}^{\mathrm{miss}}$ response function (s-channel)

(b) $E_{\mathrm{T}}^{\mathrm{miss}}$ response function (t-channel)

Figure 10.10.: The $E_{\mathrm{T}}^{\mathrm{miss}}$ response functions which are used instead of the transfer functions. The response functions include the pile-up correction given in Eq. 10.15 and 10.16. These corrections are tuned such that the agreement between distributions using ATLAS simulation and DetSimFast is improved.

10.3.2. DELPHES

Another program for performing a fast detector simulation is the DELPHES framework [Fav+14]. It accepts simulated events that are stored in the most common event formats. This includes LHEF and HepMC, which are used by MADGRAPH and PYTHIA. Therefore, the setup described in Sec. 10.1.2 can be used to study the detector response for the effective field theory model. The simulation includes the propagation of charged particles within a magnetic field, electromagnetic and hadronic calorimeters and a muon identification system. Unlike to the ATLAS simulation, which uses Geant4 to simulate the interaction of particles with the detector material, the response of all detector subsystems is fully parametrized. Therefore, no interactions with the detector material are simulated and effects such as bremsstrahlung or photon conversions are neglected. A summary of the framework, including the event generation and the definition of physics objects is given in this section. A more detailed documentation is available in the given reference.

The ATLAS Detector in DELPHES

A basic geometric model of the ATLAS detector is included in the release version 3.4.0 of the DELPHES framework[7]. It consists of a tracking volume, whose size corresponds to the magnetic field coverage of the ATLAS solenoid magnet. No tracking devices are simulated and the magnetic field is oriented parallel to the beam axis. Furthermore, the magnetic field with a strength of 2 T is fully contained in this volume. The electromagnetic and hadronic calorimeters are positioned behind the tracking volume and are perfectly overlaid. Both calorimeters only consist of a single layer of calorimeter cells. The size of the electromagnetic calorimeter cells in central region with $|\eta| < 3.0$ is $\Delta\eta \times \Delta\phi = 0.0175 \times 0.0175$. This corresponds roughly to the granularity of the second layer of the electromagnetic calorimeter. For the forward region, $3 < |\eta| < 5$, the cells have a variable size with a granularity of $\Delta\eta \times \Delta\phi = 0.175 \times (0.175 - 0.35)$. The dimensions of the hadronic calorimeter cells in the barrel region ($|\eta| < 2.5$) are $\Delta\eta \times \Delta\phi = 0.1 \times 0.175$. The forward region of the hadronic calorimeter partially overlaps with the central part and cells of the size of $\Delta\eta \times \Delta\phi = 0.2 \times 0.35$ are defined. Since the detector response is parametrized, no dedicated modules for the muon system are necessary.

The DELPHES Workflow

Single-top s-channel and t-channel events are generated with MADGRAPH. For hadronisation and shower modelling, the built-in interface to PYTHIA8 is used with a configuration that is similar to the one used for the ATLAS simulation[8]. In addition to the hard scattering process which is calculated by the event generator, DELPHES allows to include additional soft interactions from pile-up events in the simulation. Therefore, a sample of minimum bias events from proton–proton collisions at a centre-of-mass energy of $\sqrt{s} = 8\,\text{TeV}$ are generated with PYTHIA8. The number of pile-up interactions per hard-scattering event is randomly extracted from a Poisson distribution with a mean value of 20 and are placed randomly along the z-axis.[9]

All long-lived particles from hard scattering or pile-up interactions, are propagated to the calorimeters within the magnetic field. Particles that originate from a coordinate outside the tracking volume are neglected. Those particles that reach the calorimeters deposit their energy in the calorimeter cells. By default, electrons and photons are absorbed by the electromagnetic calorimeter and leave all their energy in one tower cell. Likewise, stable hadrons deposit their energy in the hadronic calorimeter cells. Although, Kaons and Λ baryons are considered as stable particles by PYTHIA, in a

[7] The ATLAS model, which includes modules for pile-up corrections, is used in this thesis. The calorimeter configuration is taken from the ATLAS model without pile-up corrections.

[8] The ATLAS simulation uses PYTHIA6 for single-top processes. For DELPHES, the ATLAS PYTHIA8 A14 configuration has been used for this thesis.

[9] This corresponds roughly to the pile-up conditions during the 2012 data-taking period [ATL16b].

real experiment, they could decay inside the tracker volume. Therefore, 30 % of their energy is deposited in the electromagnetic calorimeter, while the remaining energy is deposited in the hadronic calorimeter cells. The energy fractions that are deposited in the electromagnetic and hadronic calorimeters by these particles is based on their decay products. Muons and neutrinos do not contribute to the energy collected by the calorimeter cells. The energy deposits in each cell is smeared by resolution functions, which are defined separately for the electromagnetic and hadronic calorimeter.

Object Definition in DELPHES

Tracks of charged particles have a finite probability to be reconstructed inside the tracker volume. Tracks originating from pile-up events are removed, if their origin is more than 0.1 mm apart from the primary vertex. This corresponds to a much better z-vertex resolution than in the ATLAS detector, but it is the default configuration and different settings were not studied. Based on the track and calorimeter information, the following objects are defined: The isolation criteria for electrons and muons, as well as the b-tagging information has been updated to better suit the objects definitions (c. f. Sec. 4) used in this analysis.

Muons: The reconstruction efficiency for muons depends on the energy and pseudo-rapidity of the muon and vanished outside the tracker volume. Furthermore, the muon needs to be isolated, i. e. the sum of all tracks with a transverse momentum of $p_{\mathrm{T}}^{\mathrm{min}} > 0.5\,\mathrm{GeV}$ within a cone of $\Delta R < 0.3$ around the muon candidate must not exceed 25 % of the muons transverse momentum. The final muon momentum is obtained by applying a user-defined resolution function to the initial four-momentum.

Electrons: Electrons are reconstructed from tracks in the tracker volume. In addition to the track reconstruction efficiency, a separate electron reconstruction efficiency is applied. It is parametrized as a function of the electron energy and pseudorapidity. As for muons, the electron momentum is smeared according the electron resolution function. Furthermore, the isolation criteria requires that the sum of the transverse momenta of tracks around the electron candidate needs to be less than 12 % of the electron transverse momentum.

Jets: Jets are reconstructed from hadronic calorimeter entries using the anti-k_T algorithm [CSS08a] with a distance parameter of $\Delta R = 0.4$. The contribution from pile-up events to the jet energy is corrected by applying a residual pile-up subtraction using the jet area method [CSS08b, CS08]. The jet cluster algorithm and the pile-up suppression is performed by the FastJet package [CSS12]. Electrons and muons are likely to be reconstructed as jets or as constituents of a jet. Therefore, DELPHES automatically removes jets from the event, if they have been already reconstructed as isolated electron or isolated muon.

b-Jets: The tagging of jets is performed in the following way. First, final state partons with $p_{\mathrm{T}} > 1\,\mathrm{GeV}$ and $|\eta| < 2.5$ are matched to jets if they are within $\Delta R = 0.4$. Second, depending on the flavour of the matched parton, the jet is tagged based on the user-defined efficiencies. The efficiencies for b-tagging presented in Sec. 10.3.1 are used. The c-tagging efficiency uses the same parametrization as for b-tagging and the parameters are determined by a fit to data extracted from [ATL14b]. The parameter values used for MV1 c-tagging are $\varepsilon_0 = 0.35$, $a = 0.0418$ and $b = 0.0069$. The c-tagging efficiency is five times lower than for MV1 and the parameter ε is scaled accordingly. The mis-tagging efficiency is around 1 % for both algorithms.

Missing transverse momentum: The missing transverse momentum in DELPHES is calculated as

$$\vec{E}_{\mathrm{T}}^{\mathrm{miss}} = -\sum_i \vec{p_{\mathrm{T}}}(i) \tag{10.17}$$

where the sum includes the energy deposits from all calorimeter cells and all muons in the event. The modelling of the missing transverse momentum distribution is very much improved by including pile-up in the simulation.

10.4. Comparison between ATLAS and Simple Detector Simulations

In the previous section, alternative methods of simulating the response of the ATLAS detector have been discussed. In order to check if these simple detector simulations are appropriate to approximately describe the ATLAS response and if they can be used for this thesis, an extensive validation procedure has been carried out. A detailed study that compares the DetSimFast simulation with the ATLAS simulation can be found in [Sch17].

In case of the ATLAS simulation, events are generation in NLO QCD by POWHEG and the subsequent hadronisation of quarks and gluons is performed by PYTHIA6. This is the nominal setup used for s-channel and t-channel single top-quark production within ATLAS. However, the effective field theory model is only available in LO QCD. Therefore, SM single top-quark events are generated with MADGRAPH5 using the configuration described in Sec. 10.1.2.[10] In case of the DELPHES simulation, the parton shower is performed by PYTHIA8 with a similar configuration to the ATLAS simulation. For the DetSimFast simulation, no parton shower is used. This means that possible differences between the simple detector simulations and the ATLAS full simulation might also arise from the different event and parton shower generators. Unfortunately, no official samples for single top-quark production with MADGRAPH5

[10] All coefficients of all operators in the effective field theory model are set to zero in order to obtain the SM prediction in LO QCD.

exist. The number of generated events for each sample simulated with DetSimFast or DELPHES are adjusted based on the selection efficiency for each simulation and are listed in Tab. 10.5. The simple detector simulations are much faster than the ATLAS simulation. The typical run-time per event is about 100 s for AtlFast-II [ATL10c], 2 – 4 s for DELPHES and about 2 ms for DetSimFast.

Signal selection	Simulation	Process	
		s-channel	t-channel
2 jets (2 b-tag) (s-channel SR)	DetSimFast	200 000	300 000
	DELPHES	300 000	300 000
2 jets (1 b-tag) (t-channel SR)	DetSimFast	750 000	300 000
	DELPHES	1 500 000	300 000

Table 10.5.: Number of generated events for DetSimFast and DELPHES simulations in each signal region (SR). The number of events are adjusted based on the selection efficiency in each region to ensure sufficient statistics in all cases.

The signal selections defined in Secs. 7.2.1 and 7.3.2 for the s-channel and t-channel event selection are applied to all three samples, generated with the ATLAS, DetSimFast and DELPHES simulation. For the DetSimFast simulation, no low-momentum leptons of loose quality are simulated, because the τ-lepton does not decay in this simulation. For DELPHES, the decay of the τ-lepton is modelled by PYTHIA, however, in the DELPHES object definitions, no leptons of loose quality are defined. Their impact on the s-channel signal region is negligible. Furthermore, the differences from the detector modelling are expected to be much larger than corrections from the missing di-lepton veto in the t-channel signal region.

In Secs. 10.4.1–10.4.5, distributions of the main kinematic variables, ME likelihoods and the ME discriminant in the two signal regions are shown. All figures in these sections show distributions for the combination of the electron + jets and muon + jets selections. In order to distinguish the two signal regions, the s-channel signal selection is denoted as, "2 jets (2 tags)", while the t-channel signal selection is referred to as "2 jets (1 tag)" selection in all figures. Nevertheless, all cuts defined in Secs. 7.2.1 and 7.3.2 are applied.

10.4.1. Control Distributions, s-Channel Signal Region

The kinematic distributions for simulated s and t-channel events in the s-channel signal region are shown in Fig. 10.11–10.14.

The distributions for the transverse momentum of the lepton and jets obtained with DetSimFast and DELPHES agree sufficiently well with the ATLAS simulation. In

most cases the deviations are about 10 % between the simple simulations and the full ATLAS simulation. Larger deviations are observed for the tails of the distributions, but also the statistical uncertainty is much larger. The pseudorapidity of the lepton is modelled well by both simple simulations for single-top s-channel and t-channel events. The azimuth angle shows a deviation in the region that is approximately defined by $-2 < \varphi < -1$. These deviations are likely to be caused by the feet of the ATLAS detector, which degrades the reconstruction efficiency, as the coverage with detector elements is limited in this region. Both simulations do not take this into account and therefore the reconstruction efficiency is almost constant in φ. For s-channel events, the pseudorapidity of the leading b-tagged jet is not well modelled and shows a discrepancy for $|\eta| > 1.5$ for both DetSimFast and DELPHES. On the one hand, the reconstruction efficiencies for jets in DELPHES may not correspond to the actual ATLAS efficiencies. They are not considered at all for the DetSimFast simulation. On the other hand, the b-tagging efficiency used in the simple simulation does not depend on η, which could increase the number of reconstructed b-jets for $|\eta| > 1.5$. For simulated t-channel events, the leading jet pseudorapidity distribution obtained with the DetSimFast simulation agrees well with the ATLAS simulation. Deviations of up to 40 % are observed for the DELPHES simulation. The pseudorapidity distributions for the sub-leading jet is modelled much better by both simulations.

The distributions for the missing transverse momentum is modelled very well by the DELPHES simulation. This is remarkable, because the default configuration for pile-up events are used, only the number of pile-up events has been adapted to the conditions during the 2012 data-taking period. For the DetSimFast simulation, a specific pile-up correction is needed to model the $E_{\mathrm{T}}^{\mathrm{miss}}$ distribution. Yet, the modelling can still be improved. The distribution of the transverse mass of the W boson is narrower for the DetSimFast simulation than for the ATLAS simulation. For DetSimFast, no radiation losses due to bremsstrahlung are considered and the angular distributions of jets and leptons are not smeared. This results in a better estimate for $E_{\mathrm{T}}^{\mathrm{miss}}$ compared to the full simulation. In contrast to the DetSimFast simulation, the DELPHES simulation is able to model the $m_{\mathrm{T}}^{\mathrm{W}}$ distribution accurately in most cases. The incorporation of pile-up events in the DELPHES simulation improves the modelling with respect to the DELPHES simulation without pile-up.

10.4.2. Control Distributions, t-Channel Signal Region

The modelling in the t-channel signal region for single-top t-channel events is presented in this section. The agreement between the simple detector simulation and the ATLAS simulation is as good as in the s-channel signal region and similar statements for DetSimFast and DELPHES can be made. Therefore, only selected distributions are shown in Fig. 10.15 for this region.

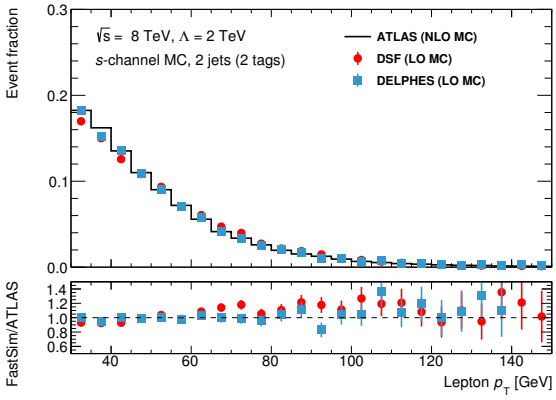

(a) Lepton transverse momentum

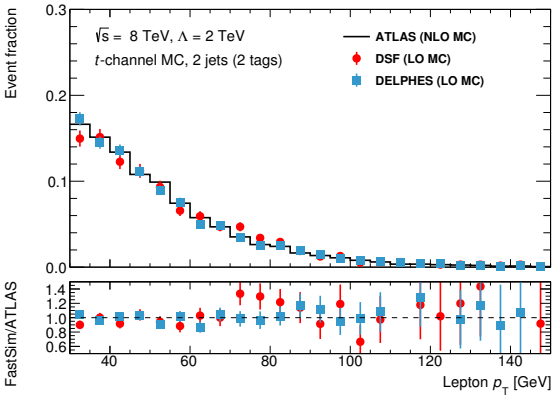

(b) Lepton transverse momentum

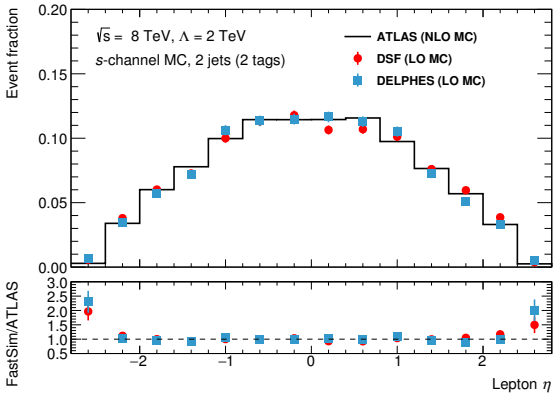

(c) Lepton pseudorapidity

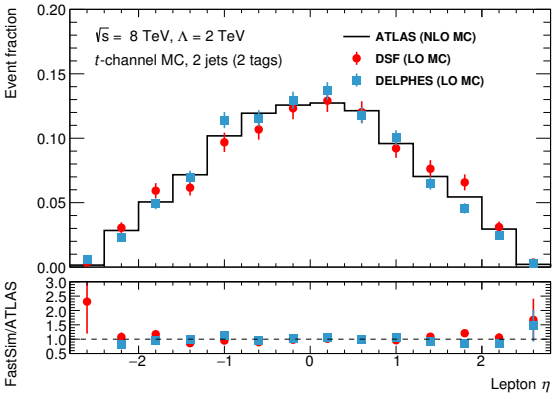

(d) Lepton pseudorapidity

Figure 10.11.: Distributions in the s-channel signal region for the ATLAS, DetSimFast and DELPHES simulations. The panels show (a) lepton transverse momentum and (c) lepton pseudorapidity using s-channel events. Panels (b) and (d) show the same distributions, but for simulated t-channel events. Only statistical uncertainties are shown.

Figure 10.12: Distributions for the lepton azimuth φ for single-top s-channel production and the ATLAS, DetSimFast and DELPHES simulations. The s-channel signal selection is used. The disagreement between the ATLAS simulation and the simple simulations in φ is likely to be caused by the less instrumentation close to the feet of the ATLAS detector, which are not taken into account by the simple detector simulations.

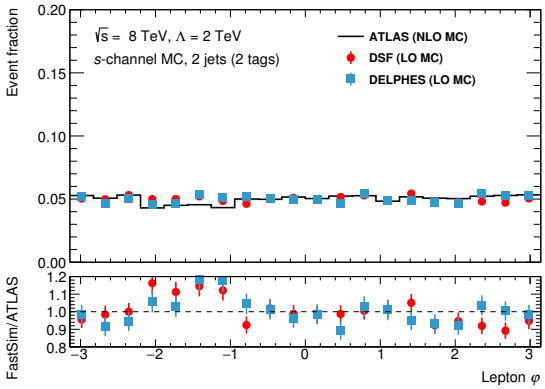

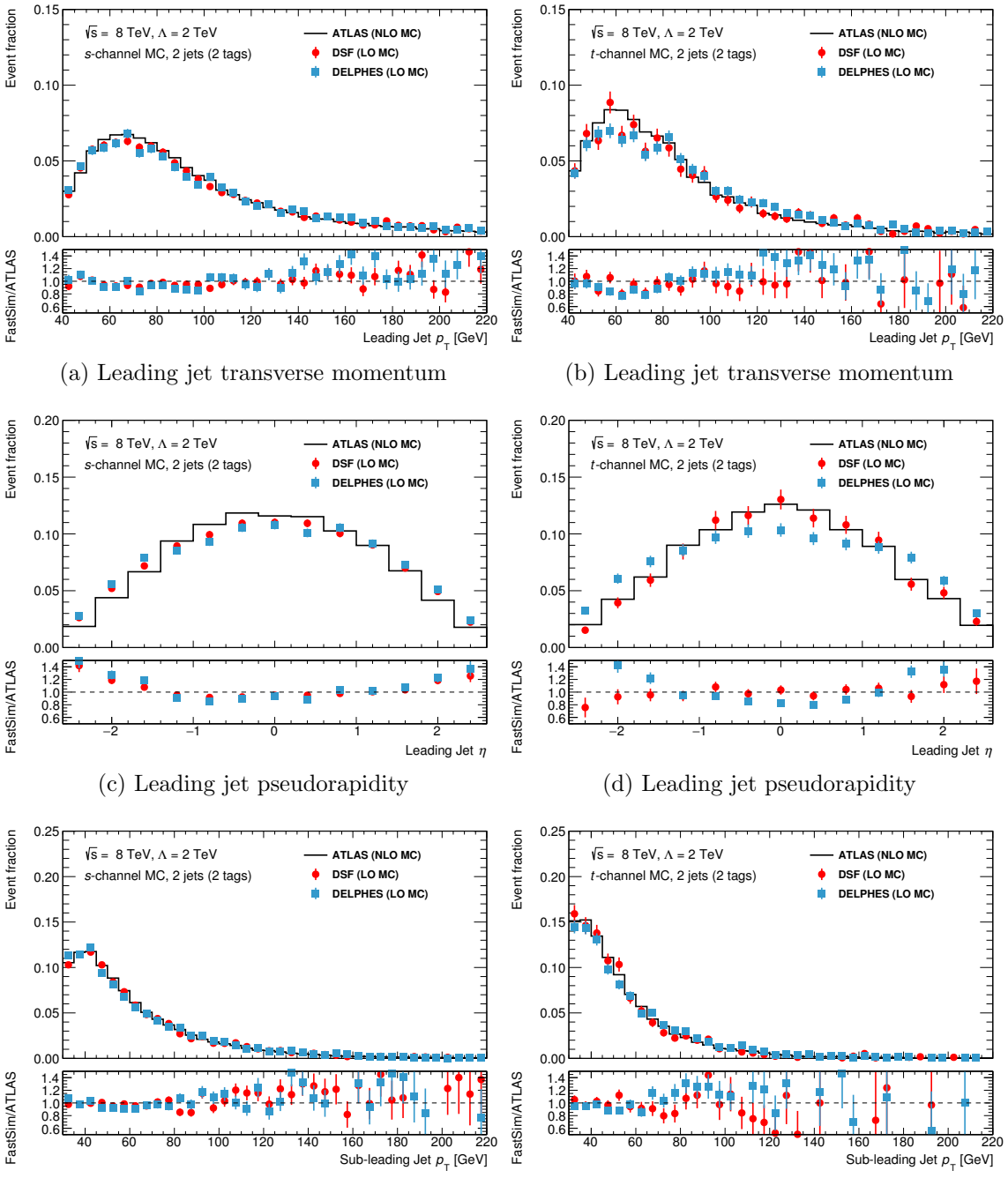

(a) Leading jet transverse momentum

(b) Leading jet transverse momentum

(c) Leading jet pseudorapidity

(d) Leading jet pseudorapidity

(e) Sub-leading jet transverse momentum

(f) Sub-leading jet transverse momentum

Figure 10.13.: Kinematic distributions in the s-channel signal region. The distributions show (a) the transverse momentum and (c) pseudorapidity of the leading jet and (e) the transverse momentum of the sub-leading jet for simulated s-channel events. The same distributions for simulated t-channel events are shown in the panels (b), (d) and (f), respectively. Only statistical uncertainties are shown.

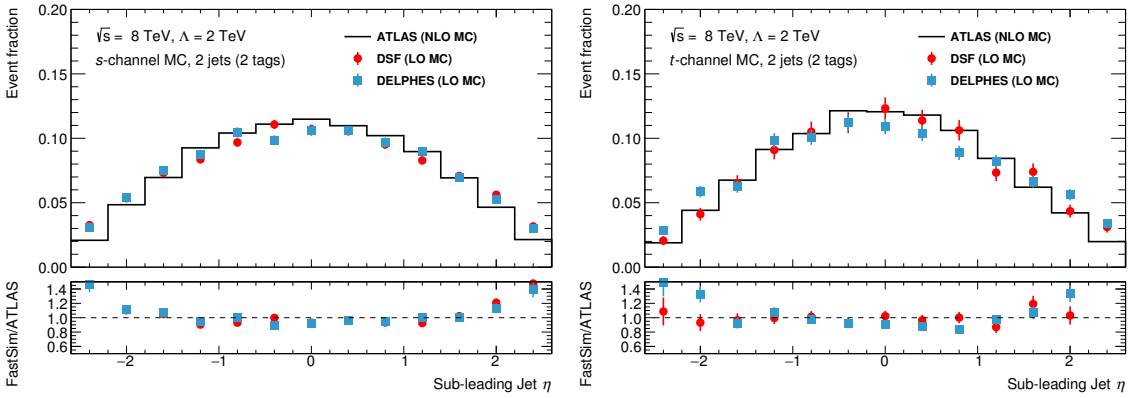

(a) Sub-leading jet pseudorapidity

(b) Sub-leading jet pseudorapidity

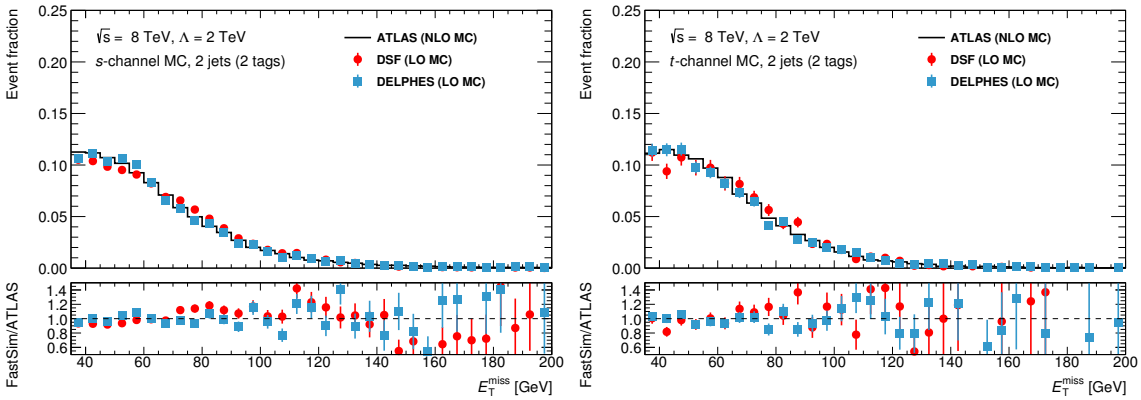

(c) Missing transverse momentum

(d) Missing transverse momentum

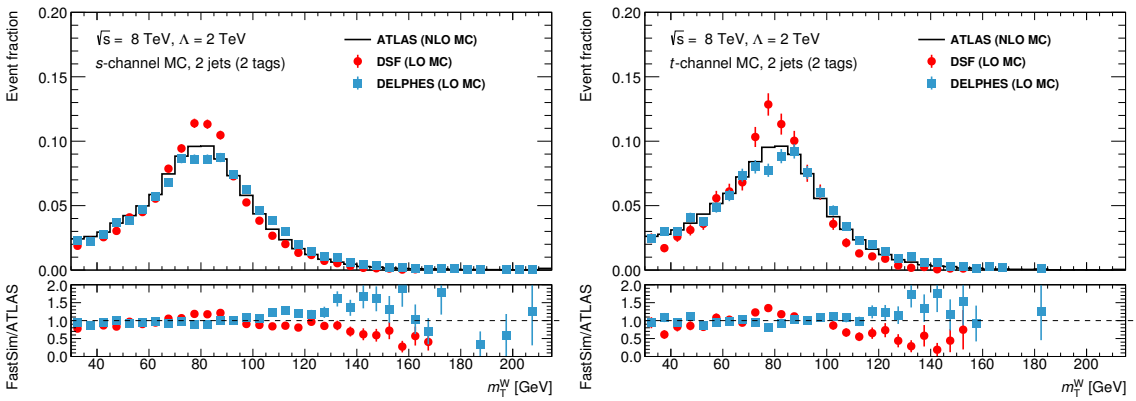

(e) Transverse W boson mass

(f) Transverse W boson mass

Figure 10.14.: Kinematic distributions for the *s*-channel signal selection and single-top *s*-channel events for the ATLAS, DetSimFast and DELPHES simulations. The panels show distributions of (a) the pseudorapidity of the sub-leading jet, (c) missing transverse momentum and (e) transverse W boson mass for simulated *s*-channel events. Panels (b), (d) and (f) show the same distributions, but using simulated *t*-channel events. Only statistical uncertainties are shown.

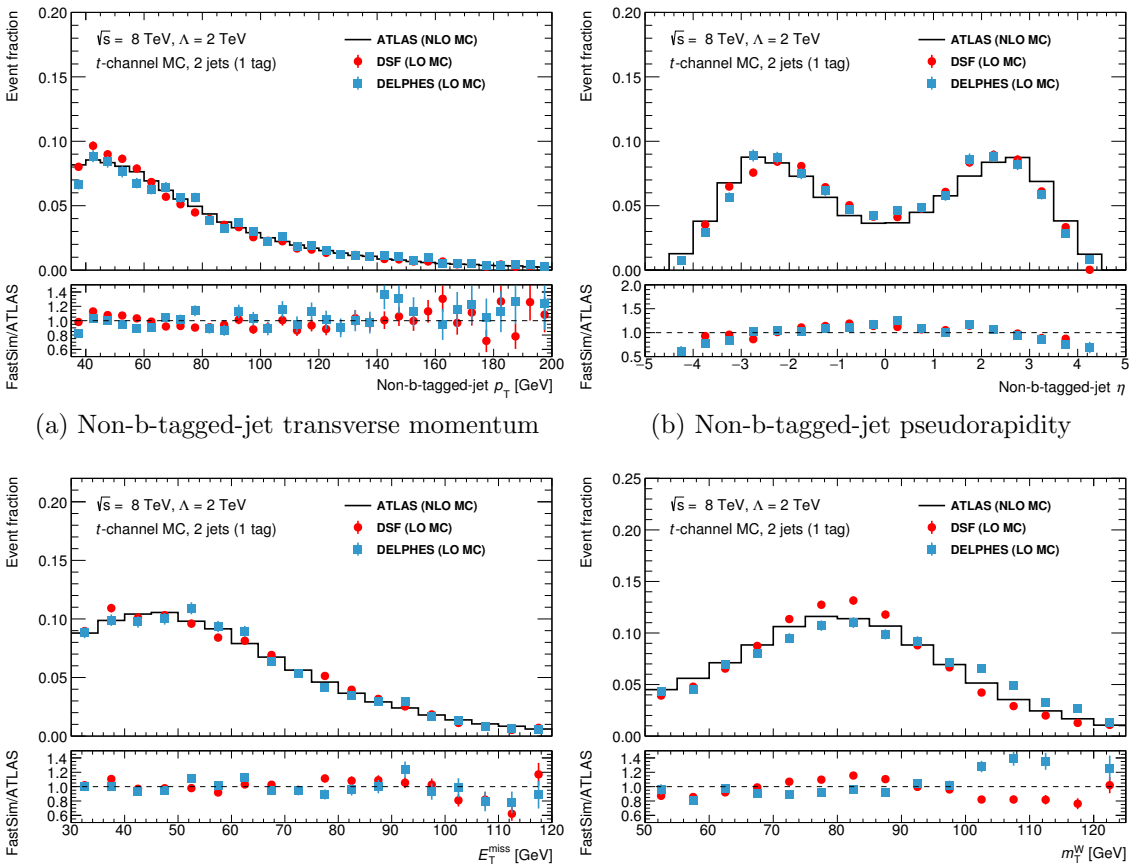

(a) Non-b-tagged-jet transverse momentum

(b) Non-b-tagged-jet pseudorapidity

(c) Missing transverse momentum

(d) Transverse W boson mass

Figure 10.15.: Kinematic distributions for the t-channel signal selection and single-top t-channel events for the ATLAS, DetSimFast and DELPHES simulations. The panels show distributions of (a) the transverse momentum and (b) pseudorapidity of the non-b-tagged jet as well as the distributions for (c) missing transverse momentum and (d) transverse W boson mass for simulated t-channel events. Only statistical uncertainties are shown.

10.4.3. Likelihood Distributions, s-Channel Signal Region

Several likelihood distributions in the s-channel signal region are shown in Fig. 10.16 for simulated s-channel events. The mis-modelling of the likelihood distributions for the single-top s-channel $2 \to 2$, single-top t-channel and $t\bar{t}$ single lepton process is similar. For large likelihood values, the distribution obtained with the simple simulations is lower compared to the ATLAS simulation. The opposite is true for small likelihood values. The distributions for the t-channel and $t\bar{t}$ likelihood obtained with the DELPHES and DetSimFast simulation are almost identical. The modelling of the likelihood for the s-channel and $W+b\bar{b}$ process are close to the ATLAS prediction for the DetSimFast simulation. Larger deviations in the distributions are observed for

the DELPHES simulation. The modelling likelihood distributions for the W+c+jet and W+jj processes are similar to the W+$b\bar{b}$ likelihood. The likelihood distribution for the $t\bar{t}$ di-lepton process shows a similar trend as the one for the $t\bar{t}$ single-lepton process.

For simulated t-channel events, the likelihood distributions for DetSimFast and DELPHES are very similar and show the same modelling issues as described above for simulated s-channel events. The distributions for the DetSimFast simulation can be found in [Kin+15].

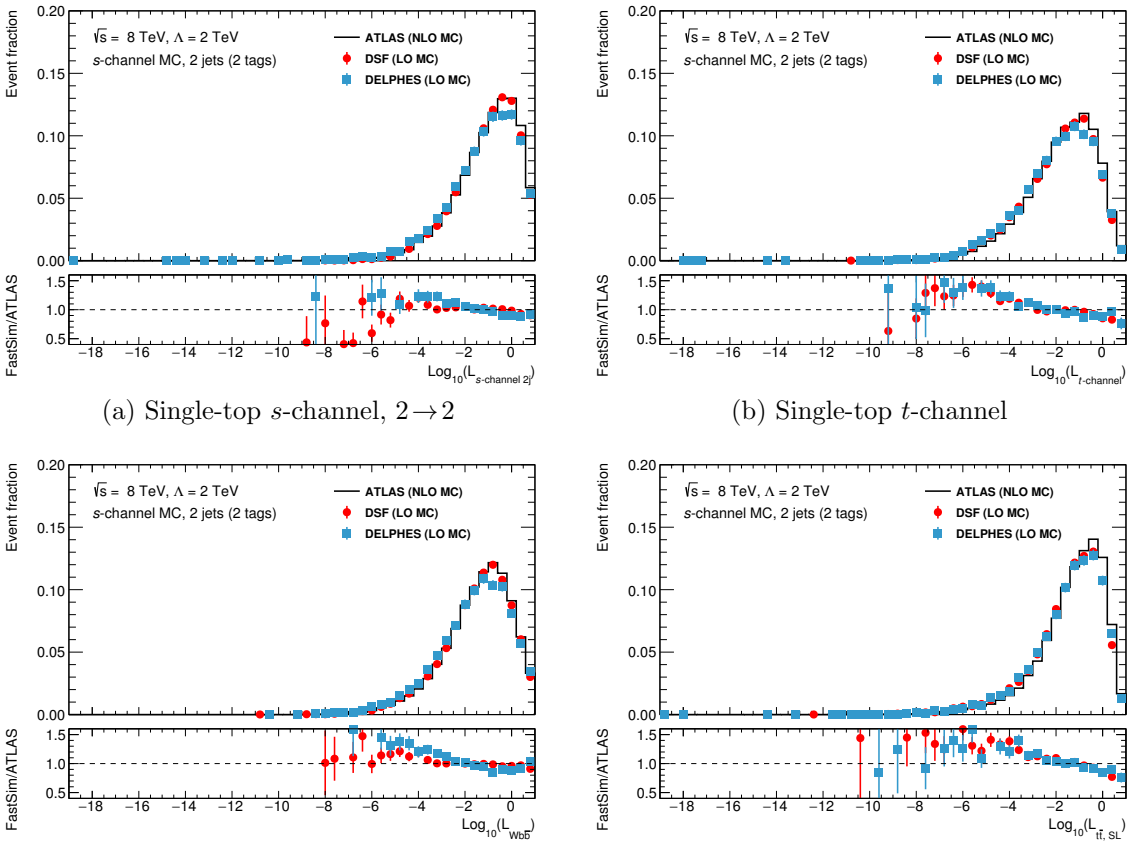

(a) Single-top s-channel, $2 \to 2$

(b) Single-top t-channel

(c) W+$b\bar{b}$ production

(d) $t\bar{t}$ production (single-lepton)

Figure 10.16.: Event likelihood distributions in the s-channel signal region using simulated s-channel events. (a) s-channel $2 \to 2$ process, (b) t-channel process, (c) W+$b\bar{b}$ production, (d) $t\bar{t}$ production (single-lepton)

10.4.4. Likelihood Distributions, t-Channel Signal Region

For the t-channel signal region, the likelihood distributions for simulated t-channel events are presented in Fig. 10.17. The t-channel and $t\bar{t}$ process for the DetSimFast

simulation is modelled well, while the W+c+jet and W+b$\bar{b}$ processes show a similar behaviour as in the s-channel signal region. For the DELPHES simulation only the t$\bar{t}$ process is close to the ATLAS prediction.

Based on the kinematic distributions presented in the previous sections, the modelling of the likelihoods is not expected to be perfect. The source of the mis-modelling might be the deviations in the pseudorapidity of the jets in the event as well as the missing dependence of the b-tagging on the pseudorapidity of the jet. More important than the likelihood modelling itself is the modelling of the discriminant distribution, which will be discussed in the next section.

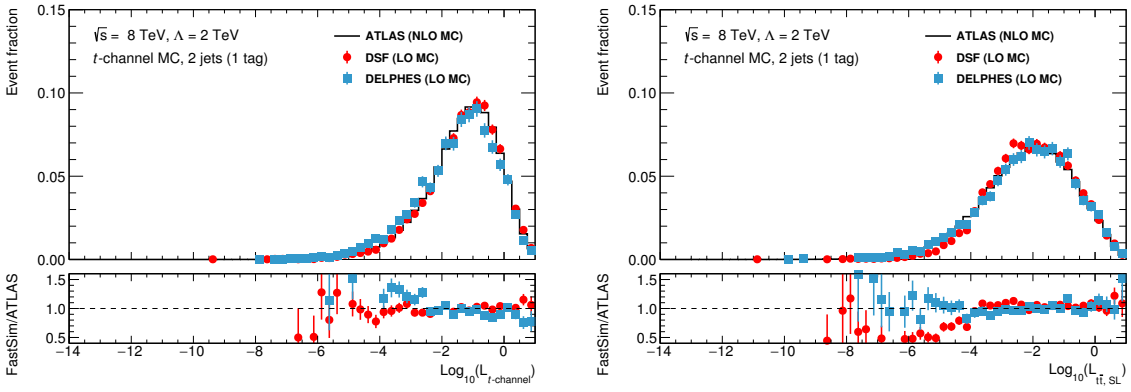

(a) Single-top t-channel

(b) t$\bar{t}$ production (single-lepton)

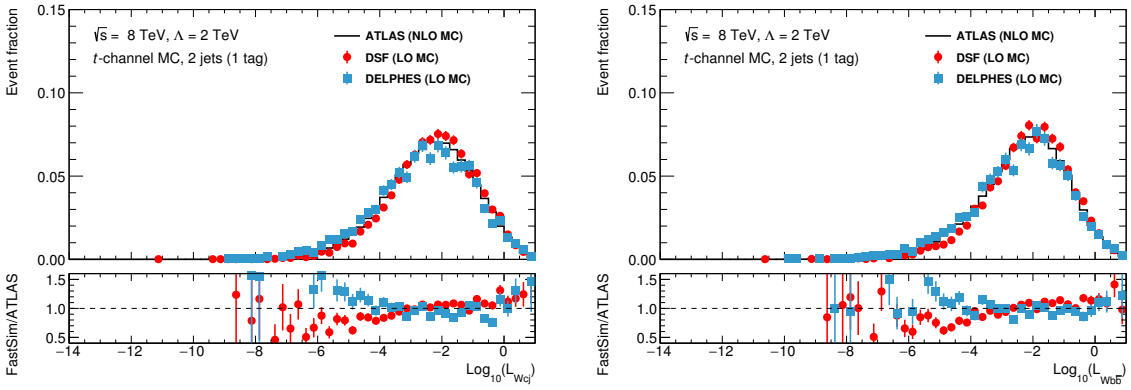

(c) W+c+jet production

(d) W+b$\bar{b}$ production

Figure 10.17.: Event likelihood distributions in the t-channel signal region using simulated t-channel events. (a) t-channel process, (b) t$\bar{t}$ production (single-lepton) (c) W+c+jet production and (d) W+b$\bar{b}$ production.

10.4.5. ME Discriminants

In both signal regions, the ME discriminant in each region is constructed from the likelihoods in the same way as described in Sec. 7.8.3. In the s-channel signal region,

the ME discriminant is computed for simulated s-channel and simulated t-channel events, while in the t-channel signal region, likelihoods are only evaluated for simulated t-channel events.

Finally, the modelling of the ME discriminants is depicted in Fig. 10.18 for the s-channel signal region. As for all distributions shown above, the results of DetSimFast and DELPHES are related. The s-channel discriminant for simulated s-channel events and using the DELPHES simulation is close to the ATLAS prediction over a wide range. The fraction of events for high discriminant values is increased with respect to the ATLAS simulation. It is even larger for the DetSimFast simulation. Thus, a discrepancy is also observed for very low discriminant values. Moreover, the s-channel discriminant for simulated t-channel events is described very well for almost all bins for both fast simulations. Overall, the simple simulations are able to reproduce the shape of the discriminant in this region to a certain degree, although the likelihood distributions show larger discrepancies to the ATLAS simulation.

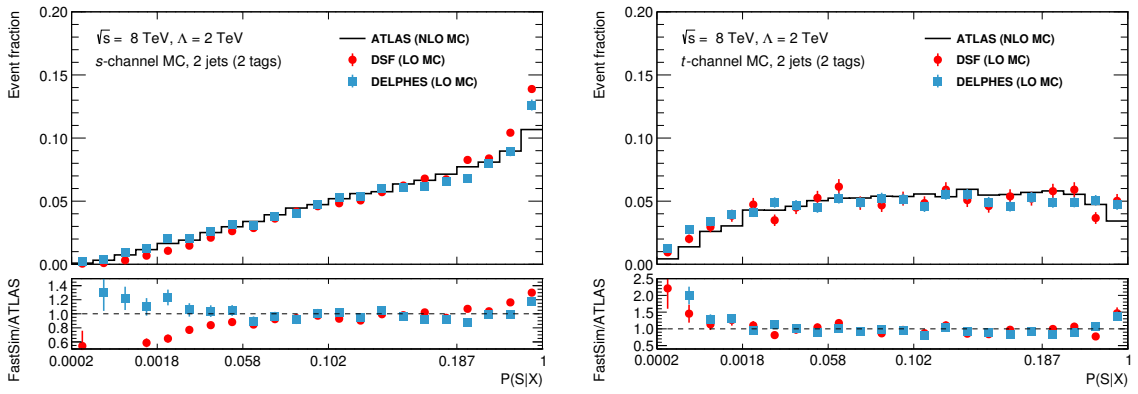

(a) s-channel ME discriminant for simulated s-channel events

(b) s-channel ME discriminant for simulated t-channel events

Figure 10.18.: ME discriminant in the s-channel signal region for (a) simulated s-channel events and (b) simulated t-channel events. Only statistical uncertainties are shown. Discrepancies with respect to the ATLAS simulation are observed for low and high discriminant values for simulated s-channel events, while the distribution for simulated t-channel events is modelled well.

The modelling of the t-channel discriminant for simulated t-channel events is shown in Fig. 10.19. The shape of the discriminant for the ATLAS simulation and the two fast simulations differs for high discriminant values. The reason for this discrepancy is unknown and could not be studied further within the scope of this thesis. As for the likelihood distributions, the pseudorapidity distributions of the two jets might be the cause of this discrepancies, but a further analysis is required. Nevertheless, the modelling of the kinematic distributions in this region is good. Furthermore, the mis-modelling of the ME discriminant in the t-channel signal region does not have an impact on the result of this analysis, which will be shown in the next two sections.

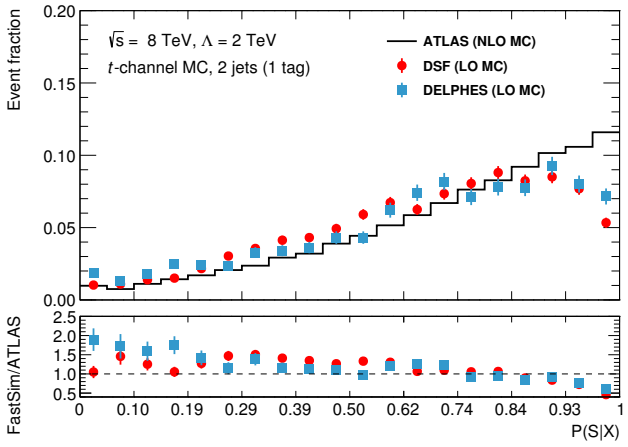

Figure 10.19: ME discriminant in the t-channel signal region using simulated t-channel events. Only statistical uncertainties are shown. Neither DetSimFast nor DELPHES is able to model the response of the ME discriminant in the t-channel signal region for high discriminant values.

10.5. Detector Response for $\bar{c}_{\mathrm{qq}}$

The kinematic distributions and the selection acceptance depend on the two couplings $\bar{c}_{\phi\mathrm{q}}$ and $\bar{c}_{\mathrm{qq}}$. In order to understand possible changes in the acceptance, it is useful to investigate the detector response for various kinematic distributions. If the strength for each coupling is varied separately, the operator $O^{(3)}_{\phi\mathrm{q}}$ simply rescales the Wtb vertex and can not be observed in angular distributions. Therefore, it is sufficient to study distributions only as a function of the coupling strength $\bar{c}_{\mathrm{qq}}$. In the following sections, the kinematic distributions for the two signal regions are shown using the DetSimFast detector simulation. Similar results are obtained for the DELPHES detector simulation as expected from the comparison shown in the previous section. Based on the cross section predictions, c. f. Sec. 10.2, the dependence on $\bar{c}_{\mathrm{qq}}$ is expected to be much larger for the s-channel single-top process than for the single-top t-channel process.

10.5.1. s-Channel Signal Region

The kinematic distributions in the s-channel signal region and for simulated s-channel events for four different values of $\bar{c}_{\mathrm{qq}}$ are shown in Fig. 10.20. A large fraction of events with a high transverse momentum of the charged lepton and of the leading jet is observed for a coupling strength $|\bar{c}_{\mathrm{qq}}| > 0$. The missing transverse momentum distributions shows the same trend. This behaviour is the expected result from a four-fermion contact interaction. The impact on the lepton pseudorapidity is minor, whereas more jets are produced in the central part of the detector. Furthermore, the reconstructed transverse W boson mass distribution is shifted to lower values, because the number of events originating from a W boson exchange decreases.

The distributions of the lepton transverse momentum and pseudorapidity, as well as the missing transverse momentum and transverse W boson mass are shown in Fig. 10.21 for simulated t-channel events in the s-channel signal region. In contrast to Fig. 10.20, the distributions corresponding to different $\bar{c}_{\mathrm{qq}}$ values do not show significant differences

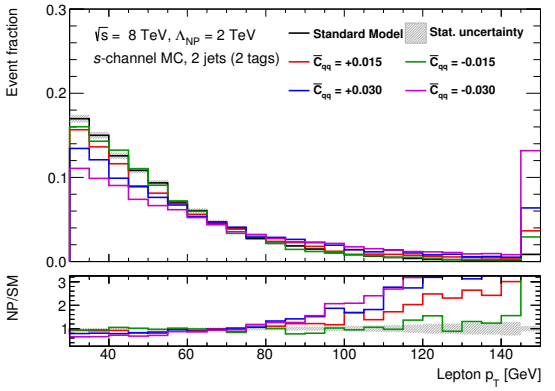

(a) Lepton transverse momentum

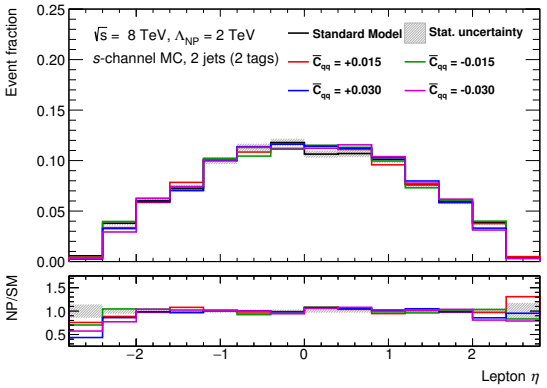

(b) Lepton pseudorapidity

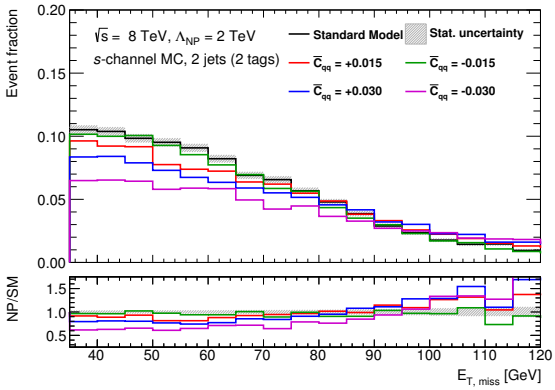

(c) Missing transverse momentum

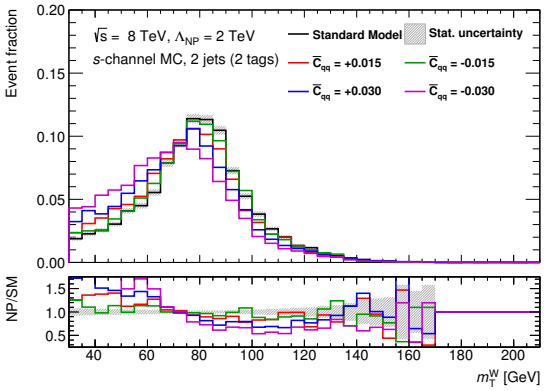

(d) Transverse W boson mass

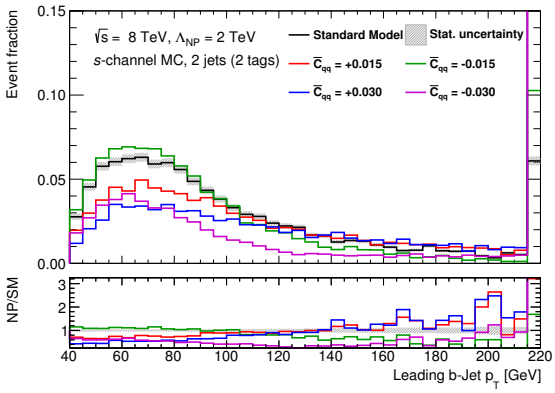

(e) Leading jet transverse momentum

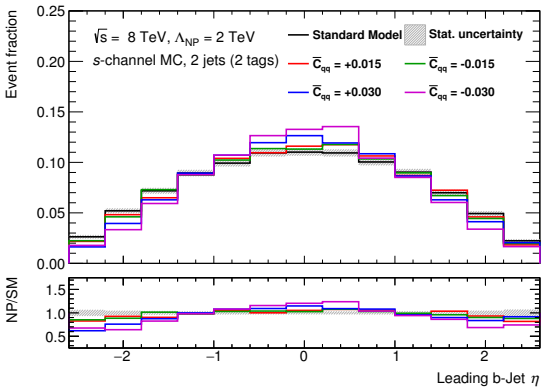

(f) Leading jet pseudorapidity

Figure 10.20.: Kinematic distributions for the *s*-channel signal selection (2 jets, 2 b-tags) and simulated *s*-channel events. The distributions show (a) Lepton transverse momentum, (b) Lepton pseudorapidity, (c) missing transverse momentum, (d) transverse W boson mass, (e) leading jet transverse momentum and (f) leading jet pseudorapidity for the combination of both selections, e+jets and μ+jets. The distributions for the second leading jet show a similar behaviour compared to the leading jet distributions. Only statistical uncertainties are shown.

with respect to the standard model prediction. In fact, the statistical uncertainties are in general much larger than the observed differences between the new physics (NP) and the standard model distributions. This characteristic is in agreement with the cross section dependence on $\bar{c}_{qq}$ for the single-top t-channel, which is much weaker compared to the single-top s-channel.

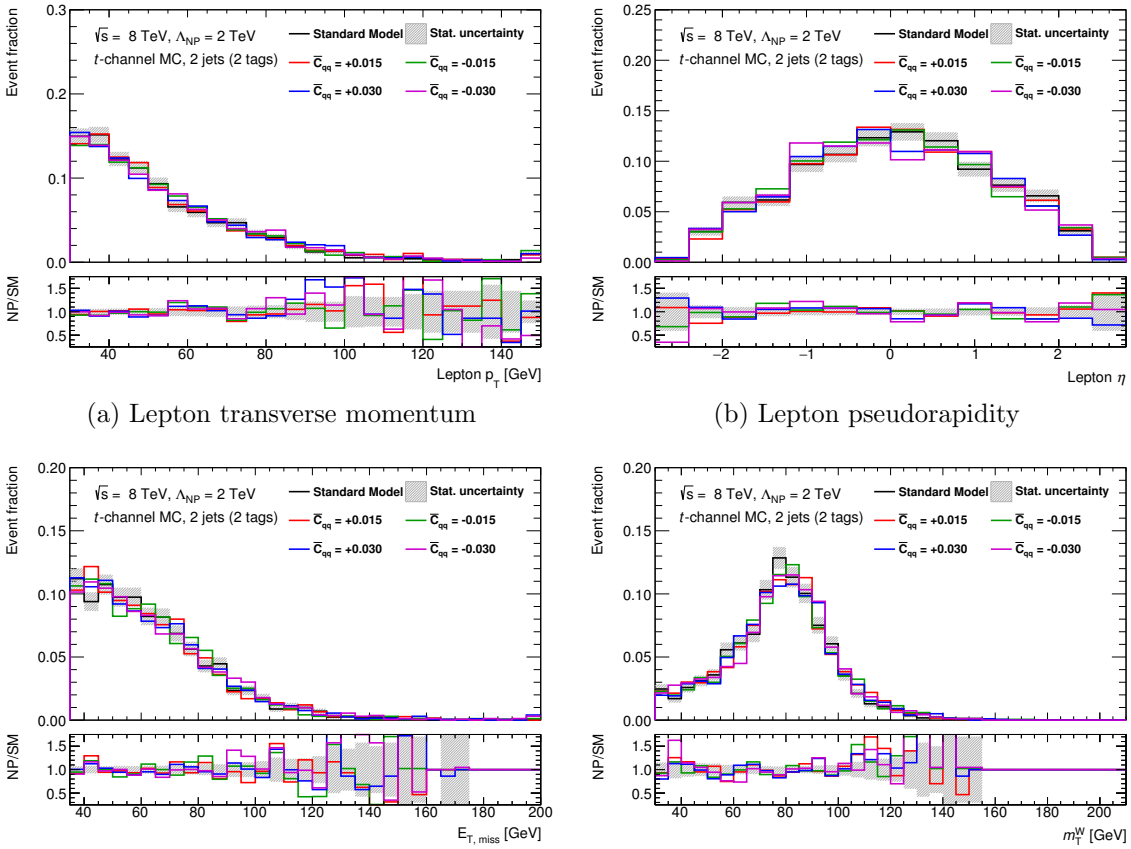

(a) Lepton transverse momentum

(b) Lepton pseudorapidity

(c) Missing transverse momentum

(d) Transverse W-boson mass

Figure 10.21.: Kinematic distributions for the s-channel signal selection (2 jets, 2 b-tags) and t-channel simulation. The distributions show (a) Lepton transverse momentum, (b) Lepton pseudorapidity, (c) missing transverse momentum and (d) transverse W boson mass for the combination of both lepton selections. Only statistical uncertainties are shown.

10.5.2. t-Channel Signal Region

The contribution from single-top s-channel events to the total number of observed events in the t-channel signal region is negligible. Therefore, only distributions using simulated t-channel events are studied and a selection of kinematic distributions is

presented in Fig. 10.22. Only minor variations with respect to the standard model are observed.

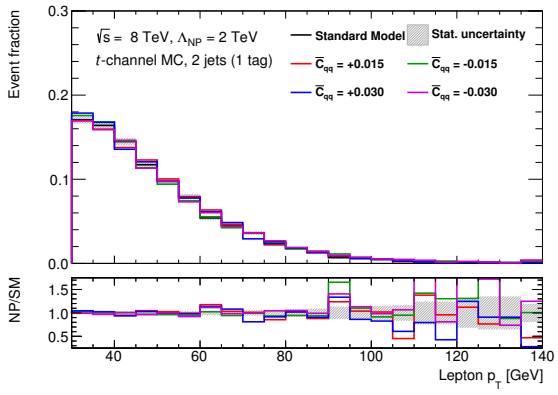

(a) Lepton transverse momentum

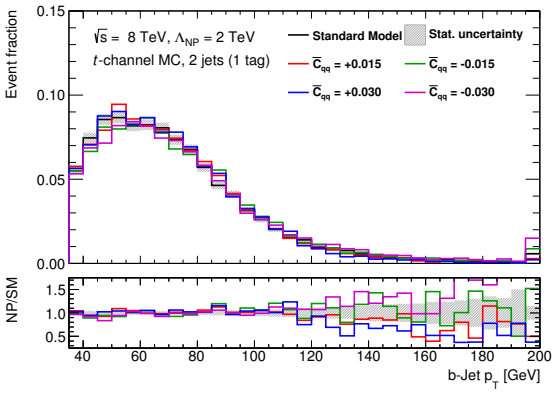

(b) Leading jet transverse momentum

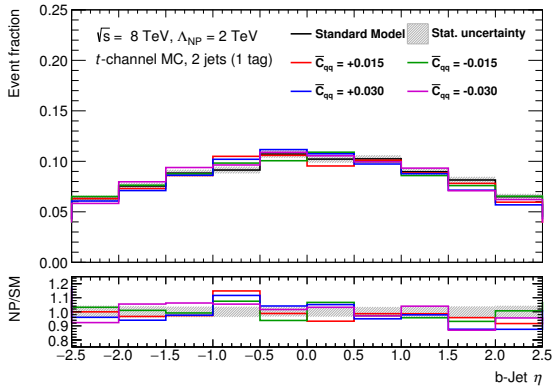

(c) Leading jet pseudorapidity

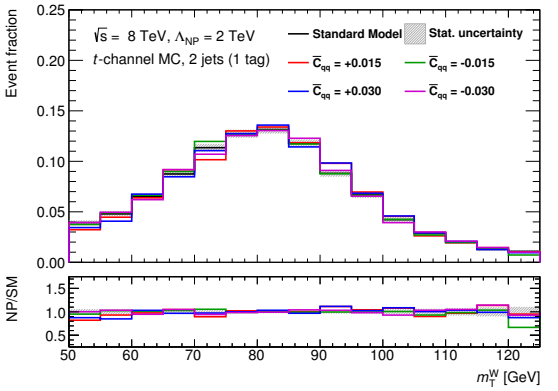

(d) Transverse W boson mass

Figure 10.22.: Kinematic distributions for the t-channel signal selection (2 jets, 1 b-tag) and t-channel simulation. The distributions show (a) lepton transverse momentum (b) leading jet transverse momentum (c) leading jet pseudorapidity and (d) transverse W boson mass for the combination of both selections, e+jets and μ+jets. Only statistical uncertainties are shown.

10.5.3. Matrix element discriminants

Finally, the impact of the coupling strength parameter $\bar{c}_{qq}$ on the matrix element discriminants is studied. The likelihoods for all processes are computed in the two signal regions for the standard model prediction and the four samples corresponding to the different choice of $\bar{c}_{qq}$. Next, the discriminants are build in the same way as described in Sec. 7.8.3. The resulting distributions are shown in Fig. 10.23 for simulated s-channel and simulated t-channel events in the two signal regions. The

s-channel discriminant exhibits a large increase in the fraction of events for the rightmost bin of the discriminant distribution. Most of the remaining bins are below the standard model prediction. Both discriminant distributions shown for simulated t-channel events show almost no variation in the shape with respect to the standard model prediction. This is in agreement with the small variations observed in the kinematic distributions in the previous sections. The computational effort for the s-channel likelihood computation is huge compared to the tiny event fraction and possible impact in the t-channel signal region. Therefore, the s-channel ME discriminant distribution is not studied in this region.

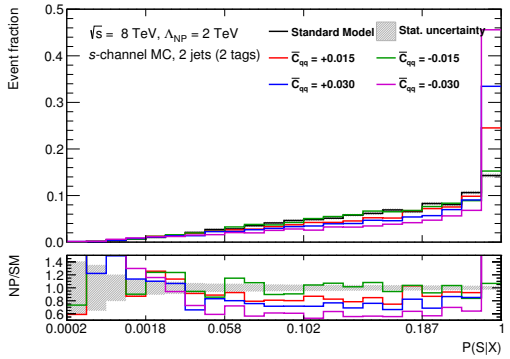

(a) s-channel ME discriminant (s-channel MC)

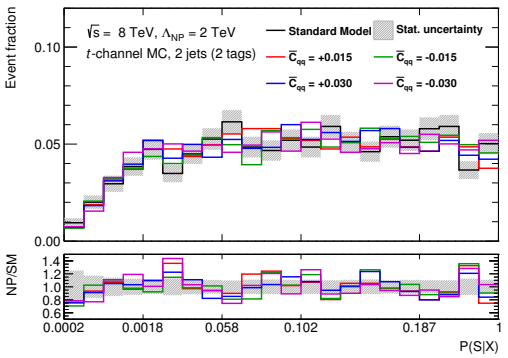

(b) s-channel ME discriminant (t-channel MC)

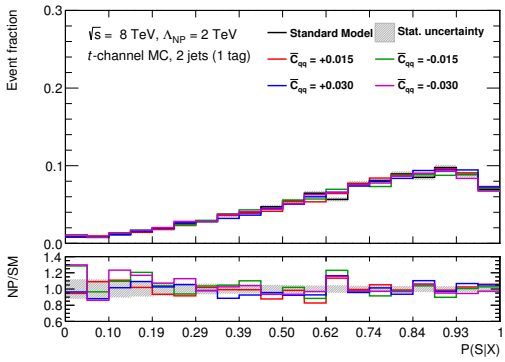

(c) t-channel ME discriminant (t-channel MC)

Figure 10.23.: ME discriminants in the s-channel and t-channel signal region using simulated s-channel and t-channel events. (a) s-channel ME discriminant (s-channel events, s-channel signal region), (b) s-channel ME discriminant (t-channel events, s-channel signal region) and (c) t-channel ME discriminant (t-channel events, t-channel signal region).

10.6. Effective Couplings Determination

In this section, the strategy for setting limits on the two parameters $\bar{c}_{\phi q}$ and $\bar{c}_{qq}$ of the effective field theory based on single top-quark cross section measurements is described. The relationship between the two couplings and the three inclusive cross sections for single top-quark production is given by Eq. 10.10. The coefficients for each channel (ch $\in \{s, t, \mathrm{Wt}\}$) are listed in Tab. 10.2. Let $\Delta\sigma = (\sigma_{\mathrm{ch}}^{\mathrm{exp}} - \sigma_{\mathrm{ch}}^{\mathrm{SM}})/\sigma_{\mathrm{ch}}^{\mathrm{SM}}$ denote the deviation of the measured cross section from the predicted one. Then, Eq. 10.10 can be rewritten as

$$\beta_{\phi q}^{\mathrm{ch}}\,\bar{c}_{\phi q}^{2} + \gamma^{\mathrm{ch}}\,\bar{c}_{\phi q}\bar{c}_{qq} + \beta_{qq}^{\mathrm{ch}}\,\bar{c}_{qq}^{2} + \alpha_{\phi q}^{\mathrm{ch}}\,\bar{c}_{\phi q} + \alpha_{qq}^{\mathrm{ch}}\,\bar{c}_{qq} - \Delta\sigma = 0. \tag{10.18}$$

Equation 10.18 is visualized in Fig. 10.24 and describes an ellipse in the $\bar{c}_{\phi q}$-$\bar{c}_{qq}$ plane, for which the values of the coupling parameters are compatible with the deviation $\Delta\sigma$ between the measurement and the SM prediction. In case of the associated Wt production, which only depends on $\bar{c}_{\phi q}$, Eq. 10.18 reduces to a simple linear equation. Each shaded band in Fig. 10.24 corresponds to the 68 % confidence interval defined by a single cross section measurement. The uncertainties for each measurement are 7 %, 17 % and 30 % for the t-channel, associated Wt and s-channel single top-quark production. For the single-top s-channel and t-channel production, the expected uncertainties obtained with the Asimov data set in this thesis are used, while for Wt production, the values are taken from the latest published ATLAS result [ATL16d] with $\sigma_{\mathrm{Wt}} = 23.0 \pm 1.3(\mathrm{stat.})^{+3.2}_{-3.5}(\mathrm{syst.}) \pm 1.1(\mathrm{lum.})\,\mathrm{pb}$. The central value of each measurement corresponds to the SM prediction.

Figure 10.24 shows that a measurement of the s-channel single top-quark cross section is most sensitive to the coupling strength associated with the four-fermion operator $O_{qq}^{(1,3)}$. Furthermore, the width of the shaded band is proportional to the measurement uncertainty. Although the t-channel is measured with an uncertainty that is about four times smaller than the s-channel, the shaded band is of similar size[11]. Therefore, an improved measurement of the s-channel cross section is of much higher interest than an improved t-channel measurement. The associated Wt production cross section measurement is only sensitive to $\bar{c}_{\phi q}$ and only constrains $\bar{c}_{\phi q}$. Moreover, it is apparent from Fig. 10.24 that a combination of all three single top-quark measurements provides the best limits on the two couplings. A tool for extracting limits by the combination of several measurements is the EFT*fitter*, which will be described in the next section. Section 10.6.2 will be dedicated to corrections from model-dependant acceptance and efficiency corrections that need to be included in the statistical analysis. Such corrections can be easily integrated into the EFT*fitter* and the results of the statistical analysis are presented in Sec. 10.6.3.

[11] With the exception close to $\bar{c}_{\phi q} = 0.1$.

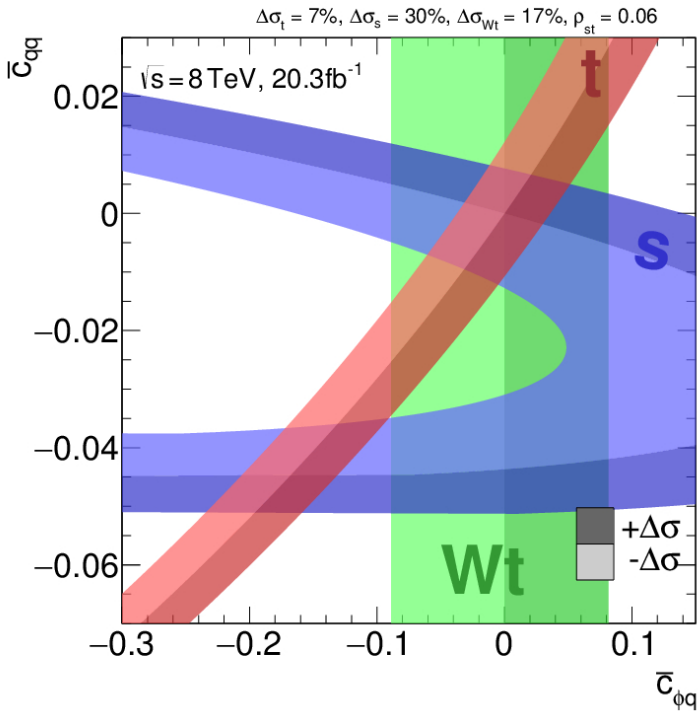

Figure 10.24.: Constraints from a single cross section measurement for each of the three single-top production channels at ATLAS with $\sqrt{s} = 8\,\text{TeV}$ in the $\bar{c}_{\phi q}$–$\bar{c}_{qq}$ plane. The central value corresponds to the SM prediction. The measurements uncertainties are represented by the three coloured bands. The darker bands indicate the upward measurement uncertainties, while the lighter coloured bands show the downward uncertainties. The measurement uncertainties for the single-top s-channel and t-channel production are based on the expected results in Sec. 9.2 of this thesis, while the uncertainty for the Wt production is taken from [ATL16d].

10.6.1. EFTfitter

The EFT*fitter* [Cas+16] is a generic tool for performing interpretations of measurements in the context of an effective field theory. The statistical treatment of combining measurement is based on Bayesian statistics. The relevant parts of the tools are outlined in this section.

The values of free parameters $\boldsymbol{\lambda}$ of a model M are estimated in Bayesian reasoning by evaluating the posterior probability

$$p(\boldsymbol{\lambda}|\boldsymbol{x}) = \frac{p(\boldsymbol{x}|\boldsymbol{\lambda}) \cdot p(\boldsymbol{\lambda})}{\int \mathrm{d}\boldsymbol{\lambda}\, p(\boldsymbol{x}|\boldsymbol{\lambda}) \cdot p(\boldsymbol{\lambda})} \tag{10.19}$$

of the parameters $\boldsymbol{\lambda}$ given a data set $\boldsymbol{x}$. The prior probability of the parameters $\boldsymbol{\lambda}$ is denotes as $p(\boldsymbol{\lambda})$, while the probability of the data, or likelihood, is denoted as $p(\boldsymbol{x}|\boldsymbol{\lambda})$. Regarding this thesis, the parameters of the model, the coefficients $\bar{c}_{\phi q}$ and $\bar{c}_{qq}$, can

not be directly measured from the data. Instead the observables $\boldsymbol{y}$, i. e. the three single top-quark cross sections depend on the parameters of the model. In order to extract limits on the two couplings, the EFT*fitter* performs a fit of these couplings based on the cross section predictions, for example defined by Eq. 10.11.

The model predictions for the observables $y_i = y_i(\boldsymbol{\lambda})$ are compared to the measurements x_i using a multivariate Gaussian model. In this case, the likelihood for a set of N observables y_i, which are estimated based on n measurements x_i can be written as[12]

$$-2 \ln p(\boldsymbol{x}|\boldsymbol{y}) = \sum_{i=1}^{n} \sum_{j=1}^{n} [\boldsymbol{x} - U\boldsymbol{y}]_i \mathcal{M}_{ij}^{-1} [\boldsymbol{x} - U\boldsymbol{y}]_j. \tag{10.20}$$

The elements U_{ij} of the $n \times N$-matrix U are unity if x_i is a measurement of the observable y_i and zero otherwise. The elements of the covariance matrix of the measurements is denoted as $\mathcal{M}_{ij}$. In the Bayesian approach, estimators are obtained by inserting the likelihood defined in Eq. 10.20 into the expression of the posterior probability in Eq. 10.19. Given that the observables y_i depend on the model parameters, the likelihood of the model in this thesis is

$$p(\boldsymbol{x}|\boldsymbol{\lambda}) = \int \mathrm{d}\boldsymbol{y}\ p(\boldsymbol{x}|\boldsymbol{y}) \cdot p(\boldsymbol{y}|\boldsymbol{\lambda}), \tag{10.21}$$

with $p(\boldsymbol{y}|\boldsymbol{\lambda}) = \delta(\boldsymbol{y} - \boldsymbol{y}(\boldsymbol{\lambda}))$. Estimators for the parameter values are obtained by the set of parameters that maximize the posterior probability. Uncertainty estimates are defined by using the marginal probabilities

$$p(\lambda_i|\boldsymbol{x}) = \int \prod_{j \neq i} \mathrm{d}\lambda_i\ p(\boldsymbol{\lambda}|\boldsymbol{x}). \tag{10.22}$$

The uncertainty on the parameter λ_i can be defined as the smallest intervals containing 68 % probability. Simultaneous estimates of the uncertainties on y_i and y_j are derived from the two-dimensional contours of the smallest intervals containing 68 % probability. The definitions for the estimators of the parameters' central values and their uncertainties given above are used in this thesis. Other possible choices are discussed in [Cas+16].

10.6.2. Acceptance Corrections

The measurement performed in Sec. 9 provides two input quantities to the EFT*fitter*, namely the single-top s-channel and t-channel cross sections. The EFT*fitter* tool compares the measured values to the cross section prediction as defined in Eq. 10.11. However, as seen in Sec. 10.5, the kinematic distributions change as a function of the model parameters, $\bar{c}_{\phi \mathrm{q}}$ and $\bar{c}_{\mathrm{qq}}$, and therefore, the selection efficiency defined as the

[12] It is assumed that each quantity y_i is measured $n_i \geq 1$ times.

ratio of the number of selected events to the number of generated events, $N_{\text{sel}}/N_{\text{gen}}$ is different for the EFT model and the SM. Moreover, the shape of the discriminant depends also on the model parameters. Such acceptance corrections[13] need to be included in the model predictions.

Therefore, Eq. 10.11 needs to be extended by an additional factor α_{ch}, which accounts for acceptance correction for the particular process:

$$\sigma_{\text{ch}}^{\text{exp}} = \sigma_{\text{ch}}^{\text{EFT}}(\bar{c}_{\phi\text{q}}, \bar{c}_{\text{qq}}) \cdot \alpha_{\text{ch}}(\bar{c}_{\phi\text{q}}, \bar{c}_{\text{qq}}). \tag{10.23}$$

Here, $\sigma_{\text{ch}}^{\text{EFT}}(\bar{c}_{\phi\text{q}}, \bar{c}_{\text{qq}})$ is the cross section prediction from the EFT model without including any acceptance corrections. Furthermore, $\sigma_{\text{ch}}^{\text{exp}}$ is the correct model prediction of the observables y_i, which should be compared to the measurements x_i by the EFT*fitter*, instead of $\sigma_{\text{ch}}^{\text{EFT}}(\bar{c}_{\phi\text{q}}, \bar{c}_{\text{qq}})$.

The acceptance corrections α_{ch} can be determined from Eq. 10.23. The quantity $\sigma_{\text{ch}}^{\text{exp}}$ is the cross section that is obtained in an analysis, such as the one presented in this thesis, if the data would correspond to a certain EFT scenario with $\bar{c}_{\phi\text{q}} \neq 0$ and $\bar{c}_{\text{qq}} \neq 0$. The data distribution, which is necessary to determine $\sigma_{\text{ch}}^{\text{exp}}$ for a specific set of EFT model parameters is unknown. It is therefore approximated by a pseudo-data set, which will be specified below. Once the pseudo-data set is at hand, the cross section $\sigma_{\text{ch}}^{\text{exp}}$ is obtained by a fit to this pseudo-data set using the same procedure as described in Sec. 9. In particular, the fit uses only SM predictions, i. e. only ATLAS templates are used to describe the pseudo-data distribution in the fit. The overall strategy is to build a couple of pseudo-data sets corresponding to different values for $\bar{c}_{\phi\text{q}}$ and $\bar{c}_{\text{qq}}$. For each of the pseudo-data sets, $\sigma_{\text{ch}}^{\text{exp}}$ and accordingly α_{ch} can be calculated. In such a way a semi-analytic expression is derived for $\alpha_{\text{ch}}(\bar{c}_{\phi\text{q}}, \bar{c}_{\text{qq}})$ and further values can be calculated by an interpolation between grid points.

The pseudo-data set for the ME discriminant distributions in the s-channel and t-channel signal region is built in the following way. The normalization and discriminant shape of the background contributions ($\text{t}\bar{\text{t}}$, Wt, W+jets, multi-jet, etc.) are simply taken from the ATLAS templates that are used in the signal extraction fit. In order to model the contribution of the s-channel and t-channel processes to the pseudo-data set, events are generated with MadGraph for different values of the two couplings $\bar{c}_{\phi\text{q}}$ and $\bar{c}_{\text{qq}}$. The employed values are identical to the ones listed in Tab. 10.1 and create an equally spaced grid in the $\bar{c}_{\phi\text{q}}$–$\bar{c}_{\text{qq}}$ plane. Additional nine grid points are added on a line at $\bar{c}_{\text{qq}} = -0.0197$ to account for the minimum in the cross section shown in Fig. 10.6(b). Subsequently, all generated events are passed on to the fast detector simulations, DetSimFast or Delphes, to model the ATLAS detector response for these events. For each grid point, the matrix element likelihoods are calculated and the ME discriminant is built. Finally, a pseudo-data set is created for each grid point by adding up the signal and background discriminants contributions. The

[13] In the following, corrections due to change in the selection acceptance or the shape of the discriminant are simply referred to as "acceptance corrections".

normalization and shape for the discriminant using simulated s-channel events is taken from the fast detector simulation. For simulated t-channel events, the shape of the ME discriminant does not differ significantly from the SM prediction, as presented in Sec. 10.5. Therefore, only the normalization of the templates for simulated t-channel events are derived from the fast detector simulation and the shape corresponds to the one obtained with the ATLAS simulation. The normalization for templates that are created using the fast detector simulations is discussed in the next paragraph.

The number of events corresponding to the integrated luminosity $\mathcal{L}$ of the ATLAS data set, $N_{\text{lumi}}^{\text{DetSimFast}}$, for each template from the DetSimFast simulation[14] is calculated as

$$N_{\text{lumi}}^{\text{DetSimFast}}(\bar{c}_{\phi\text{q}}, \bar{c}_{\text{qq}}) = \frac{\sigma_{\text{NLO}}}{\sigma_{\text{EFT}}(0,0)} \cdot \mathcal{A} \cdot \frac{\mathcal{L} \cdot \sigma_{\text{EFT}}(\bar{c}_{\phi\text{q}}, \bar{c}_{\text{qq}})}{N_{\text{gen}}^{\text{DetSimFast}}} \cdot N_{\text{sel}}^{\text{DetSimFast}}. \tag{10.24}$$

The predicted cross section for each sample is denotes as σ_{EFT}, while the number of generated and selected events for each sample are N_{gen} and N_{sel}, respectively. Equation 10.24 contains explicitly the so-called k-factor, $\frac{\sigma_{NLO}}{\sigma_{\text{EFT}}(0,0)}$, which is the constant ratio of NLO QCD cross section to LO QCD cross section.[15] Furthermore, the factor $\mathcal{A}$ accounts for the differences between the ATLAS simulation and the DetSimFast simulation. It should not be mistaken with the acceptance correction discussed in the previous paragraphs. The constant factor $\mathcal{A}$ simply accounts for the differences in the selection acceptance due to less stringent object definitions or general simplifications that apply for the fast detector simulations. For example, the DetSimFast simulation replaces the hadron shower by the corresponding transfer function. The factor $\mathcal{A}$ is fixed by the normalization condition

$$N_{\text{lumi}}^{\text{DetSimFast}}(0,0) = N_{\text{lumi}}^{\text{ATLAS}}. \tag{10.25}$$

Thus, the normalization of the simple detector simulations sample for the SM configuration is chosen, such that the number of predicted events is equal to the number of events, $N_{\text{lumi}}^{\text{ATLAS}}$, obtained with the ATLAS simulation using the nominal POWHEG +PYTHIA sample.

The acceptance correction $\alpha_{s|t}$ for the single-top s-channel and t-channel cross section can be calculated as the ratio of the cross section obtained from the fit to the pseudo-data set, $\sigma_{s|t}^{\text{fit}}$, to the predicted cross section by the EFT model, $\sigma_{s|t}^{\text{EFT}}$ (c. f. Eq. 10.11):

$$\alpha_{s|t}(\bar{c}_{\phi\text{q}}, \bar{c}_{\text{qq}}) = \frac{\sigma_{s|t}^{\text{fit}}(\bar{c}_{\phi\text{q}}, \bar{c}_{\text{qq}})}{\sigma_{s|t}^{\text{EFT}}(\bar{c}_{\phi\text{q}}, \bar{c}_{\text{qq}})}. \tag{10.26}$$

However, Eq. 10.26 needs to be extended in order to take into account that the shape of the ME discriminant is not perfectly reproduced by the analysis performed on

[14] The following equations apply in the same way to event samples obtained with the DELPHES simulation.

[15] The MADGRAPH model provides LO QCD cross sections only. The k-factor is included in Eq. 10.24 for conventional reasons. Alternatively, the acceptance $\mathcal{A}$ could be scaled by the same factor.

events that are generated with the LO MadGraph model and processed with one of the fast simulations. The problem is mitigated by using normalized quantities in Eq. 10.26 instead of absolute cross section values. Therefore, the acceptance correction α is calculated as

$$\alpha_{s|t}(\bar{c}_{\phi\mathrm{q}}, \bar{c}_{\mathrm{qq}}) = \frac{\sigma^{\mathrm{fit}}_{s|t}(\bar{c}_{\phi\mathrm{q}}, \bar{c}_{\mathrm{qq}})}{\sigma^{\mathrm{fit}}_{s|t}(0,0)} \Bigg/ \frac{\sigma^{\mathrm{EFT}}_{s|t}(\bar{c}_{\phi\mathrm{q}}, \bar{c}_{\mathrm{qq}})}{\sigma^{\mathrm{EFT}}_{s|t}(0,0)} \,. \tag{10.27}$$

Here, $\sigma^{\mathrm{fit}}_{s|t}(0,0)$ denotes the fit result to the pseudo-data set, which correspond to a SM configuration. The denominator, $\sigma^{\mathrm{EFT}}_{s|t}(0,0)$, is simply the SM LO QCD cross section calculated with MadGraph. In total, the acceptance correction is extracted for each of the 81 pseudo-data sets defined above.

The values for $\bar{c}_{\phi\mathrm{q}}$ and $\bar{c}_{\mathrm{qq}}$, that are used to generate the pseudo-data sets, form a rectangular grid in the $\bar{c}_{\phi\mathrm{q}}$–$\bar{c}_{\mathrm{qq}}$ plane. Therefore, the acceptance correction can be mapped into this plane and any value $\alpha_{\mathrm{ch}}(\bar{c}_{\phi\mathrm{q}}, \bar{c}_{\mathrm{qq}})$ inside this grid can be calculated by using a linear interpolation. However, as stated in Eq. 10.11, the cross section can be expressed as

$$\sigma^{\mathrm{EFT}}_{\mathrm{ch}} = \sigma^{\mathrm{SM}}_{\mathrm{ch}} \left(\left(1 + \frac{\bar{c}_{\phi\mathrm{q}}}{V_{\mathrm{tb}}} \right)^2 + \alpha^{\mathrm{ch}}_{\mathrm{qq}} \left(1 + \frac{\bar{c}_{\phi\mathrm{q}}}{V_{\mathrm{tb}}} \right) \bar{c}_{\mathrm{qq}} + \beta^{\mathrm{ch}}_{\mathrm{qq}} \bar{c}^2_{\mathrm{qq}} \right) . \tag{10.28}$$

The structure of this equation reflects the fact that the $c^{(3)}_{\phi\mathrm{q}}$-term in the Lagrangian simply rescales the V_{tb} vertex. The shape of any differential distribution depends only on contributions from the $O^{(1,3)}_{\mathrm{qq}}$ operator, either directly or by interference with the SM+$O^{(3)}_{\phi\mathrm{q}}$ process. Therefore, the acceptance correction should only depend on the ratio of $\frac{\bar{c}_{\mathrm{qq}}}{1+\bar{c}_{\phi\mathrm{q}}}$. The acceptance correction as a function of $\frac{\bar{c}_{\mathrm{qq}}}{1+\bar{c}_{\phi\mathrm{q}}}$ is shown in Fig. 10.25 for single-top s-channel and t-channel cross section. The rectangular grid is has an equally spacing in $\bar{c}_{\phi\mathrm{q}}$ and $\bar{c}_{\mathrm{qq}}$ direction and is therefore not suitable to generate points at the same $\frac{\bar{c}_{\mathrm{qq}}}{1+\bar{c}_{\phi\mathrm{q}}}$ positions.[16] Therefore, the average over adjacent points is calculated and displayed in Fig. 10.25, instead of 81 individual points for both, DetSimFast and Delphes, simulations. The acceptance correction for intermediate points is obtained by a simple linear interpolation. The results from the two fast simulations are very similar as expected from the distributions shown in Sec. 10.4. Currently, the Delphes simulation is not officially permitted by the ATLAS experiment, hence the acceptance corrections derived with the DetSimFast simulation will be used to constrain the parameters of the EFT model.

Based on the one-dimensional acceptance corrections in Fig. 10.25, the acceptance correction for the single-top s-channel and t-channel cross sections in the $\bar{c}_{\phi\mathrm{q}}$–$\bar{c}_{\mathrm{qq}}$ plane are visualized in Fig. 10.26.

[16] The simplification of the acceptance correction function from $\alpha(\bar{c}_{\phi\mathrm{q}}, \bar{c}_{\mathrm{qq}})$ to $\alpha(\bar{c}_{\mathrm{qq}}/(1+\bar{c}_{\phi\mathrm{q}})$ was realized only after all matrix elements likelihoods for all 81 grid points were computed. The effort to choose better suitable grid would have been tremendous in terms of computing resources.

No acceptance corrections for the Wt measurement are necessary, because the cross section for this processes does not depend on the parameter $\bar{c}_{\mathrm{qq}}$. Therefore, the acceptance corrections for this measurement are always $\alpha_{\mathrm{Wt}}(\bar{c}_{\phi\mathrm{q}}, \bar{c}_{\mathrm{qq}}) = 1$.

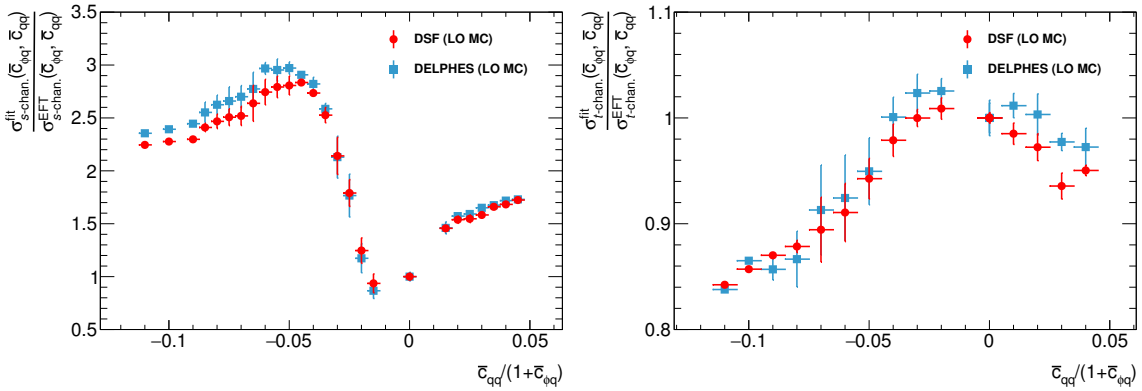

(a) $\alpha_{s\text{-channel}}$ (b) $\alpha_{t\text{-channel}}$

Figure 10.25.: Acceptance corrections α for (a) single-top s-channel cross section and (a) single-top t-channel cross section. The acceptance corrections are determined by fits to 81 pseudo-data sets. The signal contributions for these pseudo-data sets are modelled by the fast simulations, DetSimFast or DELPHES, while the background contribution are obtained from the ATLAS simulation. The acceptance correction is averaged over adjacent points.

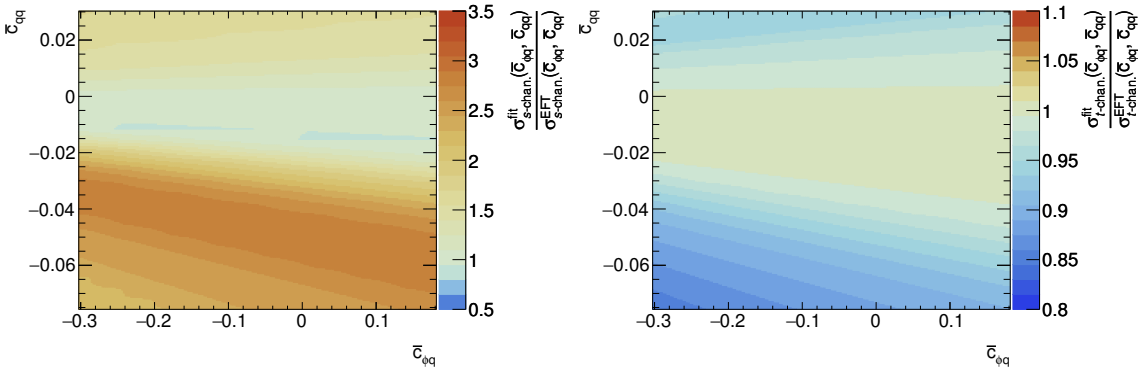

(a) $\alpha_{s\text{-channel}}$ (b) $\alpha_{t\text{-channel}}$

Figure 10.26.: Acceptance corrections α for (a) single-top s-channel cross section and (a) single-top t-channel cross section in the $\bar{c}_{\phi\mathrm{q}}$–$\bar{c}_{\mathrm{qq}}$ plane. The two-dimensional distribution is obtained from Fig. 10.25 using the DetSimFast simulation.

10.6.3. Results

The parameters $\bar{c}_{\phi q}$ and $\bar{c}_{qq}$ of the effective field theory model are fitted based on the relations given by Eq. 10.23. The acceptance corrections are derived using the DetSimFast simulation as explained in the previous section.

First, the fit is performed using the expected results for the s-channel and t-channel cross section measurements given in this thesis. The expected correlation between the two measurements is 6 %. The central value for the associated Wt production cross section is taken from the theoretical prediction by [Kid10b], while an experimental measurement uncertainty of 17 % is assumed. The result of this fit is depicted in Fig. 10.27. The cross indicates the SM value using the NLO predictions for the s and t-channel, and NLO+NNLL prediction for Wt. The dot marks the maximum of the posterior probability, which in this case is identical to the SM prediction as expected. In addition, the 1σ, 2σ and 3σ contours corresponding to the smallest intervals of 68.3 %, 95.5 % and 99.7 % probability are drawn. The 1σ interval is splitted into two distinct regions, however these two region almost overlap. The shaded bands[17] display the regions for the coupling parameters, which are compatible within the expected cross section measurements and their uncertainties. As in Fig. 10.24, these bands correspond to the constraints from a single measurement.

Secondly, the observed results for the two couplings are obtained by using the measurement results of this thesis for single top-quark production in the s and t-channel listed in Tab. 9.5. The correlation of these two measurements is $\rho_{st} = 0.08$. For the associated Wt production, the measurement result given in [ATL16d] with $\sigma_{Wt} = 23.0 \pm 3.9$pb is utilized. Any correlation between the s-channel or t-channel measurement and the Wt production is neglected. The result of the fit is shown in Fig. 10.28. The global fit maximum is close the SM expectation. The observed cross section of all three single-top production channels differ from the theoretical prediction. As a consequence, the shaded bands in Fig. 10.28 are shifted with respect to Fig. 10.27, because they represent the constraints from the observed cross section measurements instead of the expected ones. In addition, there is only one smallest 1σ-interval, which is caused by the difference between the expected and observed cross sections. Otherwise, the expected and observed results are similar in terms of the 1σ, 2σ and 3σ contours.

The marginal distributions are obtained from the posterior probability distribution for each of the two parameters. For the observed case, these distributions are presented in Fig. 10.29. The coloured areas correspond to the smallest intervals of 68.3 %, 95.5 % and 99.7 % probability. The results for the two couplings $\bar{c}_{\phi q}$ and $\bar{c}_{qq}$ are determined from the marginal distributions and the 1σ, 2σ and 3σ intervals are listed in Tab. 10.6.

[17] No acceptance corrections enter the theoretical predictions, which are used to visualize Eq. 10.18.

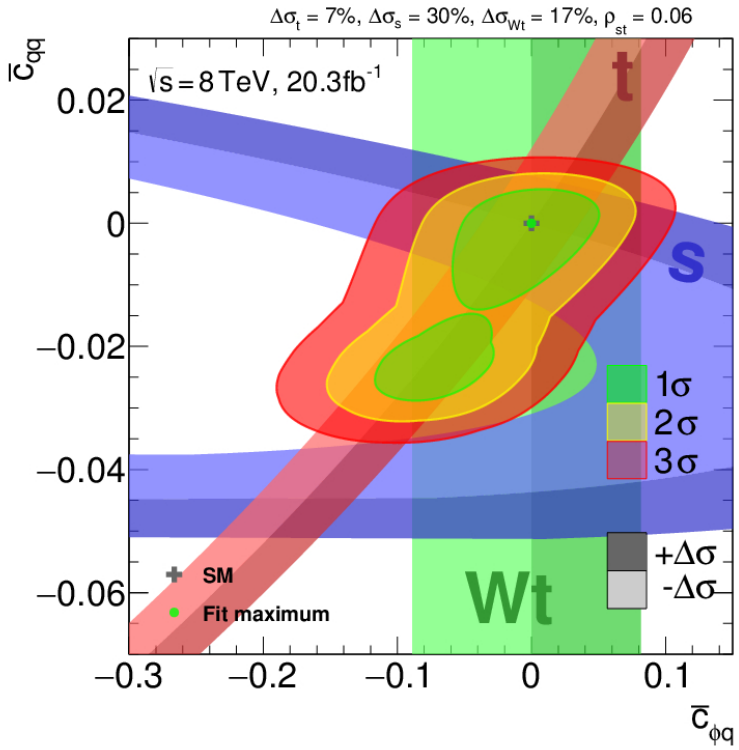

Figure 10.27.: Fit results for the effective couplings $\bar{c}_{\phi q}$ and $\bar{c}_{qq}$ based on the expected measurement uncertainties for the three single-top production channels at ATLAS with $\sqrt{s}=8\,\text{TeV}$. The three single-top cross sections and their expected measurement uncertainties are represented by the three coloured bands in the $\bar{c}_{\phi q}$–$\bar{c}_{qq}$ plane. The smallest 1σ, 2σ and 3σ intervals based on the posterior probability for $\bar{c}_{\phi q}$ and $\bar{c}_{qq}$ are displayed. The fit includes acceptance corrections derived with the DetSimFast simulation using events generated with MadGraph.

coupling	Maximum	1σ interval(s)	2σ interval	3σ interval
$\bar{c}_{\phi q}$	-0.011	[-0.082, 0.012]	[-0.132, 0.048]	[-0.178, 0.083]
$\bar{c}_{qq}$	-0.0003	[-0.0243, -0.0192] [-0.0106, 0.0045]	[-0.0283, 0.0062]	[-0.0331, 0.0095]

Table 10.6.: Results for the two coupling parameters $\bar{c}_{\phi q}$ and $\bar{c}_{qq}$. The fit maximum as well as the smallest 1σ, 2σ and 3σ intervals based on the marginal distributions are listed.

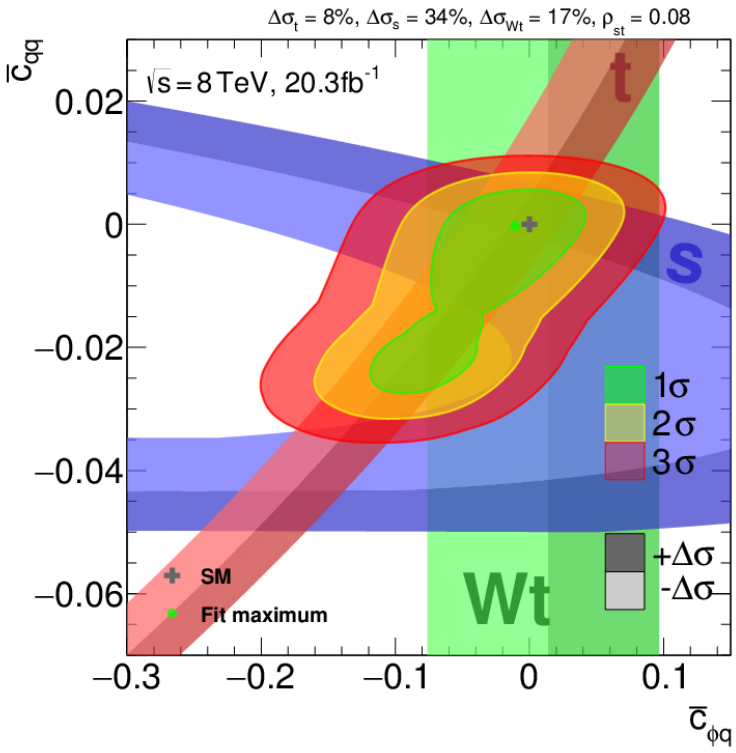

Figure 10.28.: Fit results for the effective couplings $\bar{c}_{\phi q}$ and $\bar{c}_{qq}$ based on the measurements of the three single-top production channels at ATLAS with $\sqrt{s}=8\,\text{TeV}$. The measurements and their uncertainties are represented by the three coloured bands in the $\bar{c}_{\phi q}$–$\bar{c}_{qq}$ plane. The smallest 1σ, 2σ and 3σ intervals based on the posterior probability for $\bar{c}_{\phi q}$ and $\bar{c}_{qq}$ are displayed. The fit includes acceptance corrections derived with the DetSimFast simulation using events generated with MadGraph.

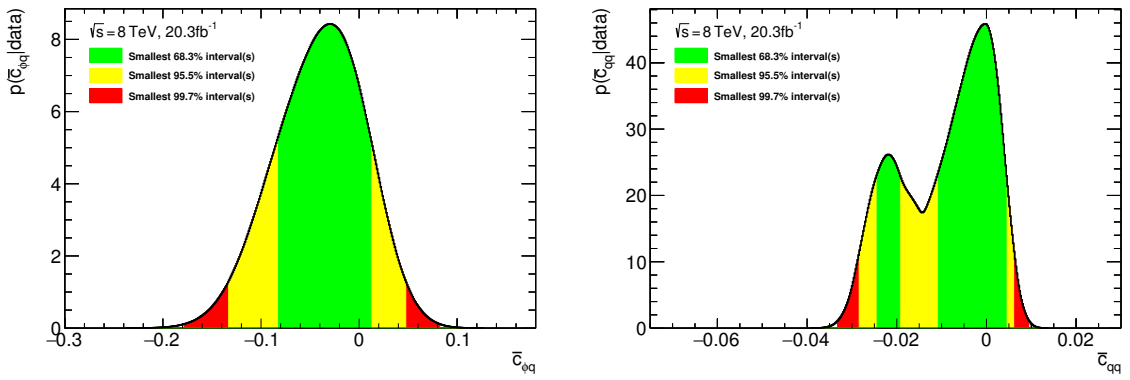

(a) Marginal distribution for $\bar{c}_{\phi q}$

(b) Marginal distribution for $\bar{c}_{qq}$

Figure 10.29.: The marginal probability distributions obtained from the posterior probability for (a) $\bar{c}_{\phi q}$ and (b) $\bar{c}_{qq}$. The fit includes the acceptance corrections derived in Sec. 10.6.2.

10.6.4. Acceptance Corrections Discussion

In this section, the impact from the acceptance corrections derived in Sec. 10.6.2 on the measurement of $\bar{c}_{\phi q}$ and $\bar{c}_{qq}$ is discussed. For the measurement results presented above acceptance corrections are included, which take into account the change of the normalization and the shape of the ME discriminant as a function of the two parameters. Furthermore, these corrections depend on the response of the DetSimFast simulation.

Different scenarios for including the acceptance corrections in the fit are tested. First, the ME discriminant in the s-channel is very sensitive to the strength at the $O_{qq}^{(1,3)}$ vertex. Therefore, the acceptance corrections are derived without taking into account possible changes in the shape of the ME discriminant. This means, that in the pseudo-data set generation, the single-top s-channel normalization is calculated with Eq. 10.24, but the shape of the template corresponds to the nominal ATLAS template. Second, the alternative fast simulation DELPHES is used. This allows to estimate a systematic uncertainty of the simulation on the acceptance corrections. As shown in Fig. 10.25, the difference between the two simulations are much larger than the indicated variation for one particular value of $\frac{\bar{c}_{qq}}{1+\bar{c}_{\phi q}}$. The acceptance corrections using the DELPHES simulation are also derived by including and excluding the shape of the ME discriminant in the pseudo-data set generation as described above. At last, the fit of the two coupling parameters is repeated without considering any acceptance corrections. The results for the acceptance corrections excluding the ME discriminant shape are collected in App. C.

Figure 10.30 shows the results for the two EFT parameters for four different scenarios: the three scenarios mentioned above and the result discussed in the previous section. The global fit maximum is robust for all four scenarios and similar central values for $\bar{c}_{\phi q}$ and $\bar{c}_{qq}$ are obtained. As expected, the results for the DetSimFast and DELPHES simulation are very similar. Only a small deviation for the smallest 1σ interval is observed. The differences between the two fast simulations does not have a large impact on the measurement of the two parameters. The impact from including or excluding shape corrections in the determination of the acceptance corrections is much larger. The differences between Fig. 10.30(a) and 10.30(d) emphasize the need to include the detector response in the model predictions. Furthermore, while acceptance corrections based on the event selection might be relatively small (c. f. Fig. 10.30(c) and 10.30(d)), the impact on the final result is sizeable based on the specific analysis strategy.

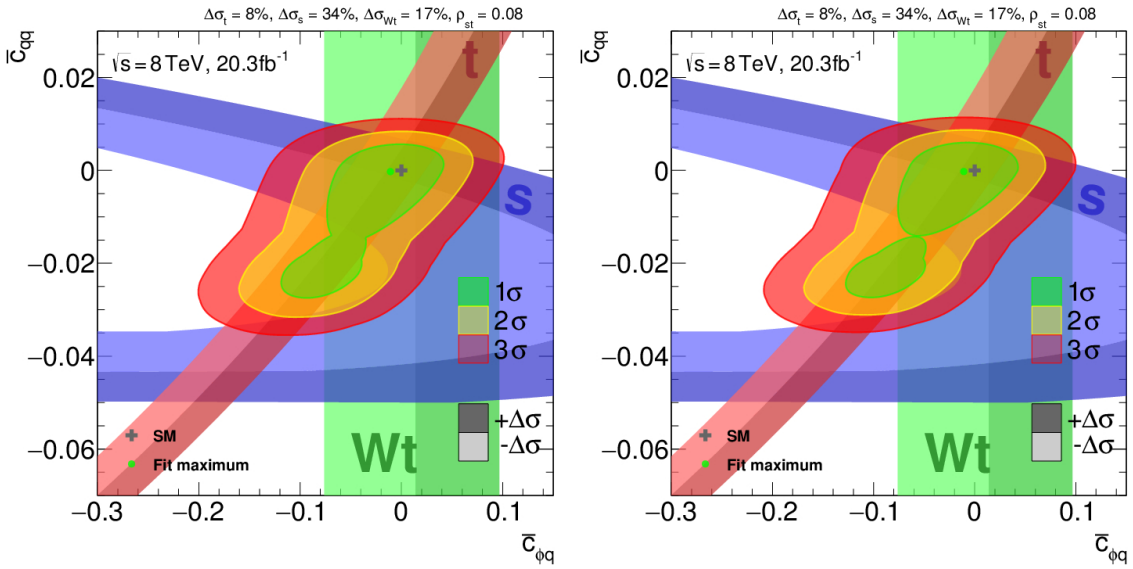

(a) DetSimFast acceptance corrections

(b) DELPHES acceptance corrections

(c) DetSimFast, excluding shape corrections

(d) Excluding any acceptance corrections

Figure 10.30.: Fit results for the effective couplings $\bar{c}_{\phi q}$ and $\bar{c}_{qq}$, see Fig. 10.28 for details. The panels show the results for acceptance corrections that are derived with (a) DetSimFast and (b) DELPHES simulations including normalization and shape corrections, while (c) uses the DetSimFast simulation, but shape corrections are excluded. For the result shown in panel (d), no acceptance corrections are considered and only the theoretical predictions are used.

11. Conclusion

In this thesis, proton–proton collision events at a centre-of-mass energy of 8 TeV were analysed. The data set was recorded in 2012 by the ATLAS detector at the LHC and corresponds to an integrated luminosity of $20.3\,\mathrm{fb}^{-1}$.

In the first part of this thesis, an advanced method for classifying collision events was introduced: the matrix element method. This method is based on the matrix element, which contains the information of the hard-scattering process and allows to calculate likelihoods for different processes. These likelihoods are a convolution of the hadronic cross section with the detector response, which is parametrized by transfer functions and relate the partonic final state to the reconstructed final state. In order to efficiently compute the likelihoods and combine them into a discriminant, the MEMTk software was developed in cooperation with the experimental group in Berlin and is described in this thesis.

The focus of the second part lies on the cross section measurement of single top-quark production in the s and t-channel. The event selection for both, the t-channel and s-channel, involves exactly one isolated lepton and two jets, of which one or two b-tags are required, respectively. Basic conditions on the missing transverse momentum and the transverse mass of the W boson need to be fulfilled to reduce the background contribution from multi-jet production. Both analyses use a discriminant built from the matrix element likelihoods. The s-channel part is based on [ATL16a], which reported the first evidence of single top-quark production in the s-channel at the LHC. In this thesis, the cross section for single-top production in the s and t-channel, as well as their correlation, is estimated in a combined maximum likelihood fit. The result for the cross sections is

$$\begin{aligned} \sigma_s &= 4.9 \pm 1.0\,(\text{stat.})\,^{+1.4}_{-1.3}\,(\text{syst.})\,\text{pb} &&= 4.9 \pm 1.7\,\text{pb} \\ \sigma_t &= 82.3 \pm 2.9\,(\text{stat.})\,^{+6.4}_{-4.7}\,(\text{syst.})\,\text{pb} &&= 82.3^{+7.0}_{-5.5}\,\text{pb} \end{aligned}$$

with a correlation between these two measurements of $\rho_{st} = 0.08$. The dominant systematic uncertainties for both cross section measurement originate from uncertainties associated with the modelling of the signal processes and the finite data statistics. For the s-channel, the MC statistics and the W+jets normalization uncertainties also contribute significantly to the total uncertainty.

In the last part of this thesis, the impact of single-top cross section measurements on new physic parameters is discussed, in particular regarding effective field theories. In

such a theory, new interactions of SM particles are described by higher dimension operators and their coefficients. Two coefficients, $\bar{c}_{\phi q}$ and $\bar{c}_{qq}$, are relevant for single top-quark production and their effect on the single-top cross sections was determined using an EFT model in LO QCD and up to orders of Λ^{-2} of the new physics scale. Furthermore, changes in the acceptance and shape of the discriminants as a function of the two parameters was investigated using fast and simplified detector simulations. The DELPHES framework and DetSimFast simulation are used. The first one includes the effects of hadronisation and pile-up in the events and the ATLAS detector response is fully parametrized. For the second one, the transfer functions used for the matrix element method, are directly applied to the partonic final state in order to relate the final state to the reconstructed objects. Both fast simulations give comparable results for the acceptance corrections. The single-top cross section measurement for the s and t-channel presented in this note as well as the measurement of the associated Wt production in [ATL16d] are combined in a statistical analysis in order to extract limits on the EFT parameters $\bar{c}_{\phi q}$ and $\bar{c}_{qq}$. The employed statistical model is formulated in Bayesian statistics using the EFT*fitter* and the effects of acceptance corrections are included. The smallest intervals which covers 95.5 % probability for the two couplings are

$$\begin{aligned} -0.132 < \quad \bar{c}_{\phi q} \quad < 0.048 \\ -0.0283 < \quad \bar{c}_{\phi q} \quad < 0.0062\,. \end{aligned}$$

The single-top cross section determined in this thesis is compatible with the SM prediction within the uncertainties of the performed measurement. The effective field theory interpretation of single-top cross section measurements of all three production modes is the first measurement within the ATLAS collaboration that includes acceptance corrections originating from the selection efficiency and the shape of the discriminants. Furthermore, the use of fast and simplified detector simulations, DELPHES and DetSimFast, is established and the first comparison study between the full simulation is presented. Such fast simulations are necessary to include acceptance corrections in the statistical models, which would otherwise be impossible due to the huge computational effort. As shown here, these corrections can have a sizeable impact on the effective field theory interpretation and can in most cases only be determined by the experiments itself.

This thesis is a first step towards the determination of many EFT parameters. The statistical analysis presented here can easily be extended to include cross section measurements at $\sqrt{s} = 13\,\text{TeV}$ or other meaningful observables. Measurements of the single-top t-channel [ATL17b] and associated Wt [ATL16c] production already exist. A measurement of the s-channel with a significance of more than 5σ is within the reach of the current data-taking period of the LHC. Moreover, measurements of the top-quark pair production are sensitive to different couplings and all measurements can be combined in a global statistical analysis in the framework of an EFT using the same techniques outlined in this thesis.

A. Simulation Samples

In this appendix the Monte Carlo samples used in this analysis are collected. Table A.1 lists the nominal configuration for the signal and background processes. Additional samples that are used for studying systematic effects, described in Sec. 8, are summarized in Tab. A.2. Table A.3 holds the samples used for evaluating the PDF uncertainty.

Sample	DSID	Generator	PDF set	σ [pb]	k-factor	N_{MC}
s-channel (ℓ + jets)	110119	POWHEG + PYTHIA6	CT10	1.6424	1.0337	5 995 993
t-channel (ℓ + jets + t)	110090	POWHEG + PYTHIA6	CT10	17.519	1.0148	4 994 481
t-channel (ℓ + jets + $\bar{\mathrm{t}}$)	110091	POWHEG + PYTHIA6	CT10	9.3964	1.0255	4 999 879
Wt (DR)	110140	POWHEG + PYTHIA6	CT10	20.461	1.0933	999 692
$t\bar{t}$ (no full-had.)	110404	POWHEG + PYTHIA6	CT10	114.51	1.1996	49 948 212
W→eν, b-quark filter	167740	SHERPA	CT10	140.34	1.10	14 992 449
W→eν, c-quark filter	167741	SHERPA	CT10	537.84	1.10	5 999 977
W→eν, c and b-quark veto	167742	SHERPA	CT10	10295	1.10	23 983 938
W→μν, b-quark filter	167743	SHERPA	CT10	140.39	1.10	14 990 863
W→μν, c-quark filter	167744	SHERPA	CT10	466.47	1.10	5 999 888
W→μν, c and b-quark veto	167745	SHERPA	CT10	10368	1.10	23 997 757
W→τν, b-quark filter	167746	SHERPA	CT10	140.34	1.10	14 999 453
W→τν, c-quark filter	167747	SHERPA	CT10	506.45	1.10	5 999 680
W→τν, c and b-quark veto	167748	SHERPA	CT10	10327	1.10	23 999 450
Z→ee + 0 parton	147105	ALPGEN + PYTHIA6	CTEQ6L1	718.97	1.18	6 298 988
Z→ee + 1 partons	147106	ALPGEN + PYTHIA6	CTEQ6L1	175.70	1.18	8 184 476
Z→ee + 2 partons	147107	ALPGEN + PYTHIA6	CTEQ6L1	58.875	1.18	3 175 991
Z→ee + 3 partons	147108	ALPGEN + PYTHIA6	CTEQ6L1	15.636	1.18	894 995
Z→ee + 4 partons	147109	ALPGEN + PYTHIA6	CTEQ6L1	4.0116	1.18	398 597
Z→ee + 5 partons	147110	ALPGEN + PYTHIA6	CTEQ6L1	1.2592	1.18	229 700
Z→μμ + 0 parton	147113	ALPGEN + PYTHIA6	CTEQ6L1	719.16	1.18	6 298 796
Z→μμ + 1 partons	147114	ALPGEN + PYTHIA6	CTEQ6L1	175.74	1.18	8 193 384
Z→μμ + 2 partons	147115	ALPGEN + PYTHIA6	CTEQ6L1	58.882	1.18	3 175 488
Z→μμ + 3 partons	147116	ALPGEN + PYTHIA6	CTEQ6L1	15.673	1.18	894 799
Z→μμ + 4 partons	147117	ALPGEN + PYTHIA6	CTEQ6L1	4.0057	1.18	393 200
Z→μμ + 5 partons	147118	ALPGEN + PYTHIA6	CTEQ6L1	1.2544	1.18	229 200
Z→ττ + 0 parton	147121	ALPGEN + PYTHIA6	CTEQ6L1	718.87	1.18	19 202 764
Z→ττ + 1 partons	147122	ALPGEN + PYTHIA6	CTEQ6L1	175.76	1.18	10 674 582
Z→ττ + 2 partons	147123	ALPGEN + PYTHIA6	CTEQ6L1	58.856	1.18	3 765 893
Z→ττ + 3 partons	147124	ALPGEN + PYTHIA6	CTEQ6L1	15.667	1.18	1 096 994
Z→ττ + 4 partons	147125	ALPGEN + PYTHIA6	CTEQ6L1	4.0121	1.18	398 798
Z→ττ + 5 partons	147126	ALPGEN + PYTHIA6	CTEQ6L1	1.2560	1.18	229 799
Z→ee + c$\bar{\mathrm{c}}$ + 0 parton	200432	ALPGEN + PYTHIA6	CTEQ6L1	11.763	1.1800	284 999
Z→ee + c$\bar{\mathrm{c}}$ + 1 partons	200433	ALPGEN + PYTHIA6	CTEQ6L1	7.1280	1.1800	499 500

Continued on next page

Sample	DSID	Generator	PDF set	σ [pb]	k-factor	N_{MC}
$Z\to ee + c\bar{c}$ + 2 partons	200434	ALPGEN + PYTHIA6	CTEQ6L1	3.3603	1.1800	498 997
$Z\to ee + c\bar{c}$ + 3 partons	200435	ALPGEN + PYTHIA6	CTEQ6L1	1.7106	1.1800	443 697
$Z\to \mu\mu + c\bar{c}$ + 0 parton	200440	ALPGEN + PYTHIA6	CTEQ6L1	11.795	1.1800	298 998
$Z\to \mu\mu + c\bar{c}$ + 1 partons	200441	ALPGEN + PYTHIA6	CTEQ6L1	7.1123	1.1800	499 799
$Z\to \mu\mu + c\bar{c}$ + 2 partons	200442	ALPGEN + PYTHIA6	CTEQ6L1	3.3708	1.1800	499 500
$Z\to \mu\mu + c\bar{c}$ + 3 partons	200443	ALPGEN + PYTHIA6	CTEQ6L1	1.7059	1.1800	443 999
$Z\to \tau\tau + c\bar{c}$ + 0 parton	200448	ALPGEN + PYTHIA6	CTEQ6L1	11.760	1.1800	299 000
$Z\to \tau\tau + c\bar{c}$ + 1 partons	200449	ALPGEN + PYTHIA6	CTEQ6L1	7.1410	1.1800	199 998
$Z\to \tau\tau + c\bar{c}$ + 2 partons	200450	ALPGEN + PYTHIA6	CTEQ6L1	3.3582	1.1800	99 800
$Z\to \tau\tau + c\bar{c}$ + 3 partons	200451	ALPGEN + PYTHIA6	CTEQ6L1	1.7046	1.1800	49 400
$Z\to ee$ + bb + 0 parton	200332	ALPGEN + PYTHIA6	CTEQ6L1	6.5083	1.1800	1 799 992
$Z\to ee$ + bb + 1 partons	200333	ALPGEN + PYTHIA6	CTEQ6L1	3.2927	1.1800	999 896
$Z\to ee$ + bb + 2 partons	200334	ALPGEN + PYTHIA6	CTEQ6L1	1.2544	1.1800	994 594
$Z\to ee$ + bb + 3 partons	200335	ALPGEN + PYTHIA6	CTEQ6L1	0.61711	1.1800	885 392
$Z\to \mu\mu$ + bb + 0 parton	200340	ALPGEN + PYTHIA6	CTEQ6L1	6.5056	1.1800	1 799 797
$Z\to \mu\mu$ + bb + 1 partons	200341	ALPGEN + PYTHIA6	CTEQ6L1	3.2904	1.1800	999 897
$Z\to \mu\mu$ + bb + 2 partons	200342	ALPGEN + PYTHIA6	CTEQ6L1	1.2601	1.1800	999 395
$Z\to \mu\mu$ + bb + 3 partons	200343	ALPGEN + PYTHIA6	CTEQ6L1	0.61882	1.1800	880 894
$Z\to \tau\tau$ + bb + 0 parton	200348	ALPGEN + PYTHIA6	CTEQ6L1	6.5062	1.1800	300 000
$Z\to \tau\tau$ + bb + 1 partons	200349	ALPGEN + PYTHIA6	CTEQ6L1	3.2935	1.1800	100 000
$Z\to \tau\tau$ + bb + 2 partons	200350	ALPGEN + PYTHIA6	CTEQ6L1	1.2485	1.1800	50 000
$Z\to \tau\tau$ + bb + 3 partons	200351	ALPGEN + PYTHIA6	CTEQ6L1	0.61363	1.1800	49 800
WW	105985	HERWIG	CTEQ6L1	12.416	1.6833	2 499 890
ZZ	105986	HERWIG	CTEQ6L1	0.99081	1.5496	245 000
WZ	105987	HERWIG	CTEQ6L1	3.6706	1.9011	999 998

Table A.1.: All nominal Monte Carlo samples used in this analysis. The cross section that is used for the normalization of the sample is given by the product of the cross section times the corresponding k-factor and includes the branching ratios. The number of generated events N_{MC} is given in the last column. The lepton sign ℓ indicates either e, μ or τ.

Sample	DSID	Generator	PDF set	σ [pb]	k-factor	N_{MC}
t-channel (ℓ + jets)	110101	AcerMC + PYTHIA6	CTEQ6L1	25.750	1.1042	8 997 672
t-channel (ℓ + jets)	110095	aMC@NLO + HERWIG	CT10	27.446	1.0360	999 896
t-channel (ℓ + jets)	110121	aMC@NLO + HERWIG	CT10	26.587	1.0321	9 993 987
t-channel (ℓ + jets + t)	110086	POWHEG + HERWIG	CT10	17.528	1.0143	4 989 993
t-channel (ℓ + jets + $\bar{t}$)	110087	POWHEG + HERWIG	CT10	9.3986	1.0252	4 997 992
t-channel (ℓ + jets + t)	110070	POWHEG + PYTHIA6	CT10F4	17.520	1.0147	4 989 989
t-channel (ℓ + jets + $\bar{t}$)	110071	POWHEG + PYTHIA6	CT10F4	9.3935	1.0258	4 999 999
t-channel (ℓ + jets + $\bar{t}$), fac. scale = 2.0, ren. scale = 2.0, radLo	110052	POWHEG + PYTHIA6	CTEQ6L1	8.5026	1.1333	1 999 997
t-channel (ℓ + jets + $\bar{t}$), fac. scale = 0.5, ren. scale = 0.5, radHi	110060	POWHEG + PYTHIA6	CTEQ6L1	9.6773	0.9957	1 999 999
t-channel (ℓ + jets + t), fac. scale = 2.0, ren. scale = 2.0, radLo	110242	POWHEG + PYTHIA6	CTEQ6L1	15.916	1.1170	1 995 000

Continued on next page

Sample	DSID	Generator	PDF set	σ [pb]	k-factor	N_{MC}
t-channel (ℓ + jets + t), fac. scale = 0.5, ren. scale = 0.5, radHi	110250	POWHEG + PYTHIA6	CTEQ6L1	17.942	0.9909	1 989 997
Wt (DR)	108346	MC@NLO + HERWIG	CT10	20.666	1.0825	1 999 194
s-channel (e + jets)	108343	MC@NLO + HERWIG	CT10	0.56395	1.0744	199 997
s-channel (μ + jets)	108344	MC@NLO + HERWIG	CT10	0.56430	1.0737	200 000
s-channel (τ + jets)	108345	MC@NLO + HERWIG	CT10	0.56434	1.0736	199 999
s-channel (ℓ + jets)	110120	aMC@NLO + HERWIG	CT10	1.6942	1.0729	2 964 982
s-channel (ℓ + jets), fac. scale = 2.0, ren. scale = 2.0, radHi	110040	POWHEG + PYTHIA6	CT10	1.6931	1.0736	1 000 000
s-channel (ℓ + jets), fac. scale = 2.0, ren. scale = 1.0	110041	POWHEG + PYTHIA6	CT10	1.6974	1.0708	999 999
s-channel (ℓ + jets), fac. scale = 1.0, ren. scale = 2.0, radHi	110042	POWHEG + PYTHIA6	CT10	1.6928	1.0737	1 000 000
s-channel (ℓ + jets), fac. scale = 0.5, ren. scale = 1.0	110043	POWHEG + PYTHIA6	CT10	1.6976	1.0707	999 996
s-channel (ℓ + jets), fac. scale = 1.0, ren. scale = 0.5, radLo	110044	POWHEG + PYTHIA6	CT10	1.6976	1.0709	1 000 000
s-channel (ℓ + jets), fac. scale = 0.5, ren. scale = 0.5, radLo	110045	POWHEG + PYTHIA6	CT10	1.6973	1.0709	999 999
$t\bar{t}$ (no full-had.)	105200	MC@NLO + HERWIG	CT10	112.94	1.2158	14 997 103
$\mathrm{t\bar{t}}$ (no full-had.)	110407	POWHEG + PYTHIA		114.47	1.1996	14 994 480
$\mathrm{t\bar{t}}$ (no full-had.)	110408	POWHEG + PYTHIA		114.47	1.1996	14 990 989
$\mathrm{W} \to \mathrm{e}\nu$ + 0 parton	147025	ALPGEN + PYTHIA6	CTEQ6L1	8127.3	1.1330	29 464 244
$\mathrm{W} \to \mathrm{e}\nu$ + 1 partons	147026	ALPGEN + PYTHIA6	CTEQ6L1	1792.7	1.1330	47 936 004
$\mathrm{W} \to \mathrm{e}\nu$ + 2 partons	147027	ALPGEN + PYTHIA6	CTEQ6L1	542.18	1.1330	17 495 947
$\mathrm{W} \to \mathrm{e}\nu$ + 3 partons	147028	ALPGEN + PYTHIA6	CTEQ6L1	147.65	1.1330	4 855 289
$\mathrm{W} \to \mathrm{e}\nu$ + 4 partons	147029	ALPGEN + PYTHIA6	CTEQ6L1	37.736	1.1330	5 403 283
$\mathrm{W} \to \mathrm{e}\nu$ + 5 partons	147030	ALPGEN + PYTHIA6	CTEQ6L1	11.962	1.1330	2 787 277
$\mathrm{W} \to \mu\nu$ + 0 parton	147033	ALPGEN + PYTHIA6	CTEQ6L1	8127.3	1.1330	31 965 655
$\mathrm{W} \to \mu\nu$ + 1 partons	147034	ALPGEN + PYTHIA6	CTEQ6L1	1792.7	1.1330	43 622 615
$\mathrm{W} \to \mu\nu$ + 2 partons	147035	ALPGEN + PYTHIA6	CTEQ6L1	542.18	1.1330	17 611 454
$\mathrm{W} \to \mu\nu$ + 3 partons	147036	ALPGEN + PYTHIA6	CTEQ6L1	147.65	1.1330	4 796 077
$\mathrm{W} \to \mu\nu$ + 4 partons	147037	ALPGEN + PYTHIA6	CTEQ6L1	37.736	1.1330	5 498 881
$\mathrm{W} \to \mu\nu$ + 5 partons	147038	ALPGEN + PYTHIA6	CTEQ6L1	11.962	1.1330	2 790 985
$\mathrm{W} \to \tau\nu$ + 0 parton	147041	ALPGEN + PYTHIA6	CTEQ6L1	8127.3	1.1330	31 877 158
$\mathrm{W} \to \tau\nu$ + 1 partons	147042	ALPGEN + PYTHIA6	CTEQ6L1	1792.7	1.1330	48 070 179
$\mathrm{W} \to \tau\nu$ + 2 partons	147043	ALPGEN + PYTHIA6	CTEQ6L1	542.18	1.1330	17 586 943
$\mathrm{W} \to \tau\nu$ + 3 partons	147044	ALPGEN + PYTHIA6	CTEQ6L1	147.65	1.1330	4 982 982
$\mathrm{W} \to \tau\nu$ + 4 partons	147045	ALPGEN + PYTHIA6	CTEQ6L1	37.736	1.1330	2 553 295
$\mathrm{W} \to \tau\nu$ + 5 partons	147046	ALPGEN + PYTHIA6	CTEQ6L1	11.962	1.1330	794 096
$\mathrm{W} \to \ell\nu + \mathrm{b\bar{b}}$ + 0 parton	200256	ALPGEN + PYTHIA6	CTEQ6L1	55.66	1.133	1 599 997
$\mathrm{W} \to \ell\nu + \mathrm{b\bar{b}}$ + 1 partons	200257	ALPGEN + PYTHIA6	CTEQ6L1	45.25	1.133	1 398 396
$\mathrm{W} \to \ell\nu + \mathrm{b\bar{b}}$ + 2 partons	200258	ALPGEN + PYTHIA6	CTEQ6L1	23.16	1.133	699 398
$\mathrm{W} \to \ell\nu + \mathrm{b\bar{b}}$ + 3 partons	200259	ALPGEN + PYTHIA6	CTEQ6L1	11.20	1.133	398 397
$\mathrm{W} \to \ell\nu + \mathrm{c\bar{c}}$ + 0 parton	200156	ALPGEN + PYTHIA6	CTEQ6L1	150.2	1.133	4 299 592
$\mathrm{W} \to \ell\nu + \mathrm{c\bar{c}}$ + 1 partons	200157	ALPGEN + PYTHIA6	CTEQ6L1	132.7	1.133	4 137 891

Continued on next page

Sample	DSID	Generator	PDF set	σ [pb]	k-factor	N_{MC}
$W \to \ell\nu + c\bar{c}$ + 2 partons	200158	ALPGEN + PYTHIA6	CTEQ6L1	71.84	1.133	2 394 394
$W \to \ell\nu + c\bar{c}$ + 3 partons	200159	ALPGEN + PYTHIA6	CTEQ6L1	30.26	1.133	985 295
$W \to \ell\nu$ + c + 0 parton	200056	ALPGEN + PYTHIA6	CTEQ6L1	808.0	1.52	22 999 046
$W \to \ell\nu$ + c + 1 partons	200057	ALPGEN + PYTHIA6	CTEQ6L1	267.7	1.52	8 198 769
$W \to \ell\nu$ + c + 2 partons	200058	ALPGEN + PYTHIA6	CTEQ6L1	69.89	1.52	2 090 290
$W \to \ell\nu$ + c + 3 partons	200059	ALPGEN + PYTHIA6	CTEQ6L1	20.56	1.52	499 498
$W \to \ell\nu$ + c + 4 partons	200060	ALPGEN + PYTHIA6	CTEQ6L1	4.308	1.52	199 499

Table A.2.: All nominal Monte Carlo samples used for systematic studies. The cross section that is used for the normalization of the sample is given by the product of the cross section times the corresponding k-factor and includes the branching ratios. The number of generated events N_{MC} is given in the last column. The lepton sign ℓ indicates either e, μ or τ.

Sample	DSID	Generator	PDF set	σ [pb]	k-factor	N_{MC}
s-channel (e + jets)	108343	MC@NLO + HERWIG	CT10	0.56395	1.0744	199 997
s-channel (μ + jets)	108344	MC@NLO + HERWIG	CT10	0.56430	1.0737	200 000
s-channel (τ + jets)	108345	MC@NLO + HERWIG	CT10	0.56434	1.0736	199 999
t-channel (ℓ + jets)	110101	AcerMC + PYTHIA6	CTEQ6L1	25.750	1.1042	8 997 672
Wt (DR)	108346	MC@NLO + HERWIG	CT10	20.666	1.0825	1 999 194
$t\bar{t}$ (no full-had.)	105200	MC@NLO + HERWIG	CT10	112.94	1.2158	14 997 103

Table A.3.: All top-quark Monte Carlo samples used for evaluating the PDF uncertainty, while for all other processes the nominal samples are used. The cross section that is used for the normalization of the sample is given by the product of the cross section times the corresponding k-factor and includes the branching ratios. The number of generated events N_{MC} is given in the last column. The lepton sign ℓ indicates either e, μ or τ.

B. Fit Results

In this section, the pulls of the remaining nuisance parameters from the fit to the real data distribution are shown in Figs. B.1–B.4. The figures also contain the prefit and postfit impact on the signal strength parameters. Entries denoted with $\gamma_{\text{stat.}}$ represent the statistical uncertainty of the given bin. The entries for each signal strength parameter are ordered by their postfit impact.

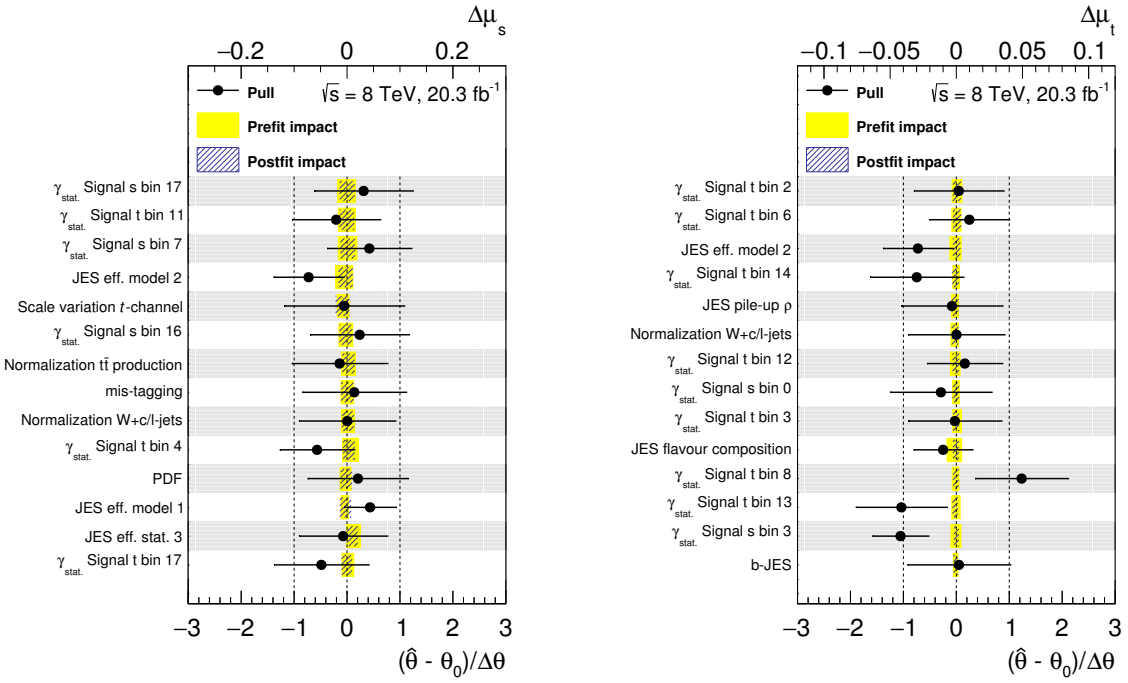

(a) Pulls 29–42 and impact $\Delta\mu$, s-channel

(b) Pulls 29–42 and impact $\Delta\mu$, t-channel

Figure B.1.: Maximum likelihood fit results for selected nuisance parameters used in the fit to the data distribution. The panels show the results for (a) s-channel signal strength parameter and (b) t-channel signal strength parameter. The entries for each signal strength parameter are ordered by their postfit impact.

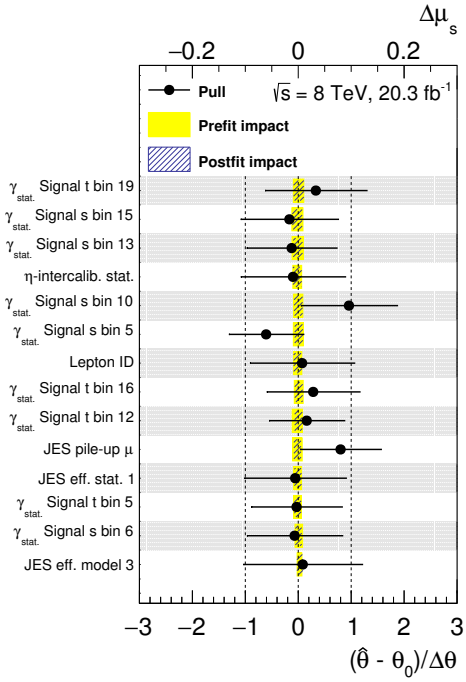

(a) Pulls 43–56 and impact $\Delta\mu$, s-channel

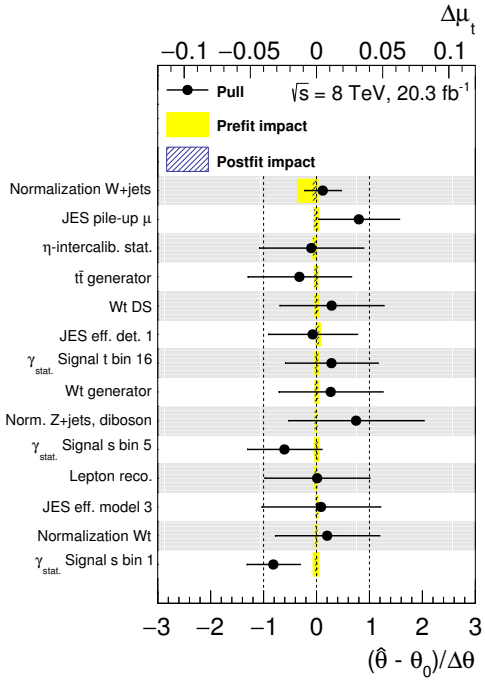

(b) Pulls 43–56 and impact $\Delta\mu$, t-channel

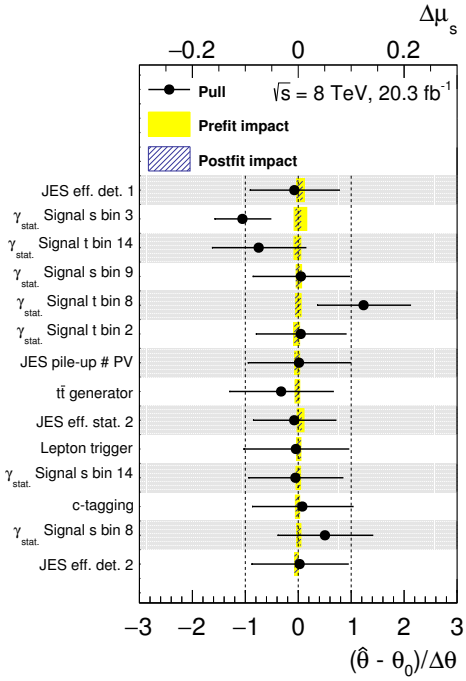

(c) Pulls 57–70 and impact $\Delta\mu$, s-channel

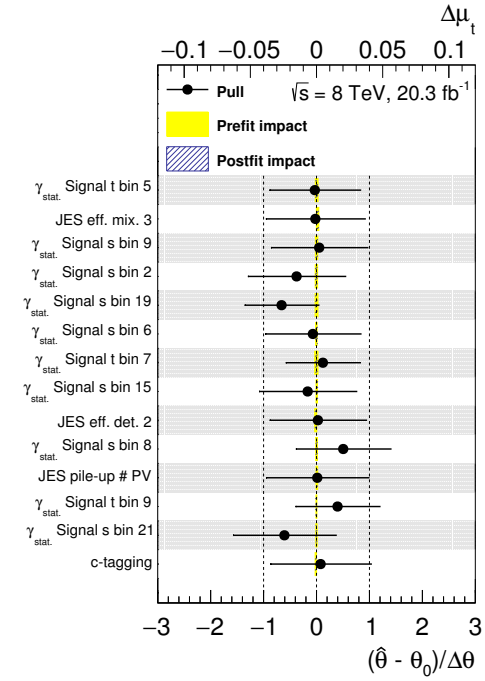

(d) Pulls 57–70 and impact $\Delta\mu$, t-channel

Figure B.2.: Maximum likelihood fit results for selected nuisance parameters used in the fit to the data distribution. The panels show the results for (a) and (c) s-channel signal strength parameter and (b) and (d) t-channel signal strength parameter. The entries for each signal strength parameter are ordered by their postfit impact.

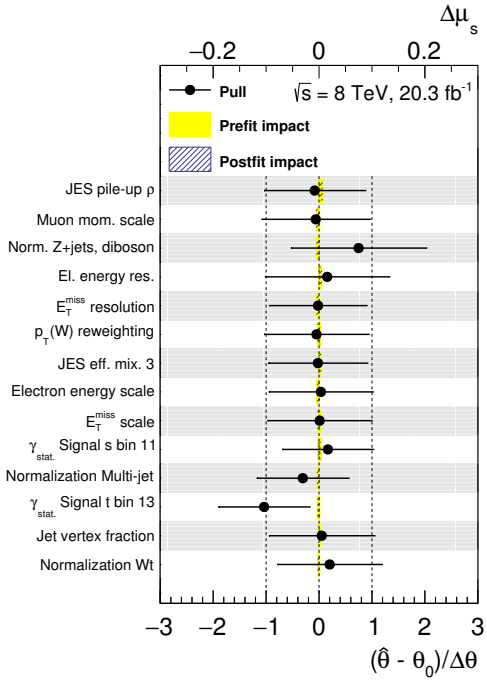

(a) Pulls 71–84 and impact $\Delta\mu$, s-channel

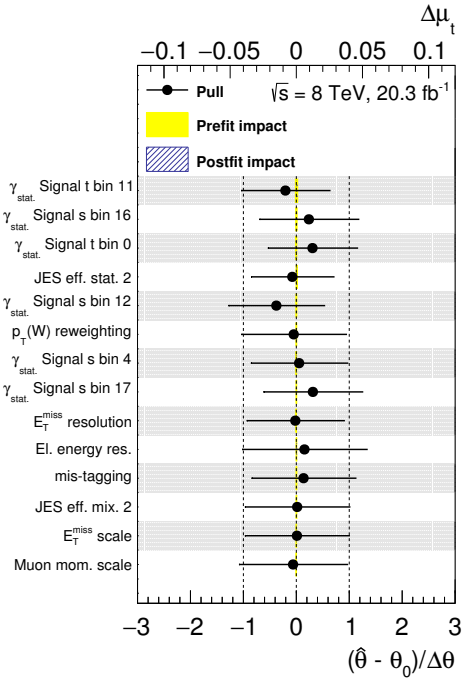

(b) Pulls 71–84 and impact $\Delta\mu$, t-channel

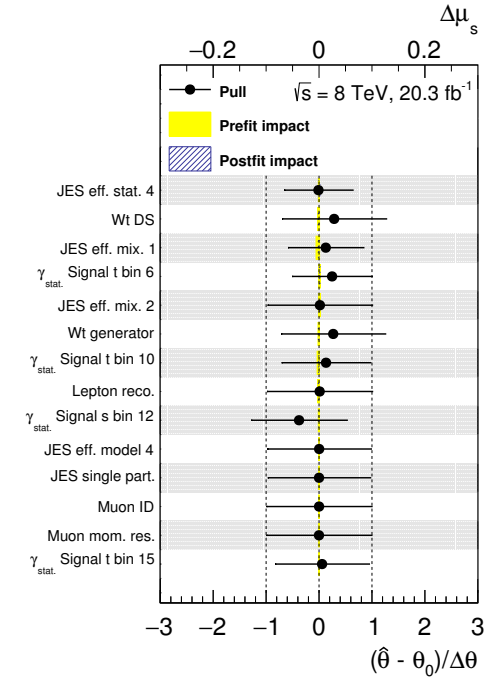

(c) Pulls 85–98 and impact $\Delta\mu$, s-channel

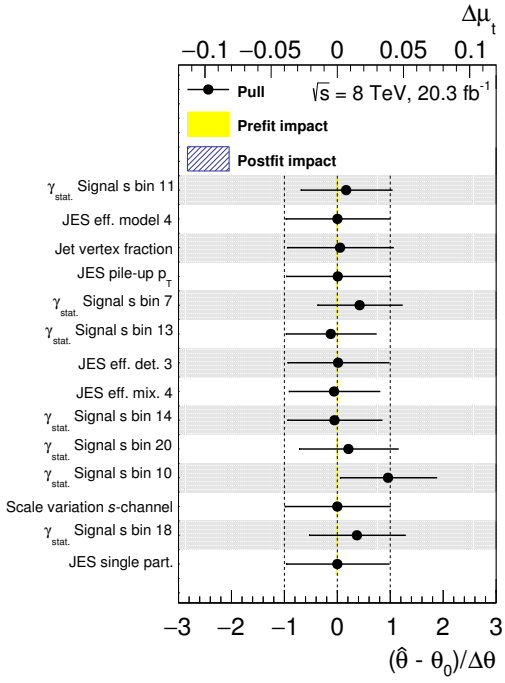

(d) Pulls 85–98 and impact $\Delta\mu$, t-channel

Figure B.3.: Maximum likelihood fit results for selected nuisance parameters used in the fit to the data distribution. The panels show the results for (a) and (c) s-channel signal strength parameter and (b) and (d) t-channel signal strength parameter. The entries for each signal strength parameter are ordered by their postfit impact.

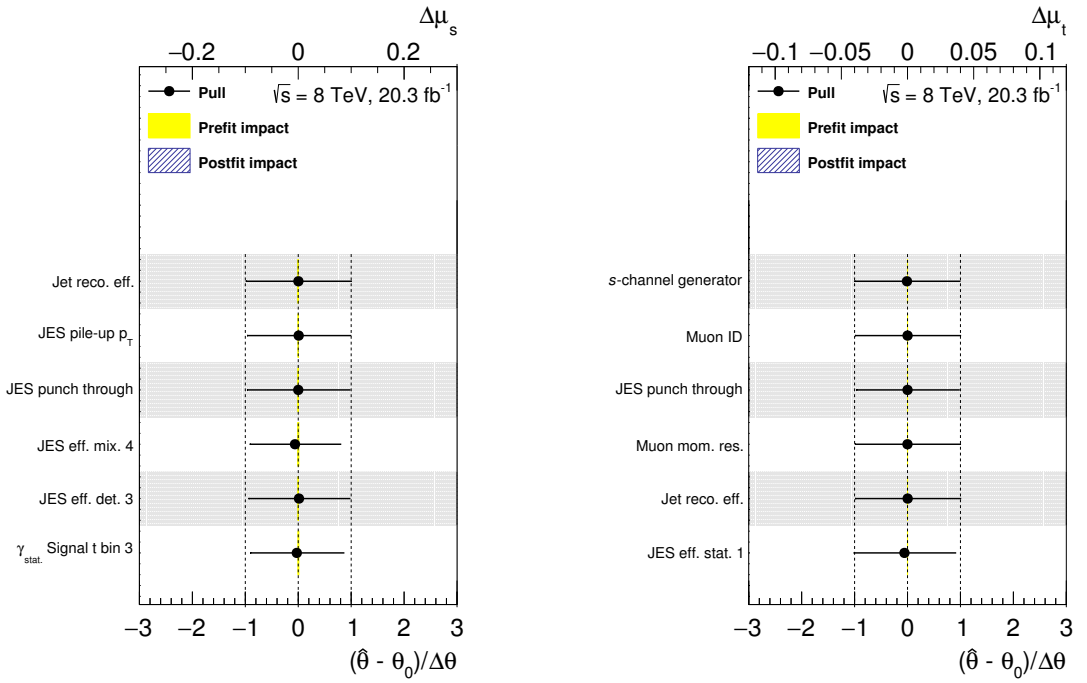

(a) Pulls 99–104 and impact $\Delta\mu$, s-channel

(b) Pulls 99–104 and impact $\Delta\mu$, t-channel

Figure B.4.: Maximum likelihood fit results for selected nuisance parameters used in the fit to the data distribution. The panels show the results for (a) s-channel signal strength parameter and (b) t-channel signal strength parameter. The entries for each signal strength parameter are ordered by their postfit impact.

C. Acceptance Corrections

In this section, the acceptance corrections derived with the DetSimFast and DELPHES simulations are shown. The same procedure as in Sec. 10.6.2 is used, but the shape of the signal contributions always corresponds to the nominal ATLAS template. Figure C.1 shows the one-dimensional distribution as a function of $\frac{\bar{c}_{qq}}{(1+\bar{c}_{qq})}$ for both simulations. From the one-dimensional distribution, the two-dimensional distribution of the acceptance correction for the DELPHES simulation is displayed in Fig. C.2.

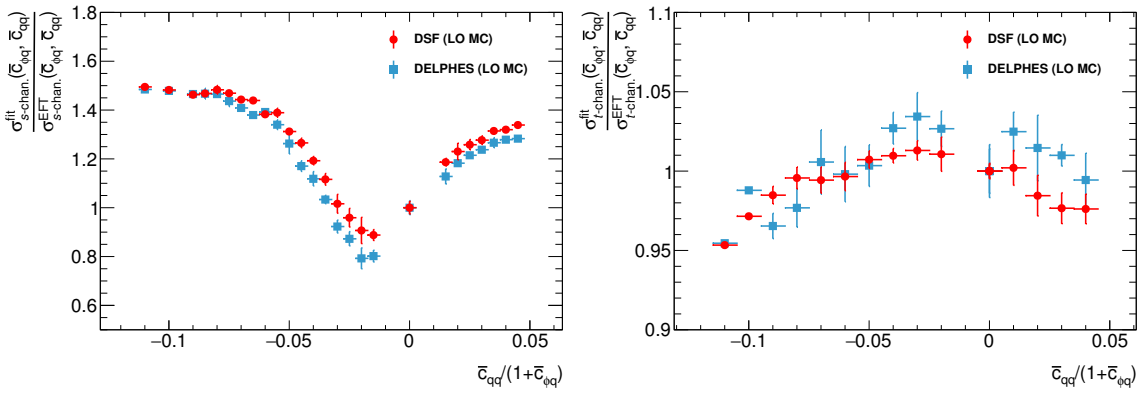

(a) $\alpha_{s\text{-channel}}$ (b) $\alpha_{t\text{-channel}}$

Figure C.1.: Acceptance corrections α for (a) single-top s-channel cross section and (a) single-top t-channel cross section. The acceptance corrections are determined by fits to 81 pseudo-data sets. The signal contributions for these pseudo-data sets are modelled by the fast simulations, DetSimFast or DELPHES, without including corrections concerning the shape of the ME discriminant. The background contributions are obtained from the ATLAS simulation. The acceptance correction is averaged over adjacent points.

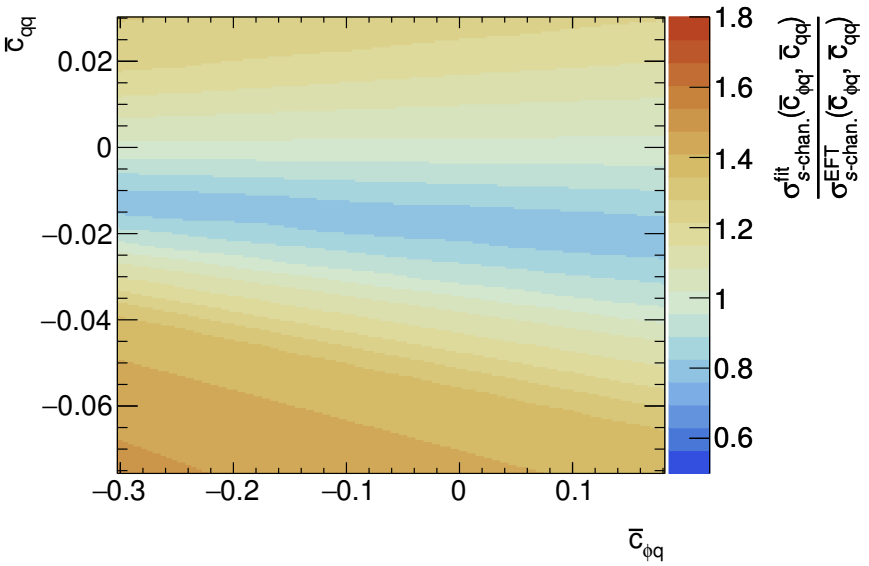

(a) $\alpha_{s\text{-channel}}$

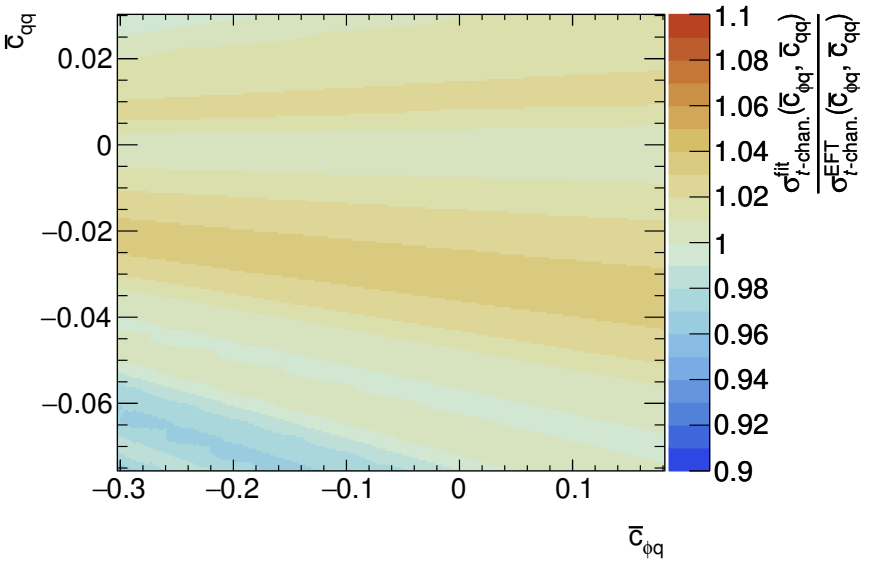

(b) $\alpha_{t\text{-channel}}$

Figure C.2.: Acceptance corrections α for (a) single-top s-channel cross section and (a) single-top t-channel cross section in the $\bar{c}_{\phi q}$–$\bar{c}_{qq}$ plane. The two-dimensional distribution is obtained from Fig. C.1 using the DELPHES simulation.

Bibliography

[Abd+06] A. Abdesselam et al., *The barrel modules of the ATLAS semiconductor tracker*, Nucl. Instrum. Meth. **A568** (2006) 642.

[Ach+13] B. Acharya et al., *Object selection and calibration, background estimations and MC samples for top quark analyses using the full 2012 data set*, ATL-COM-PHYS-2013-1016, 2013, URL: https://cds.cern.ch/record/1563201.

[Ago+03] S. Agostinelli et al., *Geant4: A Simulation Toolkit*, Nucl. Instrum. Meth. **A506** (2003) 250.

[Agu09] J. Aguilar-Saavedra, *A minimal set of top anomalous couplings*, Nuclear Physics B **812** (2009) 181, ISSN: 0550-3213.

[Ale+11] S. Alekhin et al., *The PDF4LHC Working Group Interim Report*, (2011), arXiv: 1101.0536 [hep-ph].

[ALI04] ALICE Collaboration, *ALICE: Physics Performance Report, Volume I*, Journal of Physics G: Nuclear and Particle Physics **30** (2004) 1517.

[Alw+07] J. Alwall et al., *A Standard format for Les Houches event files*, Comput. Phys. Commun. **176** (2007) 300, arXiv: hep-ph/0609017 [hep-ph].

[Alw+14] J. Alwall et al., *The Automated Computation of Tree-Level and Next-To-Leading Order Differential Cross Sections, and their Matching to Parton Shower Simulations*, JHEP **1407** (2014) 079, arXiv: 1405.0301 [hep-ph].

[Ana+04] C. Anastasiou et al., *High Precision QCD at Hadron Colliders: Electroweak Gauge Boson Rapidity Distributions at NNLO*, Phys. Rev. **D69** (2004) 094008, arXiv: hep-ph/0312266 [hep-ph].

[And+14] T. Andeen et al., *Search for single production of vector-like quarks decaying into Wb in pp collisions at $\sqrt{s} = 8$ TeV with the ATLAS detector*, ATL-COM-PHYS-2014-951, 2014, URL: https://cds.cern.ch/record/1747257.

[Arg+13] S. Argyropoulos et al., *Pile-up subtraction and suppression for jets in ATLAS*, ATL-COM-PHYS-2013-251, 2013, URL: https://cds.cern.ch/record/1522015.

[Ars+14] O. Arslan et al., *Search for single top quark production via strong FCNC in $\sqrt{s} = 8$ TeV ATLAS data*, ATL-COM-PHYS-2014-907, 2014, URL: https://cds.cern.ch/record/1745904.

[Art+10] P. Artoisenet et al., *Automation of the matrix element reweighting method*, Journal of High Energy Physics **2010** (2010) 1, ISSN: 1029-8479.

[Art+13] P. Artoisenet et al., *Automatic spin-entangled decays of heavy resonances in Monte Carlo simulations*, JHEP **03** (2013) 015, arXiv: 1212.3460 [hep-ph].

[ATL96a] ATLAS Collaboration, *ATLAS calorimeter performance Technical Design Report*, (1996).

[ATL96b] ATLAS Collaboration, *ATLAS liquid-argon calorimeter: Technical Design Report*, Technical Design Report ATLAS, Geneva: CERN, 1996, URL: https://cds.cern.ch/record/331061.

[ATL96c] ATLAS Collaboration, *ATLAS tile calorimeter: Technical Design Report*, Technical Design Report ATLAS, Geneva: CERN, 1996, URL: https://cds.cern.ch/record/331062.

[ATL97] ATLAS Collaboration, *ATLAS muon spectrometer: Technical Design Report*, Technical Design Report ATLAS, Geneva: CERN, 1997, URL: http://cds.cern.ch/record/331068.

[ATL98] ATLAS Collaboration, *ATLFAST 2.0: A Fast Simulation Package for ATLAS*, ATL-PHYS-98-131, 1998, URL: https://cds.cern.ch/record/683751.

[ATL99] ATLAS Collaboration, *ATLAS detector and physics performance: Technical Design Report, 1*, Technical Design Report ATLAS, Geneva: CERN, 1999, URL: https://cds.cern.ch/record/391176.

[ATL08a] ATLAS Collaboration, *ATLAS pixel detector electronics and sensors*, JINST **3** (2008) P07007.

[ATL08b] ATLAS Collaboration, *The ATLAS Experiment at the CERN Large Hadron Collider*, JINST **3** (2008) S08003.

[ATL09] ATLAS Collaboration, *Expected Performance of the ATLAS Experiment - Detector, Trigger and Physics*, (2009), arXiv: 0901.0512 [hep-ex].

[ATL10a] ATLAS Collaboration, *Commissioning of the ATLAS Muon Spectrometer with cosmic rays*, Eur. Phys. J. C **70** (2010) 875, arXiv: 1006.4384 [hep-ex].

[ATL10b] ATLAS Collaboration, *Readiness of the ATLAS Tile Calorimeter for LHC collisions*, Eur. Phys. J. C **70** (2010) 1193, arXiv: 1007.5423 [hep-ex].

[ATL10c] ATLAS Collaboration, *The ATLAS Simulation Infrastructure*, Eur. Phys. J. **C70** (2010) 823, arXiv: 1005.4568.

[ATL11a] ATLAS Collaboration, *Commissioning of the ATLAS high performance b-tagging algorithms in the 7 TeV collision data*, ATLAS-CONF-2011-102, 2011, URL: http://cdsweb.cern.ch/record/1369219.

[ATL11b] ATLAS Collaboration, *New ATLAS event generator tunes to 2010 data*, ATL-PHYS-PUB-2011-008, 2011, URL: http://cds.cern.ch/record/1345343.

[ATL11c] ATLAS Collaboration, *Particle Identification Performance of the ATLAS Transition Radiation Tracker*, ATLAS-CONF-2011-128, 2011, URL: http://cdsweb.cern.ch/record/1383793.

[ATL12a] ATLAS Collaboration, *Evidence for the associated production of a W boson and a top quark in ATLAS at* $\sqrt{s} = 7$ *TeV*, Phys. Lett. **B716** (2012) 142, arXiv: 1205.5764 [hep-ex].

[ATL12b] ATLAS Collaboration, *Measurement of the b-tag Efficiency in a Sample of Jets Containing Muons with* 5 fb^{-1} *of data from the ATLAS detector*, ATLAS-CONF-2012-043, 2012, URL: http://cdsweb.cern.ch/record/1435197.

[ATL12c] ATLAS Collaboration, *Measurement of the t-channel single top-quark production cross section in pp collisions at* $\sqrt{s} = 7$ *TeV with the ATLAS detector*, Phys. Lett. **B717** (2012) 330, arXiv: 1205.3130 [hep-ex].

[ATL12d] ATLAS Collaboration, *Measuring the b-tag efficiency in a* $t\bar{t}$ *sample with* 4.7 fb^{-1} *of data from the ATLAS detector*, ATLAS-CONF-2012-097, 2012, URL: http://cdsweb.cern.ch/record/1460443.

[ATL12e] ATLAS Collaboration, *Performance of the ATLAS Trigger System in 2010*, Eur. Phys. J. C **72** (2012) 1849, arXiv: 1110.1530 [hep-ex].

[ATL13a] ATLAS Collaboration, *Improved Luminosity Determination in pp Collisions at* $\sqrt{s}$=7 *TeV using the ATLAS Detector at the LHC*, Eur. Phys. J. **C73** (2013) 2518, arXiv: 1302.4393 [hep-ex].

[ATL13b] ATLAS Collaboration, *Jet energy measurement with the ATLAS detector in proton–proton collisions at* $\sqrt{s} = 7$ *TeV*, Eur. Phys. J. C **73** (2013) 2304, arXiv: 1112.6426 [hep-ex].

[ATL13c] ATLAS Collaboration, *Jet energy resolution in proton–proton collisions at* $\sqrt{s} = 7$ *TeV recorded in 2010 with the ATLAS detector*, Eur. Phys. J. C **73** (2013) 2306, arXiv: 1210.6210 [hep-ex].

[ATL13d] ATLAS Collaboration, *Jet energy scale and its systematic uncertainty in proton–proton collisions at* $\sqrt{s} = 7$ *TeV with ATLAS 2011 data*, ATLAS-CONF-2013-004, 2013, URL: http://cdsweb.cern.ch/record/1509552.

[ATL13e] ATLAS Collaboration, *Performance of Missing Transverse Momentum Reconstruction in ATLAS studied in Proton–Proton Collisions recorded in 2012 at* $\sqrt{s} = 8$ *TeV*, ATLAS-CONF-2013-082, 2013, URL: http://cdsweb.cern.ch/record/1570993.

[ATL14a] ATLAS Collaboration, *Calibration of b-tagging using dileptonic top pair events in a combinatorial likelihood approach with the ATLAS experiment*, ATLAS-CONF-2014-004, 2014, URL: http://cdsweb.cern.ch/record/1664335.

[ATL14b] ATLAS Collaboration, *Calibration of the performance of* b*-tagging for* c *and light-flavour jets in the 2012 ATLAS data*, ATLAS-CONF-2014-046, 2014, URL: http://cdsweb.cern.ch/record/1741020.

[ATL14c] ATLAS Collaboration, *Electron efficiency measurements with the ATLAS detector using the 2012 LHC proton–proton collision data*, ATLAS-CONF-2014-032, 2014, URL: http://cdsweb.cern.ch/record/1706245.

[ATL14d] ATLAS Collaboration, *Estimation of non-prompt and fake lepton backgrounds in final states with top quarks produced in proton–proton collisions at $\sqrt{s} = 8$ TeV with the ATLAS Detector*, ATLAS-CONF-2014-058, 2014, URL: http://cdsweb.cern.ch/record/1951336.

[ATL14e] ATLAS Collaboration, *Measurement of the muon reconstruction performance of the ATLAS detector using 2011 and 2012 LHC proton–proton collision data*, Eur. Phys. J. C **74** (2014) 3130, arXiv: 1407.3935 [hep-ex].

[ATL14f] ATLAS Collaboration, *Operation and performance of the ATLAS semiconductor tracker*, JINST **9** (2014) P08009, arXiv: 1404.7473 [hep-ex].

[ATL15a] ATLAS Collaboration, *Comparison of Monte Carlo generator predictions to ATLAS measurements of top pair production at 7 TeV*, ATL-PHYS-PUB-2015-002, 2015, URL: http://cdsweb.cern.ch/record/1981319.

[ATL15b] ATLAS Collaboration, *Identification and energy calibration of hadronically decaying tau leptons with the ATLAS experiment in pp collisions at $\sqrt{s}$=8 TeV*, Eur. Phys. J. **C75** (2015) 303, arXiv: 1412.7086 [hep-ex].

[ATL15c] ATLAS Collaboration, *Performance of the ATLAS muon trigger in pp collisions at $\sqrt{s} = 8$ TeV*, Eur. Phys. J. C **75** (2015) 120, arXiv: 1408.3179 [hep-ex].

[ATL15d] ATLAS Collaboration, *Search for charged Higgs bosons decaying via $H^{\pm} \to \tau^{\pm}\nu$ in fully hadronic final states using pp collision data at $\sqrt{s} =$ 8 TeV with the ATLAS detector*, JHEP **1503** (2015) 088, arXiv: 1412.6663 [hep-ex].

[ATL15e] ATLAS Collaboration, *Search for the Standard Model Higgs boson produced in association with top quarks and decaying into $b\bar{b}$ in pp collisions at $\sqrt{s} = 8$ TeV with the ATLAS detector*, Eur. Phys. J. **C75** (2015) 349, arXiv: 1503.05066 [hep-ex].

[ATL15f] ATLAS Collaboration, *Search for $W' \to t\bar{b}$ in the lepton plus jets final state in proton–proton collisions at a centre-of-mass energy of $\sqrt{s} = 8$ TeV with the ATLAS detector*, Phys. Lett. B **743** (2015) 235, arXiv: 1410.4103 [hep-ex].

[ATL16a] ATLAS Collaboration, *Evidence for single top-quark production in the s-channel in proton-proton collisions at $\sqrt{s}$ =8 TeV with the ATLAS detector using the Matrix Element Method*, Phys. Lett. **B756** (2016) 228, arXiv: 1511.05980 [hep-ex].

[ATL16b] ATLAS Collaboration, *Luminosity determination in pp collisions at $\sqrt{s}$=8 TeV using the ATLAS detector at the LHC*, Eur. Phys. J. **C76** (2016) 653, arXiv: 1608.03953 [hep-ex].

[ATL16c] ATLAS Collaboration, *Measurement of the cross-section for producing a W boson in association with a single top quark in pp collisions at $\sqrt{s} = 13$ TeV with ATLAS*, (2016), arXiv: 1612.07231 [hep-ex].

[ATL16d] ATLAS Collaboration, *Measurement of the production cross-section of a single top quark in association with a W boson at 8 TeV with the ATLAS experiment*, JHEP **1601** (2016) 064, arXiv: 1510.03752 [hep-ex].

[ATL16e] ATLAS Collaboration, *Search for single top-quark production via flavour-changing neutral currents at 8 TeV with the ATLAS detector*, Eur. Phys. J. C **76** (2016) 55, arXiv: 1509.00294 [hep-ex].

[ATL17a] ATLAS Collaboration, *Fiducial, total and differential cross-section measurements of t-channel single top-quark production in pp collisions at 8 TeV using data collected by the ATLAS detector*, (2017), arXiv: 1702.02859 [hep-ex].

[ATL17b] ATLAS Collaboration, *Measurement of the inclusive cross-sections of single top-quark and top-antiquark t-channel production in pp collisions at $\sqrt{s} = 13$ TeV with the ATLAS detector*, JHEP **04** (2017) 086, arXiv: 1609.03920 [hep-ex].

[ATL17c] ATLAS Collaboration, *Probing the Wtb vertex structure in t-channel single-top-quark production and decay in pp collisions at $\sqrt{\mathrm{s}} = 8$ TeV with the ATLAS detector*, JHEP **04** (2017) 124, arXiv: 1702.08309 [hep-ex].

[ATL17d] ATLAS Collaboration, *Search for squarks and gluinos in final states with jets and missing transverse momentum using 36 fb^{-1} of $\sqrt{s} = 13$ TeV pp collision data with the ATLAS detector*, (2017).

[ATL08c] ATLAS TRT Collaboration, *The ATLAS Transition Radiation Tracker (TRT) proportional drift tube: Design and performance*, JINST **3** (2008) P02013.

[Bal+13] R. D. Ball et al., *Parton distributions with LHC data*, Nucl. Phys. **B867** (2013) 244, arXiv: 1207.1303 [hep-ph].

[BB93] R. J. Barlow and C. Beeston, *Fitting Using Finite Monte Carlo Samples*, Comput. Phys. Commun. **77** (1993) 219.

[BCM12] P. Bärnreuther, M. Czakon and A. Mitov, *Percent Level Precision Physics at the Tevatron: First Genuine NNLO QCD Corrections to $q\bar{q} \to t\bar{t}+X$*, Phys. Rev. Lett. **109** (2012) 132001, arXiv: 1204.5201 [hep-ph].

[Ber+91] F. A. Berends et al., *On the Production of a W and Jets at Hadron Colliders*, Nucl. Phys. **B357** (1991) 32.

[Bes+16] O. Bessidskaia Bylund et al., *Probing top quark neutral couplings in the Standard Model Effective Field Theory at NLO in QCD*, JHEP **05** (2016) 052, arXiv: 1601.08193 [hep-ph].

[Beu+12] S. Beumler et al., *Kinematic Fitting of ATLAS Data Using the KinFitter Package*, ATL-COM-PHYS-2012-1554, 2012, URL: https://cds.cern.ch/record/1490366.

[Bey17] O. Bey, 'Eine Analyse der Einzel-Top-Quark-Produktion im t-Kanal bei einer Schwerpunktsenergie von $\sqrt{s} = 8\,\text{TeV}$ am ATLAS Experiment', in preparation, Bachelor thesis: Humboldt-Universität zu Berlin, 2017.

[BE95] G. Bordes and B. van Eijk, *Calculating QCD corrections to single top production in hadronic interactions*, Nucl. Phys. **B435** (1995) 23.

[Bot+11] M. Botje et al., *The PDF4LHC Working Group Interim Recommendations*, (2011), arXiv: 1101.0538 [hep-ph].

[BCM14] M. Brucherseifer, F. Caola and K. Melnikov, *On the NNLO QCD corrections to single-top production at the LHC*, Phys. Lett. **B736** (2014) 58, arXiv: 1404.7116 [hep-ph].

[BR97] R. Brun and F. Rademakers, *ROOT: An object oriented data analysis framework*, Nucl. Instrum. Meth. **A389** (1997) 81.

[BW86] W. Buchmuller and D. Wyler, *Effective Lagrangian Analysis of New Interactions and Flavor Conservation*, Nucl. Phys. **B268** (1986) 621.

[Buc+15] A. Buckley et al., *Global fit of top quark effective theory to data*, Phys. Rev. **D92** (2015) 091501, arXiv: 1506.08845 [hep-ph].

[BFS96] J. Butterworth, J. R. Forshaw and M. Seymour, *Multiparton Interactions in Photoproduction at HERA*, Z. Phys. **C72** (1996) 637, arXiv: hep-ph/9601371 [hep-ph].

[CS08] M. Cacciari and G. P. Salam, *Pileup subtraction using jet areas*, Phys. Lett. **B659** (2008) 119, arXiv: 0707.1378 [hep-ph].

[CSS08a] M. Cacciari, G. P. Salam and G. Soyez, *The Anti-k(t) jet clustering algorithm*, JHEP **04** (2008) 063, arXiv: 0802.1189 [hep-ph].

[CSS08b] M. Cacciari, G. P. Salam and G. Soyez, *The Catchment Area of Jets*, JHEP **04** (2008) 005, arXiv: 0802.1188 [hep-ph].

[CSS12] M. Cacciari, G. P. Salam and G. Soyez, *FastJet User Manual*, Eur. Phys. J. **C72** (2012) 1896, arXiv: 1111.6097 [hep-ph].

[Cac+12] M. Cacciari et al., *Top-Pair Production at Hadron Colliders with Next-To-Next-To-Leading Logarithmic Soft-Gluon Resummation*, Phys. Lett. **B710** (2012) 612, arXiv: 1111.5869 [hep-ph].

[CKK09] A. Caldwell, D. Kollár and K. Kröninger, {*BAT*} - *The Bayesian analysis toolkit*, Computer Physics Communications **180** (2009) 2197, ISSN: 0010-4655.

[CE10] J. Campbell and R. Ellis, *MCFM for the Tevatron and the LHC*, Nucl. Phys. Proc. Suppl. **205–206** (2010) 10, arXiv: 1007.3492 [hep-ph].

[CEW11] J. M. Campbell, R. K. Ellis and C. Williams, *Vector Boson Pair Production at the LHC*, JHEP **1107** (2011) 018, arXiv: 1105.0020 [hep-ph].

[CHS07] J. M. Campbell, J. W. Huston and W. J. Stirling, *Hard Interactions of Quarks and Gluons: A Primer for LHC Physics*, Rept. Prog. Phys. **70** (2007) 89, arXiv: hep-ph/0611148 [hep-ph].

[Cas+16] N. Castro et al., *EFTfitter—A tool for interpreting measurements in the context of effective field theories*, Eur. Phys. J. **C76** (2016) 432, arXiv: 1605.05585 [hep-ex].

[CDF14] CDF and D0 Collaborations, *Observation of s-channel production of single top quarks at the Tevatron*, Phys. Rev. Lett. **112** (2014) 231803, arXiv: 1402.5126 [hep-ex].

[CDF95] CDF Collaboration, *Observation of top quark production in $\bar{p}p$ collisions*, Phys. Rev. Lett. **74** (1995) 2626, arXiv: hep-ex/9503002 [hep-ex].

[CDF09a] CDF Collaboration, *First Observation of Electroweak Single Top Quark Production*, Phys. Rev. Lett. **103** (2009) 092002, arXiv: 0903.0885 [hep-ex].

[CDF09b] CDF Collaboration, *First Observation of Electroweak Single Top Quark Production*, Phys. Rev. Lett. **103** (2009) 092002, arXiv: 0903.0885 [hep-ex].

[Chr+11] N. D. Christensen et al., *A Comprehensive approach to new physics simulations*, Eur. Phys. J. **C71** (2011) 1541, arXiv: 0906.2474 [hep-ph].

[CMS08] CMS Collaboration, *The CMS experiment at the CERN LHC*, JINST **3** (2008) S08004.

[CMS12] CMS Collaboration, *Measurement of the single-top-quark t-channel cross section in pp collisions at $\sqrt{s} = 7$ TeV*, JHEP **12** (2012) 035, arXiv: 1209.4533 [hep-ex].

[CMS13] CMS Collaboration, *Evidence for associated production of a single top quark and W boson in pp collisions at $\sqrt{s} = 7$ TeV*, Phys. Rev. Lett. **110** (2013) 022003, arXiv: 1209.3489 [hep-ex].

[CMS15] CMS Collaboration, *Search for a Standard Model Higgs Boson Produced in Association with a Top-Quark Pair and Decaying to Bottom Quarks Using a Matrix Element Method*, Eur. Phys. J. **C75** (2015) 251, arXiv: 1502.02485 [hep-ex].

[CMS16] CMS Collaboration, *Measurement of spin correlations in $t\bar{t}$ production using the matrix element method in the muon+jets final state in pp collisions at $\sqrt{s}$ = 8 TeV*, Phys. Lett. **B758** (2016) 321, arXiv: 1511.06170 [hep-ex].

[Coc+13] J. Cochran et al., *Search for Pair Produced New Heavy Quarks that Decay into a W Boson and a Light Quark in pp collisions at $\sqrt{s}$ =8 TeV with the ATLAS Detector*, ATL-COM-PHYS-2013-1005, 2013, URL: https://cds.cern.ch/record/1562311.

[Con+16] R. Contino et al., *On the Validity of the Effective Field Theory Approach to SM Precision Tests*, JHEP **07** (2016) 144, arXiv: 1604.06444 [hep-ph].

[Cor+01] G. Corcella et al., *HERWIG 6: An Event Generator for Hadron Emission Reactions with Interfering Gluons (Including Supersymmetric Processes)*, JHEP **0101** (2001) 010, arXiv: hep-ph/0011363 [hep-ph].

[Cra+12] K. Cranmer et al., *HistFactory: A Tool for Creating Statistical Models for Use with RooFit and RooStats*, (2012).

[CFM13] M. Czakon, P. Fiedler and A. Mitov, *Total Top-Quark Pair-Production Cross Section at Hadron Colliders Through $O(\alpha_s^4)$*, Phys. Rev. Lett. **110** (2013) 252004, arXiv: 1303.6254 [hep-ph].

[CM11] M. Czakon and A. Mitov, *Top++: A Program for the Calculation of the Top-Pair Cross-Section at Hadron Colliders*, (2011), arXiv: 1112.5675 [hep-ph].

[CM12] M. Czakon and A. Mitov, *NNLO Corrections to Top-Pair Production at Hadron Colliders: the All-Fermionic Scattering Channels*, JHEP **1212** (2012) 054, arXiv: 1207.0236 [hep-ph].

[CM13] M. Czakon and A. Mitov, *NNLO Corrections to Top Pair Production at Hadron Colliders: the Quark-Gluon Reaction*, JHEP **1301** (2013) 080, arXiv: 1210.6832 [hep-ph].

[D0 95] D0 Collaboration, *Observation of the top quark*, Phys. Rev. Lett. **74** (1995) 2632, arXiv: hep-ex/9503003 [hep-ex].

[D0 04] D0 Collaboration, *A precision measurement of the mass of the top quark*, Nature **429** (2004) 638, arXiv: hep-ex/0406031 [hep-ex].

[D0 09a] D0 Collaboration, *Observation of Single Top Quark Production*, Phys. Rev. Lett. **103** (2009) 092001, arXiv: 0903.0850 [hep-ex].

[D0 09b] D0 Collaboration, *Observation of Single Top Quark Production*, Phys. Rev. Lett. **103** (2009) 092001, arXiv: 0903.0850 [hep-ex].

[Deg15] C. Degrande, 'Implementation of the top effective-field theory for MG5', 2015, URL: https://cp3.irmp.ucl.ac.be/projects/madgraph/attachment/wiki/Models/TopEffTh/note.pdf.

[Deg+12] C. Degrande et al., *UFO - The Universal FeynRules Output*, Comput. Phys. Commun. **183** (2012) 1201, arXiv: 1108.2040 [hep-ph].

[Deg+13] C. Degrande et al., *Effective Field Theory: A Modern Approach to Anomalous Couplings*, Annals Phys. **335** (2013) 21, arXiv: 1205.4231 [hep-ph].

[Ell+79] R. Ellis et al., *Perturbation theory and the parton model in QCD*, Nuclear Physics B **152** (1979) 285, ISSN: 0550-3213.

[EKS85] S. Ellis, R. Kleiss and W. J. Stirling, *W's, Z's and Jets*, Phys. Lett. **B154** (1985) 435.

[Erd+14] J. Erdmann et al., *A Likelihood-Based Reconstruction Algorithm for Top-Quark Pairs and the KLFitter Framework*, Nucl. Instrum. Meth. **A748** (2014) 18, arXiv: 1312.5595 [hep-ex].

[Fav+14] J. de Favereau et al., *DELPHES 3, A modular framework for fast simulation of a generic collider experiment*, JHEP **02** (2014) 057, arXiv: 1307.6346 [hep-ex].

[FNO07] S. Frixione, P. Nason and C. Oleari, *Matching NLO QCD Computations with Parton Shower Simulations: the POWHEG Method*, JHEP **0711** (2007) 070, arXiv: 0709.2092 [hep-ph].

[Fri+06] S. Frixione et al., *Single-top Production in MC@NLO*, JHEP **0603** (2006) 092, arXiv: hep-ph/0512250 [hep-ph].

[Fri+07] S. Frixione et al., *Angular correlations of lepton pairs from vector boson and top quark decays in Monte Carlo simulations*, JHEP **04** (2007) 081, arXiv: hep-ph/0702198 [HEP-PH].

[GGS99] M. K. Gaillard, P. D. Grannis and F. J. Sciulli, *The standard model of particle physics*, Rev. Mod. Phys. **71** (2 1999) S96.

[Gle+09] T. Gleisberg et al., *Event Generation with SHERPA 1.1*, JHEP **0902** (2009) 007, arXiv: 0811.4622 [hep-ph].

[Grz+04] B. Grzadkowski et al., *Probing anomalous top quark couplings induced by dimension-six operators at photon colliders*, Nucl. Phys. **B689** (2004) 108, arXiv: hep-ph/0310159 [hep-ph].

[Grz+10] B. Grzadkowski et al., *Dimension-Six Terms in the Standard Model Lagrangian*, JHEP **10** (2010) 085, arXiv: 1008.4884 [hep-ph].

[Hah06] T. Hahn, *The CUBA Library*, Nucl. Instrum. Meth. **A559** (2006) 273, arXiv: hep-ph/0509016 [hep-ph].

[Her+77] S. W. Herb et al., *Observation of a Dimuon Resonance at 9.5 GeV in 400-GeV Proton-Nucleus Collisions*, Phys. Rev. Lett. **39** (5 1977) 252.

[Her14] R. H. M. Herrberg-Schubert, 'Cross-section measurement of single-top t-channel production at ATLAS', PhD thesis: Humboldt-Universität zu Berlin, 2014, URN: urn:nbn:de:kobv:11-100217726.

[JR75] F. James and M. Roos, *MINUIT: A System for Function Minimization and Analysis of the Parameter Errors and Correlations*, Comput. Phys. Commun. **10** (1975) 343.

[Kan+15] P. Kant et al., *HatHor for single top-quark production: Updated predictions and uncertainty estimates for single top-quark production in hadronic collisions*, Comput. Phys. Commun. **191** (2015) 74, arXiv: 1406.4403 [hep-ph].

[Kap15] S. Kaphle, 'Vergleich und Optimierung von Monte-Carlo-Integrationsalgorithmen für die Matrixelementmethode', Bachelor thesis: Humboldt-Universität zu Berlin, 2015.

[KNK08] R. Kehoe, M. Narain and A. Kumar, *Review of Top Quark Physics Results*, Int. J. Mod. Phys. **A23** (2008) 353, arXiv: 0712.2733 [hep-ex].

[KR13] B. P. Kersevan and E. Richter-Was, *The Monte Carlo Event Generator AcerMC Versions 2.0 to 3.8 with Interfaces to PYTHIA 6.4, HERWIG 6.5 and ARIADNE 4.1*, Comput. Phys. Commun. **184** (2013) 919, arXiv: hep-ph/0405247 [hep-ph].

[Kid10a] N. Kidonakis, *NNLL resummation for s-channel single top quark production*, Phys. Rev. **D81** (2010) 054028, arXiv: 1001.5034 [hep-ph].

[Kid10b] N. Kidonakis, *Two-loop soft anomalous dimensions for single top quark associated production with a W- or H-*, Phys. Rev. **D82** (2010) 054018, arXiv: 1005.4451 [hep-ph].

[Kid11] N. Kidonakis, *Next-to-next-to-leading-order collinear and soft gluon corrections for t-channel single top quark production*, Phys. Rev. **D83** (2011) 091503, arXiv: 1103.2792 [hep-ph].

[Kin+] O. M. Kind et al., 'The Matrix Element Method Toolkit', in preparation.

[Kin+15] O. M. Kind et al., *Combined measurement of single top-quark production in the s and t-channel in proton-proton collisions at $\sqrt{s} = 8\,TeV$ with the ATLAS detector using the matrix element method*, ATL-COM-PHYS-2015-1462, 2015, URL: https://cds.cern.ch/record/2110644.

[Kin+14] O. Kind et al., *Measurement of single top-quark production in the s-channel in proton–proton collisions at $\sqrt{s} = 8\,TeV$ with the ATLAS detector using the matrix element method*, ATL-COM-PHYS-2014-1555, 2014, URL: https://cds.cern.ch/record/1974821.

[Kon88] K. Kondo, *Dynamical Likelihood Method for Reconstruction of Events With Missing Momentum. 1: Method and Toy Models*, J. Phys. Soc. Jap. **57** (1988) 4126.

[Lai+10] H.-L. Lai et al., *New Parton Distributions for Collider Physics*, Phys. Rev. **D82** (2010) 074024, arXiv: 1007.2241 [hep-ph].

[Lam13] M. Lamont, *Status of the LHC*, J. Phys. Conf. Ser. **455** (2013) 012001.

[Lep78] G. P. Lepage, *A New Algorithm for Adaptive Multidimensional Integration*, J. Comput. Phys. **27** (1978) 192.

[LHC08] LHCb Collaboration, *The LHCb Detector at the LHC*, JINST **3** (2008) S08005.

[Luk12] W. Lukas, *Fast Simulation for ATLAS: Atlfast-II and ISF*, Journal of Physics: Conference Series **396** (2012) 022031.

[MVZ16] F. Maltoni, E. Vryonidou and C. Zhang, *Higgs production in association with a top-antitop pair in the Standard Model Effective Field Theory at NLO in QCD*, JHEP **10** (2016) 123, arXiv: 1607.05330 [hep-ph].

[Man+03] M. L. Mangano et al., *ALPGEN, a Generator for Hard Multiparton Processes in Hadronic Collisions*, JHEP **0307** (2003) 001, arXiv: hep-ph/0206293 [hep-ph].

[Mar+09] A. Martin et al., *Uncertainties on α_s in Global PDF Analyses and Implications for Predicted Hadronic Cross Sections*, Eur. Phys. J. **C64** (2009) 653, arXiv: 0905.3531 [hep-ph].

[MU15] T. Martini and P. Uwer, *The Matrix Element Method at Next-to-Leading Order Accuracy*, Acta Phys. Polon. **B46** (2015) 2143, arXiv: 1511.07150 [hep-ph].

[MSS09] D. W. Miller, A. Schwartzman and D. Su, *Pile-up jet energy scale corrections using the jet-vertex fraction method*, ATL-PHYS-INT-2009-090, 2009, URL: https://cds.cern.ch/record/1206864.

[Mon+10] L. Moneta et al., *The RooStats Project*, PoS **ACAT2010** (2010) 057, arXiv: 1009.1003.

[NP33] J. Neyman and E. S. Pearson, *On the Problem of the Most Efficient Tests of Statistical Hypotheses*, Philosophical Transactions of the Royal Society of London. Series A, Containing Papers of a Mathematical or Physical Character **231** (1933) 289, ISSN: 02643952, URL: http://www.jstor.org/stable/91247.

[Pas+15] G. Pasztor et al., *Electron trigger performance in 2012 ATLAS data*, ATL-COM-DAQ-2015-091, 2015, URL: https://cds.cern.ch/record/2032463.

[Pat+16] C. Patrignani et al., *Review of Particle Physics*, Chin. Phys. **C40** (2016) 100001.

[Peq08a] J. Pequenao, 'Computer Generated image of the ATLAS calorimeter', 2008, URL: https://cds.cern.ch/record/1095927.

[Peq08b] J. Pequenao, 'Computer generated image of the ATLAS inner detector', 2008, URL: https://cds.cern.ch/record/1095926.

[Peq08c] J. Pequenao, 'Computer generated image of the ATLAS Muons subsystem', 2008, URL: https://cds.cern.ch/record/1095929.

[Peq08d] J. Pequenao, 'Computer generated image of the whole ATLAS detector', 2008, URL: https://cds.cern.ch/record/1095924.

[PW08] G. Piacquadio and C. Weiser, *A new inclusive secondary vertex algorithm for b-jet tagging in ATLAS*, J. Phys. Conf. Ser. **119** (2008) 032032.

[RT11] K. Rehermann and B. Tweedie, *Efficient Identification of Boosted Semileptonic Top Quarks at the LHC*, JHEP **03** (2011) 059, arXiv: 1007.2221 [hep-ph].

[Rie10] P. Rieck, 'Entwicklung eines kinematischen Fits zur Untersuchung elektroschwacher Top-Quark-Produktion bei ATLAS', Master thesis: Humboldt-Universität zu Berlin, 2010.

[Rie16] P. Rieck, 'Measurement of s-channel single top-quark production with the ATLAS detector using total event likelihoods', PhD thesis: Humboldt-Universität zu Berlin, 2016, URN: urn:nbn:de:kobv:11-100241170.

[Sch12] F.-P. Schilling, *Top Quark Physics at the LHC: A Review of the First Two Years*, Int. J. Mod. Phys. **A27** (2012) 1230016, arXiv: 1206.4484 [hep-ex].

[Sch17] J. Schürmann, 'Untersuchungen zur schnellen Detektorsimulation in Single-Top-Production bei ATLAS ', in preparation, Bachelor thesis: Humboldt-Universität zu Berlin, 2017.

[SMS06] T. Sjostrand, S. Mrenna and P. Z. Skands, *PYTHIA 6.4 Physics and Manual*, JHEP **0605** (2006) 026, arXiv: hep-ph/0603175 [hep-ph].

[Ska10] P. Z. Skands, *Tuning Monte Carlo Generators: The Perugia Tunes*, Phys. Rev. **D82** (2010) 074018, arXiv: 1005.3457 [hep-ph].

[Sol12] V. Solovyev, 'Evolution and Performance of Electron and Photon Triggers in ATLAS in the year 2011', *Proceedings, 2012 18th IEEE-NPSS Real Time Conference*, 2012, URL: http://cdsweb.cern.ch/record/1455482/.

[Sta13] S. Stamm, 'Studien zur Signalextraktion elektroschwacher Top-Quark--Produktion bei ATLAS', Master thesis: Humboldt-Universität zu Berlin, 2013.

[SSW97] T. Stelzer, Z. Sullivan and S. Willenbrock, *Single top quark production via W - gluon fusion at next-to-leading order*, Phys. Rev. **D56** (1997) 5919, arXiv: hep-ph/9705398 [hep-ph].

[SSW98] T. Stelzer, Z. Sullivan and S. Willenbrock, *Single top quark production at hadron colliders*, Phys. Rev. **D58** (1998) 094021, arXiv: hep-ph/9807340 [hep-ph].

[TY00] T. M. P. Tait and C. .-.-P. Yuan, *Single top quark production as a window to physics beyond the standard model*, Phys. Rev. **D63** (2000) 014018, arXiv: hep-ph/0007298 [hep-ph].

[Tep+15] F.-P. Tepel et al., *Measurement of the Inclusive and Fiducial Cross-Section in Single Top-Quark t-Channel Events in pp Collisions at* $\sqrt{s} = 8\,TeV$, ATL-COM-PHYS-2015-177, 2015, URL: https://cds.cern.ch/record/1999237.

[VK03] W. Verkerke and D. P. Kirkby, *The RooFit Toolkit for Data Modeling*, eConf **C0303241** (2003) MOLT007, arXiv: physics/0306116 [physics].

[Wei79] S. Weinberg, *Baryon- and Lepton-Nonconserving Processes*, Phys. Rev. Lett. **43** (21 1979) 1566.

[Wer16] S. Wertz, *The Matrix Element Method at the LHC: status and prospects for Run II*, J. Phys. Conf. Ser. **762** (2016) 012053.

[WBG05] M. Whalley, D. Bourilkov and R. Group, *The Les Houches accord PDFs (LHAPDF) and LHAGLUE*, (2005), arXiv: hep-ph/0508110 [hep-ph].

[WZ14] S. Willenbrock and C. Zhang, *Effective Field Theory Beyond the Standard Model*, Ann. Rev. Nucl. Part. Sci. **64** (2014) 83, arXiv: 1401.0470 [hep-ph].

[ZW10] C. Zhang and S. Willenbrock, *Effective Field Theory for Top Quark Physics*, Nuovo Cim. **C033** (2010) 285, arXiv: 1008.3155 [hep-ph].

[ZW11] C. Zhang and S. Willenbrock, *Effective-field-theory approach to top-quark production and decay*, Phys. Rev. D **83** (3 2011) 034006.

Danksagung

Ich bedanke mich bei meinem Doktorvater, Prof. Dr. Thomas Lohse, für die Möglichkeit zur Promotion. Für die fachliche Betreuung und den wissenschaftlichen Rat zu den verschiedenen Themen meiner Arbeit bin ich außerordentlich dankbar.

Einen sehr großen Anteil an der erfolgreichen Promotion hat Dr. Oliver Maria Kind. Vielen Dank für die Betreuung meiner Arbeiten, die in unserer gemeinsamen Zeit in der Arbeitsgruppe entstanden sind. Ich habe viel von dir gelernt und hätte mir keine bessere Unterstützung wünschen können.

Mein ausdrücklicher Dank geht auch an Veronika Schneider für das Beseitigen der vielen kleinen und großen Hürden auf dem Weg zur Promotion, sowie die vielen Gespräche abseits der Promotion.

Bei Patrick Rieck möchte ich mich bedanken für die Vorarbeiten bei der Matrixelement-Methode. I would like to thank James A. Mueller for the valuable and positive feedback on the effective field theory part.

Für die Unterstützung während unserem gemeinsamen Studiums und insbesondere in den anstrengenden Phasen der Doktorarbeit möchte ich mich ganz herzlich bei Julia und Steffi bedanken. Gleiches gilt für dich Luise und vielen Dank für die Motivation meine Doktorarbeit schneller zu schreiben.

Nicht zuletzt geht mein Dank an meine Eltern, die mir das Studium in Berlin ermöglicht haben. Ihr habt mir alle Freiheiten gegeben das Studium so umzusetzen, wie ich es wollte und dafür bin ich euch sehr dankbar. Ich danke auch meinen Geschwistern und Freunden in der Heimat für die Unterstützung in den letzten zehn Jahren und darüber hinaus.